Hugo Manuel Ramos Moreira

Master of Science in Biomedical Engineering

Investigating the mechanisms of α-particle therapy in prostate cancer

Thesis submitted in partial fulfilment
of the requirements for the degree of

Doctor of Philosophy in
Radiation Biology and Biophysics

Supervisor: Professor Kevin Michael Prise, Full Professor
School of Medicine, Dentistry and Biomedical Sciences, Queen's University Belfast

Co-supervisors: Dr. Stephen Joseph McMahon, Lecturer
School of Medicine, Dentistry and Biomedical Sciences, Queen's University Belfast

Professor Maria Alice Santos Pereira, Assistant Professor
NOVA School of Sciences and Technology

Examination Committee

Chairperson: Professor Paulo Manuel Assis Loureiro Limão Vieira

Rapporteurs: Professor Giuseppe Schettino
Professor Mark Hill

Members: Professor Kevin Michael Prise
Professor Pedro António de Brito Tavares

FACULDADE DE CIÊNCIAS E TECNOLOGIA
UNIVERSIDADE NOVA DE LISBOA

March 2020

Investigating the mechanisms of α-particle therapy in prostate cancer

ACKNOWLEDGMENTS

I want to start by thanking my supervisors Kevin Prise and Stephen McMahon for the opportunity given to me, for all their vast experience shared with me and for the countless discussions we had about this work. Every conversation was incredibly valuable and allowed me to grow and succeed after failing.

I also want to thank my colleagues from our research group at CCRCB, both students, post-docs and technicians. To the Cancer Centre staff, Cyril, Conor and Ray, for their help in building the α-source holder and collimators used in our research work.

To the Portuguese National Funding Agerncy FCT-MCTES for the scholarship they provided me (SFRH/BD/52534/2014). This work was also supported by Radiation Biology and Biophysics Doctoral Training Programme (RaBBiT, PD/00193/2012), UIDB/00068/2020 (CEFITEC) and UIDB/04378/2020) (UCIBIO).

I want to especially thank my group of friends who I met in Belfast. Fiammetta, Alessandro, Jordan, Soraia, Matt, Federica, Tommaso, Carla and Francisco. They made my life, as a stressed PhD foreigner student, easier.

To the improv community, I thank them for keeping me sane and joyful after many stressed days at the lab.

To Natalie, she supported me through light and dark days throughout my thesis. She always believed I could make it. I can't thank her enough.

From this point on I'll continue my acknowledgements in Portuguese. This is for my friends and family from Portugal, it would not sound as real and truthful as if I did it in English:

Aos meus amigos de longa data do grupo "Coubes". Fazem-me sentir perto mesmo não estando. De cada vez que volto, nunca sinto que estive longe. São a minha casa.

Finalmente, aos meus pais. O agradecimento mais importante é para eles. Sempre me apoiaram nas minhas escolhas, muitas vezes com consequências difíceis. A minha viagem para Belfast foi uma delas. Não é fácil estar longe deles. Mas fazem de tudo para que sinta que estão presentes. E estão. Esta tese é dedicada a eles.

ABSTRACT

The use of α-particle radionuclide emitters in the treatment of bone metastasis has been an active area of research within targeted radionuclide therapies. From a radiobiological perspective, α-particles are known to be more effective at killing cells in comparison to low linear energy transfer (LET) radiation particles, such as X-rays, with increased relative biological effectiveness of around a factor of 3 in most models. α-particle irradiated cells also show a reduced dependency on radioresistance mechanisms observed in the absence of oxygen, with an oxygen enhancement ratio (OER) close to 1.0. Such advantageous radiobiological properties of α-particles demonstrate their potential for radiotherapy treatments.

In recent years, the bone targeting high LET radionuclide Radium-223 (^{223}Ra) has been shown to not only have a palliative effect but also a survival prolonging effect in castration resistant prostate cancer patients with bone metastases. This has encouraged the use of ^{233}Ra in more extensive clinical trials. Despite the clinical utility of ^{233}Ra, little is known regarding the radionuclide's mechanisms of action in this treatment setting, where accurate assessments of the dosimetry underpinning its effectiveness are lacking. There is a pressing need to model and quantify α-emitter effects in pre-clinical models so the next generation of trials utilising ^{223}Ra can be optimally designed.

The research work presented in this thesis focused on studying the dosimetry involved in α-particle irradiation systems for *in vitro* and clinical settings, using computational simulation methods. We have also studied the α-particle irradiation effects on cell survival, DNA damage and tumour control, focusing specifically on ^{223}Ra treatment scenarios.

Key words: α-particles; Radium-223; prostate cancer; metastasis; tumour control; dosimetry

RESUMO

O uso de radionuclídeos emissores de partículas α para tratamentos de metástases ósseas tem sido uma das áreas de investigação científica mais ativamente exploradas no que toca a tratamentos com radionuclídeos. Numa perspetiva radiobiológica, sabe-se que as partículas α são mais eficientes na indução de morte celular em comparação com partículas radioativas de baixa transferência linear de energia (LET), como os raios-X, sendo que as partículas α têm também uma maior eficiência biológica relativa (RBE), cerca de 3 vezes mais. As células que são irradiadas com partículas α demonstram também uma redução na dependência de mecanismos de radiorresistência observados na ausência de oxigénio, apresentado valores de relação de enriquecimento em oxigénio (OER) perto de 1.0. Estas propriedades radiobiológicas demonstram o potencial das partículas α para tratamentos de radioterapia.

Nos últimos anos, o radionuclídeo Rádio-223 (^{223}Ra), tendo maior absorção no tecido ósseo, não só tem demonstrado um efeito paliativo positivo como também um efeito de maior longevidade em doentes com cancro da próstata resistente a castração e com metástases ósseas. Isso estimulou o uso do ^{223}Ra em ensaios clínicos avançados. Apesar da utilidade clínica do ^{223}Ra, pouco se sabe sobre os seus mecanismos de ação, principalmente na dosimetria e no seu efeito para a eficácia de tratamentos. Existe assim uma necessidade premente em quantificar os efeitos de radionuclídeos emissores de partículas α em ensaios pre-clínicos, de forma a que se possa otimizar a próxima geração de tratamentos com ^{223}Ra.

O trabalho de investigação apresentado nesta tese foca-se no estudo da dosimetria envolvida em sistemas de irradiação com partículas α em modelos *in vitro* e clínicos, usando métodos de simulação computacional. Neste trabalho, também se estudou os efeitos de partículas α na sobrevivência celular, deterioração de DNA e controlo de crescimento tumoral, com particular foco em cenários de tratamento com ^{223}Ra.

Palavras-chave: partículas α; Radio-223; cancro da próstata; metástases; controlo tumoral; dosimetria

CONTENTS

LIST OF FIGURES ..... **XV**

LIST OF TABLES ..... **XXI**

NOMENCLATURE ..... **XXIII**

CHAPTER 1 : INTRODUCTION **1**

1.1 CANCER 1

1.1.1 Prostate cancer *2*

1.2 RADIOTHERAPY 4

1.2.1 External beam radiotherapy *5*

1.2.2 Targeted radionuclide therapy *6*

1.3 PHYSICS OF IONIZING RADIATION IN RADIOTHERAPY 9

1.3.1 X-rays and gamma radiation *9*

1.3.2 Charged particles *10*

1.3.3 Radionuclides: Physical and biological half-lives *14*

1.4 RADIOBIOLOGY 15

1.4.1 Absorbed dose *15*

1.4.2 Linear quadratic model *16*

1.4.3 Relative biological effectiveness *16*

1.4.4 Oxygen enhancement ratio *18*

1.4.5 DNA damage and repair *19*

1.4.6 Bystander effects *20*

1.5 MICRODOSIMETRY 21

1.6 MONTE CARLO SIMULATION 22

1.6.1 Monte Carlo *22*

1.6.2 Geant4 and TOPAS *23*

1.7 PROJECT OBJECTIVES 24

CHAPTER 2 : α-SOURCE VALIDATION AND OPTIMIZATION **27**

2.1 INTRODUCTION 27

2.2 MATERIALS AND METHODS 28
2.2.1 The ^{241}Am source setup 28
2.2.2 Experimental analysis 30
2.2.3 Monte Carlo simulation of the ^{241}Am source setup 37
2.2.4 Monte Carlo simulation of cell dosimetry using the ^{241}Am source setup 41
2.3 RESULTS 45
2.3.1 Experimental data 45
2.3.2 Experimental and simulated data comparison 50
2.3.3 Monte Carlo simulation of α-particle interactions with a cell target 53
2.4 DISCUSSION 59
CHAPTER 3 : DEVELOPMENT OF A NOVEL COLLIMATOR FOR α -SOURCES 65
3.1 INTRODUCTION 65
3.1.1 Influence of collimator's geometry on particle flux 65
3.2 MATERIALS AND METHODS 68
3.2.1 3D printed collimator 68
3.2.2 Experimental analysis 69
3.2.3 Monte-Carlo simulation of the ^{241}Am source with a collimator 73
3.2.4 In vitro experimental validation 76
3.3 RESULTS 76
3.3.1 Experimental data 76
3.3.2 Experimental and simulation data comparison of a collimated α-source 80
3.3.3 Monte Carlo simulation of α-particle interactions with a cell target when using a collimator 82
3.3.4 Dose rate 87
3.4 DISCUSSION 88
CHAPTER 4 : IN VITRO ASSAYS 93
4.1 INTRODUCTION 93
4.2 MATERIALS AND METHODS 93
4.2.1 Cell culture 93
4.2.2 In vitro cell assays 96
4.2.3 External source cell irradiations 99
4.2.4 ^{223}Ra cell irradiations 100
4.3 RESULTS 106

4.3.1 α-source validation through clonogenic survival assays *106*

4.3.2 α-particle effects on cells *108*

4.3.3 ^{223}Ra effect on cells *111*

4.4 DISCUSSION 118

CHAPTER 5 : MECHANISTIC MODELLING OF RADIUM-223 TREATMENT OF BONE METASTASES 123

5.1 INTRODUCTION 123

5.2 MATERIALS AND METHODS 124

5.2.1 Tumour growth *124*

5.2.2 Modelling the effect of ^{223}Ra on tumour growth *127*

5.2.3 Clinical trial data *130*

5.2.4 Sensitivity analysis to the tumour growth model parameters *131*

5.3 RESULTS 132

5.3.1 Modelling the radiation effect on the tumour growth *132*

5.3.2 Sensitivity analysis of tumour growth model parameters *134*

5.4 DISCUSSION 141

CHAPTER 6 : CONCLUSION 145

REFERENCES 149

LIST OF FIGURES

Figure 1.1 - Estimated incidence of the ten leading male cancer types in USA, 2018..... 2

Figure 1.2 – Scintigraphy images using ^{99}Tc from two patients with multiple bone metastasis.. 4

Figure 1.3 – Schematic representation of α and β^- emissions from a radionuclide X with atomic mass A and atomic number Z..... 6

Figure 1.4 – Schematic representation of the track length of α-particles (a) and β-particles (b) while going through cells and their nuclei.. 7

Figure 1.5 - Schematic representation of the ^{223}Ra decay chain..... 8

Figure 1.6 – Bone-targeted localized mechanisms of action of the α-emitter isotope ^{223}Ra comparing treatment area ranges to other ionising radiation. 10

Figure 1.7 – Dose distributions of a photon beam and charged particle beams. 11

Figure 1.8 – LET variation with distance travelled in water of α-particles with 2 different initial kinetic energies..... 13

Figure 1.9 – Example of the calculation of the relative biological effectiveness for a cell survival fraction of 10% between deposited doses of a radiation particle and X-rays.. 17

Figure 1.10 – Oxygen enhancement ratio variation with LET.. 18

Figure 1.11 – Schematic representation of the effect of radiation particles to DNA. 20

Figure 2.1 – Decay scheme of ^{241}Am.. 29

Figure 2.2 – A) α-source used for experimental tests, composed of two ^{241}Am layers glued together. The two layers are sitting on top of a holder, with metallic edges surrounding them. B) Source holder box used to vary the distance between the target and the source. 30

Figure 2.3 - A) Mylar dish components (left side) and final assembled dish (right side). B) Source holder box with a Mylar dish positioned at the 4th step from the α-source. 30

Figure 2.4 – Representation of the relation between radiochromic film optical density and radiation dose. 31

Figure 2.5 - Schematic representation of the EBT3 film material layers. 31

Figure 2.6 – Representation of the NOD pixel averaging process to build the film horizontal NOD profile. 33

Figure 2.7 - Schematic representation of the materials present between the α-source and a target, where *d* represents the distance between the target and the source..... 34

Figure 2.8 – Schematic representation of two α-particles, travelling the same distance but with different emission angle θ, reaching different target distances. 34

Figure 2.9 - Schematic representation of the materials present between the α-source and semiconductor detector, where *d* represents the distance between the detector and the source. 36

Figure 2.10 - Schematic representation of the simulation setup of all the materials present between the α-source and a target. 38

Figure 2.11 – Schematic representation of the simulated cell target with an inner nucleus layer..... 42

Figure 2.12 - Example of an energy spectrum peak and the definition of the FWHM. 43

Figure 2.13 - EBT3 customized film scans after exposed to the α-source. 45

Figure 2.14 - EBT3 customized film areas showing calculated net optical densities (NOD) after exposure to the α-source. 46

Figure 2.15 - Average net optical density profiles of middle vertical and horizontal lines of EBT3 customized films after exposed to the α-source.. 47

Figure 2.16 - Microscope images of CR-39 samples exposed to the α-source for one minute at different distances from source to target (d). 49

Figure 2.17 - Particle flux from the α-source at different distances from source to target..... 49

Figure 2.18 - Absolute particle flux from the α-source for experimental (n=9) and simulation data, at different distances from source to target. 50

Figure 2.19 – Experimental and simulated energy spectra of α-particles hitting a target placed at different distances *d* from the α-source..... 52

Figure 2.20 - Simulated average energy of α-particles reaching the cell target at different distances from the source, with an initial α-particle energy of 5.48 MeV..... 53

Figure 2.21 - Simulated energy spectra of the α-source at a cell target positioned at different distances from the source..... 54

Figure 2.22 - Simulated distribution relating particle energy and angle with surface of the target layer (θ_S) positioned at different distances from the source..... 55

Figure 2.23 - Probability density distributions of the α-particles energy scored at 3 different material surfaces. 56

Figure 2.24 - Simulated distribution relating particle energy and angle with surface of the cell target (θ_S) positioned 14.9 mm away from the source. 57

Figure 2.25 - Simulated average α-particle energy deposition per particle in the first micrometre layer of a cell target (A) and LET profile of the α-particles irradiated from the source at different targets, based on the simulated particle energies and data from the NIST database (B).. 58

Figure 2.26 - Experimental and simulation calculations of the surface dose rate of the α-source at different cell target distances from the source. 59

Figure 2.27 - Average net optical density profiles of middle vertical and horizontal lines of EBT3 customized films after exposed to the α-source.

Figure 2.28 – Linear energy transfer (LET) of alpha particles in water, with particle energies varying from 0.1 MeV and 10 MeV. 63

Figure 3.1 – Representation of an α-particle with an emission angle θ entering a hexagon hole in two collimator examples, varying only in hole diameter ($D_1 < D_2$). 66

Figure 3.2 – Schematic representation of a cross-section from the collimator's honeycomb pattern structure.. 66

Figure 3.3 - Representation of an α-particle with an emission angle θ going through a hexagon hole in two collimator examples, varying only in thickness 67

Figure 3.4 - Representation of α-particles going through two collimators varying only in septa ($S_1 > S_2$).. 67

Figure 3.5 – Default infill options from the 3D printing software Simplify 3D. 69

Figure 3.6 – Microscope images taken of 3 hole areas from each collimator sample.. 70

Figure 3.7 – Schematic representation of the experimental setup of a Gafchromic film sample placed on top of a collimator and exposed to the α-source. 70

Figure 3.8 – EBT3 customized film sample irradiation pattern after being placed on top of collimator sample C50 and exposed to the α-source for 30 minutes. 71

Figure 3.9 - Schematic representation of the relation between the collimator's geometry parameters with the distance between 5 consecutive vertical holes (n_y=5) or 9 consecutive diagonal holes (n_{xy} = 9).... 72

Figure 3.10 - Representation of the collimator hole long diameter (D_{long}) and its relation to the shorter hole diameter (D). 72

Figure 3.11 – Simulated geometry of the C50 collimator used in Monte-Carlo simulations in TOPAS. Each side has 4.9 cm width. 74

Figure 3.12 - Schematic representation of the simulation setup of the collimated α-source..... 75

Figure 3.13 - EBT3 customized film areas showing their calculated net optical densities (NOD) normalized to the irradiation time (IR_{time}) after exposure to the α-source..... 78

Figure 3.14 - Average net optical density profiles of middle horizontal (A) and vertical (B) lines of EBT3 customized films after exposure to the α-source with without a collimator.. 79

Figure 3.15 - Particle flux from the α-source with and without collimator C50 at different distances from source to target. 80

Figure 3.16 - Experimental and simulated particle flux from the α-source with and without the collimator C50 at different distances from source to target..... 81

Figure 3.17 - Experimental and simulation data of the particle flux ratio between collimator C55 and collimator C50 at different distances from the α-source.. 82

Figure 3.18 - Simulated average energy of α-particles reaching the cell target at different distances from the source, with an initial α-particle energy of 5.48 MeV..... 83

Figure 3.19 – Simulated energy spectra of the α-source at a cell target positioned at different distances from the source..... 84

Figure 3.20 – Simulated probability distribution for α-particle angle with the cell target's surface positioned at different step distances from the source without a collimator (A) and with a collimator (B)..... 84

Figure 3.21 - Simulated density distributions relating particle's energy and angle with surface of the cell target positioned at *d*=2.9 mm (A) and 26.9 mm (B) with a non-collimated source..... 85

Figure 3.22 - Simulated average α-particle energy deposition per particle at the first micrometre layer of the cell targets (A) and LET profile of the α-particles irradiated from the source at different targets, based on the simulated particle energies and data from the NIST database (B) with and without a collimator.. 86

Figure 3.23 - Surface dose rate of the α-source based on experimental and simulation particle fluxes at different cell target distances from the source with and without a collimator..... 87

Figure 4.1 – Schematic representation of a cell sample in a 6 well plate well for clonogenic assay (A) and a cell sample plated on a 24 well plate well for DNA damage assay (B) following ^{223}Ra treatment.. 101

Figure 4.2 – A) Simulated cell as a semi-ellipsoid with 20 μm side diameters and a 7.8 μm thickness. The nucleus is simulated as a full ellipsoid with 6 μm side diameters and 3 μm thickness, centered at the middle of the cell. B) Simulated cylindrical volume of a treatment solution with α-particle emissions resulted from ^{223}Ra decays. 103

Figure 4.3 - Clonogenic survival data to the PC-3 cell line with α-particle irradiation from the α-source with and without the C50 collimator (n=3) compared to literature data for the same radiation and cell line. 107

Figure 4.4 - Clonogenic survival data comparing the PC-3, RWPE and NT01 cell lines dose responses to α -particle irradiations. 108

Figure 4.5 - Clonogenic survival data for PC-3 (A), RWPE (B) and NT01 (C) cell lines with X-ray and α-particle external beam irradiations. 109

Figure 4.6 - 53BP1foci data of PC-3 cells exposed to 0.5, 1 and 2 Gy doses of X-rays or α-particles. Cells were fixed at time points of 1 and 24h post-irradiation for 3 replicate experiments (n=3). 111

Figure 4.7 - 53BP1foci data of in PC-3 and RWPE cells exposed to a 2 Gy dose of α-particles. 111

Figure 4.8 - Clonogenic survival data for the PC-3 cell line comparing external irradiations with X-rays or α-particles to ^{223}Ra α-particle internal radiation exposure. 112

Figure 4.9 - Clonogenic survival data comparing the PC-3 (A), RWPE (B) and NT01 (C) cell lines dose responses to α-particles from external source and ^{223}Ra exposures. 113

Figure 4.10 - 53BP1foci data in PC-3 cells exposed to 0.5, 1 and 2 Gy radiation doses of external irradiations exposures to α-particles or X-rays, and internal exposures to ^{223}Ra α-particles. 114

Figure 4.11 - 53BP1foci data in PC-3 and RWPE cells exposed to a 0.5, 1 and 2 Gy doses from ^{223}Ra α-particle internal exposure (24h). 114

Figure 4.12 - 53BP1foci data in PC-3 and RWPE cells exposed to a 2 Gy radiation dose from an external source of α-particles and ^{223}Ra α-particle internal exposures (24h).. 115

Figure 4.13 - Clonogenic survival data on PC-3 cells exposed to ^{223}Ra for 6h (A) and 24h (B) using vials with similar activities.. 116

Figure 4.14 - Clonogenic survival data on PC-3 cells exposed to ^{223}Ra for t_{exp} = 6h (A) and for t_{exp} = 24h (B) using vials with different activities. 116

Figure 4.15 – Effect of the Xofigo treatment volume/dose ratios on the survival fraction (SF) of PC-3 cells. Here the SF are displayed as logarithm values. 118

Figure 5.1 - Xenograft tumour growth data from mice implanted with PC-3 metastatic prostate cancer cells..... 126

Figure 5.2 - Tumour growth curves for the Gompertz models A to F, with initial starting volumes of 0.1% and 10% of the maximum tumour volume (K). 127

Figure 5.3 - Schematic representation of the radiation exposed (orange) and non-exposed (blue) tumour volumes for the uniform (A), outer layer (B) and constant volume (C) exposure scenarios. 130

Figure 5.4 - Illustrative tumour growth curves for the uniform (A), outer-layer (B) and constant volume (C) exposure scenarios. 133

Figure 5.5 - Kaplan-Meier curves for the clinical data of placebo and treatment groups from the ALSYMPCA trial data [43], comparing to the uniform model fit with initial dose rate estimation ($D0$= 0.0103 Gy/h)..... 133

Figure 5.6 - Illustration of A_{growth} and S_{Met} model parameters which lead to plausible metastatic growth kinetics. 134

Figure 5.7 - Dependence of best fitting parameters for each radiation effect model on A_{growth} (A, C, E), S_{Met} (B, D, F) and maximum number of cells, K..... 135

Figure 5.8 - Fit quality parameter (R^2) of different radiation model as a function of A_{growth} (A) and S_{Met} (B)..... 136

Figure 5.9 - Dependence of optimum $C_{Fraction}$ in constant volume model on initial dose rate ($D0$) when fit to the ALSYMPCA treatment data, for different values of A_{growth} (A) and S_{Met} (B).. 138

Figure 5.10 - Dependence of the fit quality (R^2) on the initial dose rate ($D0$) when the constant volume model is fit to the ALSYMPCA treatment data. 138

Figure 5.11 - Variation of $C_{Fraction}$ with $D0$ for different tumour growth rates.. 139

Figure 5.12 - Effect of initial dose rate ($D0$) on the best-fitting $C_{Fraction}$ (A) and the product of $D0$and $C_{Fraction}$ (B).. 140

LIST OF TABLES

Table 1.1 – Main properties of radionuclides used in bone metastasis palliative treatment. 8

Table 2.1 – Table showing the simulated spectra maximum peak's energies ($Esim$) and maximum peak channel numbers ($Nchannel$) used for calibrating the experimental energy spectra obtained from exposing a charged particle detector to the α-source.. 41

Table 2.2 – Table showing the experimental and simulated fluxes of particles hitting a target at different distances from the source (d)..... 51

Table 2.3 - Simulated results of α-particle physical properties when reaching the cell target positioned at different distances from source to target (d)..... 64

Table 3.1 – Results of the averaged geometry parameters of the collimators C50 and C55.. 76

Table 3.2 – Simulation results of α-particle physical properties when reaching the cell target positioned at different distances from source to target with and without the collimator C50.. 92

Table 4.1 – Linear quadratic parameters obtained from experimental data of PC-3 cells exposed to α-particles compared to literature data..... 107

Table 4.2 – Linear quadratic parameters (± standard deviation) obtained from experimental data of PC-3, RWPE and NT01 cell lines exposed to X-rays and α-particles with their associated RBE for 10% survival fraction..... 109

Table 4.3 - List of Xofigo vials with corresponding activity concentrations for clonogenic experiments. 117

Table 4.4 – Decimal reduction dose (R_{10}) value estimates from the curve fits to the surviving fraction results shown in Figure 4.15..... 118

Table 5.1 - Gompertz tumour growth parameters from different tumour models in literature and experimental data. 125

Table 5.2 - Results of the highest fit quality (R^2) for the 3 tumour treatment models by varying the 3 main treatment model parameters. 136

NOMENCLATURE

53BP1	p53 Binding Protein 1
^{223}Ra	Radium-223
^{241}Am	Americium-241
A	Radionuclide activity
Act_{vial}	Activity of the Xofigo vial used in experiments
ALSYMPCA	Alpharadin in Symptomatic Prostate Cancer Patients clinical trial
$C_{Fraction}$	Ratio between the constant volume of radiation affected cells and the tumour maximum number of cells
CR-39	Allyl diglycol carbonate
CRPC	Castration resistant prostate cancer
D	Dose
$\dot{D}_{nucleus}$	Nucleus dose rate
DAPI	6-diamidino-2-phenylindole
DNA	Deoxyribonucleic acid
DSB	Double strand break
EBRT	External beam radiotherapy
eV	Electron volt
$E_{\mu t}$	Energy deposited per particle on the first micrometre layer of a target
FBS	Fetal bovine serum
FDA	US Food and Drug Administration
FWHM	Full width at half maximum
Gy	Gray
HR	Homologous recombination
H_T	Equivalent dose

IF	Immunofluorescence
IMRT	Intensity modulated radiotherapy
J	Joule
K	Maximum number of cells the tumour can have
LET	Linear energy transfer
MCA	Multichannel analyser
MRI	Magnetic resonance imaging
Mylar	Biaxially-oriented polyethylene terephthalate
n	Number of experimental repeats
NaOH	Sodium hydroxide
NHEJ	Non-homologous end joining
NIST	National Institute of Standards and Technology
NOD	Net optical density
OD	Optical density
OER	Oxygen enhancement ratio
P(E)	Probability density distribution
PBS	Phosphate buffered saline
PE	Plating efficiency
PSA	Prostate-specific antigen
PETG	Glycol-modified polyethylene terephthalate
Q	Quality factor
R_{10}	Decimal reduction dose
RBE	Relative biological effectiveness
ROS	Reactive oxygen species
SE	Standard error
SF	Survival fraction
SSB	Single strand break

SSE	Symptomatic skeletal events
Sv	Sievert
TOPAS	Tool for particle simulation
V_{10}	Decimal reduction volume
Xofigo	Radium-223 dichloride
α-particle	Helium ion (+2 charge) emitted by radioactive decay
α_1	Rate of cell killing by a single-hit particle
β_1	Rate of cell killing by multi-hit particle events
β^- particle	Electron emitted by radioactive decay
Δ	Energy cut-off threshold
θ_C	Critical angle
θ_S	Angle between a particle's direction and the detector's surface
Φ	Particle flux

CHAPTER 1 : INTRODUCTION

1.1 Cancer

Cancer is characterized by an abnormal cell proliferation which leads to the formation of malignant tumour cells. It can originate from any body part and is able to affect secondary body tissues that are either adjacent or distant to the primary location. This occurs when cancer cells spread through the bloodstream or lymphatic systems. Tumour progression and spread across different tissues occurs through the process of metastasis. [1]

Cancer formation is related to alterations in cellular physiology, which impact the regulation of controlled cell production and programmed cell death. A disruption in this process can lead cells to uncontrollably multiply, evade programmed death mechanisms and spread to secondary tissues. These cancer cell properties are examples of the hallmarks of cancer described by Hanahan and Weinberg. [2]

When a tissue has cells going through unregulated and uncontrolled growth, it becomes a neoplasm. The neoplastic cells can continue to grow and form a tumour. What differentiates between malignant tumour from a benign tumour state is the ability to spread to different tissues, usually correlated with fast growth. Malignant neoplasms, which typically grow faster and are able to spread, are more difficult to treat since removing the primary tumour might not be enough to eradicate tumour cells that metastasized. On the other hand, benign neoplasms are characterized by their slow growth and localised disease stage, usually being easier to treat. [3]

In terms of disease incidence, cancer is one of the leading causes of death worldwide. In 2018, there were 9.6 million cancer related deaths reported. [4] In the same year, it was reported to be the second leading cause of death in United States. [5] Figure 1.1 shows the estimated incidence of cases of the ten most common cancer types in men in USA, showing prostate cancer with the highest incidence.

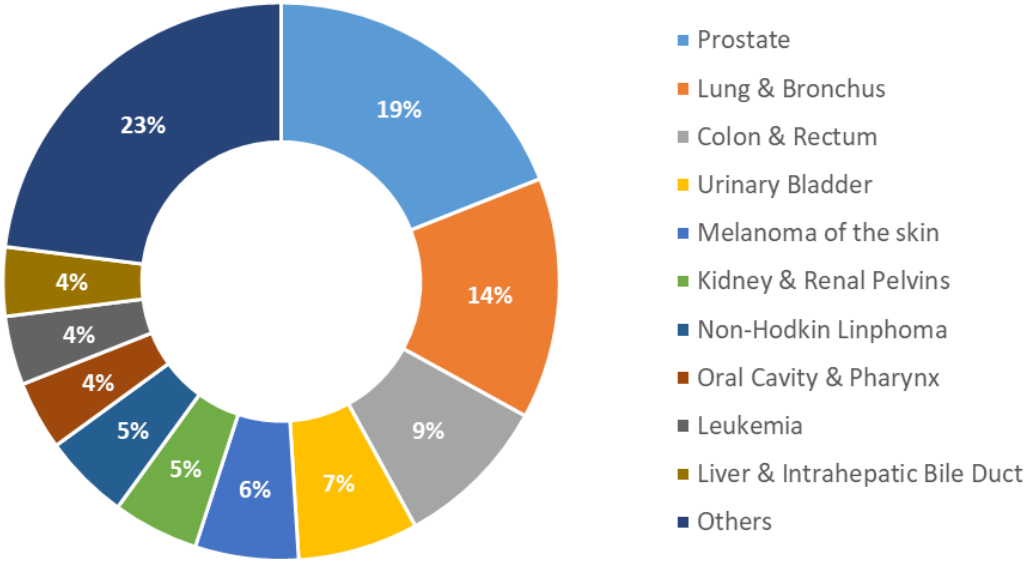

Figure 1.1 - Estimated incidence of the ten leading male cancer types in USA, 2018. Adapted from Siegel et al. [5].

1.1.1 Prostate cancer

Prostate cancer is estimated to be the third most diagnosed cancer in the world, having a worldwide incidence in men of 13.5%, being the most diagnosed male cancer in 2018. [4] According to a variety of patient statistics, prostate cancer causes are highly related to either lifestyle and environmental risk factors or family history of disease. [6–8]

1.1.1.1 Diagnosis and treatment

One of the characteristic proteins produced by the prostate gland is the prostate-specific antigen (PSA). This protein is important in fertility and in the dissolution of the seminal fluid coagulation. When a prostate tumour develops, the concentration of PSA increases. Therefore, one of the first steps on the diagnosis of prostate cancer is usually done by quantification of the PSA protein concentration in blood. However, more tests are needed since an increase of PSA concentration in blood might not necessarily be related to prostate cancer, but other diseases instead. Another important screening exam for prostate cancer is the digital rectal examination. These preliminary exams, if showing abnormal results, lead to deeper diagnosis tests, such as prostate biopsy, magnetic resonance imaging (MRI) or other imaging techniques. [9] Only after such analysis can a patient be positively diagnosed with prostate cancer.

Depending on the disease stage, there is a variety of treatment options for localised prostate cancer. One of the options is active surveillance, as certain low-grade diseases pose very few risks for patients. In these cases, patients would be actively followed-up by checking their PSA levels in blood, collecting and analysing prostate tissue samples from biopsies, and MRI checks. [10,11]

For higher-grade disease stages, there are local treatment options such as radical prostatectomy (removal of the entire prostate gland), androgen deprivation therapy or radiotherapy (external beam radiotherapy and brachytherapy). These treatment options are considered when test results indicate that cancer is progressing (increase in PSA blood levels, for example). In some cases, multimodality treatments can be used, for example using androgen deprivation as an adjuvant therapy, to reduce cancer growth stimulation by androgen, together with radiotherapy, for tumour eradication and control. Other non-standard treatment options that can be used are the recent modalities such as cryotherapy, high-intensity focal ultrasound, and photodynamic therapy, which can be considered for low grade local treatment before or after radiotherapy. [9,10]

1.1.1.2 Bone metastasis in prostate cancer

As previously mentioned, the standard-of-care for patients with advanced prostate cancer is androgen deprivation therapy. After prolonged androgen deprivation, the disease can invariably progresses to a castration-resistant stage, an ultimately fatal condition for patients. [12] At this lethal stage, a large percentage of patients with castration resistant prostate cancer (CRPC) (between 65%-90%) develop bone metastases. [13,14]

The development of bone metastasis involves primary tumour cells that invade the vascular system and reach the bone marrow, as well the bone marrow microenvironment and bone cells, which accommodate and allow the metastization of the tumour cells. [15] As metastatic cells grow and evolve, patients start feeling severe pain and develop symptomatic skeletal events (SSE), which include spinal-cord compression and symptomatic pathological fractures. [16] Figure 1.2 shows two scintigraphy images of two patients with multiple bone metastatic lesions. Bone metastases not only affect patients with CRPC, but they are also a major complication of several other solid cancers, such as breast, lung, kidney, and thyroid cancers as well as multiple myeloma. [17]

Treatment of bone metastases in patients with CRPC may involve bisphosphonates, denosumab and β^- emitting radiopharmaceuticals, which reduce pain levels and the incidence of SSE, but fail to prolong survival. Fortunately, the number of therapeutic approaches is increasing and new promising modalities have been approved based on evidence of prolonged survival. These include the use of chemotherapy (docetaxel, cabazitaxel), androgen receptor directed therapy (e.g. Abiraterone and

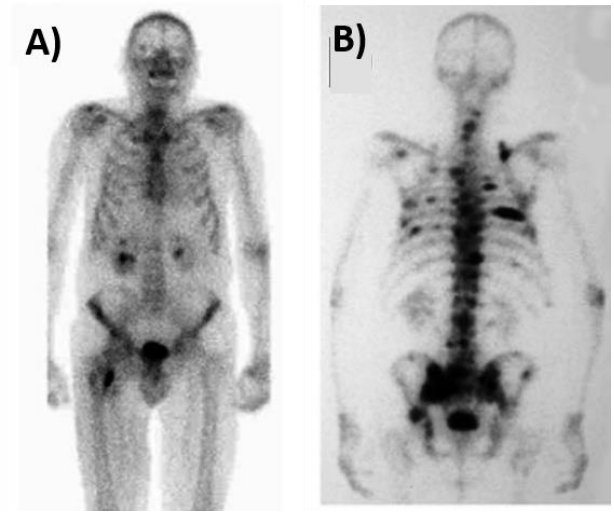

Figure 1.2 – Scintigraphy images using ^{99}Tc from two patients with multiple bone metastasis. Adapted from Chappard et al [15].

Enzalutamide) and radionuclide systemic therapy (^{223}Ra). [18] The latter has emerged as one of the most important modalities for cancer management for patients with multiple skeletal metastases.

1.2 Radiotherapy

Radiotherapy is a cancer therapy modality where radiation is used to cure or control tumours. It has been used since 1896, almost immediately after the discovery of X-rays by Wilhelm Roentgen in 1895. [19]

This treatment modality uses ionizing radiation, such as X-rays, gamma rays or electrons, which travel through body tissues. Heavier particles can also be used - protons, helium ions (α-particles) or carbon ions as part of heavy particle radiotherapy. Although they have different physical properties, all these types of ionizing radiation damage cancer cells, inducing DNA strand breaks. When cells fail to properly repair such damages, they end up dying. Subsequently, the higher the absorbed radiation dose is, the higher the chance of killing a cell. [20]

The goal of radiotherapy is the use of ionizing radiation to kill cancer cells while minimizing damage to the surrounding healthy tissues. This can be done by several radiotherapy techniques, where different radiation particles are used as part of single or adjuvant therapies. Deciding which radiotherapy approach is most appropriate depends on the tumour type, surrounding tissues, patient clinical diagnosis as well as the radiation dosimetry involved for that treatment. [21]

1.2.1 External beam radiotherapy

External beam radiotherapy (EBRT) is the most common type of radiotherapy. In this modality, one or more beams of ionizing radiation are aimed at a tumour. The goal is to deliver the highest radiation dose to the tumour, with lower doses in the surrounding healthy tissues. This is possible when a treatment plan has different sets of beams targeting the tumour from different incident angles and beam source locations. The use of multiple beams usually allows higher dose painting areas focused on the tumour while sparing other tissues from significant radiation doses.

Another important factor to consider in radiotherapy, and more specifically in EBRT, is fractionation. Fractionation is related to the number of radiation treatment sessions (fractions) that a patient is planned to receive. Opting for a treatment with a few fractions of radiation with high doses each or a treatment with higher number of fractions with low radiation doses each are important choices to make. In addition, the time delay between each of those fractions is equally important to consider.

The advantages of fractionated radiotherapy can be explained by the five R's of radiotherapy:

- Repair of sublethal cellular damage in healthy tissues
- Repopulation of cells after radiation exposure
- Redistribution of cells to more sensitive cell cycle phases
- Reoxygenation of surviving cells
- Radiosensitivity

Redistribution and reoxygenation are associated with increased cell kill, since they lead to treatment resistant cells moving into more sensitive states. On the other hand, repair and repopulation are related to increased cell survival, as they lead cells, particularly cells from healthy surrounding tissues, to recover between treatment fractions. Radiosensitivity is an intrinsic effect in radiotherapy that is related to the different cells sensitivities to different radiations and radiation doses. [22,23]

EBRT treatments mostly use photons, protons or carbon ions. These radiation particles are externally produced but have distinct physical and biological interactions with matter. Photons typically deposit most of their energy near the surface of the tissue they are travelling through. However, heavier particles like protons or carbon ions, deliver most of the treatment dose at the end of their path – commonly called the Bragg peak region. [21] These physical differences will be covered later.

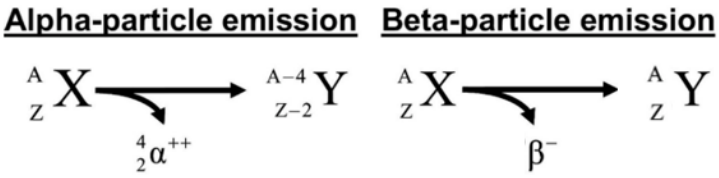

Figure 1.3 – Schematic representation of α and β^- emissions from a radionuclide X with atomic mass A and atomic number Z. The decay product is Y. Adapted from Kassis et al [25].

1.2.2 Targeted radionuclide therapy

Targeted radionuclide therapy typically consists on the use of radionuclides for internal radiotherapy exposure. It consists of the administration of radionuclide labelled drug vectors, acting as radiopharmaceuticals, that target and bind to cancer cells, inducing cytotoxic radiation effects in them. The radionuclides emit radioactive particles, such as β-particles, gamma rays or α-particles, through decay. In comparison with EBRT, this radiotherapy modality is specifically targeted at cancer sites, often with lower cytotoxic effects on healthy tissues.

Other targeted radionuclide therapies can include brachytherapy, where capsuled radionuclide materials are placed in contact with targeted cancerous tissues, such as in prostate cancer.

1.2.2.1 α and β emitter radionuclides

Most of the radionuclides used in targeted radionuclide therapy are α and β^- emitters. β^- particles, sometimes referred as β particles only, are electrons emitted through decay, usually with energies varying from a few keV to hundreds of keV. These particles have long ranges in tissue (typically >1 mm). α-particles are helium ions with +2 charge also emitted through decay. α-particles usually have higher energies than β^- particles, in their case of a few MeV, with lower ranges in tissues (< 0.1 mm). Figure 1.3 shows a schematic representation of α and β^- emissions produced through decay processes.

In comparison to β^- emitters, α-particles can only travel through a few dozens of micrometres in tissue before they are completely stopped. This has important implications when considering the microdosimetry of this therapy modality. Figure 1.4 shows a typical path length comparison between α and β^- particles at cell level. It also shows that the number of ionization events in a cell per incident particle is significantly higher for α-particles. [24,25] The number of ionization events is directly related to DNA damage and cancer cells death, as it will be discussed later.

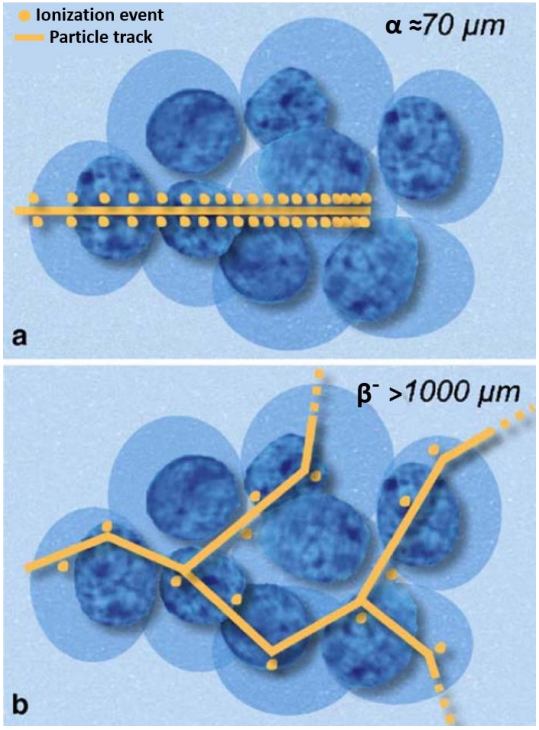

Figure 1.4 – Schematic representation of the track length of α-particles (a) and β-particles (b) while going through cells and their nuclei (coloured as darker blue). α-particles can only go through a couple of cell diameters causing multiple ionization events for a short distance while β-particles can go through multiple cell layers (final track length not represented) with few ionization events along their path. Adapted from Couturier et al [24].

1.2.2.2 Palliative treatment of bone metastasis using radionuclides

One of the uses of targeted radionuclide therapy is related to the palliative treatment of bone metastasis, often associated with breast, prostate, myeloma and lung cancers. [26] Typically, these radionuclides are labelled with bone seeking tracers. [27] By specifically targeting bone metastatic sites, the radioactive decay products will mostly affect the cancer cells, sparing healthy tissue from most of the damage. Some examples of radionuclides used for bone metastasis treatment are displayed in Table 1.1.

Some of the main differences in the radionuclides used are the type of particle emissions and their range in tissue. As shown in the previous section and in this table, β electrons can travel through more than 0.5 mm in tissue (water equivalent) before they stop. On the other hand, α-emitting radionuclides such as ^{223}Ra have particle emissions that can travel less than 0.1 mm in tissue.

Table 1.1 – Main properties of radionuclides used in bone metastasis palliative treatment – radionuclide's half-life, main particle emissions (CE stands for conversion electron), average particle energy and average particle range in water. Examples of conducted studies and clinical trials are also shown. Adapted from Tomblyn et al [26].

Radionuclide	Half-life (days)	Particle emission	Average energy (keV)	Average range (mm)	Previous trials and studies
^{32}P	14.3	β^-	695	3.0	Silberstein et al [28]
^{89}Sr	50.5	β^-	580	2.4	Zheng et al [29]
^{153}Sm	1.9	β^-	233	0.5	Ratsimanohatra et al [30]
^{186}Re	3.7	β^-	349	1.1	Minutoli et al [31]
^{188}Re	0.7	β^-	2120	3.5	Liepe, Knut [32]
^{117m}Sn	13.6	CE	127	< 0.1	Srivastava et al [33]
^{223}Ra	11.4	α	5870	< 0.1	Cabrera et al [34]

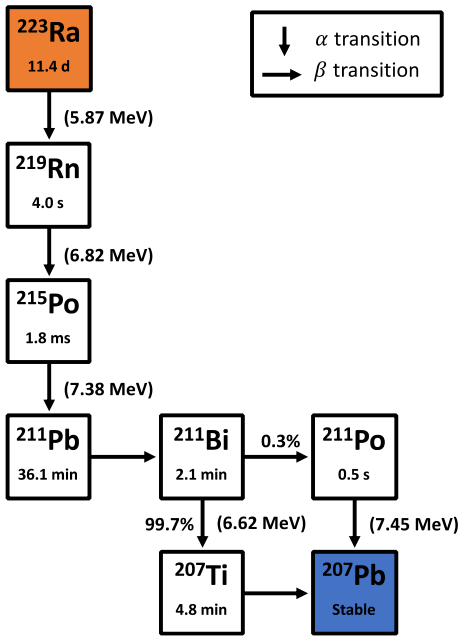

Figure 1.5 - Schematic representation of the ^{223}Ra decay chain. The energy of each emitted α-particle is shown in brackets. The physical half-life of each radionuclide is also displayed, as well as the probability of each decay emission (100% probabilities are not displayed).

1.2.2.3 ^{223}Ra use in bone metastatic prostate cancer

Over the last decades, α-emitting radionuclides have evolved from being used in *in vitro* studies to being used in *in vivo* studies and clinical trials. [24,35–38] In particular for patients with multiple skeletal metastases, ^{223}Ra has emerged as one of the most important modalities for cancer management.

Radium-223 (^{223}Ra) is a calcium-mimetic and complexes with hydroxyapatite crystals in osteoblastic bone metastases. [39] This means that when injected into the body, ^{223}Ra will specifically target tissues with high cell activity and bone turnover, such as bone metastasis. ^{223}Ra treatments have been approved by the US Food and Drug Administration (FDA) and are given to patients in the form of ^{223}Ra dichloride injections (Xofigo; Algeta–Bayer HealthCare Pharmaceuticals, Wayne, NJ). [40]

^{223}Ra has a physical half-life of 11.4 days and each ^{223}Ra decay results in the emission of 4 α-particles in the primary decay chain (Figure 1.5). [41] In treatments for bone metastatic patients, ^{223}Ra has shown a mean effective half-life of 8.2 days, based on the radiopharmaceutical biokinetics that take into account its biological clearance rate. [42] The differences between the physical and biological half-lives of radionuclides will be covered in a later section of this introduction.

The average range of ^{223}Ra emitted α-particles is about 50 µm (it varies for the different particle energies). For small lesions such as skeletal metastasis, this is important as it minimizes the damage to the surrounding bone marrow cells. A schematic representation of different radiation particles ranges compared to a bone metastatic cell cluster is represented in Figure 1.6. For these types of lesions, α-emitting radionuclides and, in particular, ^{223}Ra, offer one of the most targeted therapies.

In the recent years, ^{223}Ra radiopharmaceuticals have been shown to improve overall survival and time to first symptomatic skeletal events (SSE) of patients with multiple bone metastasis, in particular in patients with castration resistant prostate cancer (CRPC). This was demonstrated during the phase 3 clinical trial ALSYMPCA in 2013, with a total of 921 patients randomly assigned to being treated or not with ^{223}Ra. The trial results showed that the ^{223}Ra led not only to a prolonged time to the first SSE for treated patients (5.8 months) but also to a significant positive effect on overall survival (3.6 months), without evidence of long-term toxicity. [43]

1.3 Physics of ionizing radiation in radiotherapy

1.3.1 X-rays and gamma radiation

X-rays are photons that can be produced externally by the collision of accelerated electrons with a metal. In EBRT, the acceleration of electrons process usually occurs through high-frequency

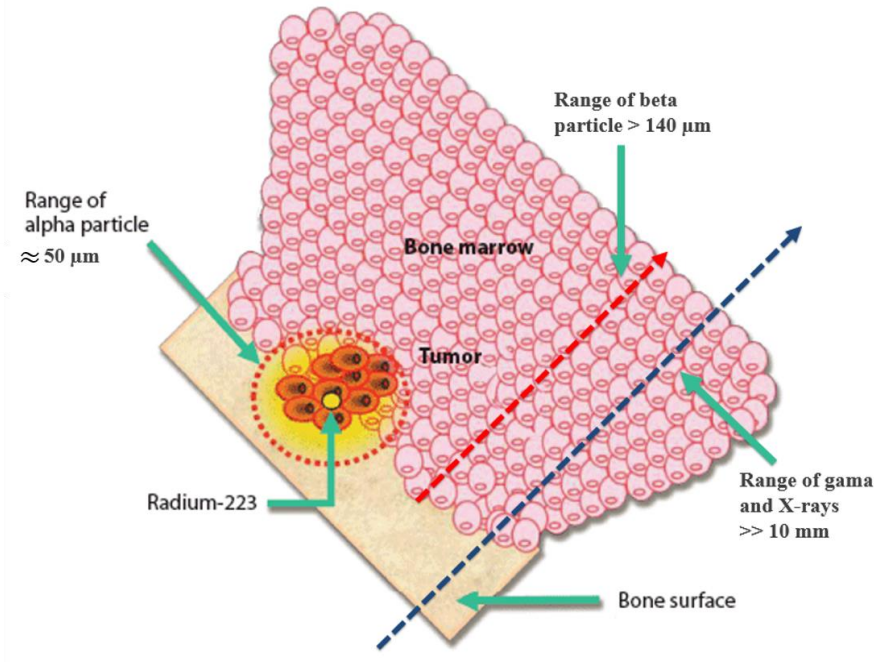

Figure 1.6 – Bone-targeted localized mechanisms of action of the α-emitter isotope ^{223}Ra comparing treatment area ranges to other ionising radiation (β particles, X-rays and gamma radiation). Adapted from Philippa et al [38].

electromagnetic waves on medical linear accelerators (Linac). The collision of these high energy electrons with a heavy metal result in an energy release in the form of heat and X-ray photons. These resulting photons have energies in the order of MeV. When interacting with cell tissues, X-rays will produce secondary ionizing events, which can lead to cell death. [44,45] This will be further discussed later.

Another form of ionizing radiation based on photons is gamma radiation (γ). γ-rays are produced through radioactive decay of radionuclides, such as ^{99m}Tc, ^{60}Co and ^{137}Cs. γ-rays are typically used for nuclear medicine imaging techniques or radiotherapy treatments, either for EBRT or targeted radionuclide therapy.

1.3.2 Charged particles

One of the disadvantages of using photons in radiotherapy is related to the dose distribution through the tissue thickness. The maximum dose peak is observed within the first centimetres of soft tissue, followed by an approximately exponential dose fall-off that continues to impact tissue cells that are distant from the tissue's entry point. This has many negative implications, especially for healthy tissues that surround the cancer. This is not the case for charged particle radiotherapy. [46]

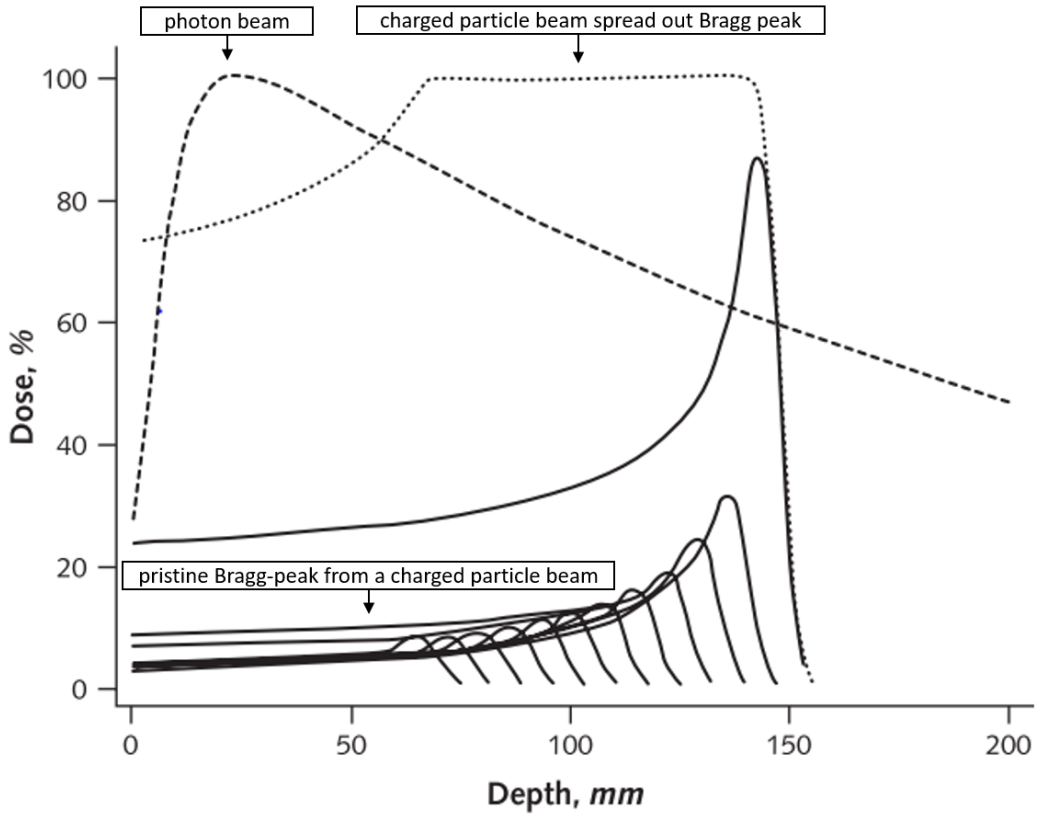

Figure 1.7 – Dose distributions of a photon beam and charged particle beams. The dashed line shows the dose distribution in depth of a 10 MV photon beam. The solid lines represent the dose distribution of 12 charged particle beams with different initial energies. The dotted line represents the dose distribution of the spread-out Bragg peak particle beam combined from the contributions from the pristine Bragg peaks of the different charged particle beams. Adapted from Levin et al [20] and Terasawa et al [47].

For treatments using charged particles, such as protons or carbon ions, it is possible to control the damage to healthy tissue with much better results than when using photons. These particles travel mostly with well-defined trajectories, depositing their energy as they interact with the electrons of a medium. As charged particles lose energy, they start to slow down. Up until a limit, the "slower" the particle is, or the lower its energy, the higher the chance to interact with matter, leading to a higher energy deposition. The higher energy deposition occurs closer to the end of the particle's path, at a region known as the Bragg peak. This position of this region mostly depends on the energy of the incident particle. [20,47,48]

The dose distribution profile of charge particles follows a Bragg peak distribution, as shown in Figure 1.7. Here we compare the dose deposition profiles of proton and photon beams. We can also take further advantages of charged particle properties and use multiple beams coming from the same entry point with different intensities and particle energies. The summed beam dose contributions follow a spread out Bragg peak distribution, as shown in the previous figure. The spread out Bragg peak is

particularly relevant when treating a tumour with a size bigger than a single beam Bragg peak, as the single beam treatment would fail to target the whole tumour.

However, unlike photon-based radiotherapy, charged particle beams can generate neutrons which will scatter into adjacent normal tissues from the target volumes. These neutrons can increase the risk of secondary malignancies as they lead to considerable biological effects in healthy surrounding tissues. Furthermore, charged particle beams become less sharp at greater depths due to the higher number of scattering events. Charged particle also lead to more sensitive biologic effects due to differences in tissue densities. In order avoid tumour underdosing and to account for tissue heterogeneity, a margin of uncertainty is usually added in such treatments. [49,50]

Charged particles are generated by decay of radioactive isotopes or produced through particle accelerators.

1.3.2.1 α-particles

As previously mentioned, α-particles are helium ions with +2 charge. These particles are emitted through radioactive decay from isotopes such as ^{241}Am, ^{238}Pu or ^{223}Ra. In radiotherapy, α-particles are used as part of internal radionuclide therapies, using ^{223}Ra injections to target bone metastasis for example. [43] In cell radiobiology research laboratories, experiments are typically conducted using α-sources – materials coated with a radioactive layer of a long-lived α-emitting radionuclide, such as ^{241}Am or ^{238}Pu. [51,52]

These α-particles have similar radiobiological properties to protons or carbon ions. The main difference is how they interact with tissue. Protons and carbon ions can travel through hundreds of millimetres of human tissue's thickness before they are stopped, as opposed to an α-particle's range – typically less than 100 micrometres. This is due to the initial energy of these particles, typically below 10 MeV for α-particles and above 100 MeV for protons and carbon ions in radiotherapy.

1.3.2.2 Linear energy transfer of α-particles

Linear energy transfer (LET) can be defined as the energy transferred to matter per unit length of a particle's track. It depends on the type of particle, its energy and the medium which the particle is travelling through. LET is an average value and its units are usually expressed as kiloelectron volt per micrometre (keV/μm). The higher the LET, the higher the number of ionization events per unit travelled.

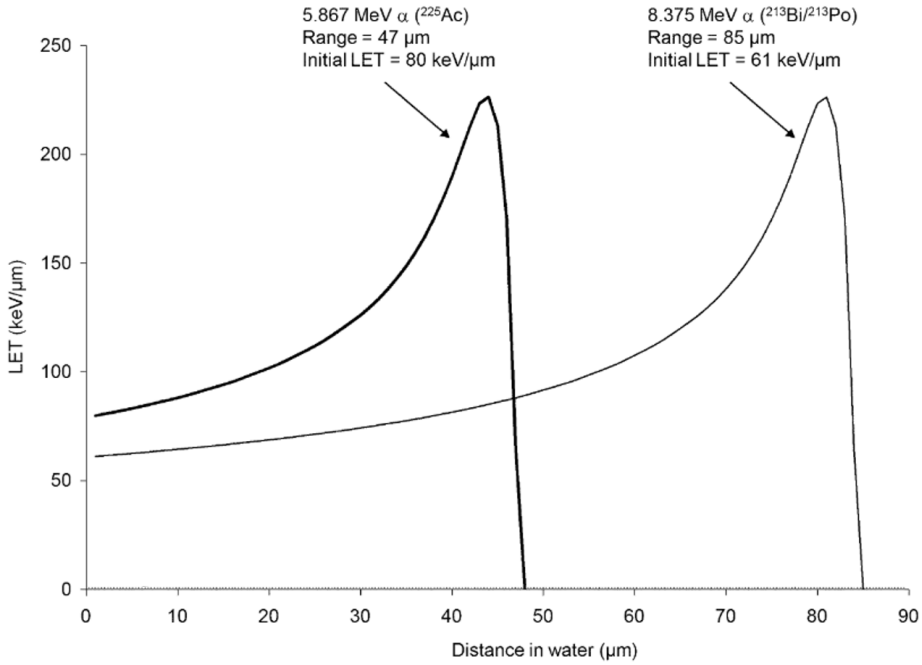

Figure 1.8 – LET variation with distance travelled in water of α-particles with 2 different initial kinetic energies (5.9 and 8.4 MeV). Adapted from Sgouros et al [55].

An ionization event from a particle track consists on the transfer of enough energy from the travelling particle to an atom, leading to the ejection of an electron from it. As a result, that atom is ionized. The ejected secondary electron can interact with other atoms and result in further ionization cascades, with multiple secondary electron ejections.

Charged particles like α-particles, protons or carbon ions are considered to be high LET particles (>10 keV/μm). These particles deposit high amounts of energy in a short distance, compared to low LET particles such as photons. As a result, high LET particles are densely ionizing with most of the ionizations occurring along the particle track. This has important implications in cell survival, as ionization events lead to DNA damage which can result in cell death. [53,54]

As previously mentioned, α-particles are high LET particles. The LET variation with travelled distance is similar to the Bragg peak behaviour, as shown in Figure 1.8. As demonstrated in this figure, the higher the initial particle energy, the longer its track path before the particle is stopped, with the highest LET occurring at a greater depth in the medium, in this case water (human tissue equivalent). [55]

The LET calculation is highly related to the stopping power of the material the ionizing particle is travelling through. It corresponds to the sum of the nuclear and electronic collision stopping power of the medium locally. The stopping power is denoted as $-\frac{dE}{dx}$, where dE is the particle's energy lost while travelling through a dx length distance. The LET and the stopping power are many times

considered to be the same. However, the main difference between the two concepts is that the LET can correspond to the restricted stopping power $-\left(\frac{dE}{dx}\right)_{\Delta}$, in the sense that it only considers particle interactions where energy transfers associated with each particle collision are lower than the energy cut-off threshold Δ. The restricted stopping power calculation does not take into account energy transfers that are higher than Δ. The reason for this is because higher energy transfers lead to the ejection of energetic secondary electrons which will travel for longer distances and produce fewer secondary ionizations in the immediate vicinity of the track in comparison to lower energetic secondary electrons. The density of ionization events per particle track is therefore lower for electrons produced through higher energy transfer events. [46,56] These electrons will more likely lead to secondary ionizations at further distances than the original particle track depth.

For certain applications with charged particles, it's relevant to consider the LET as the restricted stopping power, while for others it is acceptable to consider Δ as infinite, which approximates the LET to be the same as the stopping power. The distinction between the two concepts is not trivial, especially as it is not straightforward to properly define the energy cut-off threshold Δ. For simplification purposes we have considered the LET to be the same as the general stopping power, which should be approximate for the experimental and simulated conditions considered in this thesis work.

It is also important to distinguish track-averaged LET and dose averaged LET. Track averaged LET is the mean of each individual particle LET traversing a target. This parameter averages together particles that can have higher LET, depending on energy differences, which will typically lead to higher biological effects than lower LET particles. In order to take particle LET differences into account, the dose averaged LET weights each particle's LET according to the dose they deposit in a targeted volume. This parameter describes more accurately the LET impact of a particle beams. [57,58]

1.3.3 Radionuclides: Physical and biological half-lives

There are important aspects involved in targeted radionuclide therapy that EBRT does not involve, such as the physical and biological half-lives of the radionuclides used. These are related to the radioactive decay processes of isotopes and their clearance rate from the patient tissues after a treatment injection, respectively. Both factors should be taken into account in treatment planning as they impact the treatment dosimetry, tissue toxicity and therapy effectiveness.

The physical half-life directly affects the radioactivity of the radionuclide with time. It dictates the number of particle emissions per time, which are important to consider for radiation dose calculations. Its value represents the amount of time needed to pass for the number of the initial

radionuclide atoms to be reduced by half. The physical half-life is directly related to the radionuclide's physical decay constant (λ_p):

$$T_p = \frac{ln\,(2)}{\lambda_p} \qquad 1.1$$

The number of radionuclide nuclear disintegrations per unit time is represented by the radionuclide's activity (A) and is calculated following the equation:

$$A(t) = A_0 e^{-\lambda_p t} \qquad 1.2$$

where, $A(t)$ is the radionuclide's activity at a certain time period t and A_0 is the initial activity. Its units are usually expressed in Becquerel (Bq), as the number of nuclear disintegrations per second.

The biological half-life, T_b, is related to the biological clearance of the radionuclide labelled drug by the organ tissues. [59] It dictates the number of radionuclide atoms that remain in tissue with time. It is also directly related to the biological decay constant, λ_b. This parameter is independent of the physical activity of the radionuclide used.

The combination of T_p and T_b influences the radionuclide's activity in tissue with time:

$$A(t) = A_0 e^{-\lambda_e t} \qquad 1.3$$

where λ_e is the effective decay constant ($\lambda_p + \lambda_b$). The effective half-life is:

$$T_e = \frac{T_p\, T_b}{T_p + T_b} \qquad 1.4$$

For example, as discussed in section 1.2.2.3, ^{223}Ra effective half-life is T_e = 8.2 days, in comparison to its physical half-life (T_p = 11.4 days).

1.4 Radiobiology

1.4.1 Absorbed dose

There are different parameters that describe and evaluate ionizing radiation effects on matter. The LET is one of those, mentioned in the previous section. Another of the most important parameters is the absorbed radiation dose (D). It represents the amount of absorbed energy by matter that was exposed to a certain radiation. It is expressed with units of gray (Gy). 1 Gy corresponds to 1 Joule per kilogram of matter (J/Kg). The absorbed dose needed to achieve a certain biological effect in a tissue is dependent on the tissue and the radiation used. High LET radiation, such as α-particles, is often more biologically damaging than low LET radiation for the same dose. [44,60]

Other parameters that are important when comparing different radiation types are the relative biological effectiveness and the oxygen enhancement ratio. These radiobiological parameters provide a better radiation characterization and comparison, especially when comparing dosimetric effects at the cell level.

1.4.2 Linear quadratic model

Cells can lose their ability to divide when they are exposed to radiation. In radiotherapy, this is important to consider as the targeted cancer cells may not necessarily need to die, as long as they lose the ability to grow. The number of viable cells decreases with increasing dose. One of the models that describes this relation between growth loss ability and radiation absorbed dose is the linear quadratic model. This model has been well established as a radiobiological model for a long time and has been proved to accurately describe dose response relationship in most cell models. [44]

The model describes the surviving probability of cells when receiving a dose *D*:

$$SF = e^{-(\alpha_1 D + \beta_1 D^2)} \qquad 1.5$$

where α_1 represents the rate of cell killing by single-hit particle events, β_1 refers to the rate of cell killing by multi-hit particle events. These parameters depend on the cell type and radiation particles used, being expressed in units of Gy^{-1} and Gy^{-2}, respectively.

Assuming a target population of N_c cells, the surviving fraction of the cell population can be rewritten based on each individual cell surviving probability, SP_i: [61]

$$SF = \frac{\sum_{i=1}^{N_c} SP_i}{N_c} \qquad 1.6$$

1.4.3 Relative biological effectiveness

The relative biological effectiveness (RBE) is used to compare biological effects of radiation exposures by different radiation types. The RBE is defined by the ratio of the absorbed doses of two radiation sources that led to the same biological effect:

$$RBE = \frac{D_1}{D_2} \qquad 1.7$$

where D_1 is the radiation dose of a radiation type that led to the same biological effect of a dose D_2 of a different radiation type. We can understand if the radiation that delivered the dose D_2 is more

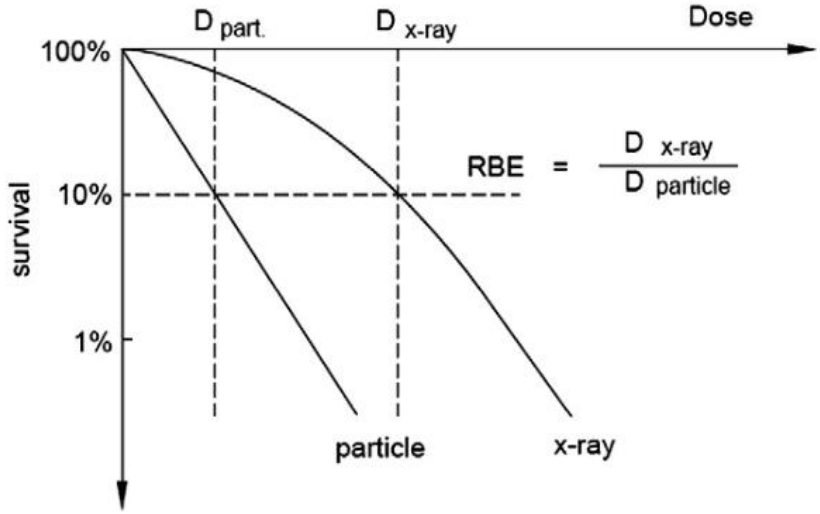

Figure 1.9 – Example of the calculation of the relative biological effectiveness for a cell survival fraction of 10% between deposited doses of a radiation particle and X-rays. Adapted from Fokas et al [53].

effective than the other if the RBE is greater than 1. The biological effect can be, for example, the same cell survival percentage after a cell population is exposed to radiation. An example is shown in Figure 1.9 comparing the doses that led to a 10% survival fraction from charged particle and X-ray exposures. [53]

It is known that high LET radiations lead to higher RBE in comparison to lower LET. [62–64] This was proved when helium ion irradiation results from hamster lung cells were compared to gamma radiation exposure from ^{60}Co decays. The RBE increased for increasing average particle LET values up until 131 keV/μm, to which the RBE values decrease for higher LET values than that. [65]

RBE is also taken into account in radiation risk calculation, through quality factors. An example of that is the calculation of the equivalent dose (H_T), which considers the radiosensitivity of tissues to a radiation type. It is expressed in units of Sievert (Sv):

$$H_T = D \times Q \qquad 1.8$$

Here, D is the absorbed dose and Q is a quality factor directly related to the radiation LET. The quality factor of photons and electrons is considered to be 1, whereas for α-particles it is typically considered to be higher than 20. [44,60]

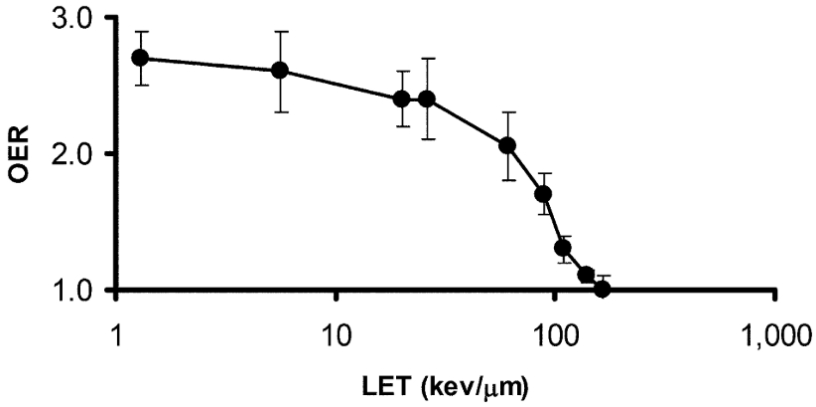

Figure 1.10 – Oxygen enhancement ratio variation with LET. The data used in this plot was from human kidney-derived cells that were incubated in air (aerobic conditions) or nitrogen (hypoxic conditions). Authors irradiated cells with α-particles of different energies (having different initial LET values) that were generated through a cyclotron. Adapted from Sgouros et al [55].

1.4.4 Oxygen enhancement ratio

The oxygen concentration in tissues and cells plays an important role in cellular dose response to radiation. The biological effect of a given radiation delivering the same dose to cells that have different oxygen concentrations can be different. Typically, cells with low oxygen concentrations (hypoxic cells) are more radioresistant. This is due to the fact that molecular oxygen is a chemical radiosensitizer, enhancing the radiation cell kill effect by increasing the chance of the production of free radicals. [66]

It is important to understand the different radiation dose responses of cells in hypoxic or aerobic conditions. The oxygen enhancement ratio (OER) characterizes that effect. It is defined as the ratio between the dose necessary to achieve a certain biological response on cells under full hypoxic conditions and the dose necessary to achieve the same response on cells under normal oxygenated conditions.

For low LET particles, the OER values are typically significantly greater than 1. This means that the dose necessary to reach a certain biological effect in hypoxic conditions needs to be higher than in aerobic conditions, for the same biological outcome. In comparison to low LET particles, α-particles have demonstrated to have lower OER values, which can be close to 1 depending on their energy. Figure 1.10 shows a comparison of α-particles OER varying with LET. [55]

The reasons OER typically decrease with increasing LET are related to the lower presence of reactive oxygen species in low oxygen concentration tissues after irradiation. The presence of these species indirectly increase DNA damage from radiation in cells. It is known, however, that high LET radiation leads to more direct and complex DNA damages, even with lower number of reactive oxygen species products. We will discuss how these products impact DNA damage levels below.

The low OER values of α-particles in comparison to low LET particles represents another advantage of radiotherapy modalities that use α-particle emitting radionuclides. The radiobiological effect of these particles to tissues that have low concentration of oxygen can practically be the same as if the oxygen concentration was higher (OER ≈ 1).

1.4.5 DNA damage and repair

Radiation induced damage to DNA are typically one of three main types: base damage, single strand breaks (SSB) or double strand breaks (DSB). For example, it is estimated that for mammalian cells, there are around 1300 base lesions, 1000 SSB and 20 to 40 DSB per cell per Gy for gamma radiation (low LET). [67] If not properly repaired, these DNA lesions can lead cells to activate cell death mechanisms. Due to both DNA strands being simultaneously broken, the DSB lesions are the most difficult to repair and the lesions that are most closely associated with cell death. [68]

These lesions can be caused directly and indirectly by ionizing radiation particles. Direct effects are related to direct DNA interactions between the secondary electrons that are ejected from the atoms that were ionized by a targeted radiotherapy particle. These secondary electrons react with DNA molecules and break the chemical bonds of their structure. Indirect damage is a result from the interaction of secondary electrons with other molecules (primarily water) in the cell. The chemical reaction between electrons and water results into radical species products such as OH^- and H^+, which again interact with other water molecules and can be recombined into $H3O^+$ molecules too. These chemical products are reactive oxygen species (ROS). ROS can react with DNA molecules and lead to DNA strand breaks. [67,69,70] Figure 1.11 shows a schematic representation summarizing the direct and indirect effects of ionizing radiation in DNA.

Some ROS species can only affect nearby DNA molecules and only live for a short period of time. This is related to ROS having different radical diffusion times and distances. The higher the reactivity of the ROS, the lower radical diffusion time and distance it has. For instance, OH^- has a half-life of around 10^{-9} seconds due to its high reactivity, in comparison to 10^{-3} seconds of H_20_2, which has lower reactivity. In this case, H_20_2 molecules can diffuse away from its source (higher radical distance) whereas OH^- will not. [71]

It is estimated that low LET radiations, such as photons, induce most (~70%) of their DNA damage lesions indirectly, as opposed to high LET radiation such as α-particles, which mostly impose DNA lesions directly. [72] High LET particles are also responsible for larger numbers of clusters of DNA damage within a short distance, due to the high density of ionizations along these particle tracks.

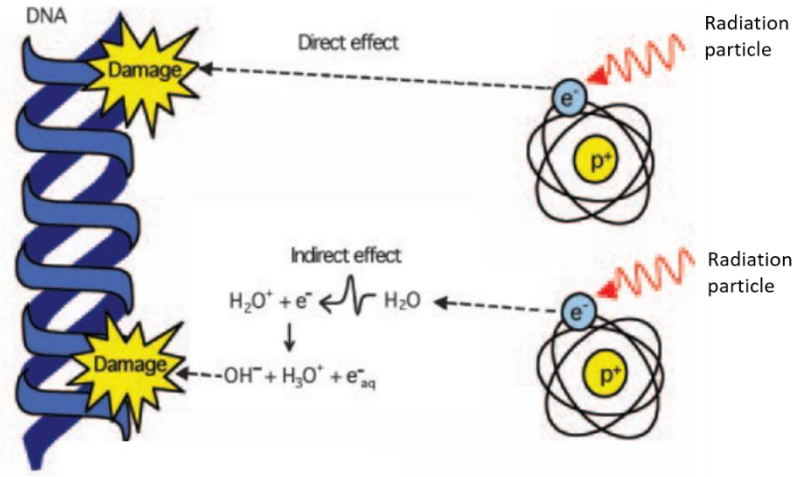

Figure 1.11 – Schematic representation of the effect of radiation particles to DNA: induced direct DNA damage from secondary electrons and induced indirect effects from water radiolysis. Adapted from Dubrova et al [70].

Clustered lesions increase the chance of cell death since all the lesion sites need be fully repaired for the cell to continue to work functionally. [73]

As it was previously mentioned, DSB lesions are the most complex to repair. The repair of these lesions can be done by two main repair mechanisms: Non-homologous end joining (NHEJ) and homologous recombination (HR). NHEJ repair mechanisms are available throughout the cell cycle and involve joining two DNA strand ends together with little or no homology. This is prone to minor errors during repair, often leading to DNA deletions and mutations. HR repair mechanisms can only be used during the S and G2 cell phases as the DNA replication chromatid is necessary to be used to reconstruct and repair its sister chromatid lesions. [74]

There are various cell cycle checkpoints to check the genomic integrity of DNA and activate the necessary repair mechanisms if needed. When the radiation induced damage is beyond repair, cellular death mechanisms will be activated. These can include programmed cell death mechanisms (apoptosis), deterioration and loss of proliferation functions (senescence), cell membrane rupture (necrosis), chromosome segregation errors during mitosis (mitotic catastrophe) and intracellular digestion of cellular dysfunctional components (autophagy). [75]

1.4.6 Bystander effects

During the last decades, there have been radiobiological studies pointing to the existence of cell damage and death through indirect radiation induced damage. In cases where a cell population was irradiated, it was shown that there was additional damage induced in neighbouring cell populations that

were not directly hit by radiation particles. This indirect damage is induced through bystander cell mechanisms. [76]

Bystander effects were initially observed by Nagasawa and Little in 1992, where their experimental results showed that in a system where only 1% of the cell population was traversed by α-particle radiation, 30% of the cells contained sister chromatid exchanges. [77] Since then bystander effects were further proved to occur with ultraviolet radiation, photodynamic therapy, heat and chemotherapy. [78–81] Bystander signalling between irradiated cells and neighbour non-irradiated cells can occur through gap junctions or through excreted soluble factors. These signalling mechanisms induce a bystander response from non-irradiated cells. [76,82] Some of the most important cell phenomenon associated with bystander effects are cells ability to have an adaptive response (related to cells radioresistance), genomic instability (related to genomic abnormalities which can lead to cell death) and abscopal effects (related to long distance clinical bystander damage in cells located further away from the radiation target). [83,84]

It is still unclear the level of impact of bystander effects for α-particle targeted therapies. For low tissue doses, the number of cells which are exposed to α-particles can be low in comparison with other radiotherapy modalities. This has important implications since the number of targeted cells have a clear relation with the magnitude of the bystander responses caused. Despite the uncertainty of bystander quantitative impacts for α-particle radiation, it has been proved to occur at different radiation doses. For instance, it has been reported that even at low doses of 0.1 Gy, non-targeted cells shown higher levels of DNA damage when nearby targeted cells were exposed to α-particles, in comparison to control cell samples. [85] Other observed bystander effects of α-particle irradiations are related to the overexpression of stress-responsive proteins in non-targeted cells. This overexpression occurred for cells within a 100 µm radius distance from treated cells. [86]

There are still many questions regarding the bystander effects mechanisms of action. This is an important radiobiologic cell response that is in need of continued investigation.

1.5 Microdosimetry

The dosimetry calculations for the absorbed dose at a macroscopic scale is often useful for EBRT, as the aim is to calculate the averaged dose deposited in the different targeted organs and tissues. However, if we want to study the dosimetry at a microscopic scale, for example at a cell level, there can be fundamental differences involved. The absorbed dose on a single cell can be significantly different than the absorbed dose at a neighbouring cell, leading to different biological responses from each targeted cell. This is especially relevant when assessing the dosimetry with high LET radiation particles, where the number of particle tracks and ionizations per cell vary considerably, leading to different

absorbed doses. Microdosimetry allows the study of the spatial and temporal distributions of radiation particles and their effects on a micrometre scale. [87,88]

Two of the most important parameters taken into account in microdosimetry are the specific energy and the lineal energy. The specific energy is defined as the ratio of energy transferred to matter by the volume of that matter (J/Kg). The lineal energy is defined as the ratio of the energy transferred to matter from a single particle energy deposition event by the mean particle track length (keV/µm). These parameters are fundamental for accurate LET and dosimetry calculations, leading to more accurate descriptions of radiation energy deposition events in microscopic simulated volumes. [89]

Microdosimetry takes into account the stochastic processes involved in the single particle track events, assuming a probabilistic distribution of single particle events to occur in micrometre scales. This can be useful to understand the probability of a particle traversing a single cell, or consequently to study the probability of DNA mutations induced by that particle. In the macrodosimetry scale, as it is often the case with X-ray EBRT, the dose absorption processes are assumed as deterministic instead of stochastic.

Some of the main advantages of microdosimetry methods, in comparison to standard radiotherapy dosimetry methods, are related to dose absorption heterogeneity within cells. α-particles have a short range in tissue, which relates to high energy deposition in just a few cells. This means that there can be a significant variation in the absorbed dose from cell to cell, especially when some cells are traversed by α-particles and others are not. [61,90] On the other hand, radionuclide injections can involve non-uniform radionuclide distributions along cells and tissues due to different tissue and tumour uptake kinetics. This variable spatial treatment distribution at cell scale cannot be taken into account with macrodosimetry techniques. [91,92]

Implementing full microdosimetry approaches in α-particle related clinical applications can, however, be challenging. There are complex variables involved that are not yet fully characterized, such as time-dependent activity distributions of radionuclides at a cellular and subcellular levels. This is the case of ^{223}Ra treatments for example, where Xofigo cellular uptake kinetics are not fully understood yet and would be significantly relevant in microdosimetry calculations.

1.6 Monte Carlo Simulation

1.6.1 Monte Carlo

One approach that complements microdosimetry methods is Monte Carlo simulation. Monte Carlo methods are a class of computational algorithms that are based on random sampling, used to

calculate probabilities of events and make numerical predictions. They are particularly useful in complex mathematical models that involve many degrees of freedom and where a solution is either impossible or unlikely to be obtained through deterministic algorithms. In deterministic algorithms, the output solution is always the same, no matter the number of attempts to re-calculate it. This is not the case in Monte Carlo methods, due to the stochastic nature of the process. As inputs are randomly generated from probability distributions, the final output of different Monte Carlo iterations can vary. [93,94] For example, the Monte Carlo simulation of a single radiation particle will have a different output for different simulation iterations. When increasing the number of simulated particles to a million, the outputs of different simulation iterations will be more similar. This is related to the law of large quantities. Unlike deterministic methods, the stochastic models related with Monte-Carlo simulations involve randomness, for example on the definition of a single particle emission direction. As the sample of particles increase, the more similar the output results from Monte Carlo simulation get, even when considering the randomness nature involved. This also allows Monte Carlo methods to better describe micro and macroscopic problems.

Monte Carlo methods can be related to the early random sampling experiment from 1901 to estimate π by dropping needles on the floor made of parallel strips of wood with the same width – the Buffon's needle experiment. [95] Nowadays, these methods are used in a variety of areas involving physics, chemistry and mathematics. One of the main areas that involve Monte Carlo methods is in the simulation of radiation particles interaction with matter, which is relevant in radiotherapy treatment planning and dosimetry calculations.

These methods can require a considerable computational power depending on the geometries and physics involved. As available computer power has increased, it is easier to implement Monte Carlo methods, using detailed 3-D geometries in radiotherapy fields such as particle accelerator facilities, particle detection simulation and patient treatment plans from computed tomography scans. In these cases, using Monte Carlo simulation makes it possible to determine the energy, position and direction of all particles being emitted through sources, as well as the particles that reach a detector or a targeted organ in a patient. [94]

1.6.2 Geant4 and TOPAS

One of the most widely used Monte Carlo packages to simulate particle interactions with matter is Geant4. It was originally built by a collaboration of particle physics institutes such as CERN, SLAC and KEK. This toolkit allows the implementation of experimental aspects, such as geometry, particle tracking, scoring and physics processes. The physics processes handled by Geant4 include processes

such as ionization events, Compton and Rayleigh scattering, bremsstrahlung, pair production, positron annihilation, photoelectric effect, synchrotron and transition radiation, Cherenkov effect, scintillation, fluorescence, Auger electron emissions, reflection, refraction and absorption. [96]

Geant4 models different interaction processes for each particle based on cross sections and model outputs. Each particle interaction with matter is simulated as a serious of small steps and each interaction result is calculated based on particle cross sections. These are easily available through physics tables. The model output is related to the interaction result – for example, particle direction, momentum, energy, secondary particle generation, etc.

Using Monte Carlo methods in Geant4 allows us to make predictions about the general behaviour of the experiment environment we are simulating. This is possible by having a large sample of simulated particles, which cover all relevant particle interaction results within the physics geometry of the simulation. These simulation results allow us to infer details about properties of the particles such as LET in matter, which cannot be measured directly, helping us to obtain a quantitative description of radiation effects, such as absorbed dose. This is particularly relevant in radiotherapy fields.

The learning process of Monte Carlo simulations in Geant4 can be challenging. The simulation toolkit is complex and it takes time for users to get the expertise necessary to be able to set simulations for different physics applications. In addition, users often find it difficult to set the appropriate settings within their Geant4 simulation code, which is built in C++. With these complexities in mind, a TOol for PArticle Simulation (TOPAS) was built. This user-friendly tool facilitates the use of Monte Carlo simulations layered on top of a Geant4 environment. Its primary use is focused on proton therapy but it allows the simulation of other charged particles, such as α-particles. [97]

All the Monte Carlo simulations done throughout this thesis were based on TOPAS.

1.7 Project objectives

Given the importance of prostate cancer and associated bone metastatic disease, this thesis focuses on the evaluation of the radiobiological aspects of α-particles and ^{223}Ra targeted radionuclide radiotherapy.

This investigation will be conducted in two parts. First, we developed a novel α-particle irradiation system to be used in laboratory experiments. During this project, our research group has acquired an ^{241}Am source to be used for this thesis research investigations as well as in other research group projects. The design of the irradiation protocol and associated dosimetry calculations were

covered during this thesis project. The experimental and simulation work performed during the first part of the project involved:

- The development and assessment of an in-house α-particle irradiation system to be used in radiobiology experiments in laboratory
- The evaluation of 3D printed collimators to be used in the improvement of α-source irradiation systems
- The validation of Monte Carlo simulation methods used in physics and dosimetry calculations for α-source irradiations

The second part of this thesis project involved using the results obtained from the α-source system design and assessment to conduct *in vitro* experiments. These experiments allowed us to compare the effects of different irradiation methods on cells, focused on cell survival and DNA damage. We also used α-particle radiosensitivity cell parameters to simulate the effect of ^{223}Ra treatments on tumour growth. The specific goals of the second part of this thesis project were:

- The comparison of the radiobiological effects of X-rays, externally emitted α-particles and ^{223}Ra cell exposures in *in vitro* experiments
- The simulation of the effect of ^{223}Ra treatment exposures in bone metastatic tumour growth and its comparison to *in vivo* clinical results

CHAPTER 2 : α-SOURCE VALIDATION AND OPTIMIZATION

2.1 Introduction

Unlike X-ray cabinet sources, which usually produce directional beams of X-rays, radioactive isotope sources naturally emit radiation particles isotropically. This is a result of the particles being emitted from nuclear decay events. α-sources used in laboratory studies are an example of such radioactive sources, being composed of a layer of a radioactive isotope, usually Plutonium-238 or Americium-241.[51,52,98–104] This radioactive layer is surrounded by a thin protective layer of a non-radioactive material. These sources can be used to study α-particles' properties and their effects on different materials, for example human tissues. Understanding α-particles' effects has become even more important since radiotherapy modalities involving radioisotopes are increasing, in particular those using α-emitters as ^{223}Ra.

In this chapter we characterize an α-source constructed for radiobiological studies and study the properties of α-particles interacting with different materials, given a specific experimental irradiation setup. This study will allow the assessment of dosimetric measurements for *in vitro* cell experiments with α-particle irradiations. To do this, this chapter's work focuses on quantifying 4 main parameters:

- Source irradiation uniformity
- Particle flux
- α-particle energy and angle distributions
- α-source dose rate

Studying the source irradiation uniformity is important in order to understand if an irradiated target area is evenly receiving the same radiation dose. This is related to the number of particles hitting different target areas as well as their energy distributions. If one target area receives significantly more particles than other areas, or if the particles' energy distributions are uneven across a target area, it will lead to a poor dose uniformity across the target. The number of particles hits is directly related to the energy deposition per volume. Therefore, the source fluence uniformity will impact the dose uniformity as well. For high LET sources this can have significant impact at low fluences where, at the cellular level, hit and non-hit cells can be present. One of the causes of poor uniformity is related to the α-source

construction, as the distribution of the radioactive isotope concentration across the source area might differ.

Furthermore, other particle hit parameters can impact dose uniformity, such as particle energy or angle. Particles with different energies or angles will deposit different energies to a volume. As we aim to study α-particles' effects on different target materials, it becomes essential to understand the α-source irradiation uniformity.

Similarly to the previous points, analysing the source's particle flux and energy distribution at an irradiated target is highly important in the study of α-particle effects. These two variables depend on the source's activity, target distance and materials between a target and the source. During the work in this chapter, we analyse the effects of the distance and materials between source and target on the particle flux and energy distributions. This is done by both experimental and simulation analysis.

Finally, we calculate the dose rate of the α-source irradiating a cell target for *in vitro* cell experiments. As one of the aims of this thesis is to study the radiobiological effects of α-particles on cells, it is necessary to assess the radiation dose delivered to a cell target by the α-source during a specific irradiation time period. This involves the combination of the analysis that were previously mentioned as well as some dosimetric simulation studies.

This chapter's results will help to further understand α-particle interactions with human tissues. Such studies are important for optimization of radiotherapy treatments that use α-emitting isotopes, such as ^{223}Ra.

2.2 Materials and methods

2.2.1 The ^{241}Am source setup

The α-source used for these experiments was obtained from Eckert & Ziegler Isotope Products GmbH. It is composed of 2 Americium-241 (^{241}Am) oxide sheets (5 x 2.5 cm width) glued together, assembling a single active layer of 5 x 5 cm in total. ^{241}Am has a half-life of 432.2 years with 5 possible α-particle decays, having energies ranging between 5.38 MeV and 5.51 MeV (Figure 2.1). Its average α-particle emission energy is 5.48 MeV. The final decay product of ^{241}Am is Neptunium-237 (^{237}Np), whose subsequent decays have little contribution due to this isotope's half-life being 2.14 x 10^6 years. [105]

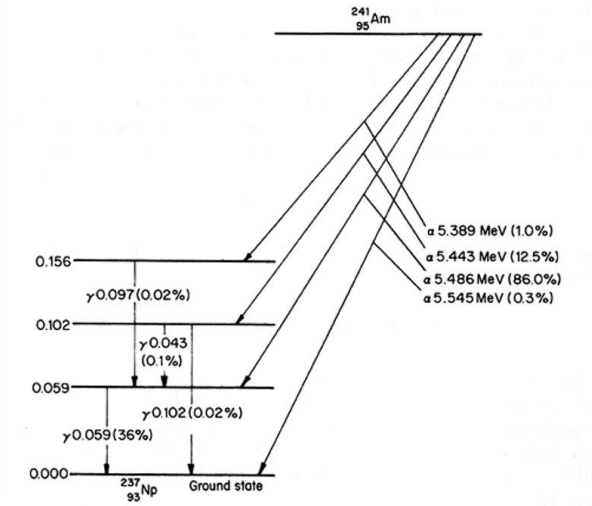

Figure 2.1 – Decay scheme of ^{241}Am. The figure displays 4 of the 5 α-particle decay possibilities. The missing α-particle decays with 5.51 MeV energy and is emitted with 0.2% chance. The final product of the decay scheme is ^{237}Np.

The ^{241}Am radioactive source layer has a thickness of 200 μm, covered with a 2 μm gold foil layer on top. Its total radiation activity is 7.4 MBq (measured from the manufacturer at 18 December 2015). This radioactive source is supported by a stainless steel holder, as shown in Figure 2.2A.

In order to facilitate all α-particle irradiations, a stainless steel box was constructed by the Medical Physics workshop at the Northern Ireland Cancer Centre (Figure 2.2B). This α-source box allows a target to be placed at different distances from the source. The holder provides 7 positions spaced apart by 6 mm, where the closest distance between the source and a target is 2.9 mm. All irradiations were performed in air.

We used Mylar dishes to support and hold a target during irradiations. These are composed of 2 metal rings, a plastic supporting white ring and the polyethylene terephthalate film sheet (Mylar), as shown in Figure 2.3. When the dish is assembled, a target can be placed on top of the Mylar sheet, being exposed to radiation particles. The open Mylar exposed area of the dish has a diameter of 3.4 cm. In all experiments, the Mylar that was used had a thickness of 0.9 μm and was purchased from Goodfellow Cambridge Ltd. A low thickness Mylar layer such as this has been commonly used for α-source irradiations, allowing α-particles to go through it, with minimal energy losses, and hit the target. [98,102,106,107]

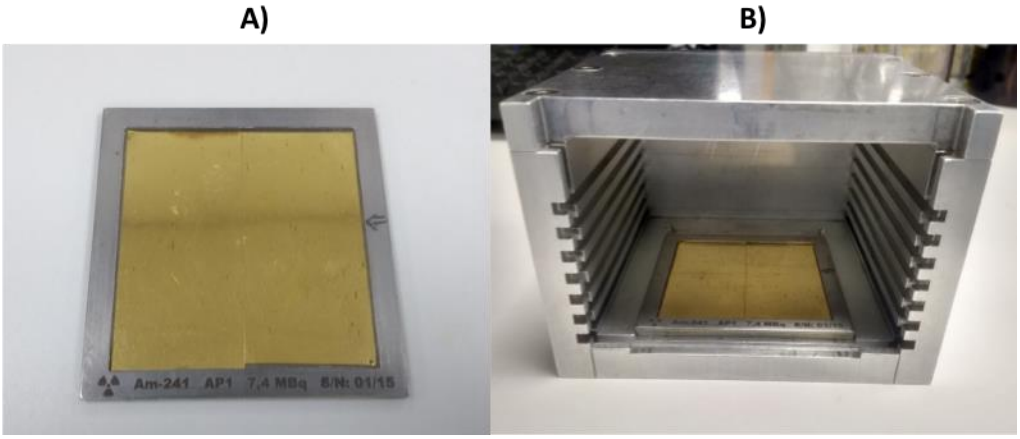

Figure 2.2 – A) α-source used for experimental tests, composed of two ^{241}Am layers glued together. The two layers are sitting on top of a holder, with metallic edges surrounding them. B) Source holder box used to vary the distance between the target and the source. There are 7 slots that can be used to place a target dish.

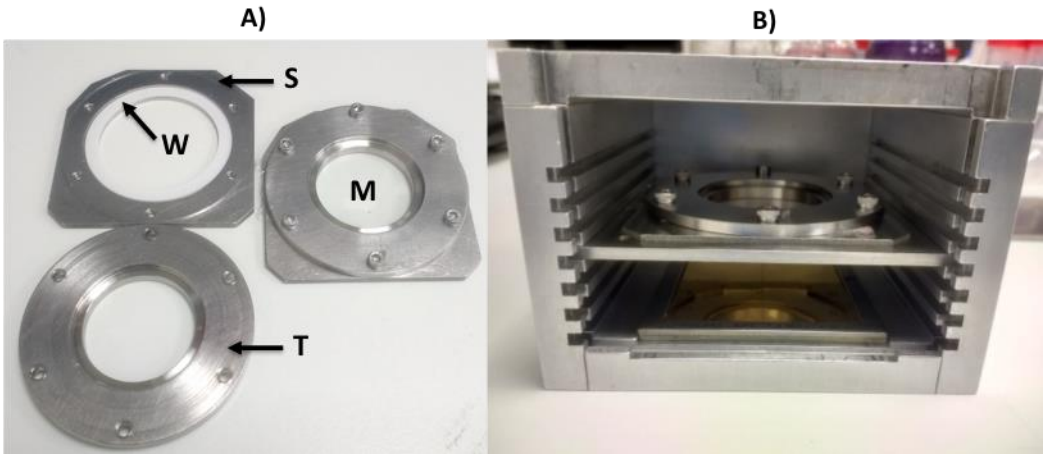

Figure 2.3 - A) Mylar dish components (left side) and final assembled dish (right side). Between the bottom metal ring (S) and the top metal ring (T) there is a white plastic support ring (W) and a transparent Mylar sheet layer (M) with 0.9 μm thickness. B) Source holder box with a Mylar dish positioned at the 4th step from the α-source.

2.2.2 Experimental analysis

2.2.2.1 Gafchromic film optical density

Radiochromic films are commonly used in physical and medical fields for radiation dosimetry. These films are self-developing chemical dosimeters, having a radiosensitive layer whose colouration changes when exposed to ionizing radiation. The higher the exposed dose, the darker the colouration becomes.[108,109] The colouration intensity is often used to calculate the film optical density, which has a non-linear relationship with the radiation dose. Figure 2.5 shows a typical dose response curve relation

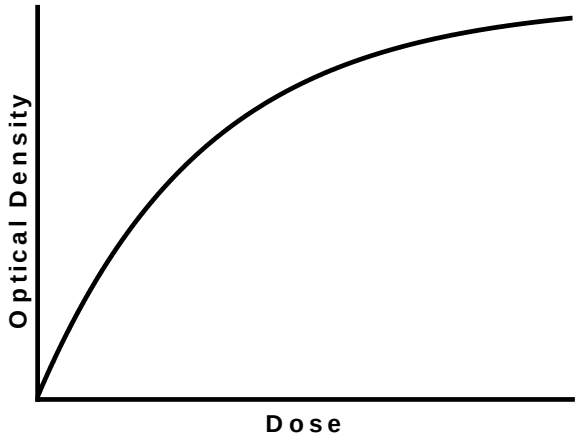

Figure 2.5 – Representation of the relation between radiochromic film optical density and radiation dose.

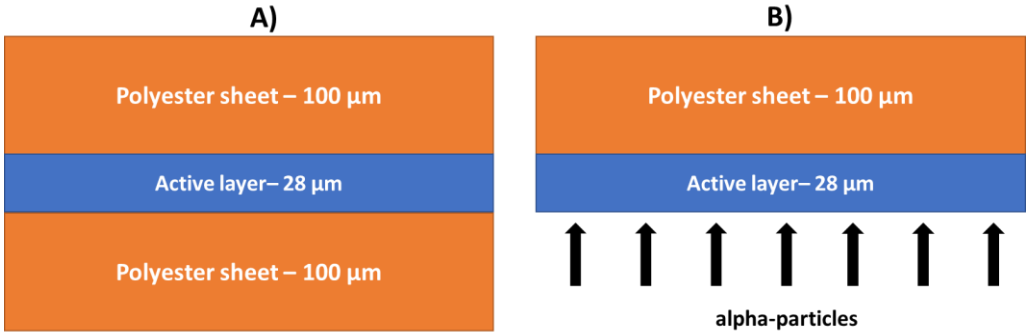

Figure 2.4 - Schematic representation of the EBT3 film material layers. A) Normal EBT3 radiochromic film. B) Customized EBT3 radiochromic film used for α-particle irradiations.

to optical density of radiochromic films. In this work we have used radiochromic films, in particular the Gafchromic EBT3 dosimetry customized film (Ashland Specialty Ingredients). These films were used to study the uniformity of α-source irradiations.

Typically, an EBT3 film has its radiosensitive layer surrounded by a protective polyester sheet on both sides (Figure 2.4). However, since α-particles have a short penetration range, the EBT3 dosimetry film used were customized by the manufacturer by removing the protective sheet from one side of the film. This allows α-particles to reach the active layer without getting stopped in the protective layer.[110] When exposed to the α-source, the unprotected side of the film was placed facing the α-source.

In the experimental setup we exposed two film samples to α-particle radiation. The first film had a 7 x 7 cm square area and was placed directly on top of the α-source stainless steel holder at a distance of 1.6 mm from the source for a 5 minute exposure. Since the film was placed directly on the metallic source holder, only the central 5 x 5 cm area was exposed to the source. The second film sample was placed at a distance of 2.9 mm from the source and exposed for 10 minutes. Since the sample was placed

on the bottom metal ring of the Mylar dish, the exposed area was limited to a circle of 4.4 cm diameter. The two film experiments were designed to analyse the source irradiation uniformity at a very close distance and at a distance where a cell target could be placed.

In all the film uniformity analysis performed in this work, a control sample was used to correct for background. The control and exposed films were scanned with a HP Scanjet G4050 scanner and its images analysed through ImageJ and Matlab 2016b (Mathworks, Inc., Natck, MA). The net optical density of the film (*NOD*) was then calculated by subtracting the control film optical density (OD_{ctr}) to the irradiated film optical density (OD_{IR}):

$$NOD = OD_{IR} - OD_{ctr} \qquad 2.1$$

This calculation was done taking into account the transmitted light intensities through the film samples, as shown by the equation 2.2:

$$NOD = log_{10}\left(\frac{I_0}{I_{IR}}\right) - log_{10}\left(\frac{I_0}{I_{ctr}}\right) = log_{10}\left(\frac{I_{ctr}}{I_{IR}}\right) \qquad 2.2$$

Here, I_0 is the intensity of the incident light, while I_{IR} and I_{ctr} represent the transmitted light intensities of the irradiated and control film samples, respectively. [110,111] For all the calculations, the film intensities represent the pixel value of the scanned images from the red channel only.

The net optical density was used to analyse the uniformity of the radiation source in two ways. The first shows the overall area uniformity of the film samples by a colourmap analysis of the film, showing each individual pixel *NOD* in a colourbar scale. The second method was used to analyse the film samples uniformity along central horizontal and vertical lines. The plotted data represents the average pixel *NOD* across central horizontal and vertical rectangle areas of the exposed films, with 6 cm length and 0.2 cm thickness. This thickness, corresponding to 5 pixels, was chosen in order to average each pixel position *NOD*, minimizing the effects of dust and scanner noise that could influence the transmitted light pixel intensities. Each pixel square had a 10 µm length size. A schematic presentation of this averaging process is shown in Figure 2.6.

All data analysis was carried out using Matlab 2016b and GraphPad Prism 6 software.

2.2.2.2 Nuclear track detector

A CR-39 plastic polymer was used for α-particle track detection. It is a solid state nuclear track detector that, when exposed to high LET radiation particles such as protons, carbons or α-particles, gets damaged at the sites where particles hit it.[112,113] Although these sites cannot be seen immediately after irradiation, the chemical etching of this polymer can make the track damages visible using a microscope.

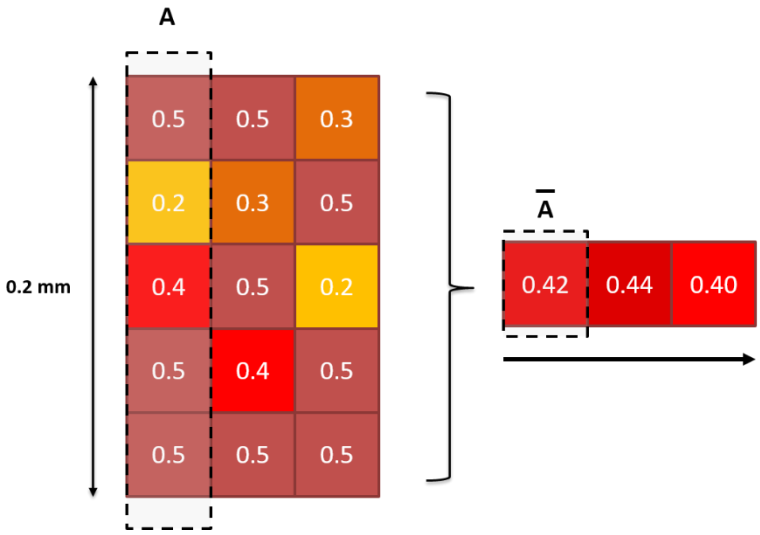

Figure 2.6 – Representation of the NOD pixel averaging process to build the film horizontal NOD profile. In this example A represents a group of 5 individual pixel NOD values, resulting in an average NOD of 0.42 for that central horizontal position of the film. Each pixel square had a 10 µm length size.

This is possible due to the faster chemical etching of the sites hit by particles compared to the etching of the non-affected sites. [114] The CR-39 samples used in this work were purchased from Track Analysis Systems Ltd, having a 2 x 2 cm square area with a thickness of 0.55 mm.

The detector samples used in this work were placed on Mylar dishes, and exposed to the α-source at different distances from the source (*d*) – 2.9, 8.9, 14.9, 20.9 and 26.9 mm. A diagram with the materials between the source and detector is shown in Figure 2.7.

For flux calculations, we exposed these samples to α-particle radiation from 30 seconds to 2 minutes, depending on the chosen *d*. This was done in order to ensure that there was a high number of particle tracks hitting each sample as we expected lower particle fluxes for more distant targets. As the distance of the target from the source increases, fewer particles are expected to reach it due to the isotropic nature of particles' emissions. This is demonstrated in Figure 2.8, which shows a representation of two α-particles, emitted from the same position and travelling the same distance, but having different emission angles θ. In this case, the particle with lower θ can only reach the target A, whereas the one with higher θ is able to reach both targets A and B.

Following the irradiation, we etched the CR-39 samples. The etching process used consisted on placing each polymer sample in a sodium hydroxide solution (NaOH) with a concentration of 6 M at a constant temperature of 60 °C in a warming bath for 90 min. After that period, the CR-39 samples were thoroughly washed with both water and a 70% ethanol solution. After the etching process, the nuclear track detector samples were placed under a Zeiss Axiovert 200M microscope, using a x40 objective.

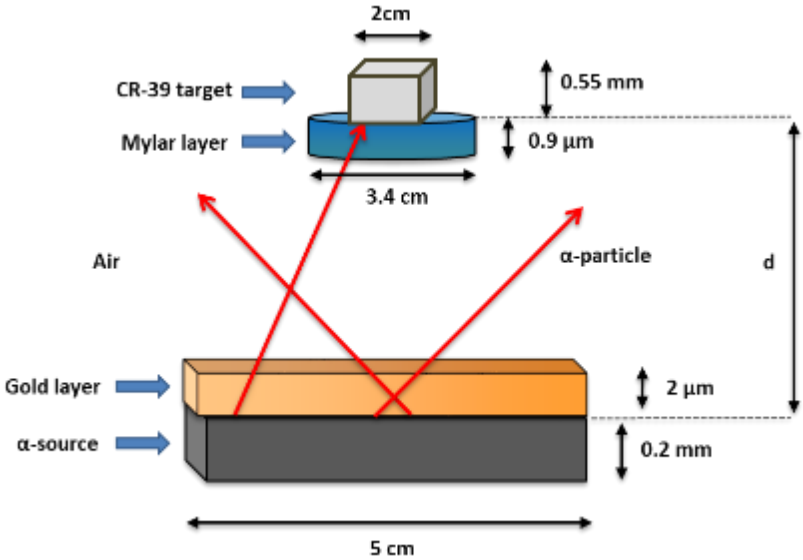

Figure 2.7 - Schematic representation of the materials present between the α-source and a target, where *d* represents the distance between the target and the source.

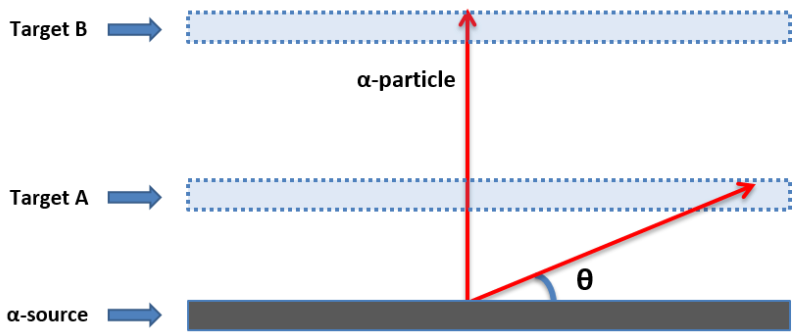

Figure 2.8 – Schematic representation of two α-particles, travelling the same distance but with different emission angle θ, reaching different target distances.

For each sample, 3 pictures at random positions were taken, each picture having 347.4 µm length and 260.5 µm height. In each individual picture, 3 random square areas with 100 µm sides were selected (A_{target}). The number of α-particle track spots was then manually counted for each A_{target} area in each picture, using the imageJ software. Having a total of 9 A_{target} areas for each CR-39 sample, we averaged the number of particle tracks counted per sample area. Since the irradiation time was adapted to the distance of the CR-39 samples from the source, we could ensure an average particle track count per A_{target} higher than 100 for all the samples. This reduces the statistical uncertainty of the mean.

The experimental particle flux was calculated taking into account the average number of particles counted (N_{exp}) along a 100 x 100 µm detector squared area (A_{target}) and the total irradiation time, in minutes (t_{IR}):

$$\Phi_{exp} = \frac{N_{exp}}{A_{target} \times t_{IR}} \qquad 2.3$$

It should be noted that nuclear track detectors have limitations regarding particle track detection. These limitations are often related to the particle's angle when they reach the detector. Certain particle tracks cannot be visually detected after etching when θ_S, defined as the angle between the particle's direction and the detector's surface, is too low. The angle at which a particle stops being detected is called critical angle (θ_C). Based on experimental data of different research groups, the critical angle can vary from 12° to 27°, depending on the particle's energy, etching conditions and the polymer type of the detector.[114,115] As this limitation can influence the particle flux calculation, it should be taken into account when comparing to other work.

2.2.2.3 Charged particle detector

In this work we used a charged particle detector in order to measure the α-particle energy spectra at different distances from the source, within an air environment. In this case, the detector used was a semiconductor silicon detector.

The detection of heavy particles with a silicon detector is done through the electric charges created in the silicon material. When an α-particle hits the radiation sensitive surface area of the detector it is stopped, as the range of the particles in silicon is lower than the thickness of the detector material. This detecting region acts as a depletion region with no free electric charges. As particles are being stopped, the interactions and energy transfers that happen between an α-particle and the silicon depletion region lead to electron-hole pair formations. The formation of a single electron-hole pair depends exclusively on the detector material properties, not being dependent on the energy of the α-particle's hitting the detector. However, the number of electron-hole pairs formed is directly proportional to the incoming particle's energy, as higher energetic particles transfer higher energies when they are being stopped, thus leading to a higher number of electron-hole pair formations.

The charge pulses created by all the electron ejections resulting from a single particle interacting with the depletion region, is then integrated and amplified through a discriminator preamplifier. The resulting pulses are then fed to a multichannel analyser (MCA), converting the analogue signal to digital channel values. The channel values are directly related to the particles' energies. As the number of particle counts increases for all the different ranges of particle energies, an energy spectrum is formed.[116]

The experimental setup used focused on obtaining the energy spectra of α-particles hitting a silicon detector at different distances from the α-source. To do this, the silicon detector was placed at 4

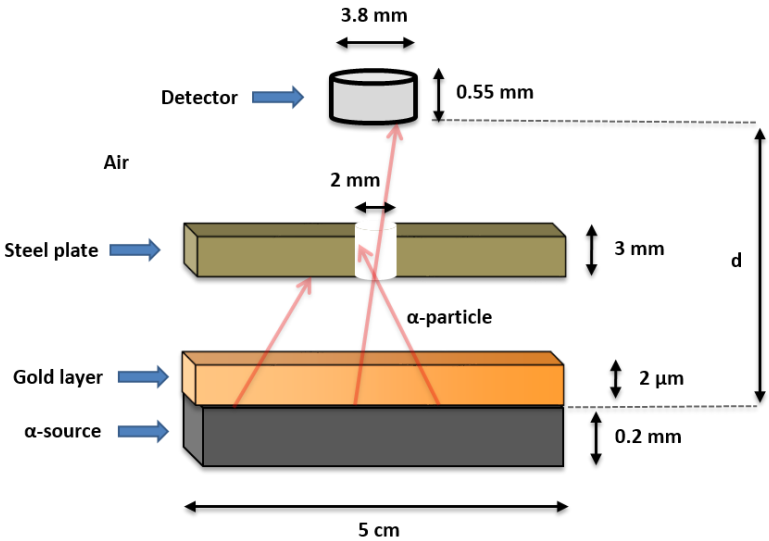

Figure 2.9 - Schematic representation of the materials present between the α-source and semiconductor detector, where *d* represents the distance between the detector and the source.

different distances *d*, spaced by 6 mm from each other and starting at a distance of 7.45 mm from the source. A 3 mm thick steel plate with a central 2 mm diameter hole was placed between the source and the detector, as shown in Figure 2.9. The steel plate, fixed at a distance of 1.45 mm from the source, acted as a particle filter in order to avoid particle count saturation at the detector, as this happened when the detector was exposed to the whole source.

Since the output of the spectrometer is in counts per channel number, an energy calibration must be conducted. Ideally, the energy calibration of a silicon detector should be done in vacuum and using a calibration α-source with known energy peaks. As we did not have access to a calibration source and a vacuum chamber, we have conducted the energy calibration using data from Monte-Carlo simulations in air, explained later in section 2.2.3.2.

All experiments were conducted in a dark room. This was done in order to avoid background noise as the detector diode is very sensitive to artificial light. No background particle counts were detected in these conditions. Other control uniformities could only have been measured with a source calibration, not available during this experiment. The silicon detector used in this work has a radiation sensitive surface area of 3.8 x 3.8 mm. The detector, discriminator preamplifier and the MCA were obtained from LD DIDACTIC GmbH. The software used to obtain the digital signal of particles' energy spectra was CASSY Lab 2 (version 2.17.5388, LEYBOLD).

2.2.3 Monte Carlo simulation of the ^{241}Am source setup

Monte Carlo simulations were performed to compare the experimental data from the source calibration. Here, we used similar conditions to those used in the real setup, adapting a few simplifications. With the exceptions of the source and the target, we followed the same range of materials and geometries shown in Figure 2.7. However, we did not add the geometries of the source holder, the setup irradiation box, or the metallic rings of the Mylar dish as these were outside the α-particle path and would not change the simulation outcome.

The simulation setup geometry used for most simulations performed in this chapter is represented in Figure 2.10 and consisted of:

- an α-particle emitting radiation source with a squared area of 5 x 5 cm and a thickness of 1 μm, composed of Hafnium to simulate a material with high atomic number.
- a gold layer placed on top of the source, with 2 μm thickness and a squared area of 5 x 5 cm
- a cylindrical volume composed of Mylar with 0.9 μm thickness and 3.4 cm diameter, placed at different distances from the source
- a cylindrical volume composed of water with 10 μm thickness and 3.4 cm diameter, placed directly on top of the Mylar layer volume, following the target distances from the source (*d*)
- a cubic air volume surrounding all the other volumes, with 12 cm side length

As previously mentioned, the simulated radiation source material chosen was Hafnium, which has an atomic number Z=72. Due to TOPAS not including radioactive materials, Americium (Z=95) could not be chosen as a material for the isotope volume source in simulations. As an alternative, a different heavy atomic number material was chosen as an approximation, in this case Hafnium. α-particles were generated from random positions within the source volume. Their emission energy was 5.48 MeV, based on the average ^{241}Am particle emissions.[105] In order to have enough data to analyse, a total number of 10 to 40 million particles, depending on the target distance, were emitted from the source. Since TOPAS does not have isotope volume sources as options to be readily used, this specific source was built as an extension that could be loaded into TOPAS.

Although the actual Am^{241} source has a thickness of 200 μm, the source simulated for this work had a thickness of 1 μm only. This thickness was chosen for two reasons. First, a thicker source would need a substantially higher number of particle emissions in order for sufficient particles to reach the target to be analysed with confidence. This could not be done as TOPAS does not allow more than 1000 million particles to be emitted from a source. We should also take into account that even if such simulations could be done, it would take several days for each individual simulation to finish. Secondly, as α-particles with 5.48 MeV are easily stopped in heavy Z materials with thicknesses of few

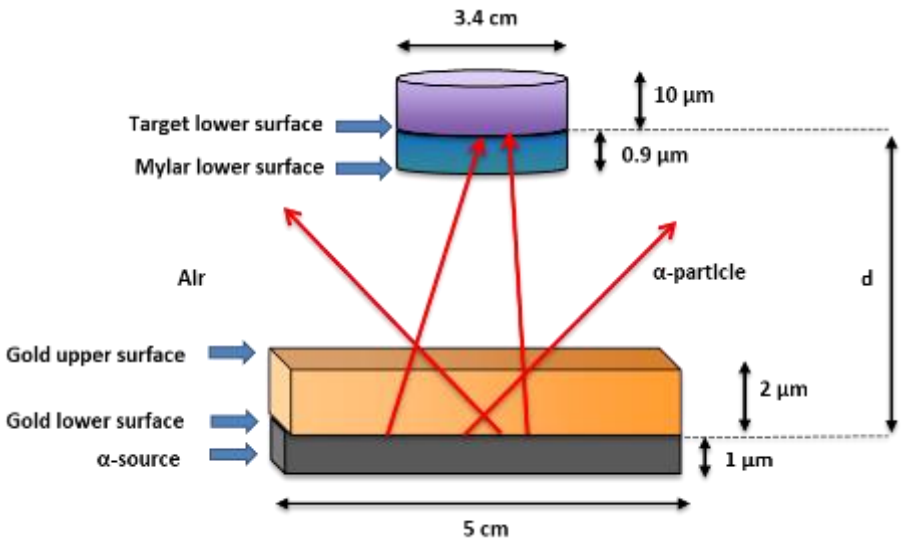

Figure 2.10 - Schematic representation of the simulation setup of all the materials present between the α-source and a target.

micrometres, it was found that a simulated thickness of 1 µm was enough as an approximation to the real source setup.

TOPAS, as a Monte Carlo simulation toolkit, also allows us to retrieve information regarding the particles that interact with the different material volumes. This is done through particle scorers placed at target volumes (volume scorers) or target surfaces (surface scorers). The volume scorers lead to a simulation output that can be, as an example, the total energy or total dose deposited in a certain volume. A surface scorer will show, as a simulation output, each particle's coordinates position, energy or angle when hitting the scored target surface. Since the surface scorers used contain all individual scored particle's information, their simulation output is given through a comma-separated value file (csv). In this work we have used surface scorers for the lower and upper surfaces of the gold layer, as well as for the lower surfaces of the Mylar and water target volumes. The volume scorers were only used for the water target volume in order to calculate energy and dose depositions. All simulation scorers used were filtered to record primary α-particles only.

All Monte Carlo simulations were performed through the Geant4 toolkit TOPAS (version 3.0), run on an Apple iMac (2012 - Intel i5 3.2GHz, manufacturer number MD096B/A). The data resulted from the simulations was analysed by both Microsoft Excel (2016) and Matlab 2016b. The results are presented in plots created by using the GraphPad Prism 6 software. All repeated simulations of an experimental setup generated similar results, with a statistical difference lower than 0.1%.

2.2.3.1 Particle flux simulation

A surface scorer was placed at the lower surface of the water target, positioned at different distances d for each simulation. Since the goal of this analysis is to compare the experimental particle flux with the simulated one, the simulation output analysis focused on the number of particles that hit the water target's lower surface. Although the water target geometry is not the same as the nuclear track samples used experimentally, the end result of this analysis will be the same as we are only interested in the number of particle hits per area.

The simulated particle flux was calculated taking into account the number of emitted particles ($N_{emitted}$), the number of particles scored at the target surface positioned at a certain distance d (N_{scored}), the area of the simulated target (A_{target}) and the actual α-source activity in an emission angle of π radians (Act_{source}), as shown by the following equation:

$$\Phi_{sim} = \frac{N_{scored} \times Act_{source}}{N_{emitted} \times A_{target}} \qquad 2.4$$

In addition, we also analysed the effect of the limitations of particle detection from nuclear track detectors, mentioned in section 2.2.2.2. As noted, CR-39 is limited in its ability to detect particles arriving with glancing angles, equal or lower than θ_C. To take that into account, simulated fluxes were also calculated by removing all particles scored at the target's surface with angles equal or lower than 20°. This corresponds to a critical angle within the range of critical angles detected for similar experimental conditions as the ones used in this work.[114,115] This allowed us to compare both simulated fluxes with and without particles that had an incident angle equal or lower than the critical angle.

2.2.3.2 Simulation of the energy spectra using a charged particle detector

In order to compare the simulated energy spectra results to the experimental data using a semiconductor detector (section 2.2.2.3), a second simulated scenario was considered. In this case we simulated the same range of materials shown in Figure 2.9, having the simulated α-source with 1 μm thickness instead. This simulation setup geometry had the following list of materials:

- an α-particle emitting radiation source with a squared area of 5 x 5 mm and a thickness of 1 μm, composed of Hafnium
- a squared volume box composed of steel with 6 cm side length and 3 mm thickness, having a central hole with 2 mm diameter, placed at a fixed distance from the source of 1.45 mm
- a squared volume box composed of silicon with 10 μm thickness and side lengths of 3.8 mm, following the detector distances from the source (d)

- a cubic air volume surrounding all the other volumes, with 12 cm side length

In this case, the source area does not correspond to the one used in the real setup. This was done to prevent longer simulation run times as a larger source would not influence the number of particles hitting the simulated detector's surface. Particles that would have been simulated outside this simulated source area would have been blocked by the steel plate. The number of particles emitted from the source varied from 60 to 280 million particles, depending on the position of the detector.

Each individual simulation had the simulated detector placed at a different distance from the source, following the same detector distance positions as in the experimental setup (d = 7.45 mm, 13.45 mm, 19.45 mm and 25.45 mm). A surface scorer was placed at the simulated detector's surface facing the source. For each target, we were able to score at least 100 thousand particles.

The simulated spectra was then obtained by analysing the surface scorer output files and generating a histogram of the number of particles in each simulated energy channel, having an energy bin of 0.02 MeV. The resulting spectra data was also used to calibrate the energy channels of the experimental output of the silicon detector (section 2.2.2.3). The energy channel calibration was performed following the equation:

$$E_{sim} = \left(N_{channel} \times E_{bin\_exp}\right) + E_0 \qquad 2.5$$

where E_{sim} is the energy of the simulated spectra for target channel, $N_{channel}$ is the channel number of the experimental spectra, E_0 is the initial energy for $N_{channel}$ = 1 and E_{bin_exp} is the energy bin that corresponds to an individual channel range. We assumed that, in both experimental and simulated spectra, the energy corresponding to the maximum number of counts for the same target distances would be the same. Following that assumption, we fitted a linear regression curve to the experimental data using equation 2.5. The maximum peak's energies and maximum peak channel numbers used for the linear regression are shown in Table 2.1.

The non-linear regression resulted in the experimental calibration parameters E_{bin_exp} = 16 keV and E_0 = - 459 keV, with a high fitting quality (R^2 = 0.994).

After calibration, both simulated and experimental spectra counts were normalized as a probability density distribution, calculated using equation 2.6:

$$\mathrm{P(E)} = \frac{N_E}{N_{counted} \times E_{bin}} \qquad 2.6$$

Table 2.1 – Table showing the simulated spectra maximum peak's energies (E_{sim}) and maximum peak channel numbers ($N_{channel}$) used for calibrating the experimental energy spectra obtained from exposing a charged particle detector to the α-source. The detector was placed at different distances *d* from the source.

d (mm)	E_{sim} (MeV)	$N_{channel}$
7.45	3.51	73
13.45	2.82	144
19.45	1.94	198
25.45	0.73	243

Here, N_E is the number of particles counted for each energy channel, $N_{counted}$ is the total number of scored particles at the target's lower surface and E_{bin} is the energy channel bin size. Normalizing both types of data as a probability density distribution allows us to compare the different spectra. Both experimental and simulation normalized spectra data were compared for the different detector positions.

2.2.4 Monte Carlo simulation of cell dosimetry using the ^{241}Am source setup

In this section´s work we analysed the dosimetry of ^{241}Am source irradiation of a cell target, focusing on the particles' energy variation and dose deposition in targets placed at different distances. Our Monte Carlo simulations were based on the source setup described in section 2.2.3, represented in Figure 2.10. However, in this case, our target, placed on top of the Mylar layer, was based on a general cell geometry, having a cell and an inner central nucleus layers, as shown in Figure 2.11. Similar to before, the cell and nucleus target materials were simulated as water. This is a common phantom material used in Monte Carlo simulations as it has similar properties to cells. [117,118]

The cell target thickness used was 10 μm and the nucleus target thickness was 5 μm, as a general approximation to all the cell types geometries used in this work. These thicknesses are also within the ranges of previous Monte Carlo simulation studies with cell geometries.[118,119] As an example, we measured the cell and nucleus average thicknesses of 20 prostate cancer derived PC-3 cells using the fluorescent microscope with HOECHST-33342 live staining of nuclear DNA. The average cell layer thickness was found to be 7.8 ± 2.5 μm and the nucleus thickness was found to be 3.9 ±1.6 μm, which are within the ranges of the simulated geometries.

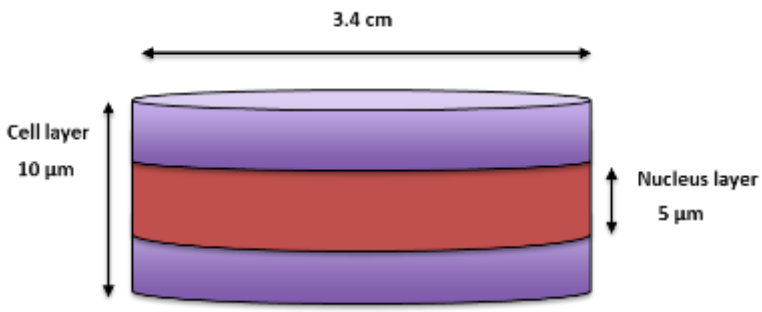

Figure 2.11 – Schematic representation of the simulated cell target with an inner nucleus layer.

2.2.4.1 Particle energy and angle distribution

Similarly to the 2.2.3, a surface scorer was placed at the cell target's lower surface. By further analysing the scorer simulation output files, we were able to calculate the average particle energy and angle when hitting a target positioned at different distances from the source.

We have also studied the particle energy spectrum at each target position. This was done by generating a histogram of the number of particles in each energy channel (0.02 MeV energy bins). Two different normalization approaches were then used. In one case the counts were normalized to the number of particles emitted from the simulated source ($N_{emitted}$) and in the second the particle counts were normalized as a probability density distribution, using equation 2.6.

In this analysis we also calculated the full width at half maximum (FWHM) of the energy spectra peaks. This is an important parameter since it provides information about the width of the energy distribution. A well-defined energy peak, with small spread, has a low FWHM. This parameter was obtained by calculating the energy range between the energies on the spectra curve at which the spectra peak reaches half of its maximum counts. An example of the energy range of the FWHM in an energy spectrum is shown in Figure 2.12.

Additionally, we analysed the particles' distribution in both energy and incident angle at the cell target's surface (θ_S) at different distances from the source, ranging from 0 mm (the lower surface of the gold coating) to 26.9 mm away. This is shown as a colourmap where the colourbar axis shows the normalized maximum ratio of particle counts:

$$\mathrm{N}_{ratio} = \frac{N_{E\theta}}{\mathrm{Max}(N_{E\theta})} \qquad 2.7$$

where $N_{E\theta}$ is the number of counts per energy and angle bin and $\mathrm{Max}(N_{E\theta})$ is the maximum number of counts $N_{E\theta}$ detected on all energy and angle bins.

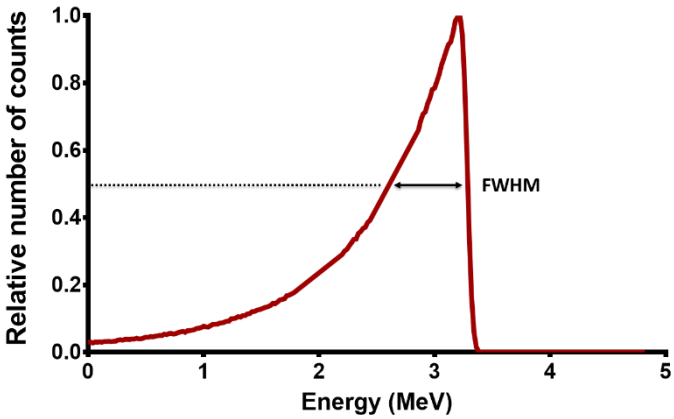

Figure 2.12 - Example of an energy spectrum peak and the definition of the FWHM.

We have also investigated the effect of the gold protective layer of the α-source on the particle energy and angle distribution. This was done by repeating simulations using the standard experimental setup (Figure 2.10) for two scenarios: one with the gold layer present and the other with the gold layer removed. In these simulations, both scenarios had the cell target placed at a distance *d* of 14.9 mm, with the Mylar layer below. α-particles were scored at different material locations: gold upper surface, Mylar lower surface and target lower surface. As before, we analysed the energy spectra and angle distribution of the incident α-particles on each scoring surface.

2.2.4.2 Energy deposition

The average energy deposited by an α-particle in the first micrometre of the water target was calculated. These simulations followed the same setup as those described in the previous sections, for a range of different distances from the source. The simulation scoring output combined the data of the total number of particle counts at the water target's lower surface (surface scorer) and the total energy deposited by the simulated particles in the first micrometre of the target (volume scorer). This allowed us to calculate the average energy deposition per scored particle on the first micrometre layer of the target ($E_{\mu t}$).

Combining the simulated average energy of the α-particles hitting the water target (section 2.2.4.1) and the stopping-power data for α-particles travelling in water from the National Institute of Standards and Technology database (NIST), we were able to calculate the expected average LET of particles hitting a water based target at different distances *d*. This was done by data interpolation of the NIST database, finding the corresponding total stopping power for each average energy of α-particles scored at the target. [120] We assume that the LET is the same as the total stopping power, for the particle energies considered in this work.

2.2.4.3 α-source dosimetry for cell irradiation

In order to use the α-source setup for *in vitro* cell experiments we also have to assess the dosimetry associated with the irradiation of a cell target by this source. This involves calculating the dose rate of the source for a particular cell target geometry, positioned at certain distance from the source. Based on the cell target's geometry represented in Figure 2.11, both cell and nucleus monolayer targets were scored in terms of number of particle hits and dose deposited, using surface and volume scorers.

Based on the experimental and simulated particle fluxes obtained using the methods described in sections 2.2.2.2 and 2.2.3.1, we could then use the resulting scored dose to predict the α-source dose rate at the cell target surface layer, i.e., the first micrometre layer of the cell:

$$\dot{D}_{surface} = \frac{D_{SimSurf} \times A_{target} \times \Phi}{N_{Scored}} \qquad 2.8$$

where $D_{SimSurf}$ is the total dose deposited from all the scored particles (N_{Scored}) in the first micrometre layer of the cell target, A_{target} is the area of the cell target and Φ is the flux of particles at the target.

Similarly, we have also calculated the average dose rate at the nucleus layer of the cell target:

$$\dot{D}_{nucleus} = \frac{D_{SimNuc} \times A_{target} \times \Phi}{N_{Scored}} \qquad 2.9$$

where D_{SimNuc} is the simulated dose deposited at the target nucleus layer.

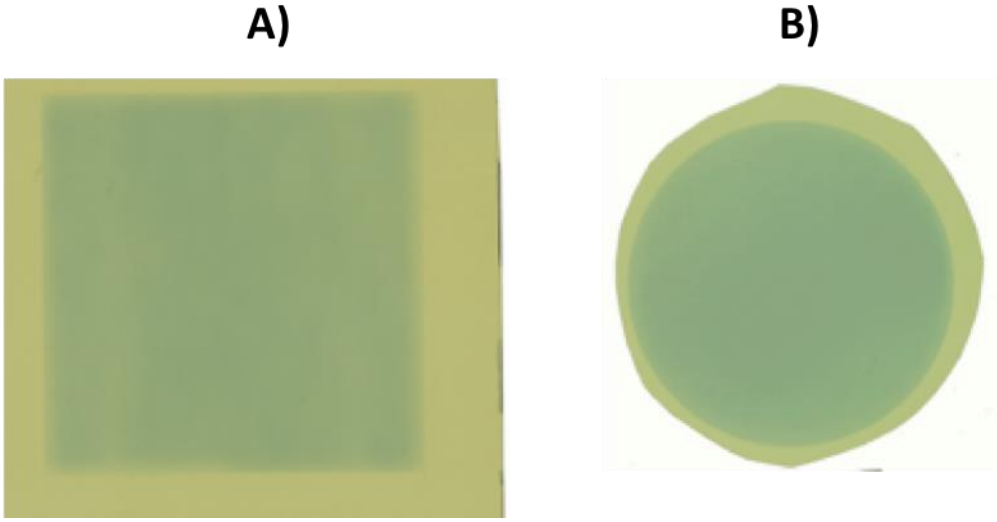

Figure 2.13 - EBT3 customized film scans after exposed to the α-source. A) The film was placed at a distance of 1.6 mm with a 5 x 5 cm exposed area for 5 minutes. The non-exposed area edges of the film were covered by the α-source holder borders. B) The film was placed at a distance of 2.9 mm with a 4.4 cm exposed diameter area for 10 minutes. The film edges were covered by the bottom metal ring surface.

2.3 Results

2.3.1 Experimental data

2.3.1.1 Source uniformity

Images of the EBT3 customized film samples placed 1.6 mm and 2.9 mm away from the α-source are shown in Figure 2.13. A net optical density colourmap analysis of these films is represented in Figure 2.14. As noticeable from the colourmap analysis of the film sample at the closest distance (Figure 2.14A), the optical density is not uniform across the film area.

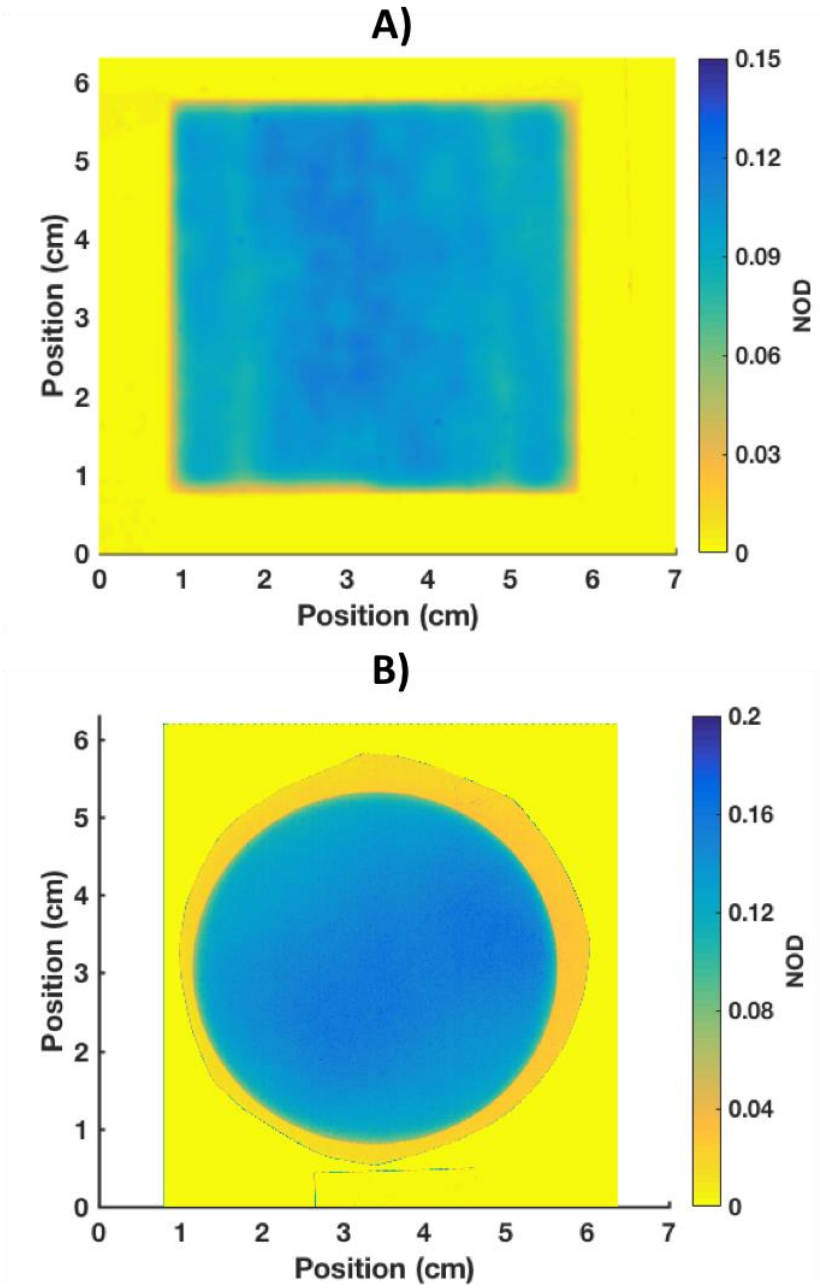

Figure 2.14 - EBT3 customized film areas showing calculated net optical densities (NOD) after exposure to the α-source. A) The film was placed at a distance of 1.6 mm with a 5 x 5 cm exposed area for 5 minutes. B) The film was placed at a distance of 2.9 mm with a 4.4 cm exposed diameter area for 10 minutes. The NOD data shown is represented through a colourmap and was calculated using the pixel intensity levels of the red channel in each image.

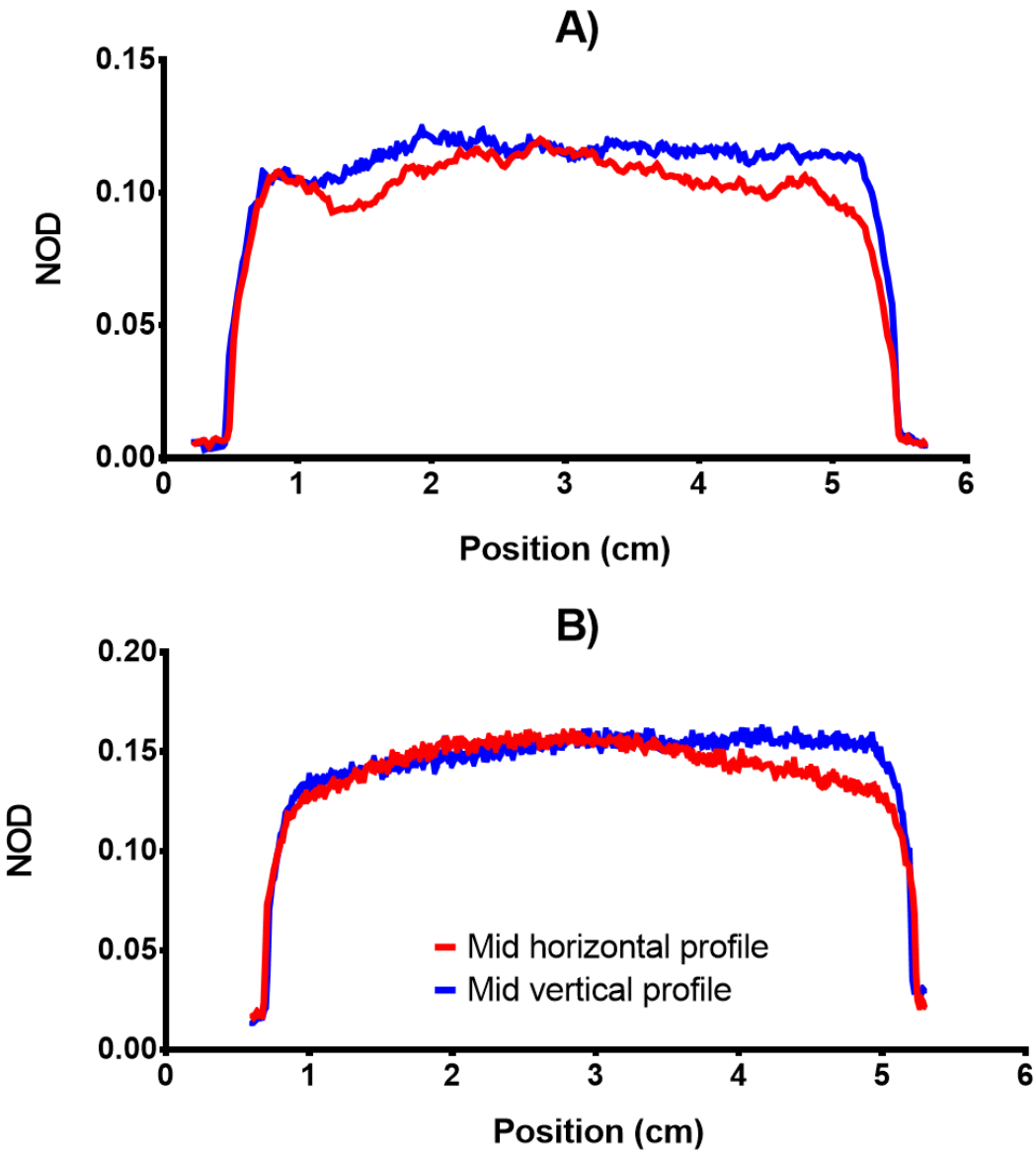

Figure 2.15 - Average net optical density profiles of middle vertical and horizontal lines of EBT3 customized films after exposed to the α-source. A) The film was placed at a distance of 1.6 mm with a 5 x 5 cm exposed area for 5 minutes. B) The film was placed at a distance of 2.9 mm with a 4.4 cm exposed diameter area for 10 minutes. The NOD data shown was calculated using the pixel intensity levels of each red channel scan image along horizontal and vertical lines with 0.2 mm width.

The average NOD across the exposed area of the film is 0.095 ± 0.015, where the standard deviation represents nearly 16% of the average NOD. Since the NOD is related to the source irradiation dose, this shows that certain film areas clearly had different dose absorption levels. This is further confirmed by the NOD profiles along middle horizontal and vertical lines of the same film, as shown in Figure 2.15A. The middle horizontal section of this film is particularly irregular, dropping by 19% to 23% of the maximum intensity in both directions from the centre. This suggests that the activity concentration of the radioisotope ^{241}Am is not uniform along the source area.

However, if a film is placed 2.9 mm away from the α-source then its NOD profile is significantly improved across the film area, as demonstrated by the colormap analysis in Figure 2.14B. The average NOD across the exposed area of the film is 0.144 ± 0.010. This represents a standard deviation of 6.9% from the average NOD, a significant improvement compared to the film exposed closer to the source. The film area corresponding to the actual area of a cell target, having a reduced diameter of 3.4 cm, is even more uniform, with a standard deviation of 5.4% from the average NOD. This will result in lower discrepancies in irradiation dose across the irradiated target area.

Further evidence of this improved dose distribution consistency is shown in Figure 2.15B, along both central line directions of the film, showing significantly improved uniformity. Given the fact that this distance from the source of 2.9 mm is the minimum distance at which a cell target will be exposed to radiation, and the maximum target diameter on top of the Mylar layer is 3.4 cm, this suggests the dose distribution across a cell layer will be relatively uniform.

2.3.1.2 Flux

As mentioned in section 2.2.2.2, the α-source particle flux was measured using nuclear track detectors placed at different distances from the source. Figure 2.16 shows examples of microscope images of detectors placed at different distances from the source and exposed for the same irradiation time period. As the detector is placed further away from the source, there are fewer particles hitting the target, as expected. It is also possible to notice an increase in particle etch pitch size as we increase the distance of the CR-39 target from the source. This is related to a decrease of particle energy with increasing target distance, resulting in higher damage areas in a nuclear track detector.

The particle flux as a function of distance is represented in Figure 2.17, using samples exposed for different times to reduce statistical uncertainties at long distances. This shows a linear relationship between the α-source flux and the target distance *d*, from 0 to 26.9 mm. The target placed 32.9 mm from the source was excluded from the flux analysis, as the number of particle tracks per area was close to 0 and there was a high degree of statistical uncertainty between different areas of the CR-39 sample.

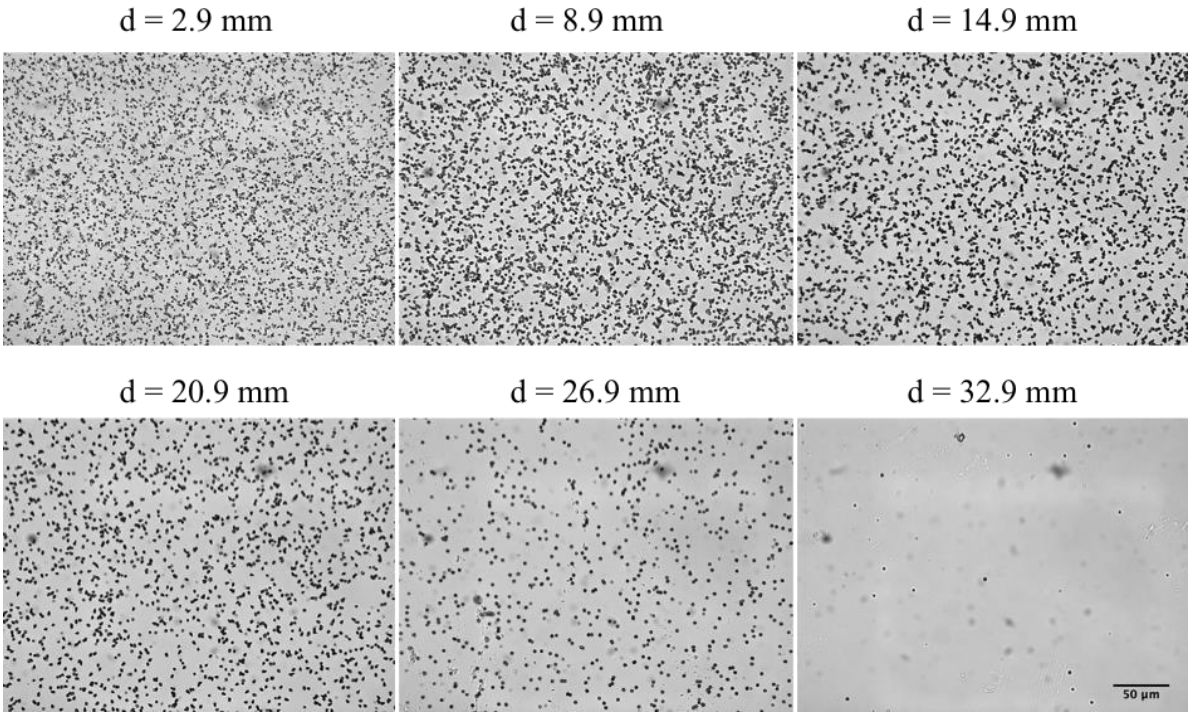

Figure 2.16 - Microscope images of CR-39 samples exposed to the α-source for one minute at different distances from source to target (d).

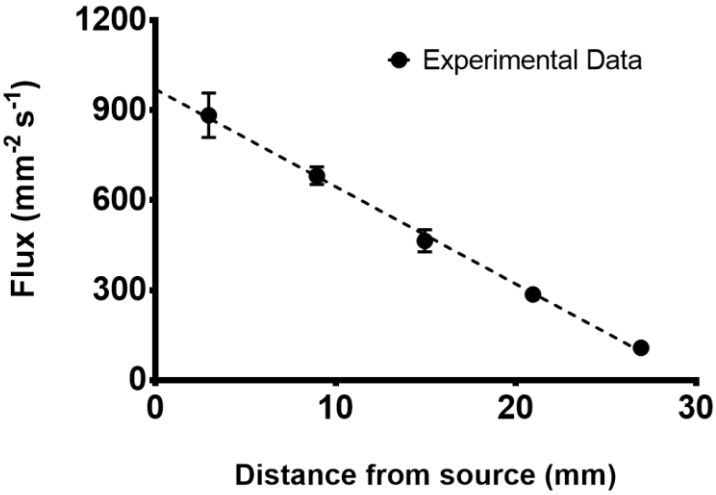

Figure 2.17 - Particle flux from the α-source at different distances from source to target. The number of tracks were counted using nuclear track detectors (CR-39). Experimental data shows the calculated flux from the average number of tracks counted in 9 different areas selected from each CR-39 sample. Error bars correspond to the experimental standard deviations. The dashed line represents a linear regression curve fit as an approximate fit to the experimental data. Depending on the distance from the source, samples were exposed to α-particles from 30 seconds to 2 minutes, in order to improve the accuracy of the flux calculations.

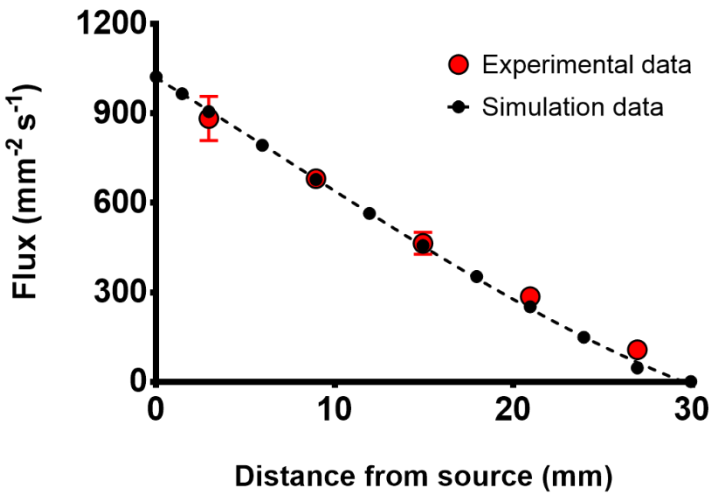

Figure 2.18 - Absolute particle flux from the α-source for experimental (n=9) and simulation data, at different distances from source to target. Error bars correspond to the experimental standard deviations. The dashed line represents the cubic interpolation curve fit of the simulation data, with a goodness of the fit to the experimental data translated by an $R^2 = 0.989$.

2.3.2 Experimental and simulated data comparison

2.3.2.1 Simulated flux

Our initial goal using Monte Carlo simulations was to validate our simulation of the α-source geometry using particle flux data measured experimentally. Taking into account the α-source activity data, we were able to obtain simulated source flux data within a good agreement with the experimental data, as shown in Figure 2.18. The simulated data fit to the experimental data was particularly good for target distances up until 20.9 mm from the source. For higher distances, the data fit quality decreased. This can be due to the lower accuracy of Monte-Carlo simulations in TOPAS regarding particles reaching a distant target having low energy ranges of just a few keV. This can be expected to happen for particles hitting a target placed at long distance.

We also investigated the effect of the critical angle in the simulation detection of α-particles. To do this, the simulated particles that had an angle equal or lower than $\theta_C = 20°$ were counted for each simulated target. The effect of the critical angle in particle detection was found to be almost negligible, having only a noticeable effect at shorter distances from the source. For instance, 2.3 % of the simulated particles scored at a target distance *d*=2.9 mm had an angle equal or lower than θ_C. If these particles were removed, this would bring the simulated flux value to be closer to the experimental one, as demonstrated by Table 2.2. However, when the target was positioned at a distance *d*=8.9 mm or further

away, the fraction of particles below the critical angle significantly drops (< 0.1 %), as lower angle particles are more likely to be stopped in air before reaching a distant target, due to their longer travel distances.

Table 2.2 – Table showing the experimental and simulated fluxes of particles hitting a target at different distances from the source (*d*). The experimental data presented shows the mean flux and its standard deviation. The simulation flux data was divided in particle fluxes with and without particles with angles lower than the critical angle θ_C.

	Experimental	Simulation	
d (mm)	Flux (mm^{-2} s^{-1})	Flux (mm^{-2} sec^{-1})	Flux without θ_c (mm^{-2} s^{-1})
2.9	883.0 ± 74.3	906.3	885.3
8.9	681.5 ± 29.1	678.1	677.6
14.9	464.4 ± 36.8	456.7	456.5
20.9	285.4 ± 20.5	251.2	251.1
26.9	107.6 ± 12.8	47.0	46.9

2.3.2.2 α-particle energy spectra

The energy spectra data obtained through experiments and simulations, normalized as a probability density function, are shown in Figure 2.19. Here we see the maximum P(E) spectrum peaks decreasing as the detector's distance from the source increases. This is consistent for both experimental and simulated data. This decrease is a result of the greater energy lost by particles in air reaching more distant targets. At greater ranges, the spectrum is also broader, which results in lower maximum probability density in the peak.

Although the energy peak positions seem to match well between experimental and simulation data, there is poorer agreement in the P(E) values, as Figure 2.19A shows, with a broader energy spread in the experimental data compared to the simulated data, resulting in lower maximum P(E) values. This may be in large part to the detector response function. For any given incident energy, the semiconductor detector response is actually a Gaussian with some characteristic width, while the simulation records the energy exactly. As a result, its peak width is expected to be narrower, as observed in these data. The Gaussian broadening effect has been reported in experimental data using spectroscopy detectors. [121–123]

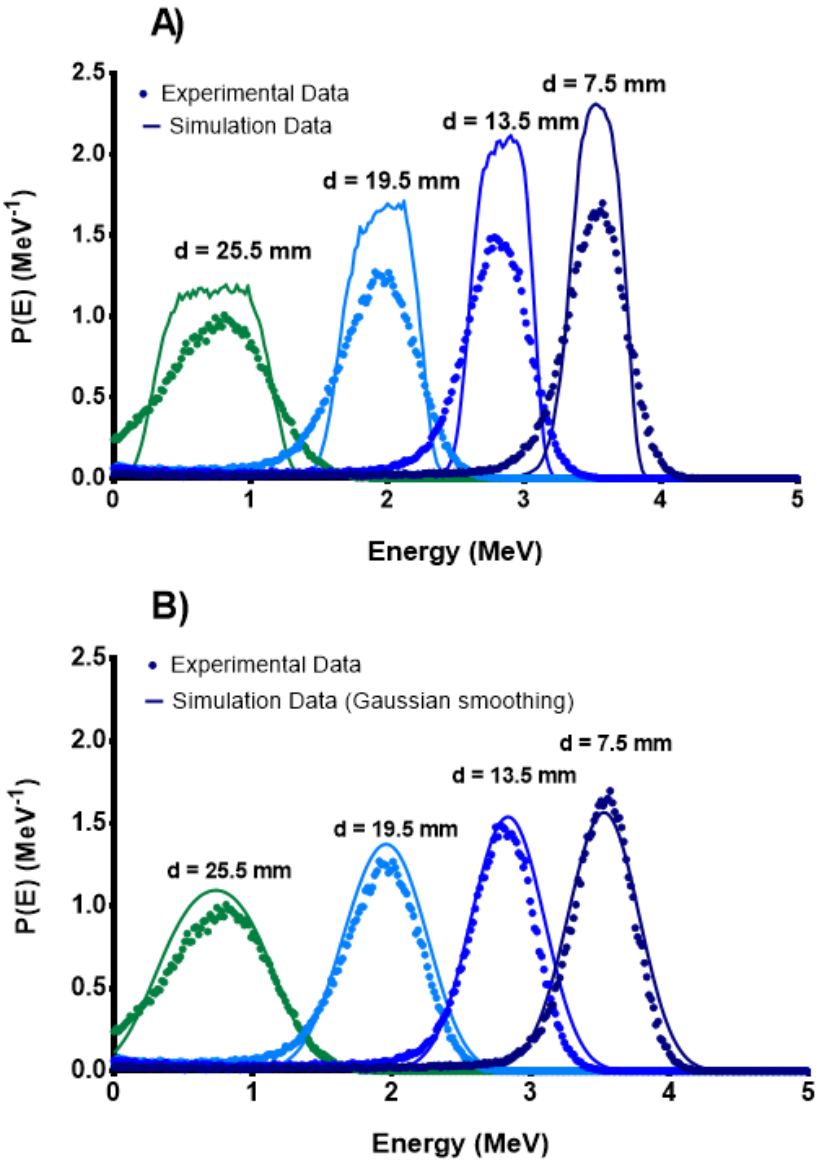

Figure 2.19 – Experimental and simulated energy spectra of α-particles hitting a target placed at different distances *d* from the α-source. The spectra are normalized as a probability density distribution P(E). In B) the simulation data was smoothed using a Gaussian filter with a standard deviation $\sigma = 0.2$ MeV^{-1}.

Figure 2.19B shows the simulated P(E) values with a Gaussian filter ($\sigma = 0.2$ MeV^{-1}) in comparison to the experimental data, as a demonstration example of the Gaussian effect from the detector response on the energy spectra.

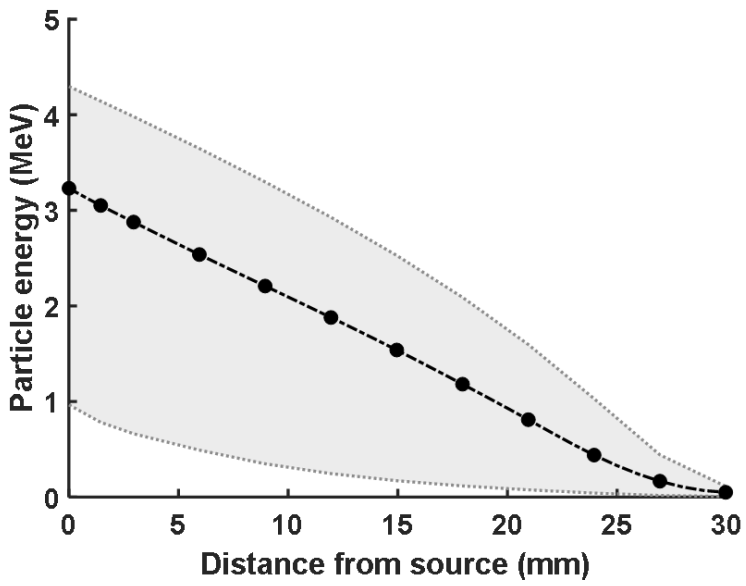

Figure 2.20 - Simulated average energy of α-particles reaching the cell target at different distances from the source, with an initial α-particle energy of 5.48 MeV. The shaded area corresponds to the energy range between the 95th and 5th percentiles for each target distance *d*. The dashed line represents a cubic interpolation curve fit as an approximation to the simulation data.

2.3.3 Monte Carlo simulation of α-particle interactions with a cell target

2.3.3.1 Energy and angle distribution

The simulated average α-particle energy at different cell target positions from the source is shown in Figure 2.20. These simulations were conducted using the methods described in section 2.2.4.1 following the simulation setup shown in Figure 2.7. Similarly to the particle flux analysis, the α-particles' average energy has an approximately linear relationship to the target distance. The highest average energy at a target using the experimental α-source setup is 2.88 MeV, corresponding to the shortest distance between a target and the source (*d*=2.9 mm). Given that the ^{241}Am source has an average particle emission energy of 5.48 MeV, this represents an average energy loss of 2.60 MeV from the particle's initial emission from source until it reaches the target surface positioned at that distance.

To evaluate the particle's energy distribution with source distance *d* in more detail, we have analysed the simulated energy spectra of α-particles at different target positions from the source (Figure 2.21). As can be seen in Figure 2.21A, the main energy spectrum's full width at half maximum (FWHM) increases as the source to target distance increases. The spectra's FWHM are 952.3, 1198.5 and 1385.2 MeV for targets placed at 2.9, 8.9 and 14.9 mm from the source, respectively. This is the result of the increased scattering seen by particles that travel longer distances in air. Targets placed 20.9 mm away from the source or further do not have well-defined peaks due to the high degree of scattering and the

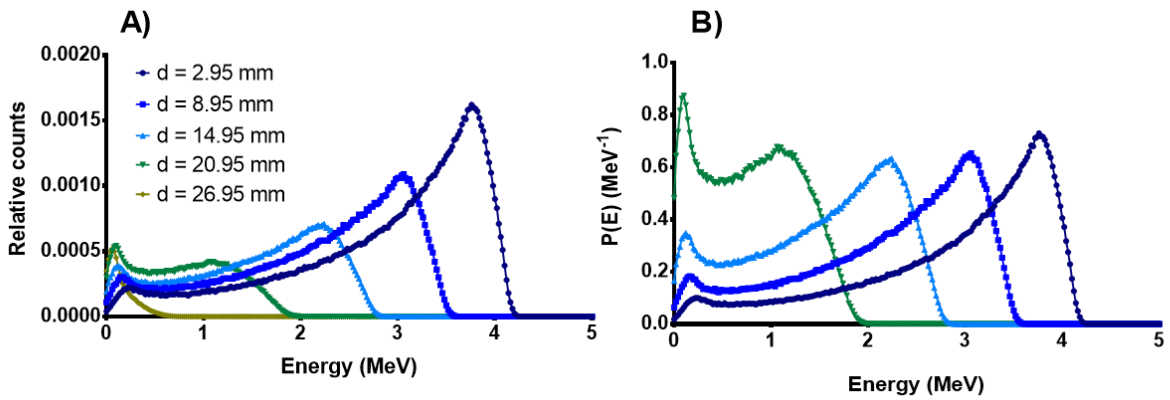

Figure 2.21 - Simulated energy spectra of the α-source at a cell target positioned at different distances from the source. A) shows the relative particle spectra normalized to the number of primary particles emitted from the source and B) shows the probability density function of the α-particles' energy at the cell target for each distance from the source. Each energy channel has a 0.02 MeV range. The last distance step (*d* =26.95 mm) was not plotted in B due to the much higher probability density of the lower energy peak compared to the other target distances.

significant contribution of low energy particles to the spectra. This contribution is particularly noticeable in Figure 2.21B as the probability density of the low energy particles is higher than 0.6 MeV^{-1} for a target placed 20.9 mm away from the source, even higher than probability density peak at higher energies.

Additionally, we have also analysed the α-particles' angle with the target, θ_S, and energy densities for targets placed at different distances *d* (Figure 2.22). Here, we show the isotropic nature of particles as they are emitted from the α-source (Figure 2.22A). Even though each particle's emission energy is 5.48 MeV, a range in energies of particles hitting the source surface results from the scattering events happening within the α-source volume itself. The angle distribution varies from 0° to 90°, with increased density as the particles' angle with the target's surface decreases. Again, due to the source thickness, the higher densities of particles occur when their angle with the target's surface is higher than 20°. Particles emitted with lower angles lose more energy and are more likely to stop within the source's volume.

When the target is placed further away from the source, the energy and angle distributions of particles change significantly (Figure 2.22B-F). In these cases, α-particles have to go through layers of gold, air and Mylar before they reach the target. This results in higher particle densities for high θ_S as the target gets more distant from the source. As an example, the average θ_S of simulated particles at a target placed at *d*=2.9 mm is 46.1 ± 16.3 °, whereas for a target placed at *d*=26.9 mm the average θ_S increases to 75.7 ± 8.3 °. This is due to α-particles with low angle emissions being stopped before reaching the target, since they would need to travel through a longer distance than a particle with a higher emission angle to reach the same target (Figure 2.8). The further away we are from the source, the closer θ_S gets to 90 °.

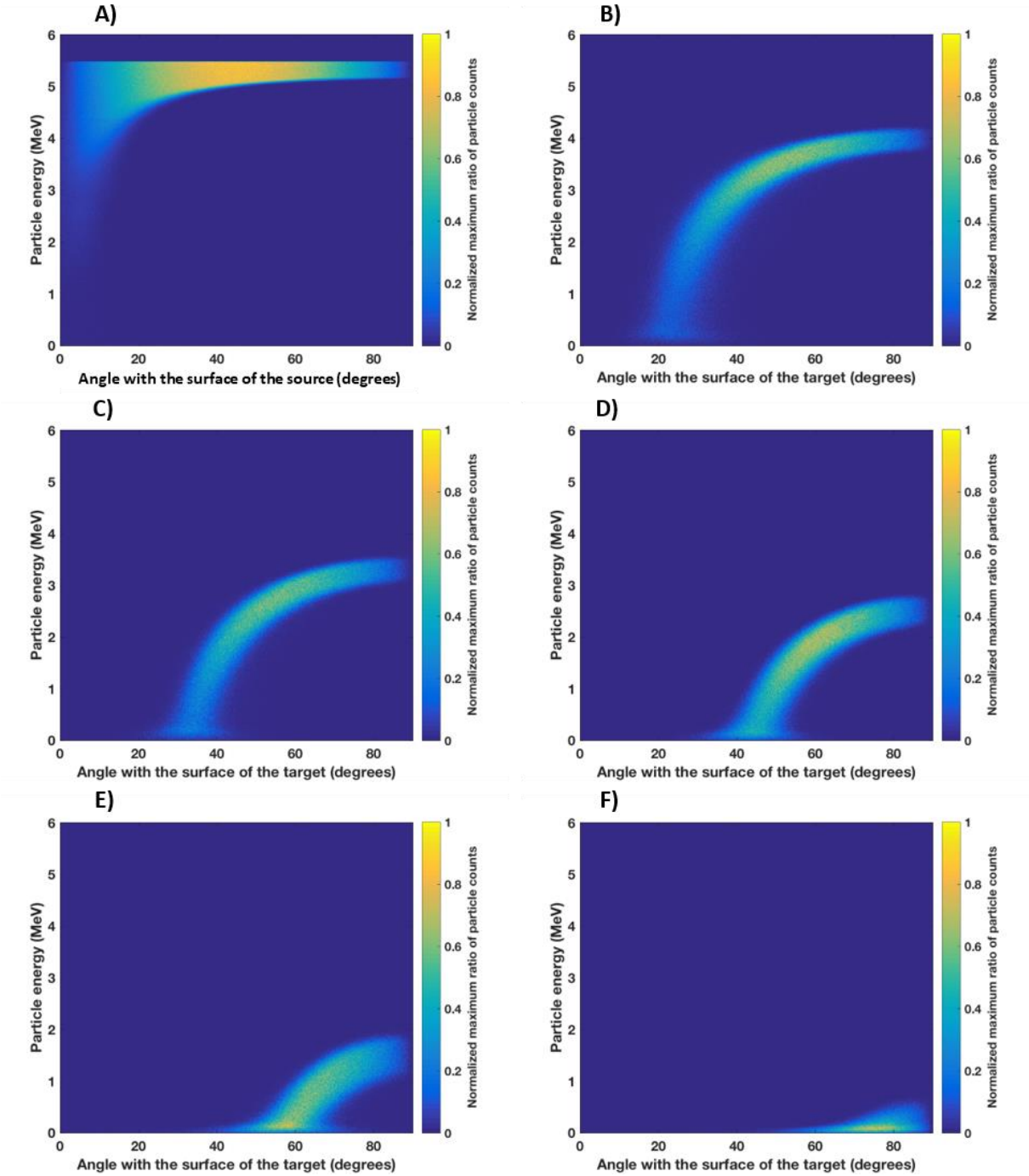

Figure 2.22 - Simulated distribution relating particle energy and angle with surface of the target layer (θ_S) positioned at different distances from the source. Distributions at the source surface (A) and at the cell targets positioned distances *d*=2.95 mm, 8.95 mm, 14.95 mm, 20.95 mm and 26.95 mm are represented (B to F, respectively). Depending on the distance between targets and source, a total of 10 to 40 million particles were simulated. The particle counts were normalized to the maximum counts for each target position, shown in the colourbar scale.

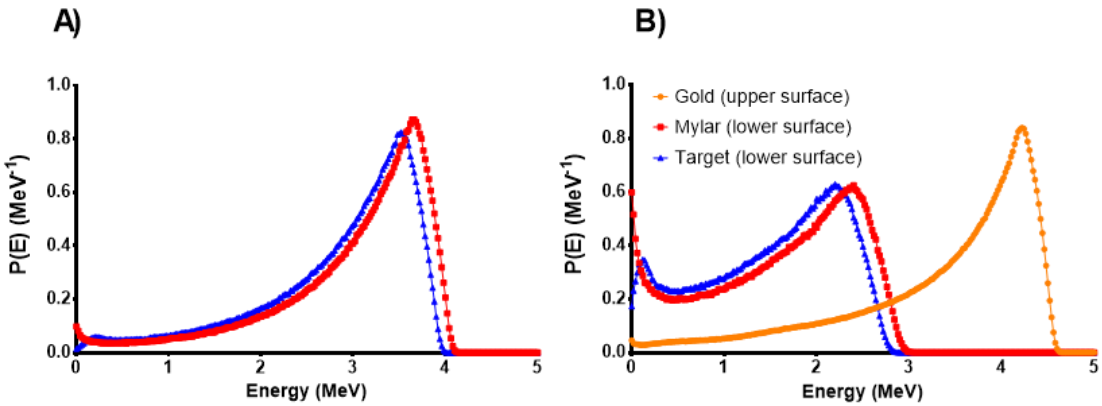

Figure 2.23 - Probability density distributions of the α-particles energy scored at 3 different material surfaces: the lower surface of the gold coating layer, the initial surface of the Mylar layer and the initial surface of the cell target positioned 14.95 mm away from the source. The simulation had 20 million particles irradiated from the source without the gold layer (A) and with the gold layer (B).

It should also be noted that particles that are scored with an angle θ_S close to 90 ° tend to have the highest energies, no matter the target position. This demonstrates that particles that travel through shorter distances, thus having a higher θ_S, have to travel less far and lose less energy to reach a target at any given distance. However, as the target is positioned further away from the source, Figure 2.22 shows a decrease of particle energy at all angles, a consequence of additional energy loss when the distance *d* increases.

2.3.3.2 Gold and mylar layers effect on energy distribution

To investigate the effects of the gold and Mylar layers on the α-particle energy distribution we have analysed the energy spectra of particles scored at different material surfaces. As shown by Figure 2.23, this effect is particularly significant immediately after particles go through the gold layer. When the gold layer is not present, the energy spectra scored at the target's lower surface, positioned at *d*=14.9 mm, has its maximum energy peak at 3.52 MeV (FWHM=0.9 MeV), with little energy loss from the Mylar layer. However, when the gold layer is present the α-particles' energy spectrum at the target's lower surface shifts to significantly lower energies (maximum energy peak at 2.20 MeV). It's also evident that with this setup there is a broader spectrum of particle energies, with the main energy peak FWHM=1.39 MeV.

Additionally, there are no significant low energy peaks at the cell or Mylar material surfaces when the gold coating is not present. These appear in simulations with the gold layer present, proving

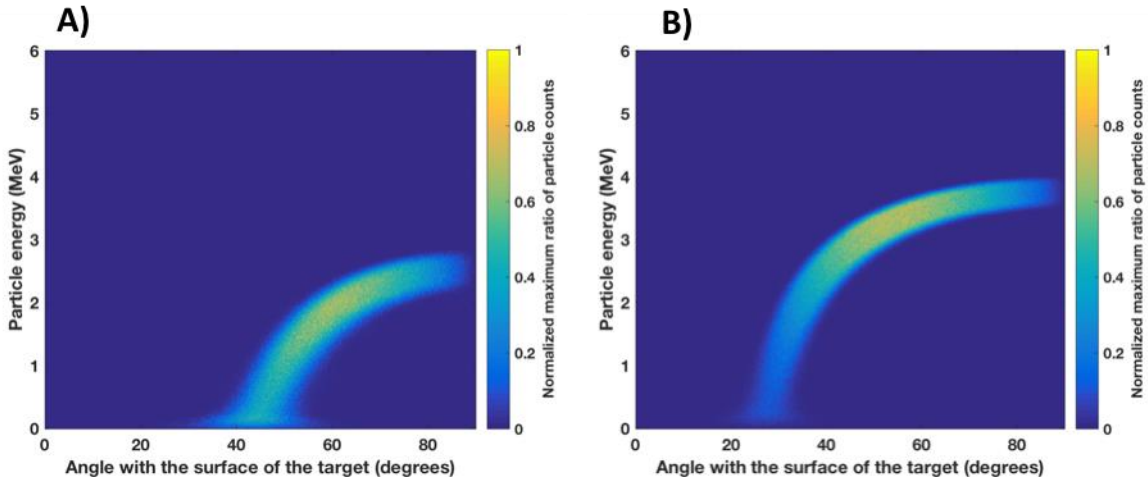

Figure 2.24 - Simulated distribution relating particle energy and angle with surface of the cell target (θ_S) positioned 14.9 mm away from the source. The simulation had 20 million particles emitted from the source with the gold layer (A) and without the gold layer (B). The particle counts were normalized to the maximum counts for each target position, shown in the colourbar scale.

that the presence of the low energy peaks is a consequence of the hard scattering events between the α-particles and the gold protective layer.

We have also calculated the average α-particle energy in simulations with and without the gold coating, focusing only on the gold layer upper surface position (*d*=2 μm). Particles scored at the end of the gold surface have an average energy of 3.38 ± 1.01 MeV In a simulation without a gold coating layer, particles have an average energy of 4.95 ± 0.73 MeV at the same position. This represents a 1.57 MeV energy difference between both averaged energies, suggesting the gold layer is a significant contribution to the energy lost by α-particles when they reach the cell target, as previously reported in section 2.3.3.

There is also a significant impact of the gold layer on the scored particles' angle and energy distribution, as shown in Figure 2.24. In this analysis, we scored the particles' angle θ_S and energy data for a lower target surface also positioned at *d*=14.9 mm. When the gold layer is not present, the plot shows little variation in angle for particles with the same energy, and an average θ_S = 51.4± 14.8 °. In the simulation with the gold layer, the angle and energy distribution is significantly different, showing increased ranges of θ_S for the same particle energy, especially for energies close to 0 MeV. In addition, the average θ_S is higher (59.2 ± 11.5 °). The difference in the average θ_S for the two simulations occurs mostly because of increased attenuation reducing the number of low-angle particles reaching the target. As an example, particles that have θ_S < 30 ° represent 0.2% of the total particle counts for a simulation with the gold layer, as opposed to a simulation without the gold layer where that fraction increases to 5.8 %.

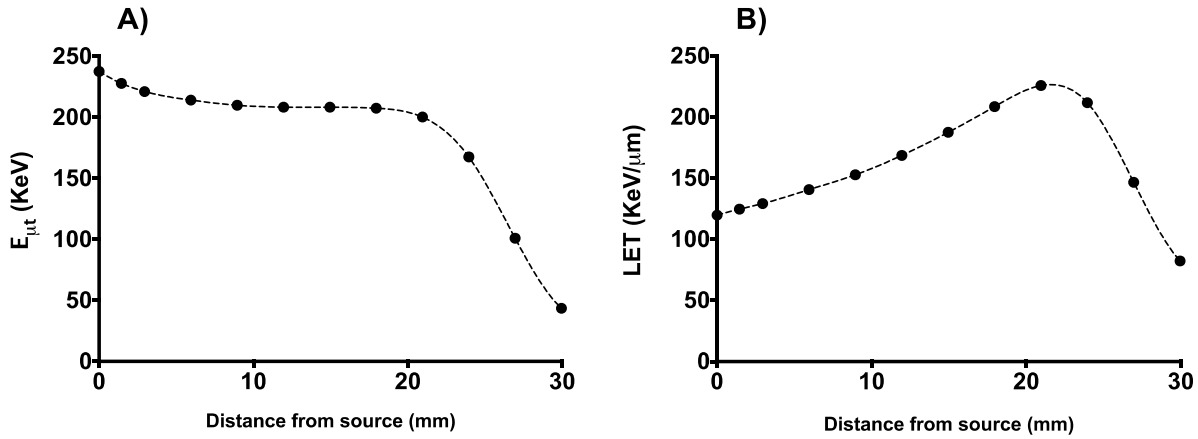

Figure 2.25 - Simulated average α-particle energy deposition per particle in the first micrometre layer of a cell target (A) and LET profile of the α-particles irradiated from the source at different targets, based on the simulated particle energies and data from the NIST database (B). Cell targets were positioned at different distances from the α-source, with initial emitting energy of 5.48 MeV. Dashed lines represent the cubic interpolation curves from the data points. Error bars from the standard deviation of 3 simulation runs are too small to be plotted.

2.3.3.3 Energy deposition

The average energy deposition per particle in the first micrometre of the cell target is shown in Figure 2.25A. As the target gets further away from the source, the energy deposition $E_{\mu t}$ decreases due to the increase of the average particles' angle θ_S, as demonstrated in section 2.3.3. This leads to shorter path lengths through this first micrometre, and reduced energy deposition per particle. The relationship between the LET and target distance *d* is significantly different though, as shown in Figure 2.25B. In this case, the LET increases for higher target distances, due to the lower energy of particles, following the Bragg peak curve for α-particles. At the greatest distances, the particle energy is too low and particles begin to stop, leading to a decrease in LET, as occurs for target distances $d > 23.9$ mm. Comparing both $E_{\mu t}$ and LET for the closest position to the source in an experimental setup (d=2.9 mm), we find the average energy deposition $E_{\mu t} = 221.2 \pm 0.24$ keV whereas the expected LET = 129.3 ± 15.2 keV/μm, based on an average particle energy of 2.88 MeV.

The energy deposition per particle will have a great influence in the dosimetry of a cell target.

2.3.3.4 Dose rate

The dose rate is a result of all the combined properties of the α-particles' flux, energy distribution and LET. Using the methods described in section 2.2.4.3, we have calculated the surface dose rate ($\dot{D}_{surface}$) for cell targets at different distances from the α-source. The comparison between the

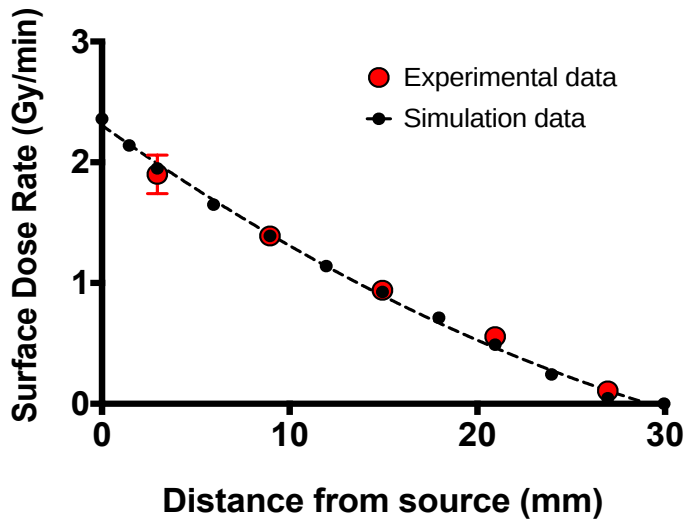

Figure 2.26 - Experimental and simulation calculations of the surface dose rate of the α-source at different cell target distances from the source. Error bars represent the standard deviation from the data points. Experimental data is based on calculated particle fluxes using nuclear track detectors. The dashed line represents a cubic interpolation curve fit as an approximation to the simulation data.

experimental and simulated $\dot{D}_{surface}$ data is presented in the Figure 2.26. As both data examples show, the greater the distance between the α-source and the target, the lower $\dot{D}_{surface}$ is.

We have also calculated the average nucleus dose, $\dot{D}_{nucleus}$, for a generic cell target geometry, with 10 μm cell thickness and 5 μm nucleus thickness. By applying equation 2.9 at a target distance of 2.9 mm using the corresponding simulated particle flux, $\dot{D}_{nucleus}$ = 1.57± 0.15 Gy/min. This will be the nucleus dose rate used for cell experiments. The standard deviation shown represents the variation between the deposited doses across each micrometre layer of the nucleus. As an example, the dose rate on the 1st micrometre layer of the nucleus is 1.35 Gy/min, whereas the one at the 5th layer is 1.78 Gy/min.

2.4 Discussion

In this chapter, we characterized an α-source setup for *in vitro* cell irradiation experiments. We have performed experimental analysis using radiochromic films and nuclear track detectors, as well as Monte Carlo simulations to fully characterize the properties of α-particles at a cell target.

The α-source setup described in this chapter can still be improved, since it is still not the most ideal experimental setup for α-particle irradiation. Using an α-source in an open air environment allows experiment setups to be set easily and with few complications. However, particles travelling through air will lose a significant amount of energy compared to those in vacuum or helium-filled chambers. This can be an issue as it is important to minimize particle scattering and attenuation through the

materials between the source and a cell target in order to deliver more reproducible radiation doses. Our experimental setup would be significantly improved by using a vacuum chamber instead of an air environment, as it would reduce the particle attenuation and scattering between the target and the source. Additionally, using a collimator system with a motor to enable constant source rotation would further improve the α-source uniformity issues. α-particle setups using such techniques are widely reported and used in research. [51,52,98,102]

Despite the need for future improvements, similar α-source systems to the one used in this work have been used for simulation and experimental cell assays with satisfying results, demonstrating that this setup is feasible for cell experiments. [100,101,103,124]

The radiochromic film experiments have shown acceptable uniformity of the α-particle irradiation for an experimental cell target at a distance from the source of 2.9 mm (Figure 2.14 and Figure 2.15). In addition, any non-uniformities resulting from edge effects should be minimized since the target area has a diameter of 3.4 cm, smaller than the source dimensions (5 cm). Nonetheless, the irradiation uniformity can be improved. As it was mentioned, one way to improve the irradiation uniformity at short distances from the source is adding rotation to the source during exposures. We have tested this for future work, where we irradiate an EBT3 customized film placed 1.6 mm away from the source, using the same conditions described in section 2.2.2.1, but split into two fractions. The second fraction, delivered immediately after the first, had the source rotated 90 ° for a simple approximation of the effect of source rotation. Both fractions lasted the same time period of 2 mins and 30 s each. The impact of source rotation can be seen by comparing the previous results in Figure 2.15 with Figure 2.27. As shown, the uniformity is significantly improved even at very close distances by a two fraction exposure, with only small changes in the normalised pixel intensity along both line profiles. As an example, the standard deviation across the 3.4 cm horizontal middle profile line reduces by 40% when using the two fraction rotation method. This demonstrates that simple source-rotation systems can definitely be used with our α-source setup for future studies.

In the work done in this chapter, we have analysed both experimental and simulated flux data. The fact that the experimental particle flux data agreed well with the simulation data, particularly for target distances lower than 20.9 mm, demonstrates that our Monte Carlo simulation of the experimental α-source setup was accurate (Figure 2.18). Both data had good agreement even when the particles with angles below the considered critical angle θ_C were excluded from the simulation, as explained in section 2.2.2.2. Nevertheless, the critical angle limitations of nuclear track detectors should be considered as this effect can influence the particle flux's calculation accuracy by more than 2%, for detectors placed at short distances from the source. The calculated particle fluxes were important for the α-particle dosimetry assessments for cell experiments, as further shown in equations 2.8 and 2.9.

The energy spectra comparison between the charged particle detector output and the simulation data also had reasonable agreement. As shown by Figure 2.19, the energy peaks detected at different target distances from the source match quite well in energy position. The most significant differences are related to the probability energy distribution values, P(E). For all distances, the width of the energy peaks in the simulated spectra is lower than the experimental one. Since the energy distribution of particles is larger, it results in a lower maximum P(E) value.

This difference between the energy distributions between simulated and experimental spectra can be related to several issues. For one, it is known that charged particle detectors produce a broader peak even for monoenergetic particles, due to variations in the charge released by a given energy deposit. These limitations combine with scattering in air to give even broader peaks. Ideally, this detector should be used in a vacuum or helium chamber, as the spectra results are more accurate and detector broadening can be calibrated using appropriate sources. Secondly, this difference can be related to the simulated source geometry. We have simulated a source thickness of 1 μm, which is significantly smaller than the actual one (200 μm). This choice was related to the limited number of particles which can be generated in a TOPAS run, and time required for simulations. A thicker simulated source would result in a broader α-particle energy spectrum, which may be more consistent with the experimental results. Additionally, this can also be affected by any small differences in material geometry between simulation and reality, particularly the detector surface geometry. In fact, the simulated detector's surface angle relation to the source is 0 °, i.e., both surfaces are parallel (Figure 2.9). However, it was noticed that the charged particle detector's sensitive surface was not perfectly aligned with the source, being slightly tilted. This can also contribute to the observed differences between simulation and experimental energy spectra results.

Regarding the simulations of the cell target, the results from the energy and angle distributions from the α-source show the high variability of particles reaching the target, as shown by Figure 2.20 to Figure 2.22. As the distance *d* increases, so does the FWHM of the energy spectra peaks, as well as the percentage of low energy particles. The α-particle energy scored at different target positions is intrinsically connected to their angle. The smaller their emission angle to the surface is, the longer their trajectory will be in order to reach the target depth (Figure 2.8). This means that a particle with an emission angle of 20 ° will lose more energy in air compared to a particle with an emission angle of 80 °.

However, the peaks of particle emissions at very low energies are mostly caused by the interactions of α-particles with the gold coating layer, as shown by Figure 2.23 and Figure 2.24. This is a result of hard scattering events from α-particles interacting with the gold coating. The gold layer also has a significant effect on the overall energy spectra peak and its FWHM, with a difference of 1.32

MeV between the peak α-particle energy reaching a target in a simulation with and without the gold layer. This is again caused by the more frequent scattering events in gold.

The energy deposition analysis revealed how the LET and the energy deposited in the 1st micrometre layer of the cell target by α-particles ($E_{\mu t}$) can vary with the target's distance (Figure 2.25). Although it would seem that $E_{\mu t}$ should follow the same distribution behaviour as the average LET variation with target distance, it should be noted that the data shown is very different from that of LET. In this case, $E_{\mu t}$ represents the energy transfer on a micrometre unit length of a target layer, taking into account particles with different θ_S angles. This means that particles travelling through a target layer thickness of 1 μm will actually have different track lengths, depending on their θ_S (Figure 2.8). Additionally, particle angles can be altered due to scattering events from interactions with the target material, changing their energy transfer as well. On the other hand, LET represents the energy transfer per unit length of a particle track. In other words, it represents $E_{\mu t}$ if a particle had an angle of 90 ° during its entire path. This explains the differences between the $E_{\mu t}$ and LET data shown, as there are more particles with low θ_S hitting a target close to the source, thus depositing more energy than in a target further away from the source which sees fewer low θ_S particle hits.

Finally, we have characterized the α-source dosimetry for a cell target. This was initially done by calculating the surface dose rate for any cell thickness ($\dot{D}_{surface}$) and the nucleus dose rate ($\dot{D}_{nucleus}$) adapted for a cell geometry composed of a 10 μm cell layer and a 5 μm nucleus cell layer (section 2.3.3.4). Since the cell dosimetry strongly depends on the particle flux, the relation between $\dot{D}_{surface}$ and the target distance follows a trend similar to the one observed in Figure 2.18. The nucleus dose rate for a target distance d = 2.9 mm was found to be $\dot{D}_{nucleus}$ = 1.57± 0.15 Gy/min. As previously mentioned, there is a variation in dose deposition between each nucleus micrometre layer (± 0.22 Gy). This is related to the LET of particles in water increasing for lower energies. This LET variation of α-particles in water for energies varying from 0.1 MeV and 10 MeV is represented in Figure 2.28. In this case, the average energy of particles hitting the cell target's lower surface is 2.88 MeV, but their energies decrease as they travel through the nucleus, thus increasing their LET. Possible future work could involve simulating cell irradiation uniformity, for example, analysing the distribution of particle hits per cell and nucleus together with the analysing the variation of dose deposition along different cells for the same target distance d.

We have summarised in Table 2.3 the main results of the α-source physical effects on a cell target positioned at different distances from the source.

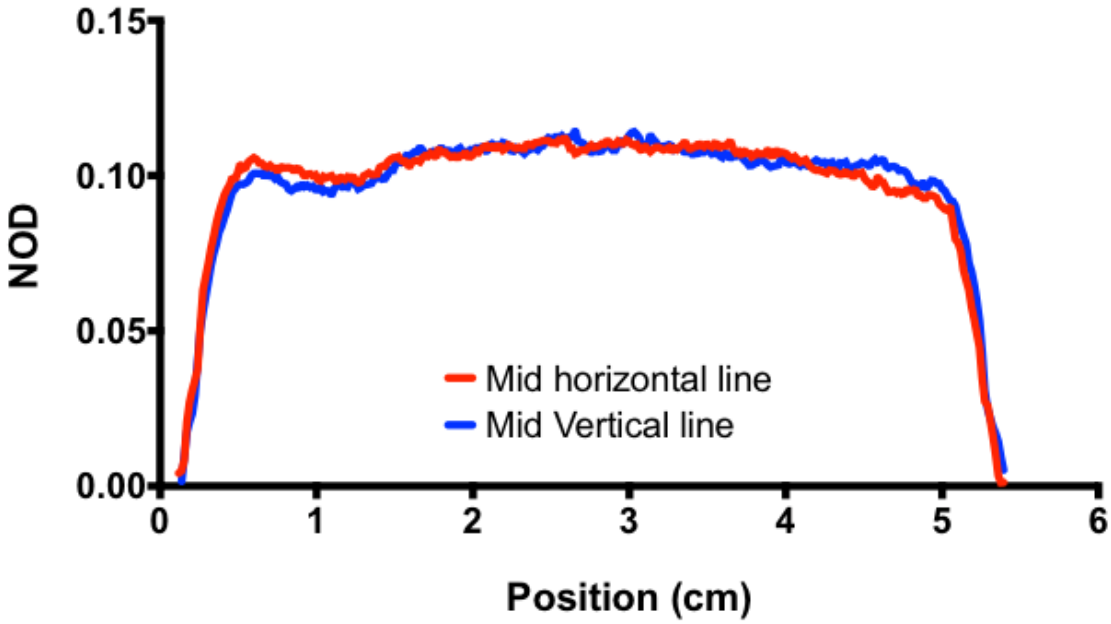

Figure 2.27 - Average net optical density profiles of middle vertical and horizontal lines of EBT3 customized films after exposed to the α-source. The film was placed at a distance of 1.6 mm with a 5 x 5 cm exposed area for 5 minutes. The experiment setup followed a two fraction irradiation with source rotation of 90 degrees halfway the exposure time. The NOD data shown was calculated using the pixel intensity levels of the red channel scan image along horizontal and vertical lines with 0.2 mm width.

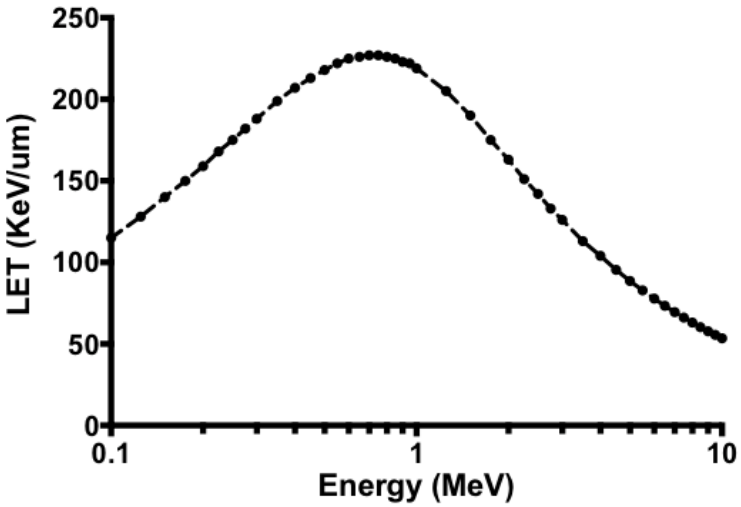

Figure 2.28 – Linear energy transfer (LET) of alpha particles in water, with particle energies varying from 0.1 MeV and 10 MeV. The energy axis is in logarithmic scale. The presented data was taken from the NIST database.[120]

Table 2.3 - Simulated results of α-particle physical properties when reaching the cell target positioned at different distances from source to target (d). The FWHM data is not shown for longer distances due to poor energy peak definition. $\dot{D}_{surface}$ data was calculated using the simulated particle flux. All uncertainties are represented as the standard deviations from data.

d (mm)	Flux (mm^{-2} sec^{-1})	Mean Energy (MeV)	FWHM (MeV)	Eμt (keV)	θ_s (°)	$\dot{D}_{surface}$ (Gy min^{-1})
2.9	906.3	2.88 ± 1.04	0.95	221.2	46.1 ± 16.3	1.95
8.9	678.2	2.21 ± 0.91	1.20	210.0	52.3 ± 13.9	1.39
14.9	456.7	1.54 ± 0.74	1.39	208.4	59.1 ± 11.5	0.93
20.9	251.2	0.81 ± 0.49	--------	200.3	67.0 ± 9.1	0.49
26.9	47.0	0.17 ± 0.13	--------	101.0	75.7 ± 8.3	0.05

CHAPTER 3 : DEVELOPMENT OF A NOVEL COLLIMATOR FOR α -SOURCES

3.1 Introduction

The use of collimators in α-particle source radiobiology has been widely reported. [52,125–127] Typically, the collimators used with α-sources have a honeycomb hole pattern. They reduce the angle and energy spread of particles hitting a target, allowing for more accurate dose depositions. A collimator can be of great use for this project as we are using an α-source for radiobiology experiments.

3D printers have been widely used in the past years in medical physics fields to build phantoms designed for dosimetric tests of radiation treatment plans, tissue models for cell growth systems, etc. [128–130] Expanding the use of recent advances in 3D-printing technology, with more precise and faster printing methods, can also have a big impact in other research areas. These can include easily built, accessible and customized collimators for α-particle sources used in biology research.

With the new 3D printing developments, we can test 3D printed samples of collimators specifically designed for our α-source setup. A similar approach has been used for x-ray irradiation experiments with encouraging results. [131] This 3D printing process represents a novel way to produce, test and use different collimators.

In this chapter, we will evaluate a set of 3D printed sample collimator designs. We will also test their use in our α-source setup, analysing their experimental and simulated effect on particle flux, energy distribution and dose deposition in a cell target.

3.1.1 Influence of collimator's geometry on particle flux

The flux of α-particles going through a collimator is directly dependent on the collimator's geometry. The geometry parameters that have an influence in the collimation of particles are the collimator's thickness (*T*), hexagon diameter (*D*) and septa (*S*). Here, *D* is the closest distance between 2 opposite sides of a hexagon hole and *S* is the shortest distance between two consecutive holes. Collimators with hexagonal holes are the most common because they are generally the most efficient

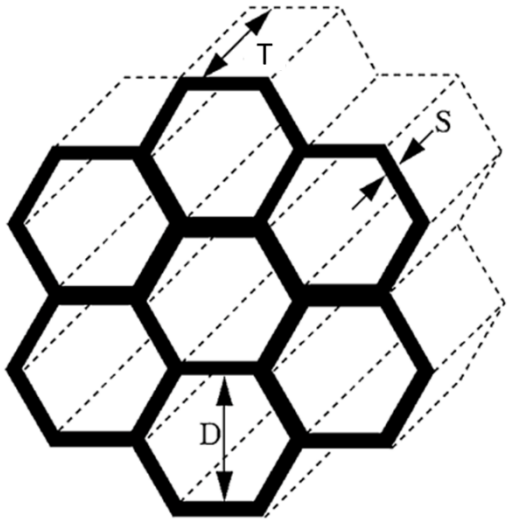

Figure 3.1 – Schematic representation of a cross-section from the collimator's honeycomb pattern structure. *T* represents the collimator's thickness, *S* represents its septa and *D* the hole diameter.

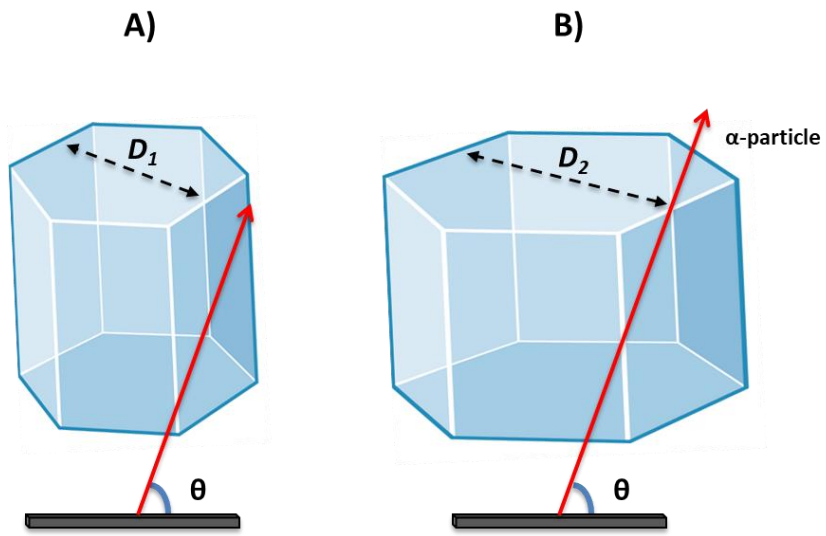

Figure 3.2 – Representation of an α-particle with an emission angle θ entering a hexagon hole in two collimator examples, varying only in hole diameter ($D_1 < D_2$). The particle is blocked in A), which has a shorter diameter, but goes through the hole in B), which has a longer diameter.

in terms of open area ratio, in comparison to other hole geometry patterns. A schematic representation of a honeycomb collimator's cross-section, with each parameter represented, is shown in Figure 3.1.

Each parameter influences the particle flux by allowing the collimator to block more or less particles from passing through it. A hole with a bigger diameter will lead to particles with wider angles going through the collimator, when compared to a collimator with a smaller hole diameter. Figure 3.2A demonstrates an example of that, where an α-particle with an emission angle θ travelling through a collimator's hole with diameter D_1 hits the collimator's wall. In a different scenario (Figure 3.2B), the same particle can go through the hole of a collimator with a wider diameter (D_2). In this case, the

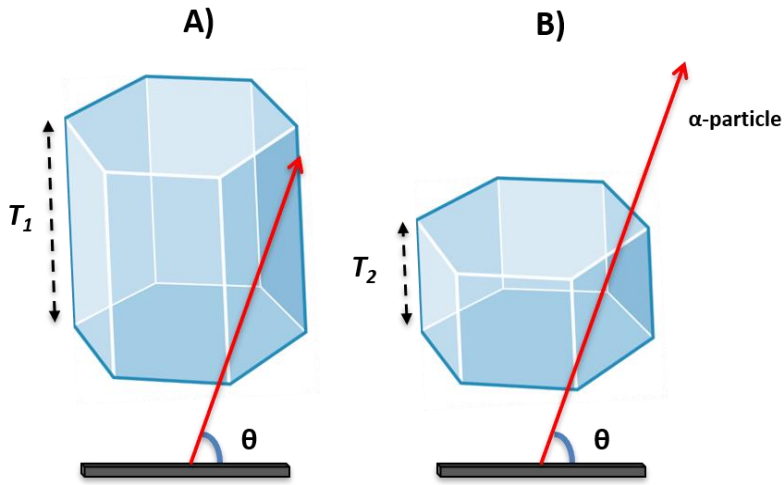

Figure 3.3 - Representation of an α-particle with an emission angle θ going through a hexagon hole in two collimator examples, varying only in thickness ($T_1 > T_2$). The particle is blocked in A), which has a longer thickness, but goes through the hole in B), which has a shorter thickness.

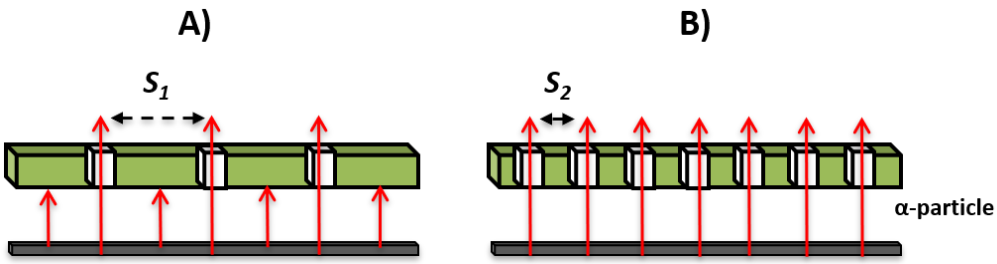

Figure 3.4 - Representation of α-particles going through two collimators varying only in septa ($S_1 > S_2$). More particles are blocked in A), which has a longer septa, whereas no particles are blocked in B), which has a shorter septa.

narrower the hole diameter the smaller the range of particle angles allowed to go through the collimator. This will also influence the energy distribution of particles that go through the collimator. As explained in the 2.2.2.2, the wider the emission angle of a particle, the longer distance it will travel and the lower the energy it will have when hitting a target, provided its angle remains the same during the Coulomb scattering in air.

A similar scenario happens for two collimators varying only in thickness (Figure 3.3). However, in this case, the collimator's thickness is inversely proportional to the number of particles that go through it. A thicker collimator will block wider angled particles going through its holes, thus reducing the particle flux and particle energy range when hitting a target.

The collimator's septa does not directly influence the particle angle collimation threshold or the energy distribution of particles going through it. Instead, this parameter influences the total number of hexagon holes per collimator area, which leads to the absorption of more particles for collimators with

a longer septa, almost regardless of particle emission angles. Figure 3.4 shows an example of this, where a collimator with a longer septa (S_1) results in fewer hexagon holes for particles to go through.

The combination of these three geometry parameters (diameter, thickness and septa) play a fundamental role in a collimator's effect on the flux and energy distribution of particles that pass through it.

The material of which a collimator is made of may also play an important role in particle absorption. However, as collimators are usually made of materials that can easily absorb α-particles (within just a few micrometres of thickness), we can assume that the collimator's material has little or no influence in α-particle collimation.

3.2 Materials and methods

3.2.1 3D printed collimator

In this work we test a polymer based α-particle collimator and produced by a 3D printer. This represents a novel collimator production method since most state of the art α-particle collimator materials are metal-based and produced by different methods. [52,125,131–133]

The 3D printer used to print the collimators was a German RepRap X400, available in the Radiotherapy Physics Department of the Northern Ireland Cancer Centre. This 3D printer has a maximum position accuracy of ± 0.1 mm, with a minimum printed layer thickness of 0.05 mm. The material used to print the collimator samples used was glycol-modified polyethylene terephthalate (PETG), a high temperature resistant polymer typically used in 3D printing.

The German RepRap X400 printer offers six different default solid infill printing options. These infill option styles are represented in Figure 3.5. Since most used α-particle collimators have a honeycomb structure, we have opted to print the collimators with the full honeycomb infill style. Compared to the fast honeycomb option, the full honeycomb option allows the collimator structure to be more robust and stable, as well as providing a better honeycomb pattern uniformity across the collimator.

When choosing a default infill printing style there is limited control of the desired solid geometry. During the printing process, we can only control the side lengths of the collimator, as well as its thickness. The geometry of the honeycomb pattern, i.e, the hexagon hole diameter (D) and septa (S) distances, cannot be directly controlled by the user. However, these parameters are dependent on the printing infill ratio, which the user can define. A higher infill ratio will result in a collimator with smaller

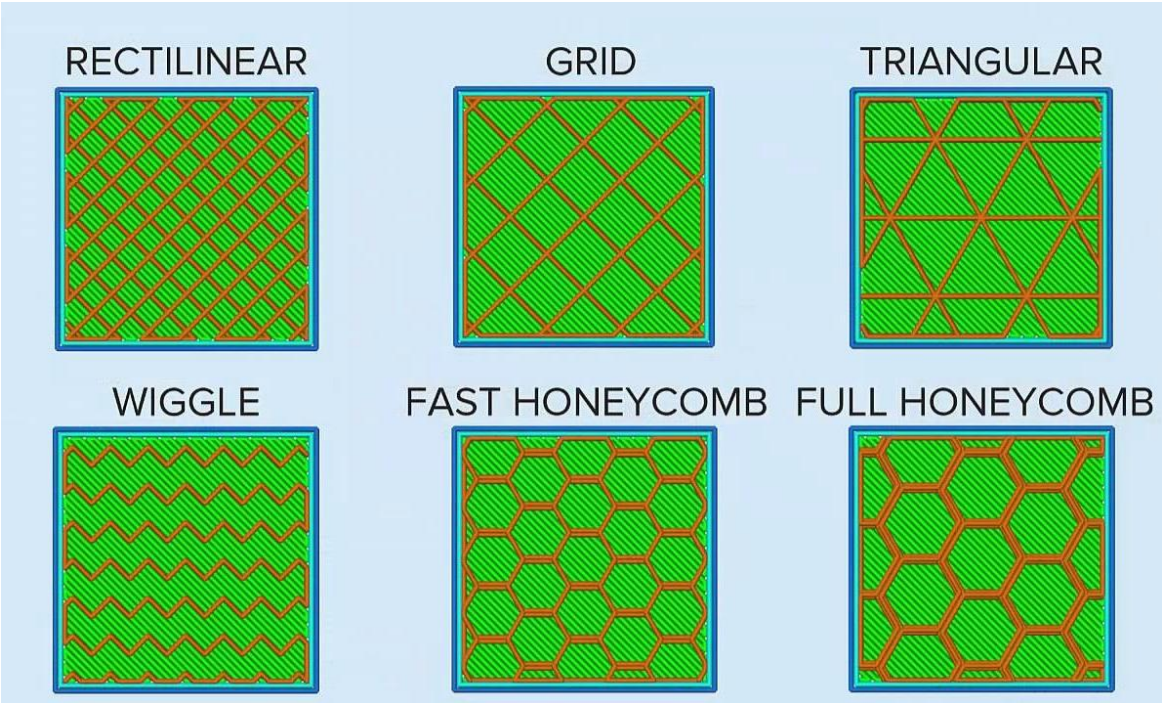

Figure 3.5 – Default infill options from the 3D printing software Simplify 3D. The collimators used in this work were printed with a German RepRap X400 printer using the full honeycomb filling style. [174]

hexagon hole diameter and a higher septa. These geometry parameters can be posteriorly assessed, after printing.

In order to have different collimator geometry options, three different samples were printed, each with an approximate thickness of 0.4 mm but different infill ratios – 50%, 55% and 60%. Based on the α-source setup, the printed collimators were chosen to have a square shape with side lengths of 4.9 cm. This allows for the collimators to fit directly to the source setup.

3.2.2 Experimental analysis

3.2.2.1 Geometry assessment with gafchromic film

The geometry parameters of the 3D printed collimators were measured experimentally. The thickness was measured with a calliper. The collimator's hexagon holes were initially observed through a microscope (Zeiss Axiovert 200M), using a x5 objective. Using the microscope, we obtained images of 3 different hole areas of each collimator sample (Figure 3.6). This first observation allowed us to understand that the honeycomb hole geometry of the 3D printed collimator does not correspond to a perfect hexagon. Additionally, it is also noticeable that the hole geometry varies from different sites of the collimators. This is expected as the 3D printer used has a printing position inaccuracy.

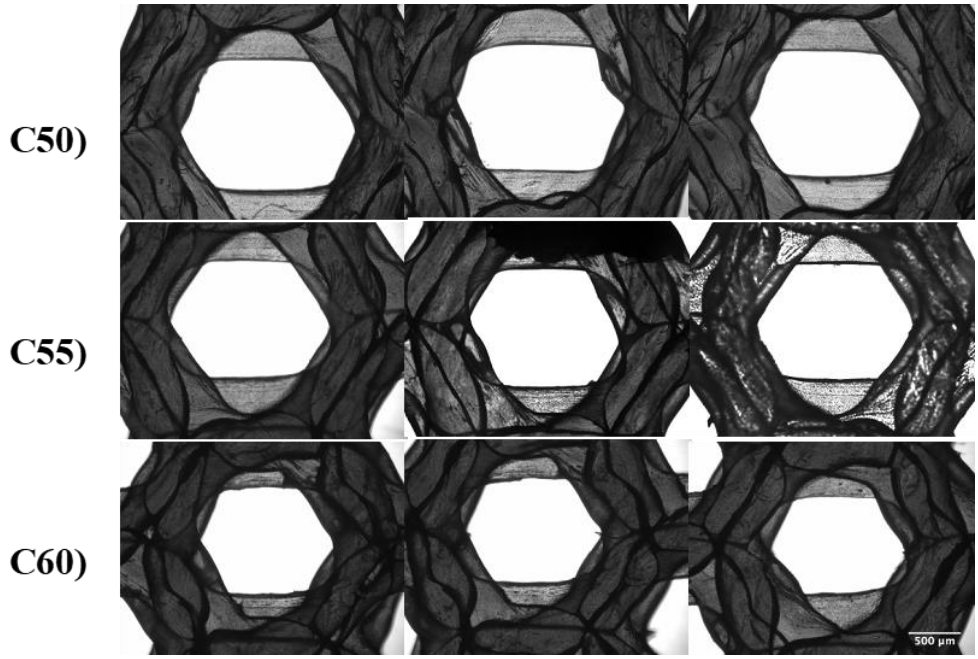

Figure 3.6 – Microscope images taken of 3 hole areas from each collimator sample. The 3 collimator samples were printed with different infill ratios (50%, 55% and 60%). These images were taken with a x5 objective. The bar scales represents 500 µm.

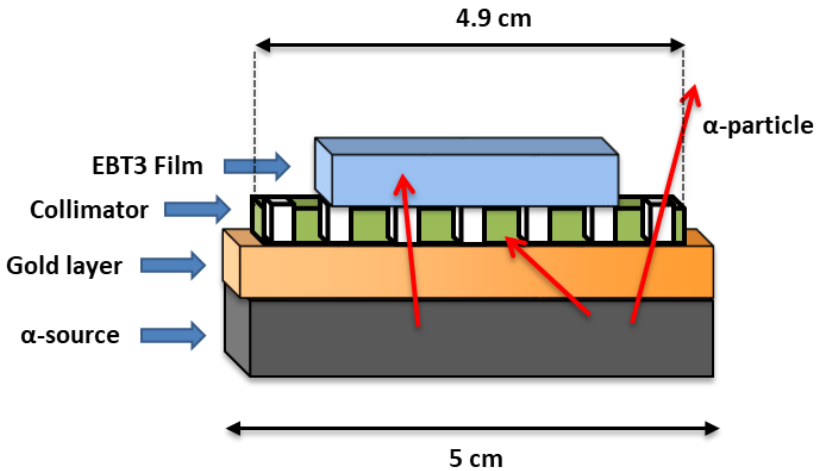

Figure 3.7 – Schematic representation of the experimental setup of a Gafchromic film sample placed on top of a collimator and exposed to the α-source. The α-particles that hit the collimator septa walls do not go through.

The two 3D collimators with the lowest infill ratios (C50 and C55) were chosen for geometry evaluation and further experiments. In order to obtain the average hole diameter and septa across the different collimators we have used customized EBT3 gafchromic films. As explained in section 2.2.2.1, this film's coloration is changed when exposed to ionizing radiation. Using this film's physical property, we have individually placed each collimator sample on top of the α-source and placed a film sample on top of the corresponding collimator, as shown by the schematic representation of the experimental setup in Figure 3.7. Each film sample was exposed to α-particle radiation for 30 minutes. After irradiation,

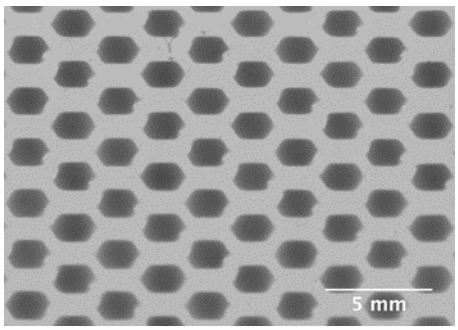

Figure 3.8 – EBT3 customized film sample irradiation pattern after being placed on top of collimator sample C50 and exposed to the α-source for 30 minutes.

the film samples were scanned with a HP Scanjet G4050 scanner, allowing us to obtain images of the film irradiation patterns as the one shown in Figure 3.8.

The film scan images were then used to calculate the average hole diameter (*D*) and septa (*S*) for each collimator. These were obtained by two calculation processes. First, to calculate the average hole diameter (*D*), we processed the film scan images with ImageJ software, applied a binary colour filter, used the software's 2-D object recognition to identify hexagon holes and calculated the hexagon hole area for 50 selected hexagons. As the hexagon area can be calculated using the hexagon diameter, we used the average of hexagon areas obtained to calculate the average collimator hole diameter:

$$D = \sqrt{\frac{2A_{hex}}{\sqrt{3}}} \qquad 3.1$$

where A_{hex} is the area of a hexagon hole.

Regarding the collimator's average septa, we calculated the distance between the center of 9 consecutive hexagons in a diagonal row and the distance between 5 consecutive hexagon holes in a vertical row. A schematic example of both distances is shown in Figure 3.9. These distances are directly related to both *D* and *S* collimator geometry parameters, as demonstrated by the following equations:

$$d(n_y) = (n_y - 1) \times (\mathrm{D} + \mathrm{S}) \qquad 3.2$$

$$d(n_{xy}) = (n_{xy} - 1) \times (\mathrm{D}_{long} + \mathrm{S}) \qquad 3.3$$

where $d(n_y)$ and $d(n_{xy})$ are the distances between the center of n_y consecutive vertical hexagon holes and n_{xy} diagonal hexagon holes, respectively. D_{long} is the hexagon long diameter, representing the distance between two furthest hexagon edges, as shown in Figure 3.10. D_{long} is directly proportional to the short hexagon hole diameter D:

$$\mathrm{D}_{long} = \frac{2}{\sqrt{3}}\,\mathrm{D} \qquad 3.4$$

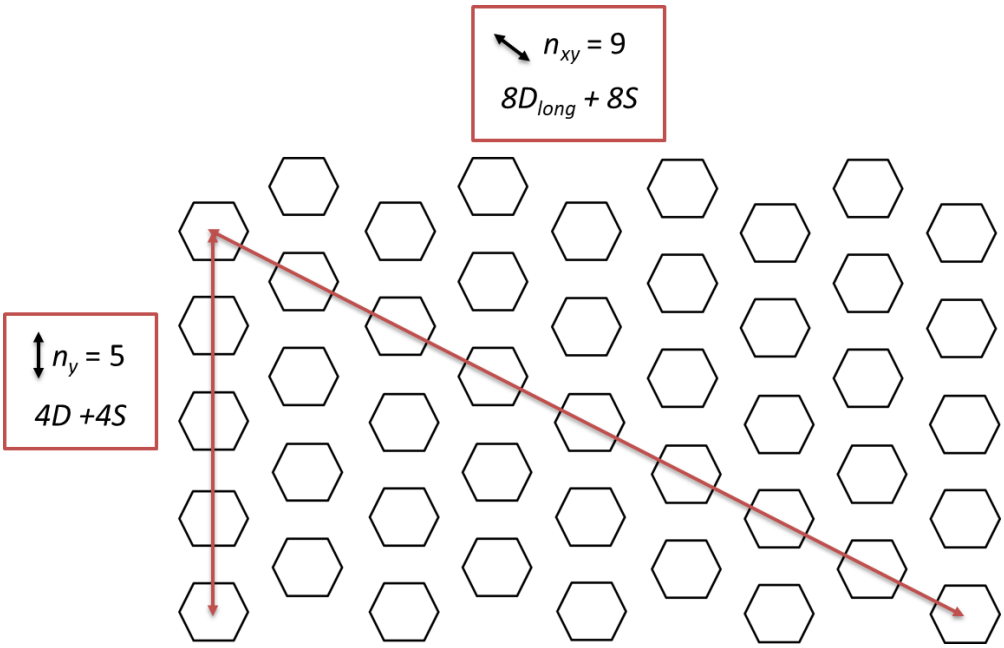

Figure 3.9 - Schematic representation of the relation between the collimator's geometry parameters with the distance between 5 consecutive vertical holes (n_y=5) or 9 consecutive diagonal holes (n_{xy} = 9). These distance relations were used to calculate the average diameter (D) and septa (S) from the gafchromic film samples.

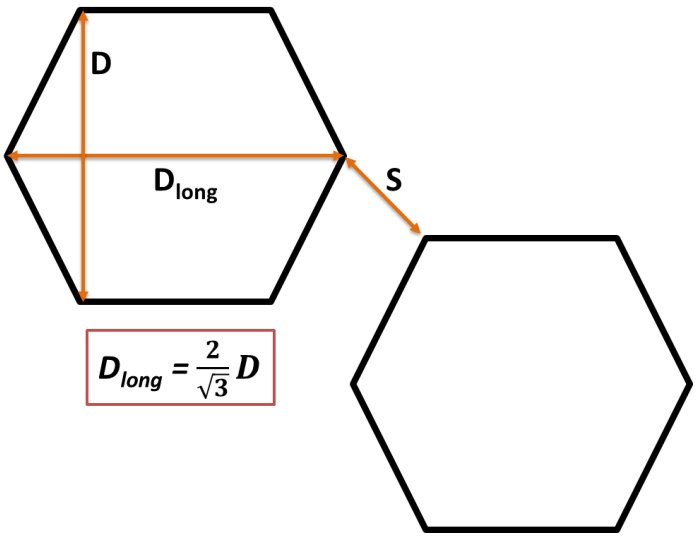

Figure 3.10 - Representation of the collimator hole long diameter (D_{long}) and its relation to the shorter hole diameter (D).

Having D and D_{long} values, we calculated S by both horizontal and vertical approaches. The results from the diagonal calculations were averaged together with the results from the vertical calculations, to obtain the averaged septa for each collimator sample.

3.2.2.2 Uniformity of the collimated source with gafchromic film

We have also used radiochromic films to study the effect of a 3D printed collimator sample on the uniformity of α-source irradiations. Using the same methods described in the previous chapter (section 2.2.2.1), we compared the net optical density (NOD) variation across film samples that were exposed to the α-source with and without a collimator present. As before, the film samples were placed at a distance of 2.9 mm from the source, with an exposed diameter of 4.4 cm. One sample was exposed for 10 minutes to a non-collimated source and the other exposed for 30 minutes to a collimated source. The collimator used for this analysis was the one with the lowest infill ratio, C50.

After irradiation, the film samples were scanned, processed in ImageJ and the NOD variation was analysed in two ways. First, we obtained an area NOD density of each film by doing a colormap analysis, where each pixel represented an individual NOD. The results from both experimental setups were then compared by calculating the average NOD at the exposed film circle areas, together with both samples' standard deviation. In order to compare the results from both samples, we normalized each pixel corresponding NOD to the source irradiation time (IR_{time}) used for each sample. The second approach focused on analysing the vertical and horizontal line NOD profiles, using the same NOD pixel average approach as the one described in the previous chapter. Here, we have normalized the NOD pixel values to the maximum NOD obtained for each line profile.

3.2.2.3 Nuclear track detector

Similarly to the previous chapter, we used nuclear track detectors to calculate the flux of the α-source with a collimator on top, using the same methods (section 2.2.2.2). As before, the CR-39 samples were placed on top of Mylar dishes at different distances from the source (*d*) – 2.9, 8.9, 14.9, 20.9 and 26.9 mm. These particle flux results were then compared to the section 2.3.1.2 results from the α-source without the collimator. This comparison allowed us to analyse the effect of the collimator's geometry on the particle flux.

3.2.3 Monte-Carlo simulation of the ^{241}Am source with a collimator

We have simulated irradiations from a collimated source in order to better understand the physical effect of the collimators on the α-source irradiations. This was done by using the Geant4 Monte-Carlo

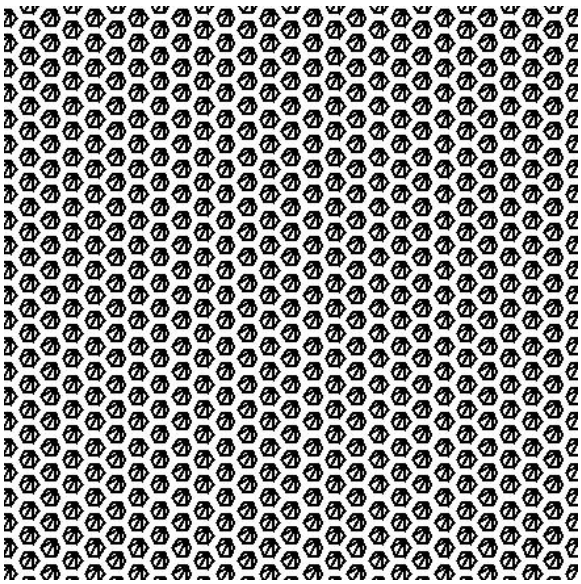

Figure 3.11 – Simulated geometry of the C50 collimator used in Monte-Carlo simulations in TOPAS. Each side has 4.9 cm width.

toolkit TOPAS, using the same simulation setups and methods explained in sections 2.2.3 and 2.2.4 from the previous chapter, with the addition of a simulated collimator geometry.

Based on the results obtained from the experimental analysis of the collimator geometry, we simulated a "perfect" honeycomb collimator structure with a uniform hexagon hole pattern along the simulated solid. The hole diameters (*D*) and septa distances (*S*) were the same as the averaged *D* and *S* obtained from the geometry analysis (section 3.2.2.1). These geometry parameters were used as an approximation to account for the irregularities in the 3D printed hole pattern. The simulated collimator objects had side lengths of 4.9 cm and the same thicknesses as measured from the real collimators. Figure 3.11 shows the TOPAS simulated collimator used based on the C50 collimator. The chosen material of the simulated collimator was Mylar to provide a plastic polymer approximation to the collimator sample's material, as the 3D printed material was not available in the Geant4 database.

These simulations were performed using the same methods as those mentioned in the previous chapter (sections 2.2.3 and 2.2.4) with the addition of a honeycomb collimator on top of the α-source in each simulation. Figure 3.12 shows a schematic representation of the collimator setup used. The α-particles travelled through the hexagonal holes of the collimator, hitting the water target placed on top of the Mylar layer. To compensate for the particles being blocked by the collimator, a total of 20 million to 60 million particles, depending on the target's position, were emitted from the source. Similarly to the previous chapter's methods, we used surface scorers to track the particles hitting the target's surface facing the source. The simulation results were then used to study the effect of the simulated collimator geometry on:

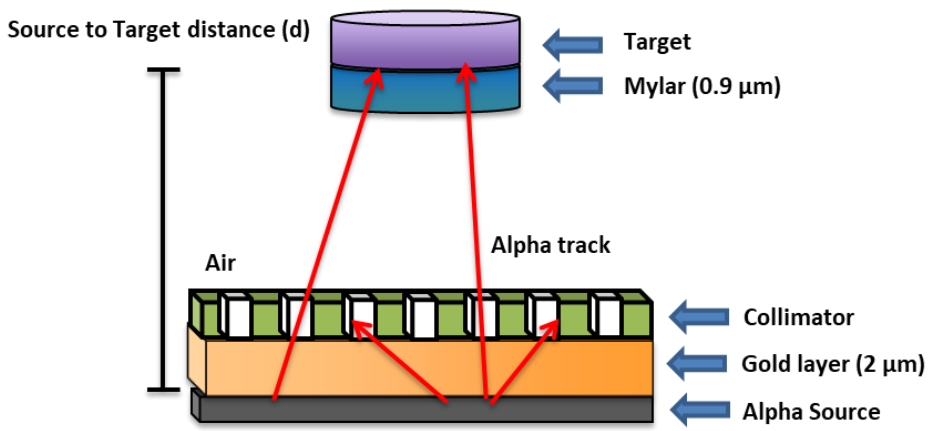

Figure 3.12 - Schematic representation of the simulation setup of the collimated α-source. All the materials present between the α-source and a target are shown, including the collimator.

1) Particle flux
2) Particle energy distribution
3) Particle angle distribution
4) Energy deposition and dose delivered on a cell target

The results from the particle flux simulations, with and without the collimator present, were then compared to the experimental measurements. This also allowed us to validate the collimator geometry parameters used.

Additionally, to further validate the results of these simulations, we compared the simulation and experimental particle flux results between two collimators with different geometries (C50 and C55).

This was done by calculating the simulated and experimental particle flux ratio between the two collimators for each target distance (d):

$$ratio_{Flux}(d) = \frac{Flux_{C55}(d)}{Flux_{C50}(d)} \qquad 3.4$$

where $Flux_{C55}$ and $Flux_{C50}$ are the particle fluxes calculated at targets placed at a distance d from a source with the collimator sample C55 and C50 placed on top, respectively. In addition to the particle flux ratio, we calculated the open area ratio between the two collimators. We used the software ImageJ to analyse collimator scans and obtained the open area for each collimator, i.e. the area sum of all the collimator holes. We then calculated the ratio of the open area between the C55 and C50 collimators, comparing it to the experimental and simulated particle flux ratios.

Finally, the simulated dose deposition analysis was used to calculate the dose rate of the collimated source to a cell target, whose results were also compared to a target exposed to a non-collimated α-source.

3.2.4 In vitro experimental validation

In order to experimentally support the collimator analysis results obtained in this chapter, we used the α-source with and without a collimator to irradiate cells. This analysis is described and presented in the next chapter, focused on *in vitro* experiments.

3.3 Results

3.3.1 Experimental data

3.3.1.1 Geometry assessment of 3D-printed collimators

As described in the methods (section 3.2.2.1), we analysed the EBT3 customized film samples placed on top of two collimators after irradiation. This allowed us to obtain both the averaged diameter (*D*) and septa (*S*) distances from the two 3D printed collimators. Their thickness was measured using a calliper. The results are shown in Table 3.1.

These results show that the sample C50 has wider holes than the sample C55, with an average hexagon diameter increase of 10.3%. However, the collimator C50 has longer spaces between its holes than the collimator C55, a septa difference of 8.9%. The difference in thickness will also be an important factor in the flux reduction difference between both samples. In this case, the sample C50 is 13.6% thinner than C55.

Table 3.1 – Results of the averaged geometry parameters of the collimators C50 and C55. The measurement errors shown represent the standard deviations from the diameter and septa calculations and the calliper uncertainty for the thickness measurement from a digital calliper.

Parameter	C50	C55
Diameter (mm)	1.50 ± 0.33	1.36 ± 0.26
Septa (mm)	0.90 ± 0.12	0.82 ± 0.09
Thickness (mm)	0.39 ± 0.01	0.45 ± 0.01

3.3.1.2 Uniformity

The net optical density colormap analysis of the film samples exposed to a collimated and non-collimated source is shown in Figure 3.13. In order to compare both samples we normalized the NOD to the irradiation time (IR_{time}) used for each sample. The sample from a non-collimated source showed an average NOD/IR_{time} of $14.4 \times 10^{-3} \pm 1.0 \times 10^{-3}$ across the exposed film area (diameter = 4.4 cm). On the other hand, the film exposed to a collimated source presented an average NOD/IR_{time} of $3.07 \times 10^{-3} \pm 0.23 \times 10^{-3}$ across the same film area. The standard deviations represent 7.0% and 7.5% of the average values, respectively. This shows that the average NOD/IR_{time} from a sample exposed to the collimated source represents 21.3 ± 2.1% of the average NOD/IR_{time} from the sample exposed to a non-collimated source.

When considering the area of an exposed cell target, with a diameter of 3.4 cm instead, the averaged area NOD/IR_{time} values become $14.8 \times 10^{-3} \pm 0.8 \times 10^{-3}$ and $3.17 \times 10^{-3} \pm 0.17 \times 10^{-3}$ for a non-collimated and collimated source, respectively. The standard deviations of these normalized ratios are reduced to 5.3% and 5.5%, respectively. It's also important to understand that the NOD/IR_{time} standard deviations mentioned also include the error associated with the film and scanner noise. For instance, for a scanned non-irradiated film sample (2x2 cm), we observed a 1.12% pixel intensity standard deviation from the mean value. This means that the irradiated film NOD errors, associated with the irradiation uniformity only, are even lower than that.

The difference in the average NOD/IR_{time} values is related to the expected flux and particle energy range difference between a collimated and a non-collimated source. Despite the higher exposure time for the sample B, the number of particles hitting that sample was still lower than for sample A. This will be confirmed further on in this chapter.

The horizontal and vertical NOD profiles of both samples, shown in Figure 3.14, confirm a similar irradiation uniformity profile for both experimental setups, with and without a collimator present. As in a similar analysis shown in the previous chapter (section 2.3.1.1), we have to consider that the exposed film area here analysed is bigger than the target exposed area of a Mylar dish. In this case, the film samples had an exposed diameter of 4.4 cm, whereas the target diameter sitting on top of the Mylar layer of a dish is 3.4 cm. Having a reduced target area on a Mylar dish will reduce the variability of the irradiation profile, when irradiating a cell target.

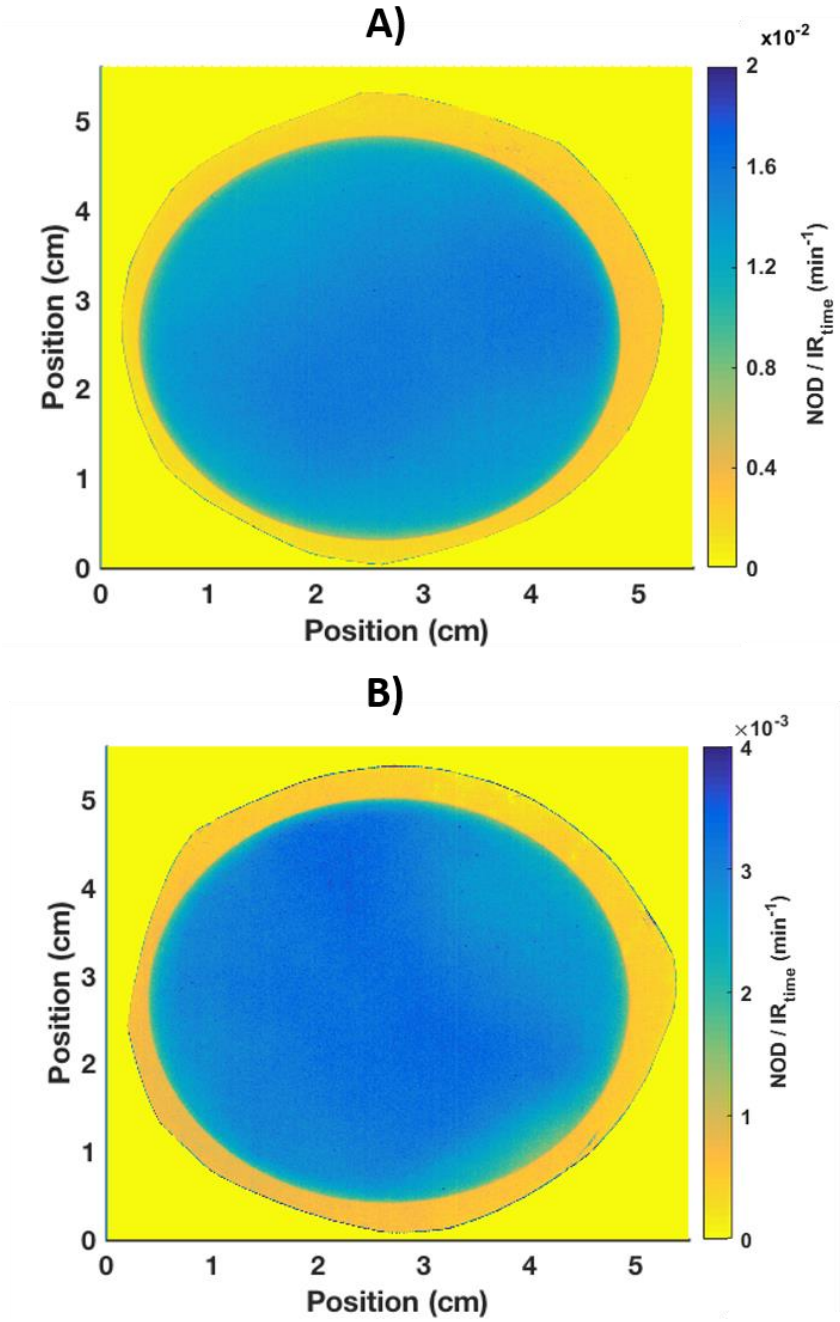

Figure 3.13 - EBT3 customized film areas showing their calculated net optical densities (NOD) normalized to the irradiation time (IR_{time}) after exposure to the α-source. The films were placed at 2.9 mm distance with a 4.4 cm exposed diameter area and irradiated for 10 minutes without a collimator (A) and for 30 minutes with the collimator C50 (B). The NOD data shown is represented through a colormap and it was calculated using the pixel intensity levels of each scanned image's red channel.

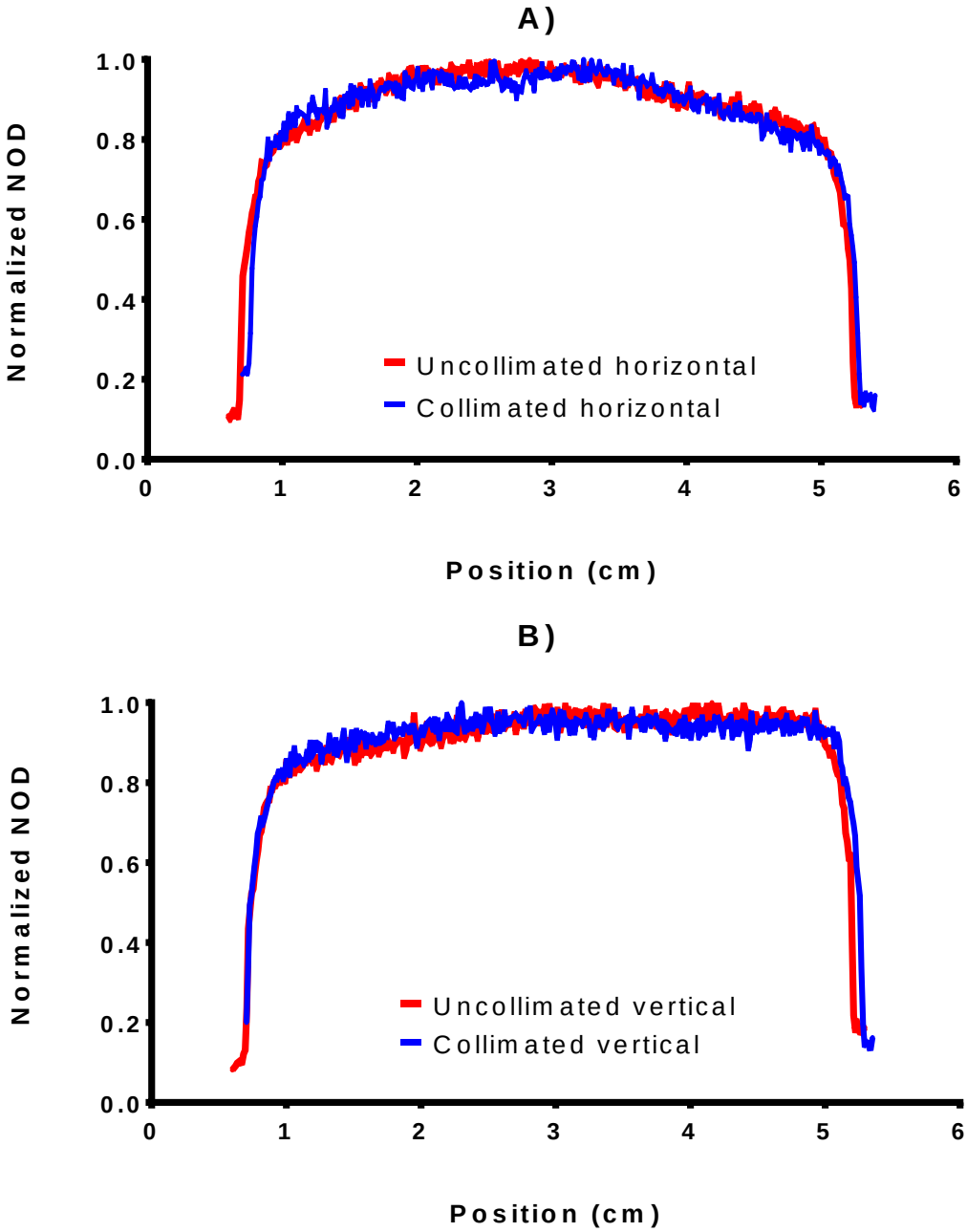

Figure 3.14 - Average net optical density profiles of middle horizontal (A) and vertical (B) lines of EBT3 customized films after exposure to the α-source with without a collimator. Both films were placed 2.9 cm away from the source and had a 4.4 cm exposed diameter. The sample exposure times to radiation were 10 and 30 minutes for a non-collimated and collimated source, respectively. The NOD data shown was calculated using the pixel intensity levels of the red channel of each scanned image along horizontal and vertical lines with 0.2 mm width. Each positional NOD value was then normalized to the maximum NOD obtained from each profile.

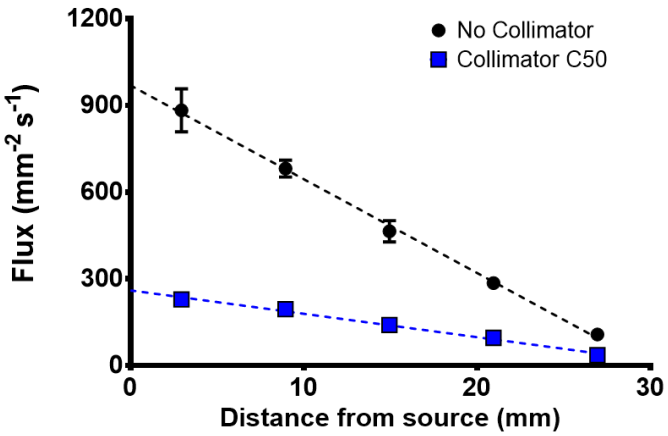

Figure 3.15 - Particle flux from the α-source with and without collimator C50 at different distances from source to target. The number of tracks were counted using nuclear track detectors (CR39). Experimental data shows the calculated flux from the average number of tracks counted in 9 different areas selected from 3 CR-39 sample images for both data sets. Error bars correspond to the experimental standard deviations. The dashed lines represent linear regression curve fits as an approximation fit to the experimental data.

3.3.1.3 Flux

As described in section 3.2.2.3, we calculated the experimental particle flux from a collimated α-source using nuclear target detectors, placed at different distances from the source. We then compared those results to a non-collimated source, with both results shown in Figure 3.15. As it can be seen, the difference in particle fluxes is larger the closer the target is to the source. As an example, at the closest distance (d = 2.9 mm), the flux from a collimated source represents 25.9% compared of the flux from a non-collimated source at the same target distance. However, at the furthest distance (d = 26.9 mm) this percentage increases to 33.2 %. This difference is related to a higher percentage of particles being blocked with low angles at a short distance, compared to a target placed at a higher distance. At higher distances particles are mostly blocked by the septa areas of the collimator instead of particles being blocked at the collimator holes due to their lower angles.

3.3.2 Experimental and simulation data comparison of a collimated α-source

3.3.2.1 Particle flux from a collimated source

The simulation results for the particle flux are shown in Figure 3.16, comparing both experimental and simulated fluxes from a collimated and non-collimated source at targets placed at

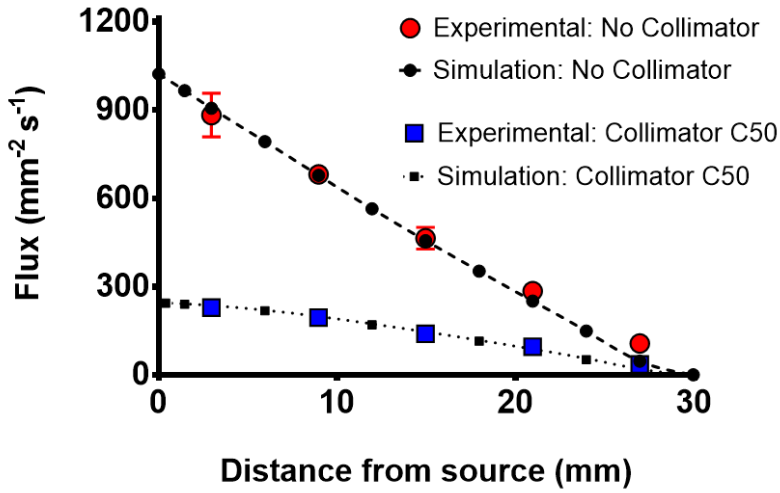

Figure 3.16 - Experimental and simulated particle flux from the α-source with and without the collimator C50 at different distances from source to target. The experimental data points are the same as the ones shown in Figure 3.15. The dashed lines represent the cubic interpolation curve fit of the simulation data, with a goodness of the fit to the experimental data characterised by an $R^2 = 0.989$ with no collimator and $R^2 = 0.997$ with the collimator.

different distances from the source. The simulation results show good agreement with experimental data, especially for the shortest target distances. This suggests that the geometry assessment of the collimator C50 and its simulation is accurate.

3.3.2.2 Particle flux from two different collimators

We also compared the particle fluxes of experimental and simulated setups using two different collimators (C50 and C55). The results from this analysis is shown in Figure 3.17, which demonstrates that the number of particles going through the collimator C50 is higher than when using the collimator C55. The difference of particle ratios is bigger the closer the target is to the α-source and the collimator. Furthermore, as the simulation data has good agreement with the experimental data shown, it also demonstrates the accuracy of the geometry assessment done as well as the α-particle simulations with the two collimators.

Additionally, we compared the flux ratio results with the open area ratio between the two collimators. The C50 collimator has an open area of 46.6%, whereas the C55 collimator has 46.4%. The differences of open area percentages are due to the different geometry parameters (diameter and septa). The open area ratio between the collimator C55 and the collimator C50 is about 1.0.

We see that the flux ratio experimental and simulated data points are represented below the C55/C50 collimator open area ratio. However, as the distance between the source and target increases, so does the experimental and simulate flux ratios, which get closer to that value. For longer distances,

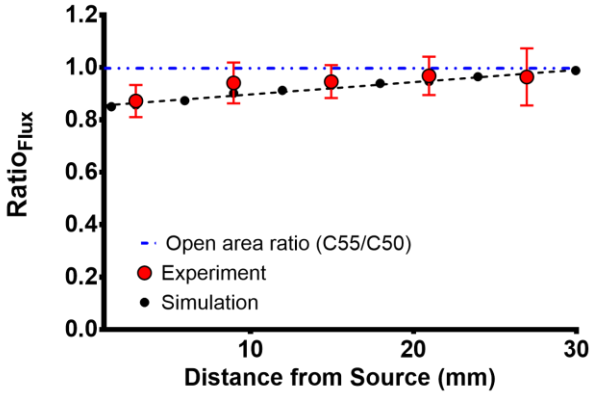

Figure 3.17 - Experimental and simulation data of the particle flux ratio between collimator C55 and collimator C50 at different distances from the α-source. Error bars correspond to the experimental and simulation standard deviations. The black dashed line represents the linear regression curve fit as an approximation fit to the simulation data. The blue dashed line corresponds to the open area ratio between the C55 and the C50 collimators (open area ratio ≈ 1.0).

when the particles going through both collimators have the same angle ranges, the flux ratio becomes the same as the open area ratio.

3.3.3 Monte Carlo simulation of α-particle interactions with a cell target when using a collimator

3.3.3.1 Energy distribution on cell target

Figure 3.18 shows the simulated averaged energy of α-particles scored at different cell target positions from a collimated and a non-collimated source setup. The results from both simulations are similar to each other, especially for targets placed at longer distances from the source. As the target gets closer to the source we start seeing differences in the average particle energy and energy spread between the collimated and non-collimated source simulations. For instance, at a distance d =2.9 mm, the averaged particle energy scored at the target using the C50 collimator, is 3.11 MeV, compared to the averaged energy of 2.88 MeV from a non-collimated source. This represents an averaged energy difference of 7.6%. The difference between energy ranges of the 5th percentile is also evident, demonstrating the smaller spread of particle energies when a collimator is present.

At greater distances from the source, the simulated particle energy profiles become more similar to each other. At 20.9 mm away from the source, the averaged energies from a collimated and non-collimated source are 0.83 MeV and 0.81 MeV, respectively, representing a difference of only 3.0 %. The energy spread differences are also barely noticeable (less than 0.5% different), as the collimator

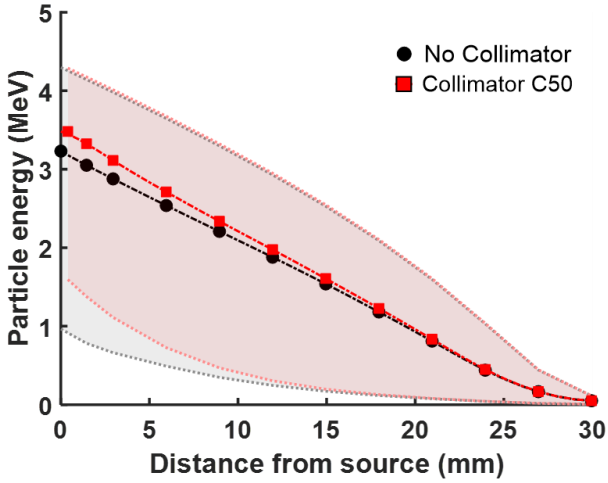

Figure 3.18 - Simulated average energy of α-particles reaching the cell target at different distances from the source, with an initial α-particle energy of 5.48 MeV. The two simulations show results with and without the presence of the collimator C50. Shaded areas correspond to the energy range between the 95th and 5th percentiles for each target distance *d* from simulations with and without a collimator (red and grey coloured respectively). The dashed lines represent cubic interpolation fits as an approximation to the simulation data.

effect on α-particle energy distribution has only significant impact at targets placed at closer distances to the source.

These findings are also demonstrated in Figure 3.19, showing the simulated energy spectra scored at a cell target placed at different distances *d* from a collimated and non-collimated α-source. The energy spread is lower when a target is exposed to a collimated source, especially at shorter distances (Figure 3.19A and B). As an example, the simulated FWHM scored at a target placed at *d*= 2.9 mm with a non-collimated and a collimated source is 0.95 MeV and 0.76 MeV, respectively. This represents a significant improvement in energy distribution uniformity when using a collimator for shorter target distances.

The probability density distribution plots highlight the difference in the ratios of lower energy particle contributing to the energy spectra (Figure 3.19C and D). When the collimator is present, the lower energy peaks ratios are visibly smaller at *d* = 2.9 mm and 8.9 mm.

Figure 3.20 shows the simulated probability density distribution of α-particles scored angles at different targets. Although not immediately visible, the averaged particle angle with the cell target surface are slightly increased when a collimator is present. For example, the averaged angles measured at a target placed 2.9 mm and 26.9 mm away from a non-collimated source are 46.1 ± 16.3° and 75.7 ± 8.3°, respectively. When adding the simulated collimator, the averaged particle angles change to 50.5 ± 15.9° and 75.9 ± 8.2°, for the same distances *d*. This further demonstrates that the shorter the distance to the source, the greater the difference between particle angles scored from simulations with and without a collimator. The collimation effect on particle angle spread is more significant for targets closer to both source and collimator. As *d* increases, both averaged angles and angle spreads tend to converge to the same values for simulations with and without a collimator.

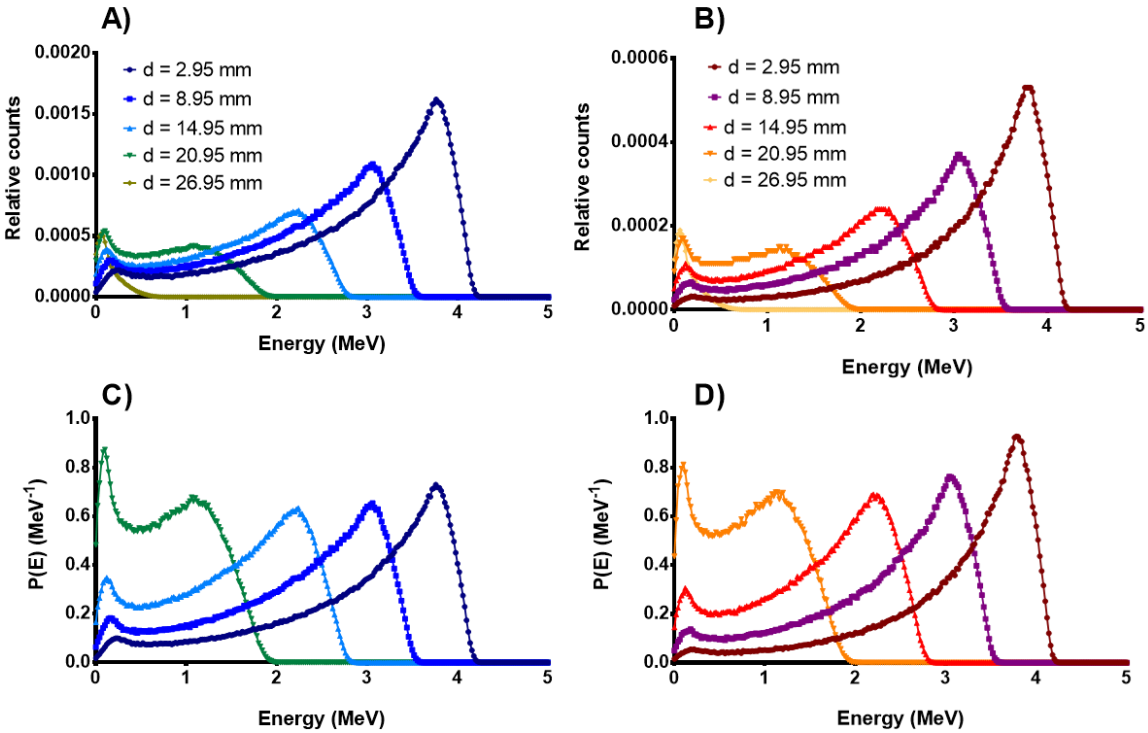

Figure 3.19 – Simulated energy spectra of the α-source at a cell target positioned at different distances from the source. Figures A and B show the relative particle spectra normalized to the number of primary particles emitted from the source without a collimator (A) and with a collimator (B). Figures C and D show the probability density distribution of the α-particles energy at the cell target for each distance from the source without a collimator (C) and with a collimator (D). Each energy channel has a width of 0.02 MeV. The last target distance (*d*=26.9 mm) was not plotted in C and D due to the higher probability distribution of the lower energy peak compared to the spectra at other cell distances.

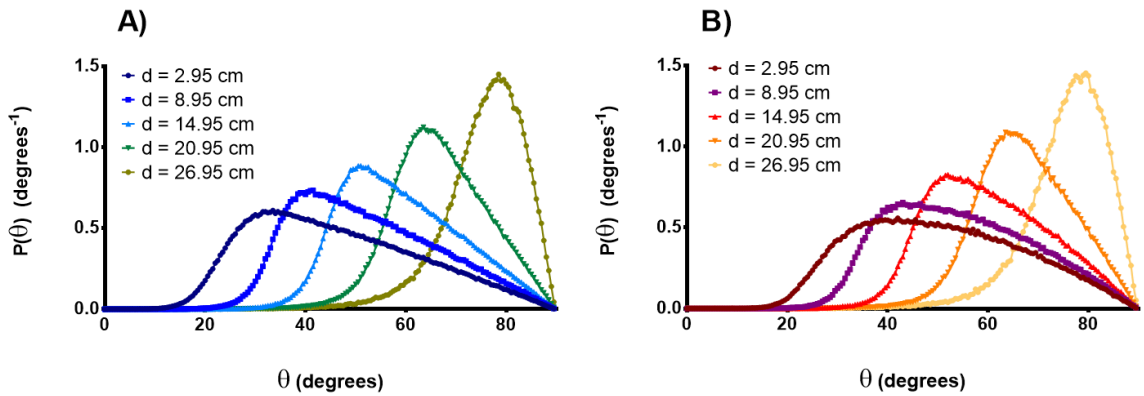

Figure 3.20 – Simulated probability distribution for α-particle angle with the cell target's surface positioned at different step distances from the source without a collimator (A) and with a collimator (B). Each angle channel has a 0.5 degree width.

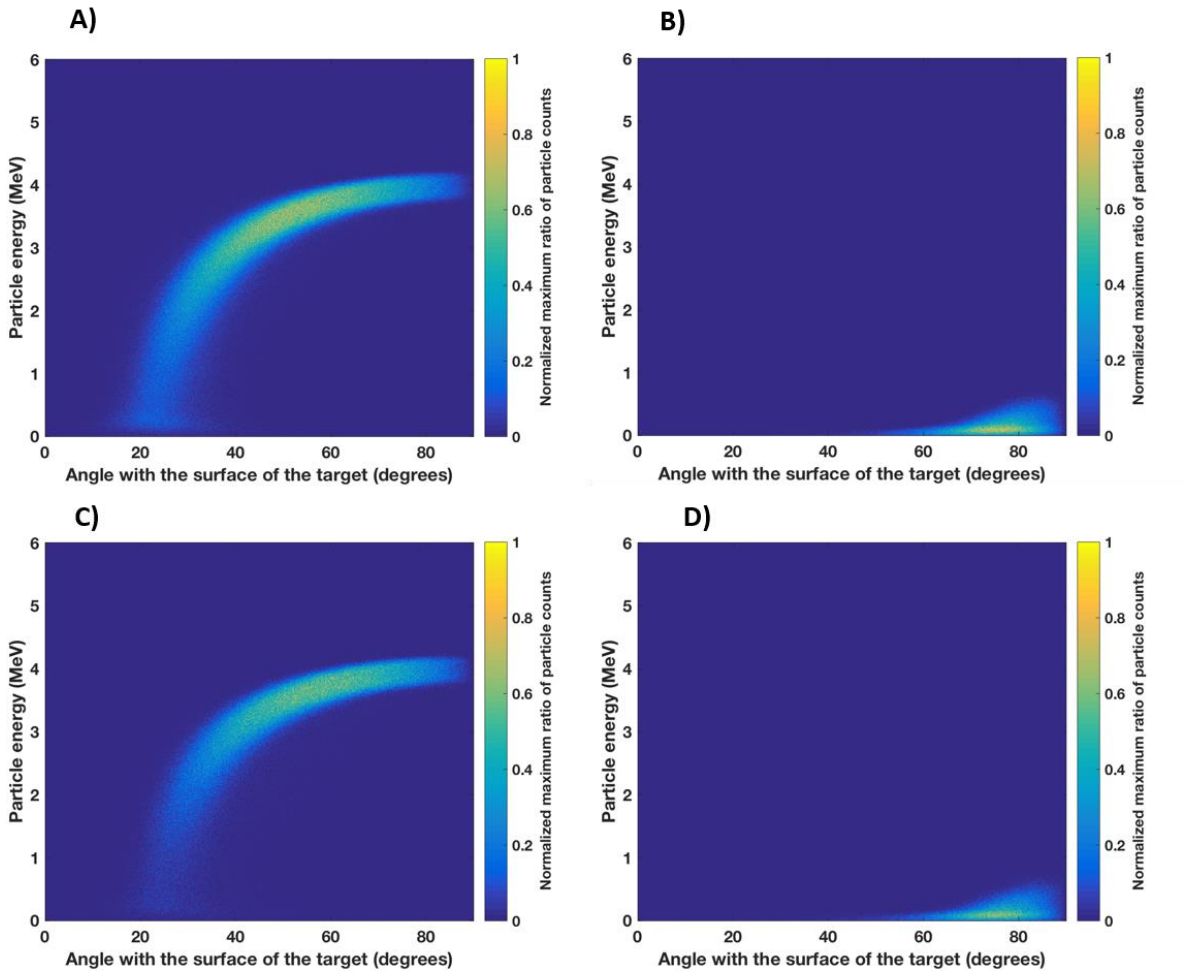

Figure 3.21 - Simulated density distributions relating particle's energy and angle with surface of the cell target positioned at *d*=2.9 mm (A) and 26.9 mm (B) with a non-collimated source. Figures C) and D) represent the density distributions at the cell target when the collimator is present. Depending on the distance between targets and source, a total of 10 to 60 million particles were simulated, and the particle counts were scored and then normalized to the maximum scored counts for the colorbar scale.

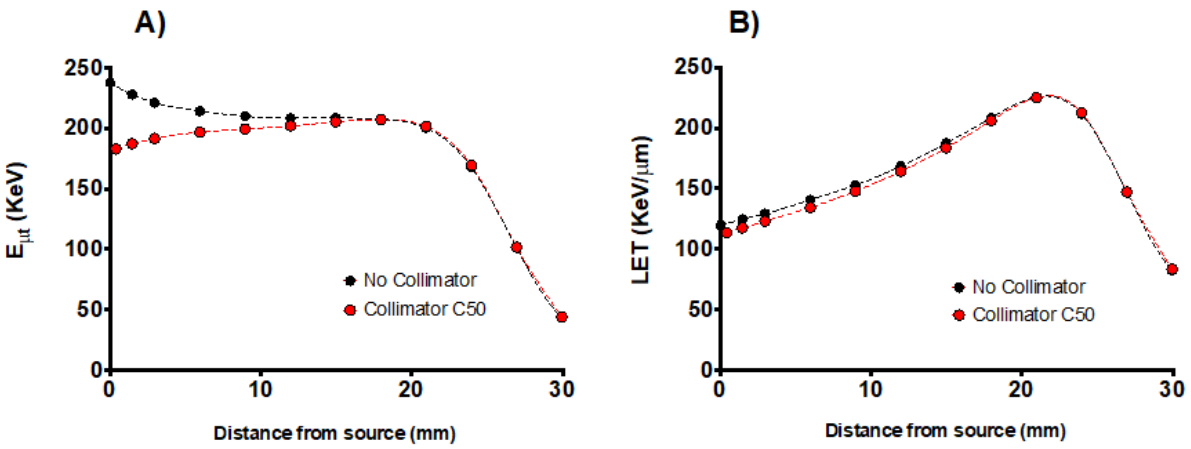

Figure 3.22 - Simulated average α-particle energy deposition per particle at the first micrometre layer of the cell targets (A) and LET profile of the α-particles irradiated from the source at different targets, based on the simulated particle energies and data from the NIST database (B) with and without a collimator. Cell targets were positioned at different distances from the α-source, with initial emitting energy of 5.48 MeV. Dashed lines represent the cubic interpolation curves from the data points shown. The error bars represented as standard deviations from 3 simulations are too small to be noticed.

The same observation can be made when the particle density distribution, comparing particles' scored energies and angles, is analysed. As Figure 3.21 shows, the contribution of scored particles with lower angles and lower energies is substantially reduced for a closer target when the simulated collimator is present (Figure 3.21A and C). As *d* increases, the scored particle's density distribution profiles become similar, especially at the last simulated target distance (Figure 3.21B and D).

3.3.3.2 Energy deposition

Figure 3.22A shows the averaged energy deposition per α-particle in the first micrometre of a cell target (E_μ), from a simulation with and without a collimator. In agreement with the results shown in the previous section (3.3.3.1), the most significant differences are seen for the shorter distances between the target and the source. The two initial energy deposition profiles have very different trends, with decreasing E_μ for increasing *d* when there is no collimator present, as opposed to slowly increasing E_μ for increasing *d* in simulations with a collimator present. This is the result of the collimator's blocking α-particles emitted with low angles, which consequently reduces the number of scored particles with lower angles reaching the surface of the target.

The second plot shown in Figure 3.22B shows the averaged LET profile of particles scored at targets placed at different *d*. The averaged LET values are slightly higher for simulations with no collimator at closer distances to the source. The two LET profiles follow the same trend with distance *d*, becoming more similar to each other the further away the targets are from the source. This stage of

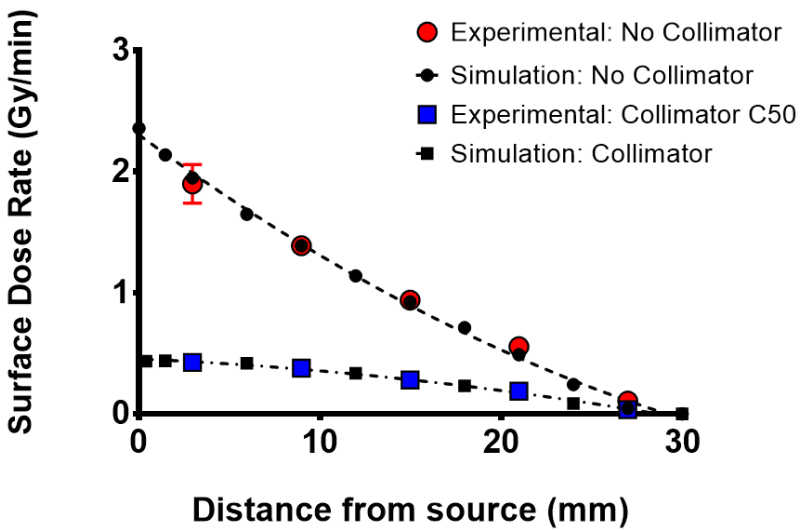

Figure 3.23 - Surface dose rate of the α-source based on experimental and simulation particle fluxes at different cell target distances from the source with and without a collimator. Error bars represent the standard deviation from simulation and experimental data. The dashed lines the cubic interpolation curves fit curves as an approximation fit to calculated data points.

LET profile similarity is again related to the particles' energy and angle distributions being almost the same at large distances.

3.3.4 Dose rate

The experimental and simulated surface dose rates calculated at different cell target distances for both collimated and non-collimated source scenarios are shown in Figure 3.23. The two surface dose rate profiles have a similar trend to the experimental and simulated flux curves (sections 3.3.1.3 and 3.3.2.1). This is expected as the number of incident particles per unit time is closely related to the total energy deposited on each cell layer.

The simulated averaged nucleus dose rate for a target placed at the closest experimental distance to a collimated source (d=2.9 mm) was calculated to be $\dot{D}_{nucleus}$ = 0.41± 0.02 Gy/min. This represents a difference of 1.16 Gy/min when compared to the average dose rate obtained from a simulation with a non-collimated α-source to the same distance ($\dot{D}_{nucleus}$ = 1.57± 0.15 Gy/min).

3.4 Discussion

The use of 3D printing techniques for collimators is not new. Typically, this involves additive manufacturing and laser sintering using metallic materials. [131,134,135] These 3D printing methods have a high resolution and printing accuracy which are important for X-ray and neutron collimator research, for example. However, this involves high printing costs - more than 900 € per sample. In α-particle research these costs can be significantly reduced if using polymer based 3-D printers. As these particles are easily absorbed, even by non-metallic materials, using a polymer based 3-D printer can be a revolutionary, fast and cheap way to build α-particle dedicated collimators.

In this chapter we have shown that we can use accessible 3-D printers to easily build collimators for α-particle sources. The polymer based printed collimators were tested in a variety of experiments and compared to Monte Carlo simulations, including geometry analysis, α-particle flux and beam quality effect. The obtained results demonstrated that 3-D printed collimators improve the overall beam quality of α-particle irradiation setups, reducing the energy spread.

From the geometry analysis, it was shown that the 3D printed collimators are not perfectly uniform due to limitations of the 3-D printing process. Specifically, the honeycomb hole structure is not consistent across the collimator area, as seen in Figure 3.6 and demonstrated in Table 3.1. There are significant variations in both hole diameter and septa distances, with standard deviations representing 22.0% and 13.3 % of the averaged *D* and *S*, respectively, for the collimator C50. Regarding the collimator C55, the variations are 19.1% and 11.1% for the same geometry parameters. These results suggest that, for the dimension scale considered, the higher the printing infill ratio, which translates into lower *D* and *S* distances, the lower the percentage variation of the honeycomb pattern structure of the collimator.

In terms of thickness, we found that collimator C50 had a lower T (0.39 ± 0.01 cm), in comparison to collimator C55 (0.45± 0.01 cm). The lower thickness combined with the larger average hole diameter allows a higher number of α-particles to pass through compared to the C55 sample. This is confirmed by the results shown in Figure 3.17, showing higher particle flux ratios calculated from targets exposed to an α-source collimated by the C50 sample, in comparison to the C55 sample. Collimator C50 was used in most of the analysis of this chapter because of these higher particle fluxes. Having a low number of particles coming through the collimator would not be ideal for an experimental setup of a cell target irradiation.

The uniformity analysis on the films exposed to a collimated and non-collimated source showed similar overall NOD percentage variations from the average values (section 3.3.1.2). When considering a cell dish target area (diameter = 3.4 cm), the NOD standard deviations represented 5.5% and 5.3%

with and without a collimator, respectively. It should be noted that this error includes noise from the scanner and film samples, which account for 1.12%. Since the NOD is directly related to the energy deposited by α-particles and given that there is a small difference between experimental standard deviations, this suggests that the collimator used does not appear to significantly reduce the variation in energy deposited across the sample. However, this is not necessarily true since the α-source does not seem to have a uniform activity across the ^{241}Am layer, as discussed in the previous chapter (section 2.3.1.1). That impacts this analysis, where a uniform source activity would be preferred in order to get a better understanding of the NOD variation across an irradiated target from a collimated source. In addition, this can also be the result of the non-uniformity in the honeycomb pattern previously discussed. If different collimator areas let more particles with wider angles to go through compared to other areas, this can result in energy deposition variations across different target areas. Naturally, this variation is more significant the closer the target is to the collimator.

The α-particle flux, in both experimental and simulation setups with and without a collimator, showed significant differences especially for target distances closer to the source (Figure 3.15 and Figure 3.16). The experimental particle flux calculated at a target placed at d = 2.9 mm from a collimated source represented about a quarter of the flux obtained from a non-collimated source. This ratio is relevant when comparing to the C50 collimator open area ratio, which is near 0.47. As the target distance increased, this flux ratio increased as well (0.33 flux ratio at d = 26.9 mm). This is expected as the particles reaching higher distances should have angles closer to 90°, compared to the particles scored at shorter distances. This demonstrates that collimators have a greater impact the closer the target is to the source surface, as they block the larger fraction of particles with angles closer to 0°. Future work could also involve experimental and simulation analysis on varying the distance between the collimator and the source, as this will also have an impact in particle flux, angle and energy when hitting a target.

The good agreement of both simulation and experimental data for collimated and non-collimated source setups also demonstrate the accuracy of the collimator geometry assessment as well as the simulated conditions and approximations used. This is further demonstrated in the experimental and simulated flux ratios between source setups using two 3D collimators (Figure 3.17).

Additionally, the results showed in Figure 3.17 also prove that the collimator C50 allows more particles to go through it, especially at shorter target distances. Despite the shorter septa (S), the collimator C55 has a smaller average hole diameter (D) and a longer thickness (T) than collimator C50, which lead to a higher percentage of particles being blocked, particularly those with wider angles. As d increases, the range of particle angles scored becomes more similar between both setups, eventually leading to a particle flux ratio getting closer to 1, which is the open area ratio between the two collimators.

The Monte-Carlo simulation results presented in section 3.3.3 highlight the effect of using a collimator on particles angle and energy distributions across a target's surface. This is first demonstrated in Figure 3.18, showing a higher average energy of particles hitting the surface of targets exposed using a collimated source compared to a non-collimated source. This is more evident the closer the target is to the α-source. The reason for the higher average energies is related to the lower number of incident particles at wide angles, which would reach the target with lower energies if they were not blocked by the collimator. A proof of this is shown by the differences in the particles' energy ranges, with incident particle energy's 5th percentiles being 1.11 MeV and 0.66 MeV for a target placed at *d*=2.9 cm from a collimated and a non-collimated α-source, respectively. This is further proved in the results demonstrated by Figure 3.19 and Figure 3.20, which show a more significant effect of the collimator on particles energy spectra and angle for targets placed closer to the source. For a target placed at *d*=2.9 cm, the average incident particle angle is 5.4° higher when using a collimator. As *d* increases, the difference in averaged angles is reduced. Possible future work could involve analysing experimental energy spectra using a charged particle detector, in order to compare to the open source results.

The particle density distribution plots shown in Figure 3.21, relating the particles' scored energies and angles, further reiterate the relation of α-particles' energy and scored angle. The lower the emission angle, the less energy the particle will have when reaching a target. Since the collimator blocks particles emitted at lower angles, the low energy contributions decrease as a consequence. For targets at longer distances, the contribution of lower angle emission particles is reduced even without a collimator, which makes the particle distribution profiles similar for simulations with and without a collimator.

It is also evident that the collimation of lower angle particles has a significant effect on simulated energy deposition at the cell target when looking at the results from section 3.3.3.2. Figure 3.22A, together with the previous results, show that the absence of those low angle particles results in different initial E_μ trends with target distance, compared to a simulation without a collimator. This is explained by the longer distance travelled by low angle particles in the first micrometre layer, as mentioned in section 2.3.3.3 of the previous chapter. The longer the distance travelled by a particle, the more scattering events it will experience, with higher chances of energy transfer to the cell target layer. If these particles are blocked by a collimator, less energy transfer events occur per particle per target layer, on average.

A second cause for the different E_μ profiles is related to the averaged LET for different target distances *d* (Figure 3.22B). In this case the particle's travelled distance is normalized regardless of their angle. At the Bragg peak, lower energy particles have, until a certain limit, a higher LET. This is demonstrated in Figure 2.28 from the previous chapter (section 2.4). As noted above, these lower energy particles are typically those emitted at low angles. In a scenario with a collimated source, these particles

are blocked and the averaged LET is consequently lower than the averaged LET for a non-collimated source.

For a non-collimated simulation, as the target distance increases, the average particle angle increases as well, which results in fewer energy transfer events per particle. This is highly related to the decrease of E_μ as *d* increases. On the other hand, in a simulation with a collimator, higher averaged LET are expected with increasing *d*. This explains this scenario of an increase of E_μ up to a certain *d* limit. Beyond that limit, the averaged LET rapidly decreases, following the Bragg peak's decrease for the very low particle energies scored at the most distant targets (E < 0.9 MeV). Both E_μ and LET profiles are very similar to each other during this phase, as the collimated and un-collimated spectra have similar energy and angle distributions.

All the previous discussed aspects contribute to the collimated α-source surface dose rate discussed in section 3.3.4. For cell irradiation experiments using a collimator, we will place the cells at *d*=2.9 cm, the closest experimental distance to the source. For that, the simulated nucleus dose rate is $\dot{D}_{nucleus}$ = 0.41± 0.02 Gy/min. However, it is important to understand that both surface dose and nucleus dose rate results are based on the simulated collimator's geometry, which assumes a perfectly uniform honeycomb pattern with the hole diameter and septa distances approximated to the averaged ones obtained from the geometry assessment experiments. This assumption means that the variation in collimator's geometry pattern is not entirely being taken into account, possibly affecting the uncertainty in both the surface dose and nucleus dose rates.

The key results obtained in this chapter are summarised in Table 3.2. Here, we represent the main results of the collimated and non-collimated α-source simulation effects to cell targets positioned at different distances *d*.s

The main goal of this chapter was to test a novel technique to build a collimator, through 3D printing, focusing on its application for a cell target irradiation setup. The 3D printing technique used is still not accurate enough to design a perfectly uniform honeycomb collimator, but the generated collimators are still potentially usable. Even with these observed discrepancies in geometry, the experimental and Monte-Carlo simulation results showed very good agreement. The results shown in this chapter prove the enormous potential of 3D printing techniques to enable researchers to build easy and low-cost collimators for α-particle radiobiology research applications with accurate outcomes.

Table 3.2 – Simulation results of α-particle physical properties when reaching the cell target positioned at different distances from source to target with and without the collimator C50. All uncertainties are represented as the standard deviations from data.

d (mm)	Mean energy (MeV)	FWHM (MeV)	$E_{\mu t}$ (keV)	θ_s (°)	$\dot{D}_{surface}$ (Gy min^{-1})
			No Collimator		
2.9	2.88 ±1.04	0.95	221.2	46.1 ± 16.3	1.95
8.9	2.21 ± 0.91	1.20	210.0	52.3 ± 13.9	1.39
14.9	1.54 ± 0.74	1.39	208.4	59.1 ± 11.5	0.93
20.9	0.81 ±0.49	--------	200.3	67.0 ± 9.1	0.49
26.9	0.17 ± 0.13	--------	101.0	75.7 ± 8.3	0.05
			Collimator		
2.9	3.11 ± 0.89	0.76	191.5	50.5 ± 15.9	0.44
8.9	2.34± 0.86	0.95	199.4	54.6 ± 14.0	0.38
14.9	1.60 ± 0.73	1.19	205.2	60.3 ± 11.6	0.28
20.9	0.83± 0.49	--------	201.6	67.5 ± 9.2	0.19
26.9	0.17 ± 0.13	--------	101.8	75.9 ± 8.2	0.04

CHAPTER 4 : IN VITRO ASSAYS

4.1 Introduction

As mentioned in sections 1.3 and 1.4, different radiation particles and irradiation methods will lead to different effects on cell survival and DNA damage. Therefore, it is fundamental to study these effects in order to understand the biological consequences of radiotherapy treatments on targeted tissues. This leads to more accurate treatment planning.

One of the main focuses of this thesis is to compare the effects of X-rays, which are commonly used in radiotherapy treatments, and externally emitted α-particles on cells. We also aim to study the effects of targeted radionuclide therapies using α-emitting radionuclides, such as ^{223}Ra, on tumour and normal cells. To achieve those goals in this chapter, we aim to experimentally compare the *in vitro* effects of externally emitted X-rays and α-particles, together with ^{223}Ra internal cell exposures. The *in vitro* experimental work presented in this chapter consisted on:

1. Validating the α-source dosimetry through *in vitro* clonogenic assays
2. Studying the effects of X-ray and α-particle irradiation methods on normal and prostate cancer cells survival
3. Comparing the DNA damage effects from X-ray and α-particle irradiation methods on normal and prostate cancer cells
4. Studying Xofigo solution toxicity on cells

4.2 Materials and methods

4.2.1 Cell culture

4.2.1.1 Cell lines

In this work we used both normal and cancer prostate cells. We aimed to test the effect of the different radiation sources. The cell lines used were:

- PC-3 - Human prostate cancer cells isolated from bone metastasis originated from a grade IV prostatic adenocarcinoma (62 year-old Caucasian male).
- DU145 - NT01 - Human prostate PTEN-expressing cancer cells isolated from brain metastasis (69 year-old Caucasian male).
- RWPE - Human epithelial cells derived from a normal prostate (54 year-old Caucasian male).

4.2.1.2 Cell incubation

The tissue culture flasks used for cell growth (T175, T80 and T25 slide flasks) were obtained from ThermoFisher Scientific (Massachusetts, USA). These flasks were used to incubate the cells before they were ready to be used for the experimental sets. Incubation conditions included a constant temperature of 37 °C and 5% CO_2 flow under a cell incubator. The incubator's water was changed at least every 2 weeks and an anti-bacterial solution (Aqua Resist, VWR) was added to it in order to prevent cell infections. Additionally, to test for mycoplasm infections, a mycoplasm test was regularly carried out. This was done by using a mycoplasm detection kit (mycoAlert®, Lonza Group Ltd. Switzerland).

Each cell line was incubated with its appropriate cell medium. The PC-3 and NT01 cells were incubated in Roswell Park Memorial Institute medium (RPMI 1640) supplemented with 10% fetal bovine serum (FBS). The media was additionally supplemented with 1% Penicillin-Streptomycin for PC-3 cell growth, whereas for NT01 cell growth it was supplemented with 1% puromycin instead. The RWPE cells were incubated in Keratinocyte Serum Free Medium (K-SFM, ThermoFisher), provided with pituitary extract (BPE) and human recombinant epidermal growth factor (EGF).

When cells reached a confluence around 80% they were split. At this stage the culture flask's medium was thrown away and cells were washed with a low volume of phosphate buffer saline (PBS) for about 15 seconds. The PBS volume added varied from 2 mL to 10 mL depending on the flask size. This step was done to ensure that most of the residual medium was properly washed away. Afterwards, cells were exposed to a trypsin solution (1% concentrated in PBS) and kept in the incubator for about 5 minutes. If a T175 slide flask was being used, the volume of the added diluted trypsin solution was 2 mL. After this, the cells were detached from the surface of the flask and collected in a falcon tube in a new medium solution. A fraction of this cell suspension solution would be added to the previously washed flask, containing new medium. The split volume of the cell solution to be used for the new passage varied from 10% to 20%, depending on the cell line used and how fast it grew. A new flask was used for the new cell passage at least every 3 consecutive passages.

All cell work was done inside a Biomat 2 Class II microbiological safety cabinet (Thermo Electron Corporation). The FBS and trypsine solutions were obtained from Gibco TM (ThermoFisher Scientific, Massachusetts, USA).

4.2.1.3 Cell counting

A cell counter was used to calculate the concentration of cells in a cell culture medium solution. This was important for plating the desired number of cells for each experiment. The cell counting step would be done after the trypsinization of cells from a slide flask, as previously mentioned in section 4.2.1.2. 100 µL of the cell suspension solution was added to 9.9 mL of isotonic solution. After gently mixing the new solution, a Z2 Beckman Coulter counter (Indianapolis, USA) was used. This counter uses the electric zone sensing principle, which relates the passage of a cell volume through a small aperture to an electrical current signal drop. This signal is proportional to the cell passing through the machine aperture. [136]

For every experiment, a control count of cells was also done using a pure isotonic solution without any cells inside. Every control and cell volume count was repeated twice and added together to compensate for single measurements inaccuracies. The control count would be subtracted from the cell sample counts. Additionally, the Coulter counter's aperture was washed with isotone between sample counts.

4.2.1.4 Cell storage

Cell samples that were not needed for upcoming experiments were preserved in freezing conditions in a -80 °C freezer (New Brunswick C760). The freezing process of cells started after trypsinization from a T175 slide flask, as mentioned in section 4.2.1.2. Each cell suspension was afterwards transferred to a 15 mL tube that was spun at 5000 rpm for 5 minutes inside a centrifuge (Eppendorf Centrifuge 5702). After this step the cell suspension was concentrated in a pallet at the bottom of the tube. The medium solution was thrown away and the pallet was resuspended in 1 mL of medium. After counting the number of cells using the methods described in section 4.2.1.3, we diluted the suspension solution in a cryoprotectant solution composed of FBS with 10% dimethly-sulfoxide (PanReac AppliChem, Barcelona, Spain), achieving a cell concentration of about 2 million cells/mL. Following this, the cell solution would be aliquoted in 1.5 mL cryotubes, which were then placed in a Mr Frosty freezing container (Thermo Fisher Scientific), filled with 100% isopropyl alcohol. The

cryotubes inside the Mr Frosty were subsequently placed inside the -80 °C freezer for at least 3 hours before being retrieved from the Mr Frosty and stored inside the same freezer.

4.2.2 *In vitro* cell assays

4.2.2.1 Clonogenic survival assay

The clonogenic survival assay is widely used to study the effect of external biological agents on cell proliferation and survival. In this case, the external agent was ionizing radiation. By exposing cell samples to different radiation doses and giving them time to grow after, we can study the survival probability of a cell line following exposure to different radiation types. [44]

The clonogenic assays tests the cell's ability to grow into a viable colony of descendant cells after being exposed to X-rays or α-particles, in this work. A surviving cell will grow into a colony, whereas a cell damaged beyond repair will not form a colony. This analysis is done by leaving the cells to grow for a certain period of time after irradiation and counting the number of viable grown colonies. The survival fraction (SF) is then calculated as follows:

$$\mathrm{SF} = \frac{N_{colonies}}{N_{seed} \times PE} \qquad 4.1$$

$N_{colonies}$ is the number of colonies counted, N_{seed} is the number of seeded cells and PE represents the platting efficiency, which is calculated as the percentage of seeded cells that grew into colonies from a control sample, i.e., a non-irradiated sample.

For irradiated cells, it has been shown that cell SF has a linear quadratic relation with the radiation dose following the equation parameters:

$$SF = e^{-(\alpha_1 D + \beta_1 D^2)} \qquad 4.2$$

where α_1 represents the rate of cell killing by a single-hit events, β_1 refers to the rate of cell killing by multi-hit events and *D* corresponds to the absorbed dose. This is further explained in section 1.4.2.

For X-ray exposures, we plated cells into 6 well plates (Sarstedt AG & Co, Germany), leaving them to incubate overnight in 2 mL of medium in each well. The plates were irradiated to doses of 0, 2, 4, 6 and 8 Gy. For α-source exposures, the cells were instead irradiated in mylar dishes, to doses that ranged from 0 to 2 Gy. After α-particle irradiation, the cells were trypsinized, counted and transferred to 6 well plates, following the same conditions and experimental steps as the plates exposed to X-rays. The small differences in the experimental protocols between X-ray and α-particle irradiations, related

to trypsinization, is still taken into account by the control sample results, allowing the analysis of both experimental irradiations to be compared.

Since a higher dose would kill a higher percentage of cells, a different number of cells was plated depending on the radiation dose to be delivered. This was done in order to ensure we would have enough viable colonies to count (around 50 to 100 for each well).

After irradiation, cells were left to incubate and grow inside the plates. The growth period for PC-3 and RWPE cells was 10 days, while the NT01 cells grew for 8 days only. The next step was washing the medium solution out of all wells, followed by the staining of cells with a solution of 0.5% crystal violet in 70% methanol. 2 mL of the staining solution was pipetted into each well for a minimum period of 1 hour. All wells were rinsed in water thereafter, to remove the excess crystal violet staining solution. The crystal violet staining allowed the surviving colonies to be easily visualised. We then used a Stemi 2000-C microscope (Carl Zeiss™) to count all surviving colonies per well. We assumed that a colony was viable if it contained at least 50 cells.

After repeating this process for all wells and plates, we averaged the number of counted colonies for all wells exposed to the same dose (3 to 6 wells per dose point, depending on the experiment) to provide a SF estimate for an individual experiment. This SF was then averaged across multiple independent biological replicates to account for experimental uncertainties. The final surviving fraction results were then presented in a logarithmic scaled plot, together with a non-linear regression of the linear quadratic dose response, as explained in section 1.4.2. For each experiment, two to three independent experimental replicas were done.

The resulting SF and linear quadratic dose curve equations were then compared for all different radiation sources and all cell lines used. We also compared the radiation effect of α-particles to X-rays for each cell line by calculating the relative biological effectiveness (RBE) for SF = 10%:

$$RBE_{SF=10\%} = \frac{D_x}{D_\alpha} \qquad 4.2$$

D_α and D_x are the radiation doses absorbed by a cell line that lead to a SF=10% from irradiations with α-particles and X-rays, respectively. These doses were extrapolated from the linear quadratic dose response equations for each cell line.

4.2.2.2 DNA damage assay

To investigate the radiation damage at the DNA level we tracked DNA double strand breaks (DSBs) with immunohistochemical techniques. This was achieved by staining and tracking the 53BP1 protein (Novus Biologicals).

Similarly to the clonogenic survival assay, cells were treated with different radiation doses depending on the radiation used. When using X-rays, 150 000 cells were plated onto plastic coverslips attached to the wells of 6 well plates. Each well was filled with 2 mL of medium. When the irradiations were performed with α-particles, the cells were treated in mylar dishes instead.

The staining assay was conducted after cell irradiation. Cells were allowed to repair in an incubator for different time periods before staining, typically 1 or 24 hours. If the cell samples were meant to be preserved before staining in the next day, they were fixed in a 50:50 methanol - acetone solution. This allowed samples with different recovery times to be stained at the same time.

When samples were ready for staining, they were rinsed 3 times with PBS and then incubated at room temperature with a blocking buffer solution (0.2% milk, 5% fetal bovine serum and 0.1% Triton X-100 in PBS) for 1 hour. Following that and after washing everything with PBS, we started a 2-step antibody staining procedure where the primary antibody, (53BP1 antibody, Novus Biological), recognizes the 53BP1 protein. The second antibody which targets the primary antibody, carries a fluorophore substance that will emit fluorescence at the light wavelengths of 568 nm.

The staining procedure consisted of adding a solution of 1 mL to each sample of the 53BP1 antibody diluted in blocking buffer with a dilution factor of 1:5000. The samples were then left to incubate for 1 h at room temperature. The next staining step was conducted after washing all samples with PBS 3 times. We then added a solution of 1 mL of the Alexa Fluor 568 Goat anti Rabbit secondary antibody (Life Technologies) diluted in blocking buffer with a dilution factor of 1:1000. The cells were then left to incubate at room temperature, covered in foil to block light, and then rinsed again 3 times with PBS.

The coverslips were then mounted onto slides with mounting medium containing DAPI (Thermo Fisher, UK). The DAPI staining allows the visualization of a cell nucleus by fluorescence. The stained samples were kept in a freezer and later analysed with the Zeiss Axiovert 200 microscope (Carl Zeiss MicroImaging), using a x63 objective.

To analyse these samples, the number of 53BP1 foci per cell were counted for 50 cells in each sample. The average number of foci per cell was then calculated, having subtracted the average number of foci in the corresponding 0 Gy control samples from the average foci numbers in the irradiated samples. The obtained foci averages were then used to compare DNA damage levels between samples exposed to different radiation doses and incubated for different recovery time periods. Additionally, we also compared the foci numbers in irradiated samples that had a recovery time of 1h or 24h. This comparison was performed by foci number normalization. This involves calculating the ratio of the average foci between the two experimental conditions for each cell line and absorbed dose:

$$Foci_{ratio} = \frac{N_{\text{foci (24h)}}}{N_{\text{foci (1h)}}} \quad 4.3$$

Here $N_{\text{foci (24h)}}$ and $N_{\text{foci (1h)}}$ represent the average foci per cell obtained from cell samples exposed to the same experimental conditions but with a treatment recovery time of 24h and 1h, respectively. The resulting foci ratio allows us to analyse the level of DNA repair between 1h and 24h post-treatment.

4.2.3 External source cell irradiations

4.2.3.1 X-ray irradiations

The X-ray irradiations used for clonogenic or DNA damage assays were performed using an X-RAD 225 cabinet irradiator (Precision X-ray Inc., USA) controlled by an Isovolt Titan E (General Electric, USA). The 6 well plates containing the cells were exposed to 225 kVp X-rays hardened by a 2 mm copper filte (with a 13.3 mA current) at a distance of 50 cm from the source. In these conditions the dose rate was 0.591 Gy/min. The X-RAD cabinet dosimetry was externally calibrated by RPS Services.

4.2.3.2 α-particle irradiations

The α-particle irradiations followed the methods described in chapter 2. This consisted on plating cells on Mylar dishes and then irradiate them externally with the α-source. The Mylar layer, having 0.9 μm thickness, allows α-particles that go through it, losing only a small amount of energy before hitting cells. All cell irradiations had the Mylar dishes placed at a distance of 2.9 mm from the α-source. For most irradiation experiments in the work presented in this chapter, there was no collimator present. In those conditions, the nuclear dose rate was $\dot{D}_{nucleus}$ = 1.57± 0.15 Gy/min. Irradiation time was adjusted to deposit the desired dose. When the irradiation time was up, the mylar dish would be immediately removed, manually, from the α-source holder box. There could be a small uncertainty on irradiation time of about 1 second due to the process of the mylar dish removal. This can impact the delivered dose with a small error of 0.03Gy.

We have also tested the α-source with the collimator C50 present in order to validate the work done in chapter 2. For this experimental setup, the dose rate was $\dot{D}_{nucleus}$ = 0.41± 0.02 Gy/min. Here we compared clonogenic assay results from source irradiations with and without the C50 collimator.

The purpose of this experiment was to evaluate the accuracy of the collimator simulation done in the previous chapter. If the clonogenic survival curves for both experimental setup approaches, with and without the collimator, are significantly different, then the calculated dose rate is not accurate. The same would apply to the previous simulation results (flux, energy and angle distribution, etc.). If the results are similar, it proves that the geometry assessments made are correct, demonstrating the accuracy of Monte-Carlo simulations with α-particles, even when using the collimator's approximated geometry parameters. Most importantly, it would support the use of 3D printed collimators with α-particle sources as a fast and low cost way to collimate α-particles for physics and biology radiation experiments, with accurate dosimetry predictions.

The Mylar dishes used for α-particle irradiations are non-sterile materials and were re-used in experiments. Prior to their use in cell experiments, they were washed in a Virkon solution (Dupont™). Additionally, they were exposed to UV light inside a tissue culture hood overnight for sterilization. When used in cell experiments, a cell medium suspension containing 100,000 to 150,000 cells, depending on the cell line, was plated on the sterilized Mylar dishes. Prior to α-particle irradiations, cells were left to incubate and attach to the Mylar for 1 or 2 days.

4.2.4 ^{223}Ra cell irradiations

We also treated cells with ^{223}Ra dichloride (Xofigo). The access to Xofigo resulted from a collaboration with the ADDRAD trial in the Northern Ireland Cancer Centre. Our research group could access spare ^{223}Ra drug vials that were not used during treatment when patients missed a treatment day.

Each Xofigo vial contains a 6 kBq ^{223}Ra dichloride solution of 6 mL at the reference date. The other drug ingredients are 6.3 mg/mL sodium chloride USP (acting as the tonicity agent), 7.2 mg/mL sodium citrate USP (used for pH adjustment), 0.2 mg/mL hydrochloric acid USP (used for pH adjustment), and water USP for injection. [137]

We used these drug vials for research experiments, more specifically for *in vitro* clonogenic survival and DNA damage assays. These experiments allowed us to study the radiobiological effects of ^{223}Ra.

4.2.4.1 *In vitro* experiments using ^{223}Ra

For these experiments we used 6 well plates for clonogenic assays and 24 well plates for the DNA damage assays. Cells were plated directly into plates for the clonogenic assay, or on a glass coverslip

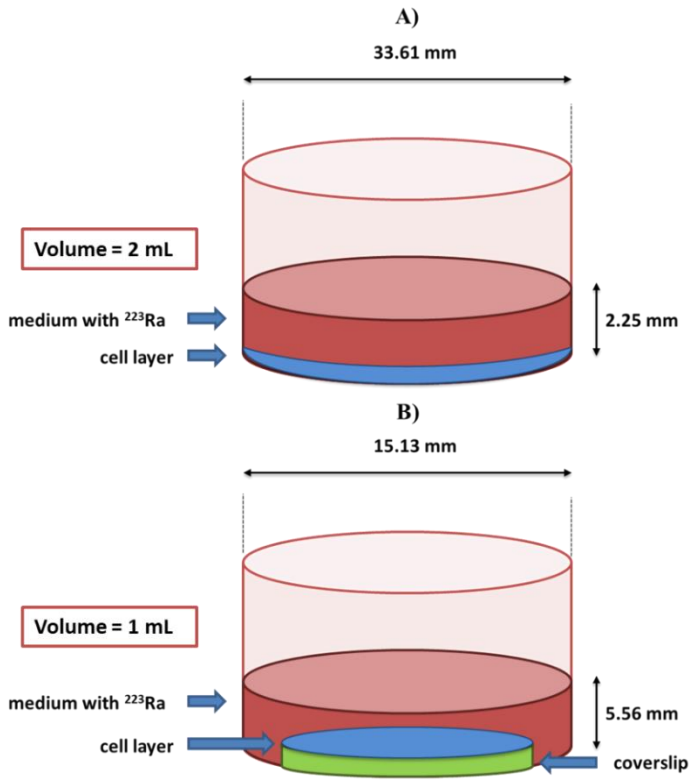

Figure 4.1 – Schematic representation of a cell sample in a 6 well plate well for clonogenic assay (A) and a cell sample plated on a 24 well plate well for DNA damage assay (B) following ^{223}Ra treatment. The cells are plated directly on the well bottom in A, whereas in B the cells are plated on a coverslip attached to the well bottom. The treatment volumes and well dimensions are different for both experimental setups.

for the DNA damage assay, similarly to external-source irradiation experimental setups. After plating, the cells were left to incubate overnight before treatment in medium (2 mL per well for clonogenics and 1 mL per well for DNA damage assays). A schematic representation of clonogenic and immunofluorescence experimental setups is shown in Figure 4.1.

After the initial incubation time, the wells were washed out and the ^{223}Ra, saline and medium solutions were added, filling the appropriate 2 mL or 1 mL volumes for each well, depending on the type of plate used. As ^{223}Ra decay delivers radiation dose over a prolonged period, different culture medium solutions had to be prepared containing different concentrations of ^{223}Ra to deliver planned doses in a particular exposure time. Determining the appropriate concentration required both the initial ^{223}Ra activity, exposure time, and decay rate to be taken into account, as described in more detail below. A saline solution of sodium chloride (6.3 mg/mL) was also prepared. As Xofigo is suspended in saline, this is used to ensure the same total volume of saline was added in each experiment regardless of the amount of ^{223}Ra, to remove salinity as a potential confounding variable.

In the clonogenic assay, cells were treated with doses of 0, 0.05, 0.1, 0.25 and 0.5 Gy, delivered over exposure periods of either 6 or 24 h. After the exposure time finished, the treatment medium was taken out and the wells were washed 3 times with PBS. Afterwards, 2 mL of medium was added per

well and cells were left to incubate and grow during 8 to 10 days, depending on the cell line used. Due to ^{223}Ra availability, each experimental SF dose point was based on the average result from 3 wells. All experiments were repeated 2 more times, with the exception of the NT01 cell clonogenic assay. Similarly to what was described in section 4.2.2.1, each individual obtained SF was then averaged together with the other replicate experimental dose point results.

For the immunofluorescence assays, we treated PC-3 and RWPE cells with doses of 0, 0.5, 1 and 2 Gy. This allowed us to compare the DNA damage level on PC-3 cells between the three irradiation methods used during this work: external X-rays, external α-particles and ^{223}Ra. We also compared the effects of Xofigo in DNA damage between PC-3 and RWPE cells for the same doses. Due to Xofigo availability, we were only able to do a single DNA immunofluorescence experiment for each of the cell lines, with no repeats.

4.2.4.2 ^{223}Ra *in vitro* simulation dosimetry

We used Monte Carlo simulation to assess the dosimetry for the ^{223}Ra cell irradiation experiments. The simulation was based on the experimental geometry setup represented in Figure 4.1, simulating a small scale approximation of cell irradiations by a ^{223}Ra treatment solution.

In this simulation, we irradiated a semi-ellipsoid cell geometry (20 μm diameter and 7.8 μm thickness) with a centred ellipsoid nucleus (6 μm diameter and 3 μm thickness). A representation of the simulated cell is shown in Figure 4.2A. The model cell and nucleus thickness values are based on the measured cell and nucleus thicknesses for PC-3 cells attached to a surface.

The simulated cell was attached to a small section of a well of a plate. The simulated well geometry had 200 μm diameter. It was covered with 'media' with a total height of 100 μm. The ^{223}Ra treatment solution medium was approximated as water, as the full material composition was not available in TOPAS.

In this simulation we considered 10 million α-particle cascade decays from ^{223}Ra, simulating all the α-particle consequent emissions from the ^{223}Ra decay cascade, following its decay scheme (Figure 1.5). This means that each decay would result in the emission of 4 α-particles with different energies. The total number of simulated particles were

- 1×10^7 α emissions with E_α = 5.87 MeV (1st cascade emission - 100% probability)
- 1×10^7 α emissions with E_α = 6.62 MeV (2nd cascade emission - 100% probability)
- 1×10^7 α emissions with E_α = 7.38MeV (3rd cascade emission - 100% probability)
- 9.97×10^7 α emissions with E_α = 6.62 MeV (4th cascade emission - 99.7% probability)

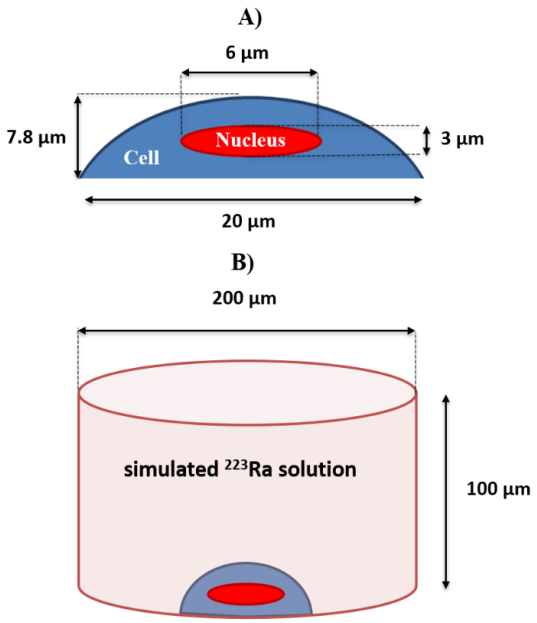

Figure 4.2 – A) Simulated cell as a semi-ellipsoid with 20 µm side diameters and a 7.8 µm thickness. The nucleus is simulated as a full ellipsoid with 6 µm side diameters and 3 µm thickness, centered at the middle of the cell. B) Simulated cylindrical volume of a treatment solution with α-particle emissions resulted from ^{223}Ra decays. A simulated geometry of a cell with its nucleus is placed at the bottom of the simulated well. The simulated well geometry has 200 µm base diameter, having 100 µm height.

- 3×10^5 α emissions with E_α = 7.45 MeV (4th cascade emission - 0.3% probability)

The 4th α-particle emission can result from 2 different possible decay paths, with differing emission probabilities, which is taken into account in the total number of simulated particles. We also assumed that, during a simulated treatment period, full decay chains occur following each ^{223}Ra decay. This is an acceptable approximation as the half-life of the longest daughter radionuclide is less than 0.3% of that of ^{223}Ra.

All particles were isotropically emitted from random positions inside the simulated well volume of water. The only emission restriction imposed was that emission only occurred outside the cell geometry. We assumed a uniform distribution of ^{223}Ra within the simulated solution, with no cell uptake. Clinically, ^{223}Ra treatments have been considered to uniformly affect a targeted tissue and its cells. [42]

Due to the short half-lives of ^{223}Ra initial decay daughters, the single cascade α-particle decays from ^{223}Ra, ^{219}Rn and ^{215}Po had the same origin positions. For the 4th cascade decay, the simulated α-particle emissions had different random origin coordinates as ^{211}Bi and ^{211}Pb have longer half-lives. As a result, these isotopes may travel some distance before decaying. Based on all α-particle decays from the ^{223}Ra cascade, the average α-particle emission energy from a Xofigo solution is 6.67 MeV, with an average entrance LET = 72 KeV/µm in water.

The simulated media volume for this simulation is large enough to encompass any α-particles which may reach the cell, taking into account the short penetration range of α-particles with 8 MeV energy in water (78 μm).[120] Particles with lower energies than that will have an even shorter range in water. A bigger well geometry would result in considerably slower simulations, as it would require the simulation of a higher number of particles randomly emitted within the simulated well geometry to compensate. The bigger the geometry, the lower the probability of a simulated isotropically emitted α-particle, with random initial position, hitting the cell geometry.

The simulated nucleus was scored in terms of delivered dose. The resulting dose in nucleus for 10^7 initial decays was $D_{sim} = 6.99 \times 10^3$ Gy. Since the simulations represented a very large number of decays per unit volume, the dose per ^{223}Ra decay in 1 mL volume was calculated as follows:

$$D_{1\,mL/N} = \frac{D_{sim} \times V_{sim}}{N_{sim}} = 2.198 \times 10^{-9}\ \text{Gy/decay} \qquad 4.4$$

where D_{sim} is the simulated dose at the nucleus, V_{sim} is the volume of the simulated well geometry (3.14×10^{-6} mL) and N_{sim} is the number of ^{223}Ra decay events that resulted in α-particle emissions (1×10^7 decays). To calculate the number of decays for a treatment solution volume $V_{solution}$ to deliver a nucleus dose of 1 Gy, we used the following expression:

$$N_{1Gy} = \frac{V_{solution}}{D_{1\,mL/N}} \qquad 4.5$$

For a $V_{solution} = 1$ mL, the number of decays to deliver a nucleus dose of 1 Gy is $N_{1Gy} = 4.55 \times 10^8$ decays. For a 2 mL treatment volume per well for a clonogenic assay, the corresponding number of decays is doubled (9.1×10^8 decays).

4.2.4.3 Xofigo's volume for *in vitro* treatment

We now know the number of ^{223}Ra decays necessary to deposit 1 Gy to cells attached to wells with different treatment solution volumes. For each experiment, we exposed cells to different radiation doses by adding different volumes of Xofigo to the treatment solution. The volume that was used for a treatment sample was calculated based on 4 variables:

- number of ^{223}Ra decays necessary to deposit 1Gy (N_{1Gy})
- planned delivered treatment dose (D_{treat})
- treatment exposure time (t_{exp})
- Xofigo vial activity at treatment starting time (Act_{vial})

To calculate the corresponding added volumes, we firstly calculated the number of ^{223}Ra decays from a 1 Bq activity solution between a treatment time of 0 to t_{exp} seconds:

$$N_{1Bq} = \int_0^{t_{exp}} e^{\lambda_{Ra} \times t}\, dt \qquad 4.6$$

where λ_{Ra} is the decay constant of ^{223}Ra. This value is based on ^{223}Ra physical half-life (T_p = 11.4 days):

$$\lambda_{Ra} = \frac{\ln(2)}{T_p} = 7.04 \times 10^{-7} \text{ seconds}^{-1} \qquad 4.7$$

Taking N_{1Gy} and N_{1Bq} for a sample treated for t_{exp}, we calculated the necessary initial ^{223}Ra activity per mL of a treatment solution to deliver a treatment dose D_{treat}:

$$Act_{D_{treat}} = \frac{N_{1Gy} \times D_{treat}}{N_{1Bq}} \qquad 4.8$$

Having the target ^{223}Ra activity for a 1 mL treatment solution, we can now calculate the volume of Xofigo to add to a treated cell sample:

$$V_{Xofigo} = \frac{Act_{D_{treat}} \times V_{solution} \times V_{vial}}{Act_{vial}} \qquad 4.9$$

where V_{vial} is the volume of Xofigo vial with an activity Act_{vial}.

The planned treatment doses and exposure times for clonogenic assays were:

- D_{treat} = 0, 0.05, 0.1, 0.25 and 0.5 Gy
- t_{exp} = 6 and 24h

For immunofluorescence assays, the treatment conditions were:

- D_{treat} = 0.5, 1 and 2 Gy
- t_{exp} = 24h
- recovery time after treatment = 1 and 24h

4.2.4.4 Impact of Xofigo volume for *in vitro* treatment

We also investigated the effect of the added Xofigo volume (V_{Xofigo}) on cells. To account for the need to deliver different volumes for a given dose we normalised V_{Xofigo} to the treatment dose (D_{treat}) and plotted each volume/dose ratio with the corresponding surviving fraction (SF) values obtained from the clonogenic assays. We then characterised the impact of this volume/dose ratio on

survival by fitting a least-square fit regression curve to our data points, assuming an exponential dependence of survival on this ratio. [138–140] The curve fit was based on the equation:

$$log_{10}(\mathrm{SF}) = -\frac{1}{R_{10}} \times \frac{V_{Xofigo}}{D_{treat}} \qquad 4.9$$

Here, R_{10} corresponds to the treatment volume per dose ratio ($\frac{V_{Xofigo}}{D_{treat}}$) which kills 90% of a cell population, reducing it by a factor of 10 compared to the radiation-only effect. For a fixed dose and exposure time we can also estimate the decimal reduction volume V_{10}, by multiplying this ratio by the delivered dose.

For each curve fit and R_{10} estimation we fixed the experimental conditions:

- D_{treat} = 0.05, 0.1, 0.25 and 0.5 Gy
- t_{exp} = 6 and 24h

This analysis will allow us to understand if the effect of each ^{223}Ra treatment dose on the cell survival fraction is independent of the Xofigo volume added and the treatment time.

4.3 Results

4.3.1 α-source validation through clonogenic survival assays

The first goal of our *in vitro* experiments was to assess and validate the previous work done related to the α-source dose rate calculations, presented in the previous chapters. To do this, we performed a clonogenic assay on PC-3 cells using the α-source with the corresponding calculated dose rate and compared our experimental results to similar data from the literature with the same cell line (n=3).[103] We include the results from both collimated and non-collimated source experimental irradiations. This is presented in Figure 4.3, showing the clonogenic SF of both experimental datasets with literature data.

Regarding the non-collimated source, these results show that the linear quadratic curve obtained in this work for the mentioned cell line and radiation source is in good agreement with the literature's, with a fitting R^2 = 0.992. It also demonstrates the accuracy of the α-source simulations conducted in chapter 2, as the data collected from them led to the calculation of the dose rate used for these experiments. Table 4.1 shows the different linear quadratic parameters obtained for these datasets.

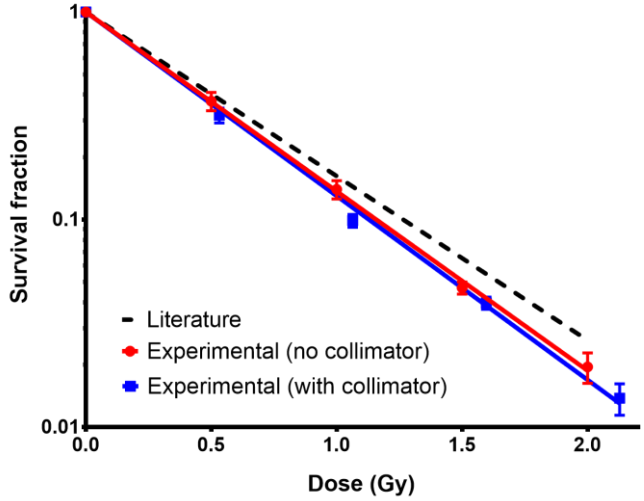

Figure 4.3 - Clonogenic survival data to the PC-3 cell line with α-particle irradiation from the α-source with and without the C50 collimator (n=3) compared to literature data for the same radiation and cell line. Error bars indicate the standard error of the mean. Curve lines represent the linear quadratic model fits to the experimental data. The experimental SF values obtained from the non-collimated source had a fitting $R^2 = 0.992$ to the literature's linear quadratic equation.

When comparing the collimated α-source results, using the C50 collimator, we notice that the linear quadratic curve fit is very similar to the curve from the non-collimated source results. This is also noticeable in Table 4.1, as the linear quadratic parameters of both experimental datasets differ by less than 3%. This similarity is important as it further validates the dosimetry calculations done for the collimated source approach.

For the next result sections in this chapter, the α-source was used without any collimator.

Table 4.1 – Linear quadratic parameters obtained from experimental data of PC-3 cells exposed to α-particles compared to literature data

	$\alpha_1 \pm$ SEM (Gy^{-1})	$\beta_1 \pm$ SEM (Gy^{-2})
Literature [103]	1.82	≈ 0
Experimental (no collimator)	1.988 ± 0.031	≈ 0
Experimental (with collimator)	2.040 ± 0.130	≈ 0

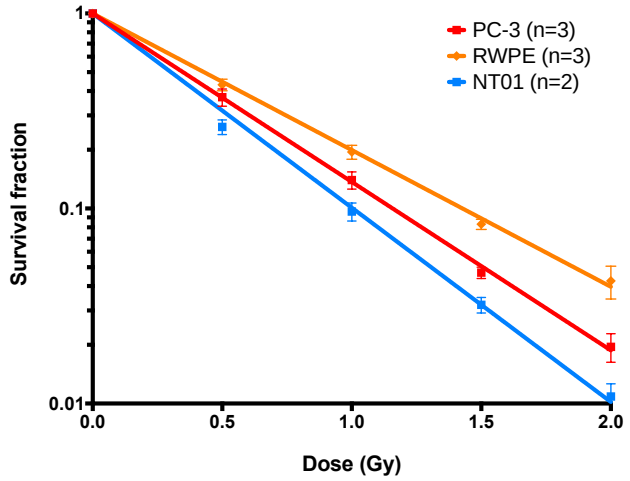

Figure 4.4 - Clonogenic survival data comparing the PC-3, RWPE and NT01 cell lines dose responses to α -particle irradiations. Error bars indicate the standard error from the mean. Curve lines represent the linear quadratic model fits to the experimental data with the number of experimental replicates (n).

4.3.2 α-particle effects on cells

4.3.2.1 Cell survival

Once the dose-rate of the α-particle source was validated, we repeated these clonogenic assays for all of the cell lines under consideration (PC-3, RWPE and NT01), as shown in Figure 4.4. This shows that the normal epithelial cell line (RWPE) has higher α-particle resistance, demonstrating lower cell kill rates at any delivered α-particle dose. The cancer line NT01, shows the highest radiosensitivity.

When comparing α-particle and X-ray clonogenic results for the three cell lines, we see that all cell lines are significantly more sensitive to α-particles, as expected (Figure 4.5). As before, RWPE cells have also the highest radioresistance to X-rays while the NT01 cells have the lowest. However, when analysing the $RBE_{SF=10\%}$ values for the 3 cell lines, we notice that the RWPE cells have the highest RBE for α-particle radiation. This is shown in Table 4.2, which also shows the different linear quadratic parameters obtained for α-particles and X-rays for each of the 3 cell lines used.

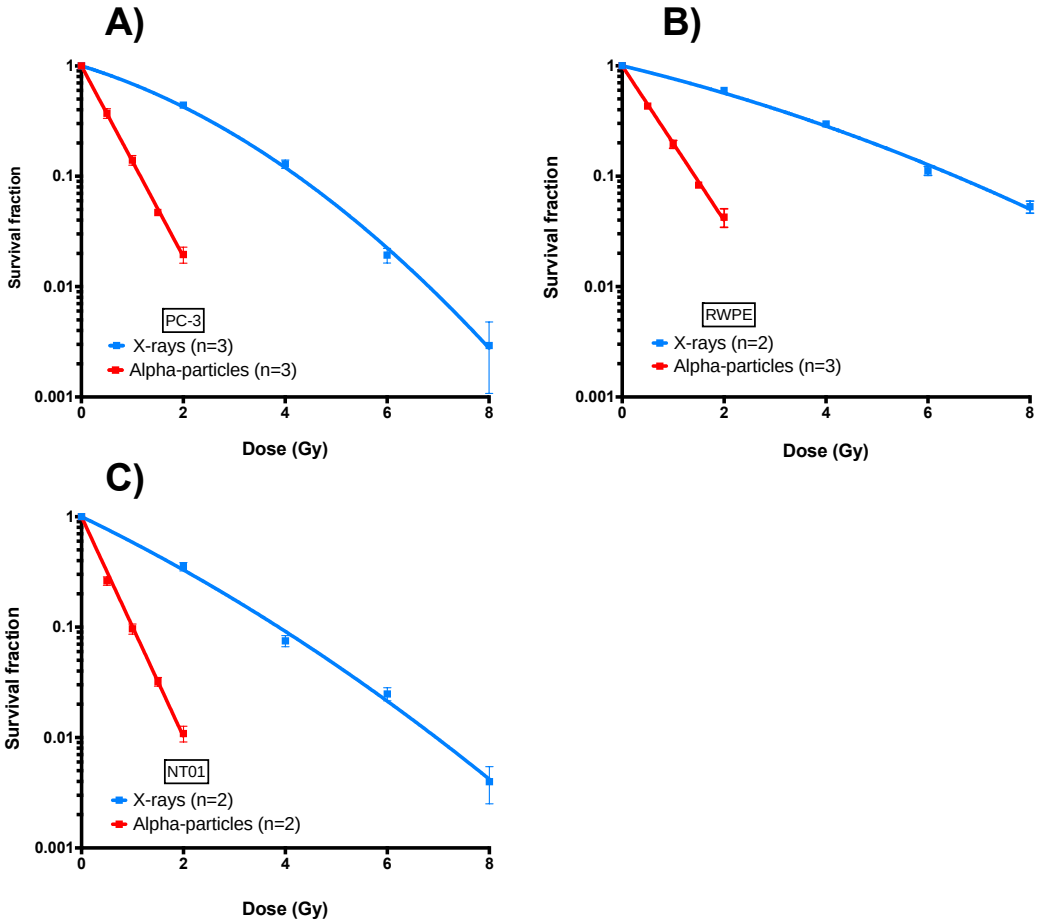

Figure 4.5 - Clonogenic survival data for PC-3 (A), RWPE (B) and NT01 (C) cell lines with X-ray and α-particle external beam irradiations. Error bars indicate the standard error of the mean. Curve lines represent the linear quadratic model fits to the experimental data with the number of experimental replicates (n).

Table 4.2 – Linear quadratic parameters (± standard deviation) obtained from experimental data of PC-3, RWPE and NT01 cell lines exposed to X-rays and α-particles with their associated RBE for 10% survival fraction.

	X-rays		α-particles		
	$\alpha_1 \pm$ SD (Gy^{-1})	$\beta_1 \pm$ SD (Gy^{-2})	$\alpha_1 \pm$ SD (Gy^{-1})	$\beta_1 \pm$ SD (Gy^{-2})	$RBE_{SF=10\%}$
PC-3	0.324 ± 0.037	0.051 ± 0.005	1.988 ± 0.031	≈ 0	3.66 ± 0.40
RWPE	0.255 ± 0.032	0.015 ± 0.004	1.613 ± 0.092	≈ 0	4.35 ± 0.66
NT01	0.512 ± 0.056	0.021 ± 0.008	2.293 ± 0.168	≈ 0	2.18 ± 0.43

4.3.2.2 DNA damage

The immunofluorescence assay results from PC-3 cells exposed to X-ray and α-particle radiation external sources are shown in Figure 4.6. As expected, the number of DSBs is significantly higher for both irradiated samples when the treatment recovery time is 1h compared to 24h. However, the two radiations result in different levels of DNA damage regardless of the recovery times. Although there is a significantly higher level of DNA DSBs with X-rays after 1h incubation post irradiation, there is clearly a slower DSB repair mechanism with α-particles. This is particularly evident when we look at the foci ratios normalized to 1h recovery times (Figure 4.6B). Here it can be seen that approximately 75% of X-ray induced DSBs are repaired after 24 hours, but only approximately 40% of α-induced DSBs are repaired in a similar timescale. For all experimental results, the average control number of foci was lower than 6.

When comparing the results from PC-3 cells to the normal epithelial RWPE cells exposed to 2 Gy doses of α-particles radiation, we see that the number of DNA DSB foci for both radiation treatment setups and recovery times is very similar (Figure 4.7). There is a slightly higher DNA DSB repair rate from RWPE cells after a recovery time of 24h (0.50 ± 0.16 foci ratio as opposed to the PC-3 0.59 ± 0.15 foci ratio), but this is not statistically significant.

In both analysis we see an increase of foci in X-ray exposures compared with α-particle irradiations after 1h of treatment. This is related to the higher number of X-ray hits in nuclei compared with α-particles. For the same averaged dose, there are significantly less α-particle hits (average cell dose higher than 0.1 Gy per particle). The relation between dose and foci numbers is also not linear. However, as a single α-particle leads to higher levels of DNA damage complexity, we see higher numbers of foci for α-particle irradiations when the recovery time is 24h, even though there were less particle hits than X-ray exposures.

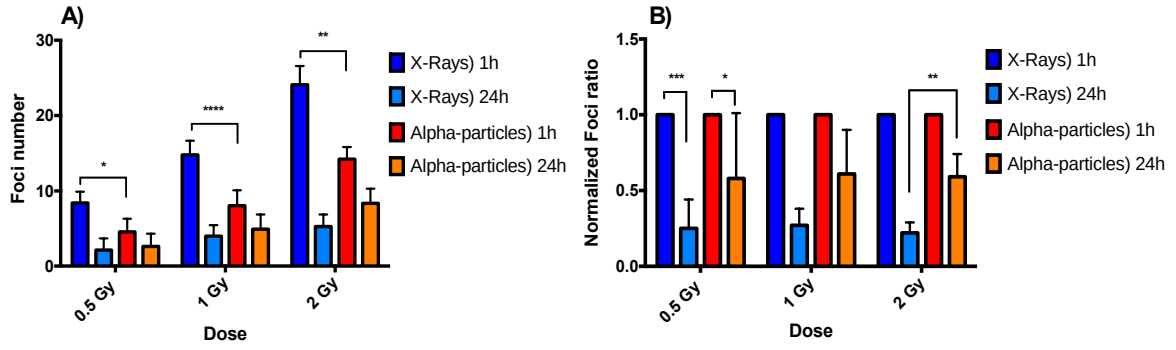

Figure 4.6 - 53BP1foci data of PC-3 cells exposed to 0.5, 1 and 2 Gy doses of X-rays or α-particles. Cells were fixed at time points of 1 and 24h post-irradiation for 3 replicate experiments (n=3). Foci numbers were corrected to unirradiated controls and are shown in absolute scale (A) and normalized to 1h post-irradiation time points (B). Error bars indicate the standard deviation from the mean. Statistical significance was calculated using a two-tailed unpaired t-test with p >0.05 indicating non-significance (NS) and p<0.05 indicating different levels of significance (p<0.05 (*), p<0.01 (***), p<0.001 and p<0.0001 (****)).

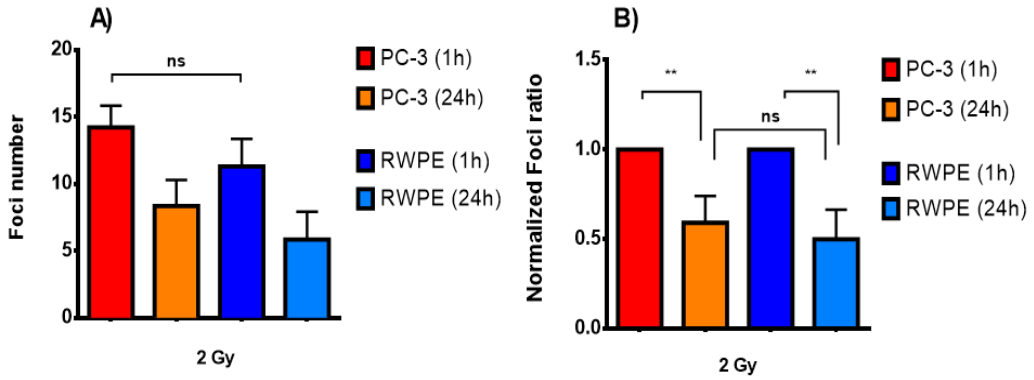

Figure 4.7 - 53BP1foci data of in PC-3 and RWPE cells exposed to a 2 Gy dose of α-particles. Cells were fixed at time points of 1 and 24h post-irradiation for 3 replicate experiments (n=3). Foci numbers were corrected to unirradiated controls and are shown in absolute scale (A) and normalized to 1h post-irradiation incubation time points (B). Error bars indicate the standard deviation from the mean. Statistical significance was calculated using a two-tailed unpaired t-test with p >0.05 indicating non-significance (NS) and p<0.05 indicating different levels of significance (p<0.05 (*) and p<0.01 (**)).

4.3.3 ^{223}Ra effect on cells

4.3.3.1 Cell survival

The clonogenic assay results from *in vitro* ^{223}Ra exposures of PC-3 are shown in Figure 4.8, compared with X-rays and external α-particles. For this experiment the ^{223}Ra treatment exposure time was set at t_{exp} = 24h. The comparison shows a significantly higher dose response from PC-3 cells exposed to ^{223}Ra in comparison to exposure to external sources emitting X-rays or α-particles.

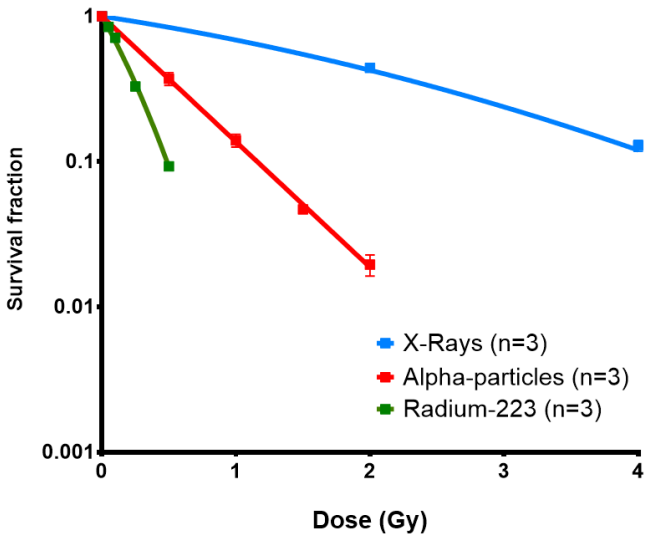

Figure 4.8 - Clonogenic survival data for the PC-3 cell line comparing external irradiations with X-rays or α-particles to ^{223}Ra α-particle internal radiation exposure. Error bars indicate the standard error of the mean. Curve lines represent the linear quadratic model fits to the experimental data with the number of experimental replicates (n). The Xofigo vials used for the 3 replicas of ^{223}Ra exposures had activities Act_{vial} varying between 1.95 to 2.35 MBq. The exposure time was the same for all ^{223}Ra treatment replicas (t_{exp} = 24h).

When comparing the effect of external α-particle irradiations with ^{223}Ra *in vitro* irradiations for the 3 cells lines used, we see that the treatment dose response to ^{223}Ra is higher regardless of the cell line used (Figure 4.9). The treatment sensitivity is particularly higher for PC-3 and NT01 cells when the treatment dose D_{treat} = 0.5 Gy (SF = 0.09 ± 0.01 and 0.11 ± 0.03, respectively). The RWPE cells are significantly more resistant at this dose (SF = 0.29 ± 0.01).

The fact that the ^{223}Ra *in vitro* irradiation and α-particle external irradiation results are consistently different from each other for all three cell lines suggest that there is an effect from the Xofigo treatment solution that is not being taken into account in our *in vitro* irradiation hypothesis. A small part of the difference between these results can be related to the difference in treatment dose rates, as Xofigo exposures require longer treatment exposure times in comparison to external particle irradiations. But this effect alone could not explain such significant variation. This will be further discussed in this chapter.

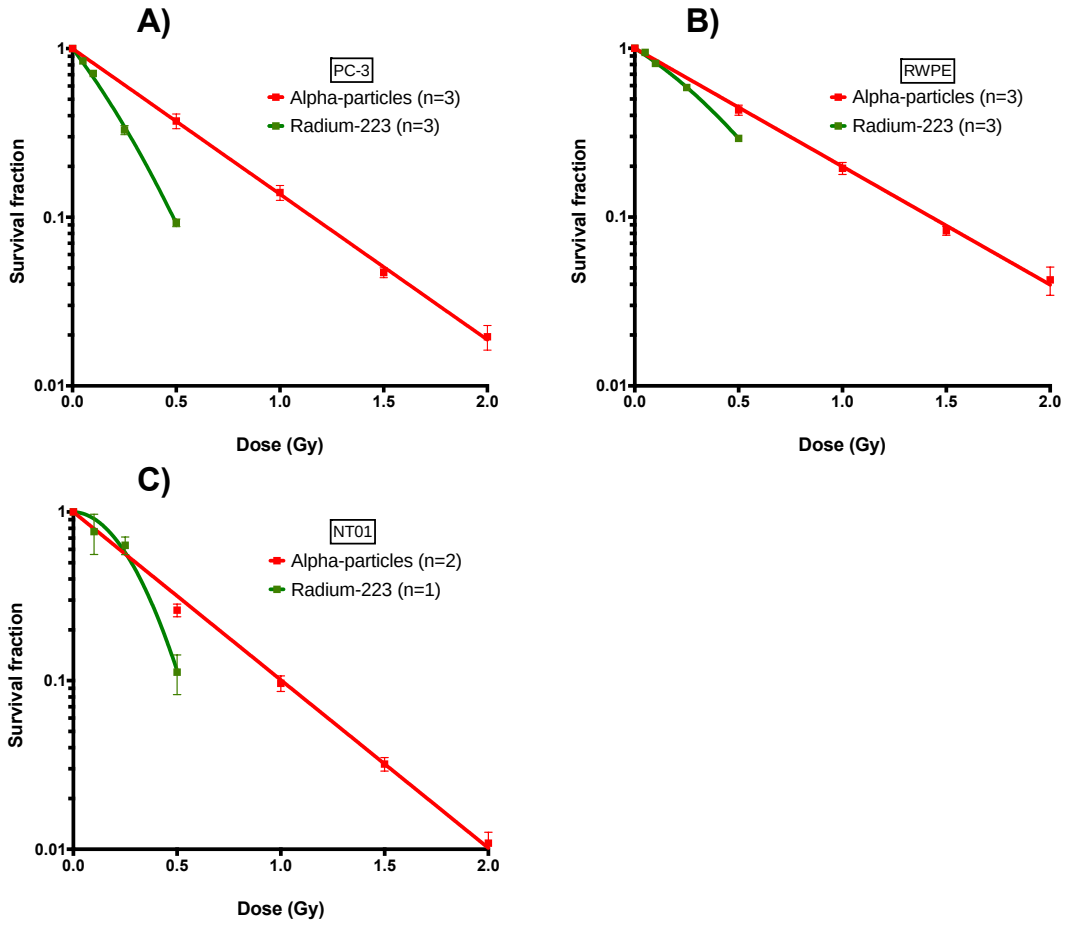

Figure 4.9 - Clonogenic survival data comparing the PC-3 (A), RWPE (B) and NT01 (C) cell lines dose responses to α-particles from external source and ^{223}Ra exposures. Error bars indicate the standard error from the mean. Curve lines represent the linear quadratic model fits to the experimental data with the number of experimental replicates (n). The Xofigo vials used for all experiment replicas of ^{223}Ra treatments had activities Act_{vial} varying between 1.95 to 2.35 MBq. The exposure time was the same for all ^{223}Ra treatment replicas (t_{exp} = 24h).

4.3.3.2 DNA damage

The results from the immunofluorescence assay for DNA damage in PC-3 cells exposed to ^{223}Ra is shown in Figure 4.10, compared with X-rays or external α-particles. For ^{223}Ra exposures, each cell sample received a different treatment dose (D_{treat} = 0, 0.5, 1 and 2 Gy) for a single treatment exposure time (t_{exp}= 24h).

In comparison to external α-particle irradiations, the average number of counted foci from ^{223}Ra exposures was greater for all doses and recovery times (Figure 4.10A). However, when analysing the fraction of foci repaired after a recovery time of 24h normalized to 1h, the results suggest that the repair rate is similar between ^{223}Ra and α-particle exposed PC-3 cells (Figure 4.10B). Repair levels from α-

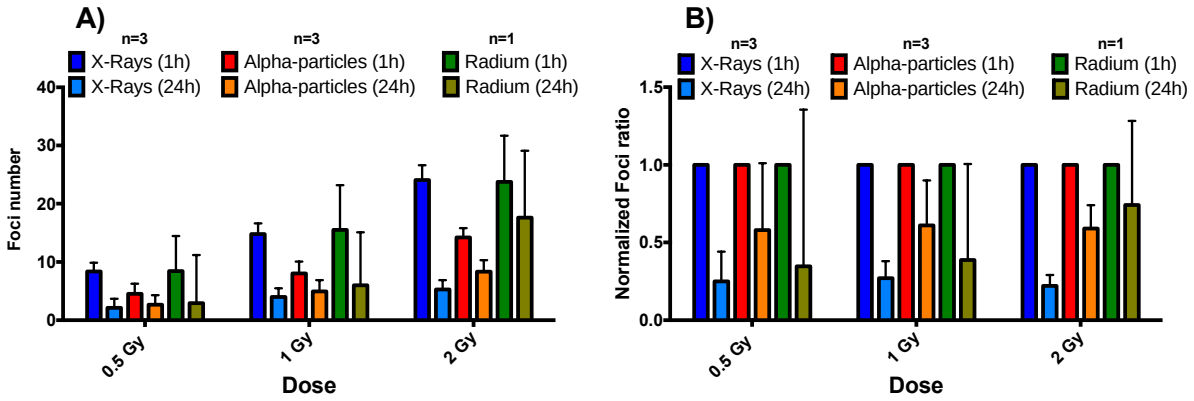

Figure 4.10 - 53BP1foci data in PC-3 cells exposed to 0.5, 1 and 2 Gy radiation doses of external irradiations exposures to α-particles or X-rays, and internal exposures to ^{223}Ra α-particles. Cells were fixed at time points of 1 and 24h post-irradiation for n replicate experiments. Foci numbers were corrected to control and are shown in absolute scale (A) and normalized to 1h post-irradiation time points (B). Error bars indicate the standard error from the mean.

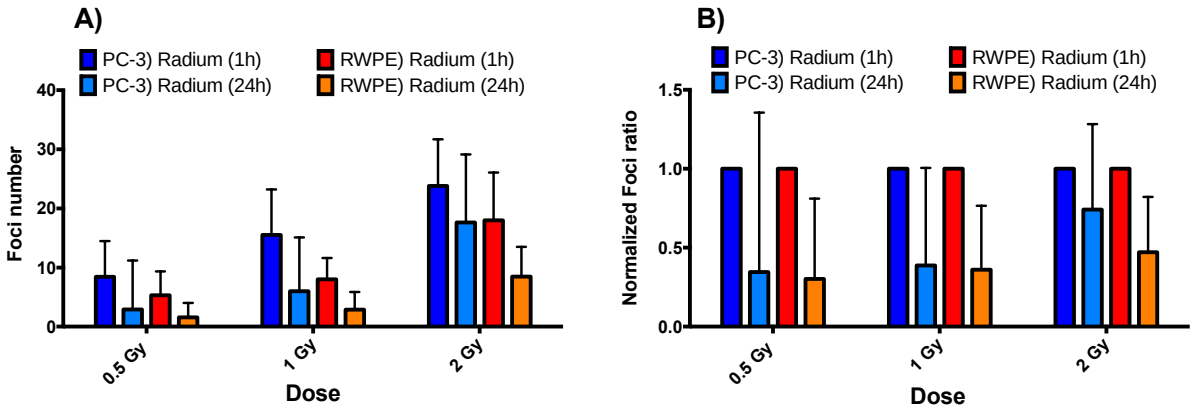

Figure 4.11 - 53BP1foci data in PC-3 and RWPE cells exposed to a 0.5, 1 and 2 Gy doses from ^{223}Ra α-particle internal exposure (24h). Cells were fixed at time points of 1 and 24h post-irradiation. Foci numbers were corrected to control and are shown in absolute scale (A) and normalized to 1h post-irradiation time points (B). Error bars indicate the standard deviation for a single experiment (n=1).

particle and X-ray external emission experiments appear to be independent of dose. There is suggestion of a difference in ^{223}Ra exposures, but this is not significant due to the limited repeats.

Figure 4.11 shows the comparison between the IF results from ^{223}Ra exposures of both PC-3 and RWPE cells. The normal epithelial cells have lower levels of DNA damage across all doses, showing a lower initial sensitivity to damage than the prostate metastatic cells (Figure 4.11A). The rate of DNA repair following ^{223}Ra exposure appears similar for both cell lines at doses of 0.5 and 1 Gy (Figure 4.11B). While there appear to be some differences at 2 Gy, again this is not statistically significant.

We then compared the treatment effects on DNA damage from 2 Gy doses delivered by external α-particle irradiations and ^{223}Ra *in vitro* exposures for these two cell lines. This comparison is

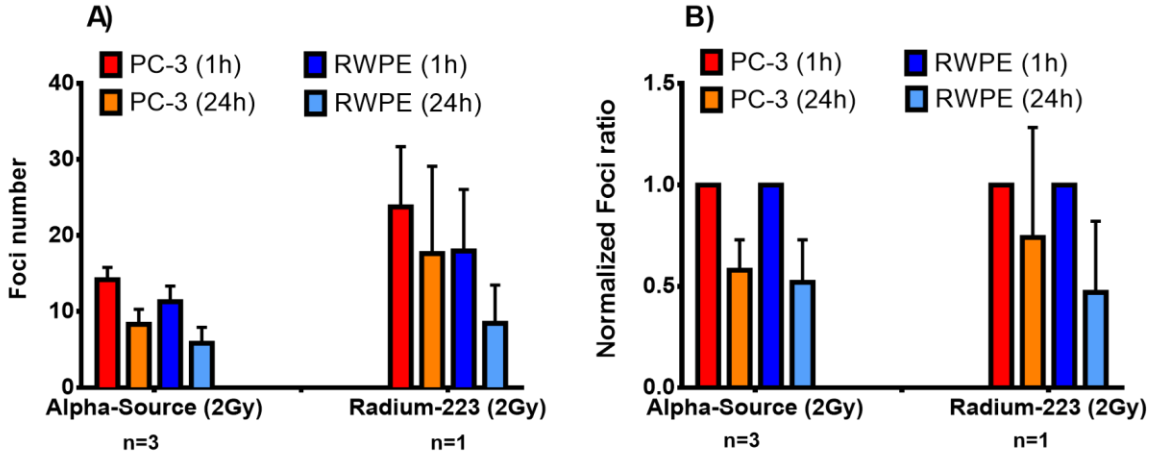

Figure 4.12 - 53BP1foci data in PC-3 and RWPE cells exposed to a 2 Gy radiation dose from an external source of α-particles and ^{223}Ra α-particle internal exposures (24h). Cells were fixed after post-irradiation incubation time points of 1 and 24h for n replicate experiments. Foci numbers were corrected to control and are shown in absolute scale (A) and normalized to 1h post-irradiation incubation time points (B). Error bars indicate the standard error from the mean for replicated experiments (n=3) or the standard deviation for a single experiment (n=1).

represented in Figure 4.12, showing a significantly higher number of foci for both cell lines treated with ^{223}Ra, especially for 1h recovery time periods.

When we analyse the foci ratios at 24h recovery normalized to 1h recovery results, we notice that the repair rate in 24h is similar for RWPE cells regardless of the irradiation method (Figure 4.12B). On the other hand, the PC-3 show a higher DNA damage repair rate for α-particle external irradiations, as previously shown. This suggests that PC-3 cells repair less efficiently from ^{223}Ra induced DNA damage when compared with RWPE cells, although there is insufficient experimental data to fully support this (n=1).

4.3.3.3 ^{223}Ra solution toxicity

The effect of the ^{223}Ra treatment exposure time t_{exp} on PC-3 cell dose response curves was explored. These results are shown in Figure 4.13, showing the SF from clonogenic assays on PC-3 cell exposed to ^{223}Ra for 6h and 24h t_{exp}. For both exposure times, the calculated delivered doses were the same and we used Xofigo vials with similar activities (around 2 MBq). The results from these two approaches are significantly different, showing considerably greater survival for the longer exposure time. For example, for a 0.5 Gy dose, the SF was over 10% for t_{exp} =24h, as opposed to being lower than 0.2% when t_{exp} =6h. Part of the difference in results can be due to the difference of treatment dose rates, but not only. There is a higher cell recovery level for longer exposures times, for the same

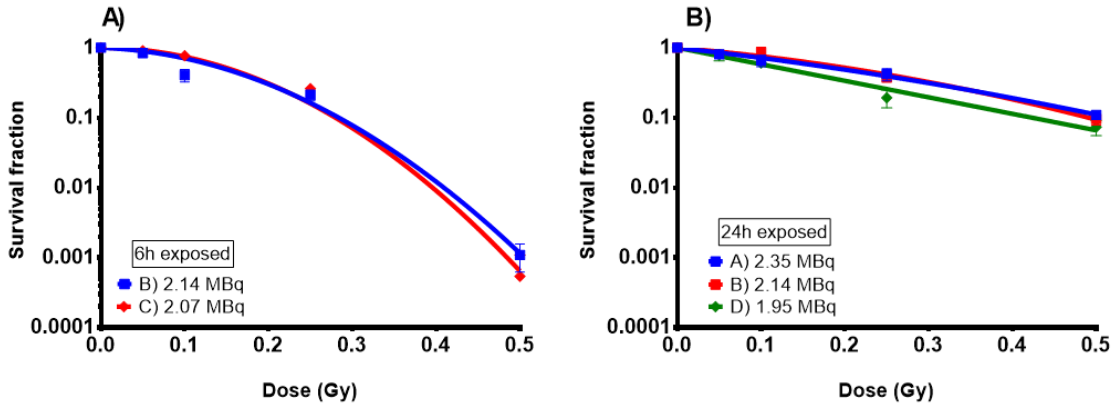

Figure 4.13 - Clonogenic survival data on PC-3 cells exposed to ^{223}Ra for 6h (A) and 24h (B) using vials with similar activities. Error bars indicate the standard deviation from experimental data. Curve lines represent the linear quadratic model fits to the experimental data with a single experimental replicate for each vial (n=1).

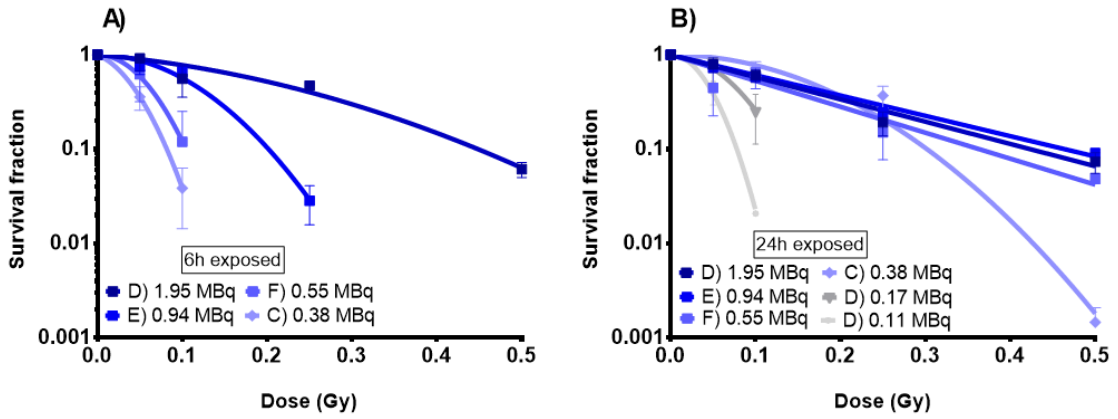

Figure 4.14 - Clonogenic survival data on PC-3 cells exposed to ^{223}Ra for t_{exp} = 6h (A) and for t_{exp} = 24h (B) using vials with different activities. Error bars indicate the standard deviation from experimental data. The error bars represent the standard deviation of the SF obtained from individual experimental replicates (n=1). Curve lines represent the linear quadratic model fits to the experimental data.

dose, but the cell kill effects of long ^{223}Ra exposures are still higher than externally α-source irradiations. These data were reproduced across a number of experimental replicates using different Xofigo vials, suggesting this is not an isolated experimental error. Instead, this suggests that there may be some effect causing toxicity in these solutions in addition to radiation effects.

Additionally, we also explored the effect of the volume of Xofigo used for treatment, which was higher for lower vial activities (Act_{vial}). This is shown in Figure 4.14, demonstrating that the dose response in PC-3 cells appears to be consistent for longer irradiations (t_{exp} =24h) and high initial activities (Act_{vial} >0.55 MBq). For shorter irradiation exposures (t_{exp} =1h) or Act_{vial} <0.55 MBq, the dose responses are considerably different.

This is related to the volumes of Xofigo added to each treatment solution. As the added volume increases (either due to shorter delivery times or reduced Act_{vial}), the cells appear to show significantly greater sensitivity to a given dose.

We summarized the list of vials and corresponding ^{223}Ra activities used for the clonogenic experiments in Table 4.3.

In order to further study the increasing cell sensitivity to low activity Xofigo vials, we analysed the effect of the Xofigo treatment volume V_{Xofigo} on cell survival. The parameter V_{Xofigo} is directly related to the vial activity used. To deliver the same radiation dose, as the vial activity decreases, the treatment volume increases (section 4.2.4.3).

The analysis results are shown in Figure 4.15, displaying the SF of PC-3 cells to the treatment volume/dose ratios ($\frac{V_{Xofigo}}{D_{treat}}$). The curve fits represent an exponential fit between SF and the volume dose ratios. For all different treatment dose and exposure times, the cell survival decreases when the Xofigo volume/dose increases.

These results are also summarized in Table 4.4, showing the corresponding R_{10} fit estimates for each condition. Additionally, we also show each minimum observed treatment volume/dose ratio that resulted in a 0% SF. These results demonstrate that there is a Xofigo volume effect on cell survival that is not only radiation dose dependent.

Table 4.3 - List of Xofigo vials with corresponding activity concentrations for clonogenic experiments.

Vial	Activity (MBq)
A	2.35
B	2.14
C	2.07; 0.38
D	1.95; 0.17; 0.11
E	0.94
F	0.55

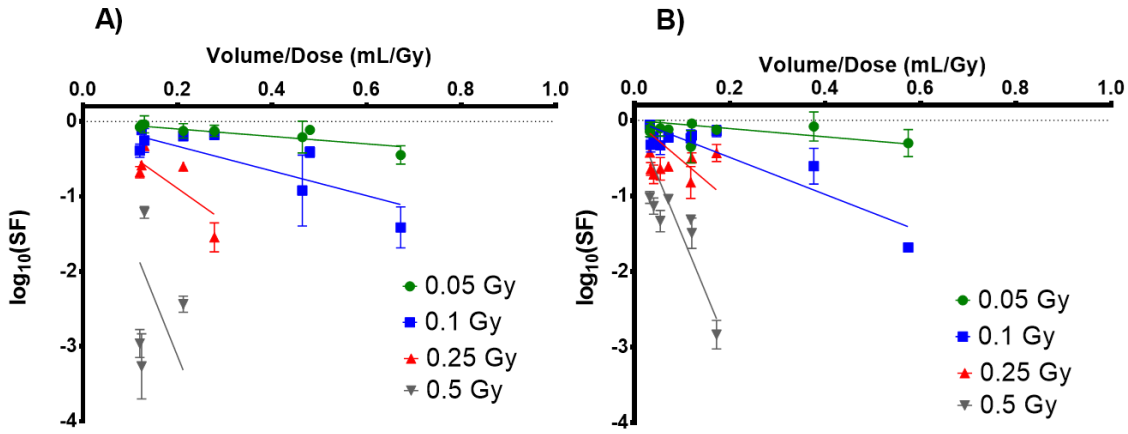

Figure 4.15 – Effect of the Xofigo treatment volume/dose ratios on the survival fraction (SF) of PC-3 cells. Here the SF are displayed as logarithm values. The cells were exposed to α-particle doses of 0.05, 0.1, 0.25 and 0.5 Gy calculated from ^{223}Ra treatment exposures for t_{exp} = 6h (A) and t_{exp} = 24h (B). The lines represent an exponential fit to the experimental volume/dose surviving fraction results obtained for the different radiation dose and exposure conditions. There were no surviving colonies for volume/dose ratios higher than 1.47 mL/Gy across all dose conditions when t_{exp} = 6h. The error bars represent the standard deviation of the $\log_{10}$(SF) obtained from technical replicates from within single independent experiments

Table 4.4 – Decimal reduction dose (R_{10}) value estimates from the curve fits to the surviving fraction results shown in Figure 4.15. The R_{10} estimates are shown for each condition: treatment dose (D_{treat}) and exposure time (t_{exp}). The decimal reduction volume (V_{10}) and the R^2 for each curve fit is also shown. The R^2 values not displayed result from very poor goodness of fit ($R^2 < 0.1$). The observed minimum volume/dose ratios that resulted in 0% cell survival ($R_{SF=0}$) are also displayed.

	t_{exp} = 6h				t_{exp} = 24h			
D_{treat} (Gy)	R_{10} ± SD (mL/Gy)	V_{10} ± SD (mL)	R^2	$R_{SF=0}$ (mL/Gy)	R_{10} ± SD (mL/Gy)	V_{10} ± SD (mL)	R^2	$R_{SF=0}$ (mL/Gy)
0.05	2.01 ± 0.26	0.10 ± 0.01	0.75	1.47	1.84 ± 0.59	0.09 ± 0.03	---	---
0.1	0.61 ± 0.09	0.06 ± 0.01	0.71	1.47	0.41 ± 0.05	0.04 ± 0.01	0.81	---
0.25	0.22 ± 0.03	0.05 ± 0.01	0.66	0.46	0.19 ± 0.05	0.05 ± 0.01	---	0.38
0.5	0.06 ± 0.02	0.03 ± 0.01	---	0.28	0.06 ± 0.01	0.03 ± 0.01	0.49	0.38

4.4 Discussion

In this chapter we studied the effects of α-particles in cells through *in vitro* clonogenic and immunofluorescent assays. We first validated the external α-particle source dosimetry, calculations of which are shown in chapter 2 (sections 2.2.4.3 and 2.3.3.4), and then compared the cell effects of

externally emitted α-particles with X-rays. Additionally, we were also able to compare these results with internal α-particle irradiation methods, through ^{223}Ra solution internal cell exposures.

The clonogenic assay results obtained from PC-3 cells exposed to the α-source were shown to be similar to those from literature, as demonstrated by Figure 4.3. The linear quadratic curve regression from the open source irradiation was very close to that found in the literature, with a fitting R^2=0.992. This further demonstrates the accuracy of chapter 2 results, from the cell target geometry and irradiation Monte-Carlo simulations which provided our estimate of the α-source dose rate.

When comparing the clonogenic results from the α-source with and without the collimator C50, we observe that the linear quadratic curves are very similar. As mentioned in section 4.3.1, the radiosensitivity parameters of the curve equation differ by less than 3%, which validates the collimator analysis and dosimetry calculations done in chapter 3. The small differences between this work and the literature cell survival results are likely related to minor experimental differences, such as cell culture conditions, cell passage, etc. The exact replication of results from different research groups within the same experimental conditions is known to be difficult to achieve.

After comparing the X-ray and α-particle radiation dose response results from PC-3, NT01 and RWPE cells, we can see that the cancer cells used are more sensitive to both radiation sources than the normal epithelial cells (Figure 4.4 and Figure 4.5). This is important for radiation treatments, as normal cells should have the least amount of cell kill and cell damage compared to the targeted cancer cells. However, the RWPE cells also show the highest α-particle $RBE_{SF=10\%}$ (Table 4.2). This suggests that the cell repair efficiency difference between radiation sources is bigger for RWPE, when compared to the other two cell lines.

Regarding PC-3 DNA damage, we notice that the number of foci is higher with X-rays after 1h of treatment, comparing to α-particle irradiations (Figure 4.6A). This occurs for 0.5, 1 and 2 Gy delivered doses. For the samples fixed after 24h of recovery we see the inverse happening, with higher number of counted foci for cells irradiated with α-particles. It was also observed a difference in foci characteristics, such as higher intensity and size when cells were exposed to α-particles. It would be relevant, as future work, to study the difference in foci characteristics in PC-3 cells when exposing cells to different radiation particles.

The reason for the initial higher number of foci in X-ray irradiated cells is related to the number of radiation particles travelling through a nucleus for a particular dose. In this case, for the same delivered dose, the number of X-rays hitting the cell nucleus is higher than the number of α-particles hitting it, due to the difference of LET from both radiations. Therefore, a greater fraction of the nucleus area will be hit by X-rays in comparison with α-particles, resulting in higher chances of multiple distinct foci formation. But after 24h of treatment, the X-ray exposed cells have faster and more efficient DNA

damage repair mechanisms, resulting in a lower number of foci counted per nucleus, in comparison with α-particle irradiated cells. This is also confirmed in Figure 4.6B, as the 24h recovery foci ratio is significantly higher for PC-3 cells exposed to α-particles, especially for a 2 Gy dose.

Looking at α-particle effects on DNA damage, we compared the IF assay results from PC-3 and RWPE cells after 1h and 24h of recovery post-treatment. For both cells and recovery times, the average number of foci was not significantly different (Figure 4.7A). The 24h recovery foci ratios were very similar as well (Figure 4.7B). This is an extrapolation from two recovery times analysed only. It would be useful for future work to analyse longer treatment recovery periods.

When investigating the effects of ^{223}Ra on cells using Xofigo, we noticed that all cell lines showed greater sensitivity to doses from ^{223}Ra exposres in comparison with external X-rays and α-particle irradiations. This is shown in Figure 4.8 and Figure 4.9, with lower SF at the same calculated doses for all cells when exposed to ^{223}Ra. This is important as it demonstrates that a uniform distribution of ^{223}Ra within the cell treatment solution might not be an accurate model for these *in vitro* experiments, assuming cell kill effects arise from α-particle damage only.

This different response from ^{223}Ra and external α-particle exposures is further proved with immunofluorescence assays (Figure 4.10). In PC-3 cells, higher foci levels are seen for ^{223}Ra exposures for 1h and 24h recovery time and all dose points. This may indicate greater levels of initial damage or altered levels of DNA repair in these exposures. However, the uncertainties in the foci yields following ^{223}Ra exposures are too great to draw definite conclusions in this area. Additional experimental replicates and future studies will help us to better understand this effect, leading to more meaningful conclusions too. Possible future work that would add to these results could be to simulate and calculate the number of α-particles which stop inside the cells for Xofigo and external α-particle irradiations.

If comparing PC-3 and RWPE ^{223}Ra effects on DSB DNA damage, we see that the number of foci is higher for PC-3 cells, but the 24h repair rate is similar (Figure 4.11). The only exception is in the 2 Gy dose point. When comparing the 2Gy results from RWPE cells exposed to ^{223}Ra and externally emitted α-particles, it is possible to see a similar DNA damage repair rate after 24h in both cases. This is different for PC-3 cells, which showed a significantly lower DNA damage repair rate when exposed to externally emitted α-particles in comparison to ^{223}Ra for the same 2 Gy dose (Figure 4.12). However, future experimental work is needed again to fully understand the DNA damage repair rate between the two cell lines and radiation treatment methods since the DNA damage results from ^{223}Ra exposures are based on one experimental repeat only. For instance, experimenting with different dose rates (leading to higher variation of exposure times) and analyse consequent cell dose rate effects.

However, it is important to take into account that the irradiation exposure times are significantly different for external α-source irradiations and internal α-particle emissions with ^{223}Ra. This treatment

exposure difference will affect the cells recovery time. For example, for immunofluorescense experiments, we can expect higher levels of DSB repair for the same doses when doing ^{223}Ra exposures, due to the prolonged treatment time (6 or 24 hours) compared to external α-particle emissions (a few minutes). Future work would be fundamental in order to understand the level of DNA damage repair during treatment exposure times with ^{223}Ra.

We further explored the high toxicity effect of Xofigo solution in PC-3 cells. This analysis is shown in section 4.3.3.3. When using vials with considerably different activities for clonogenic assays (Act_{vial} ranging from 1.98 to 0.11 MBq), we noticed that for the same treatment dose, there was significantly higher cell killing as Act_{vial} decreases. This is noticeable for all Act_{vial} results when t_{exp} =6h and for Act_{vial} below 0.55 MBq for t_{exp} =24h (Figure 4.14). For example, the resulting SF of PC-3 cells exposed to 0.1 Gy for t_{exp} =24h is 0.61 ± 0.09 when Act_{vial} = 1.95 MBq, whereas SF = 0.02 ± 0.00 when Act_{vial} = 0.11 MBq. This shows a 30-fold reduction in cell killing for the lower activity vial, despite having both treatments deliver the same calculated dose.

There is additional evidence of Xofigo treatment volume toxicity on PC-3 cells as we explore the treatment volume analysis (Figure 4.15 and Table 4.4). Here we analysed the relation between PC-3 cell SF and treatment volume/dose ratios (inversely proportional to activity). The curve fits were based on the first-order exponential volume/dose equation (section 4.2.4.4). The goodness of the fit, extrapolated from the least square fitting R^2 values, are not good enough to fully understand the relation between cell's SF and the volume/dose ratio. However, there is clearly a decreasing trend in cell survival as we increase the treatment volume/dose ratio across all treatment dose and exposure time conditions (Figure 4.15).

There were even treatment volumes that led to 0% cell survival even at doses which led to significant survival when V_{Xofigo} was lower. This is demonstrated by the observed minimum volume/dose ratios ($R_{SF=0}$) displayed in Table 4.4. Since we fixed D_{treat} and t_{exp}, we can extrapolate the treatment volumes where this occurred for each experimental condition. As an example, for D_{treat} = 0.05 Gy and t_{exp} = 6h, PC-3 cells had a SF = 0.84 ± 0.02 for V_{Xofigo} = 6.5 x 10 µL in comparison to SF = 0.00 ± 0.00 for V_{Xofigo} = 73.7 x 10 µL. The differences in treatment volumes were due to the different vial activities (1.95 MBq and 0.17 MBq, respectively).

The effect of radiation treatment dose on cells is evident in this analysis too. As D_{treat} increases, the negative linear curve fit slope increases as well. This is shown in Table 4.4, which displays the R_{10} value estimates that decrease for increasing doses when t_{exp} is fixed. Since the curve slope is inversely proportional to R_{10}, decreasing R_{10} leads to increasing negative curve slopes (equation 4.9). A similar effect can be observed for decreasing treatment exposure times, although standard deviations and

goodness of the fit do not allow for confident conclusions when comparing results from the same D_{treat} with different t_{exp}.

In summary, these last results have demonstrated that PC-3 cell survival from Xofigo treatments might not only be dependent on the ^{223}Ra radiation calculated dose. This is significant as it leads to two possible conclusions. The first is that the assumption of a uniform distribution of ^{223}Ra isotopes in a cell environment, simulated as *in vitro* experiments, might not be accurate. The ^{223}Ra dosimetry calculations in this work are based on that uniformity assumption and on consequent randomly distributed α-particle emissions across a cell treatment volume (section 4.2.4.2). These results suggest that the dosimetric model used to calculate Xofigo treatment doses can be inaccurate.

The second possible conclusion is that there is a non-radiation toxicity effect from Xofigo prepared solutions on PC-3 cells. This hypothesis has been suggested throughout this chapter from multiple analysis, such as clonogenic and immunofluorescent assays comparing external α-particle irradiations with ^{223}Ra exposures (sections 4.3.3.1 and 4.3.3.2). It was shown that both methods led to different cell survival, DSB DNA damage and DSB recovery. The results from vial activity and related treatment volume/dose effect on cells (section 4.3.3.3) also suggest the possibility of a non-radiation toxicity effect.

Either one or both possibilities are true, which makes it important to continue research in this area, especially as we are using drug preparations such as Xofigo solutions. Future studies with chemical analysis on Xofigo would be helpful to complement this discussion. Additionally, using vials with extremely low activities ($Act_{vial} < 0.01\ MBq$) for further *in vitro* experiments would be equally useful to complement the results presented in this chapter.

CHAPTER 5 : MECHANISTIC MODELLING OF RADIUM-223 TREATMENT OF BONE METASTASES

This chapter represents an extended version of the published manuscript "*Mechanistic modelling of Radium-223 treatment of bone metastases*" International Journal of Radiation Oncology, Biology, Physics (2019). [141]

5.1 Introduction

As previously mentioned, ^{223}Ra is a calcium-mimetic and complexes with hydroxyapatite crystals in osteoblastic bone metastases. This allows ^{223}Ra to target bone metastatic tissues, as they show high cell activity and bone turnover.

^{223}Ra has a physical half-life of 11.4 days and an effective biological half-life of 8.2 days. Each ^{223}Ra decay results in the emission of 4 α-particles in the primary decay chain. Targeted radionuclide therapies using ^{223}Ra became more available during the last years. It has been widely accepted that α-emitting radionuclide therapies, such as ^{223}Ra, are a promising treatment for small tumours. For instance, ^{223}Ra therapy has demonstrated positive results in bone metastatic prostate cancer, leading to prolonged time to the first SSE (5.8 months) and better overall survival (3.6 months) for CRPC treated patients.[43,142,143] Nevertheless, relatively few studies to date have fully explored ^{223}Ra uptake kinetics and their impact on the dosimetry of such therapies. [42,144] This is also important as new α-particle targeted approaches are starting to be utilized clinically. [145–147]

The application of radiobiological models to better understand the mechanisms of action of high LET radiation has already demonstrated its value in other areas of radiation therapy. These models are an essential component of techniques to maximize benefits and reduce side effects for targeted radiotherapy.[148]

The analysis presented in this chapter aims to simulate different ^{223}Ra treatment scenarios and calculate the time necessary for a simulated patient group to reach the first SSE, to compare with clinical data and provide insight into the underlying mechanisms of ^{223}Ra uptake.

5.2 Materials and methods

5.2.1 Tumour growth

5.2.1.1 The Gompertz model

The Gompertz growth model was chosen to simulate bone metastatic site growth for the work presented in this chapter. This is an established growth model that describes an initial rapid growth phase which later slows, reflecting factors such as competition for nutrients, limited space availability, etc. It has been shown to have one of the best fits to experimental data for solid tumours [149–151]. The Gompertz equation is:

$$N(t) = K \times \left(\frac{N_0}{K}\right)^{e^{-A_{growth} \times t}} \qquad 5.1$$

In the context of a tumour growth, N_0 is the initial number of cells, K is the maximum number of cells the tumour can have and A_{growth} determines the tumour growth rate. The Gompertz growth rate equation of our tumour model is then given by the following expression:

$$\frac{dN(t)}{dt} = A_{growth} \times N(t) \times ln\left(\frac{K}{N(t)}\right) \qquad 5.2$$

5.2.1.2 Choosing Gompertz growth parameters

There is currently no validated model for bone metastatic growth. However, there are different tumour growth models published using Gompertz growth kinetics. Based on these publications, we estimated Gompertz model parameters and converted these as standard expressions in terms of A_{growth} and K. A list of published data and corresponding parameters is presented in Table 5.1.

Table 5.1 - Gompertz tumour growth parameters from different tumour models in literature and experimental data. SE represents the standard error from the averaged values (shown when available).

Model	Tumour type	Parameter	Averaged value	SE
A) Pitchaimani, M., Ori, G. Eakin, Tim (2014) [152]	Osteosarcoma	A_{growth}	0.159 (day^{-1})	
		K	2.66 x 10^9	
B) Lamont, C., Beheshti, A., Tracz, A., Ebos, J. M. L., & Hlatky, L. (2014) [153]	Lung	A_{growth}	0.0792 (day^{-1})	0.0336 (day^{-1})
		K	7.34 x 10^9	3.63 x 10^9
C) Lamont, C., Beheshti, A., Tracz, A., Ebos, J. M. L., & Hlatky, L. (2014) [153]	Breast	A_{growth}	0.0719 (day^{-1})	0.0190 (day^{-1})
		K	1.59 x 10^{10}	5.12 x 10^9
D) Norton, L. (1988) [154]	Breast	A_{growth}	0.055 (day^{-1})	
		K	3.1 x 10^{12}	
E) Iwata, K., Kawasaki, K., & Shigesada, N. (2000) [155]	Liver metastasis	A_{growth}	0.00286 (day^{-1})	
		K	7.3 x 10^{10}	
F) Experimental tumour growth of PC-3 in mice [156]	Bone metastasis	A_{growth}	0.0129 (day^{-1})	0.0012 (day^{-1})
		K	3.84 x 10^{10}	

In addition to the published datasets models A-E shown in Table 5.1, we also calculated the Gompertz growth kinetics based on mice xenograft experiments performed in our laboratory (model F). For these experiments we used bone metastatic PC-3 cells and implanted them in mice. From the tumour volume growth results, we extrapolated the growth parameter A_{growth} by fitting equation 5.1 to growth data (Figure 5.1).

For the least square fit of the xenograft data, we set the maximum metastatic volume to be equal to the volume of a sphere whose diameter matched the maximum metastasis diameter reported in a clinical study (40 mm). [157] The maximum cell number, K, was then calculated assuming spherical tumour cells of radius 5 μm, packed with a cell volume occupation fraction of 60%, corresponding approximately to a random close packing.

To test the plausibility of the parameter sets from the literature and experimental data, we calculated metastatic growth predictions in the absence of radiation. We simulated growth for two different starting volumes, N_0 = 0.1% K and N_0 = 10% K, corresponding to undetectable and

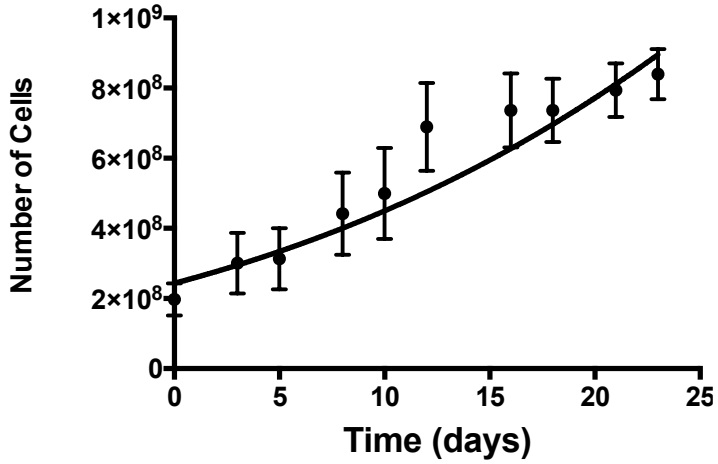

Figure 5.1 - Xenograft tumour growth data from mice implanted with PC-3 metastatic prostate cancer cells. Data points show median tumour volumes, as number of cells, of 11 mice. Error bars represent the standard deviation. The curve corresponds to a Gompertz growth model fit to the experimental data with A_{growth} = 0.0129 ± 0.0012 day^{-1}, N_0=2.47 x 10^8 ± 2.7 x 10^7 cells and K= 3.84 x 10^{10} cells. The parameter uncertainties represent the standard error from the Gompertz equation fit. The maximum tumour volume, K, was constrained based on the maximum diameter size found from a bone metastasis (40 mm).[157]

detectable metastatic tumours respectively. The analysis of these results determined which model is more suitable for the bone metastatic growth considered in this chapter.

The resulting curves comparing tumour growth curves can be seen in Figure 5.2. The growth kinetics for published primary tumour models showed that for both initial tumour volumes, an untreated patient would reach 90% of the maximum volume within less than 2.5 months. Consequently, this tumour growth appears to be too rapid when compared to the observed progression of untreated metastases (Figure 5.2A-D). By contrast, a model based on liver metastasis data was shown to grow too slowly, taking three or more years to progress (Figure 5.2E).

The most suitable model appears to be that based on bone metastasis models in mice. With both initial volumes N_0, an untreated metastasis would reach reach 90% of the maximum volume within 10 and 7 months, respectively. Therefore, we have chosen this growth model for subsequent models of ^{223}Ra treatment, giving Gompertz parameters of A_{growth} =0.0129 day^{-1} and K=3.84x10^{10} cells.

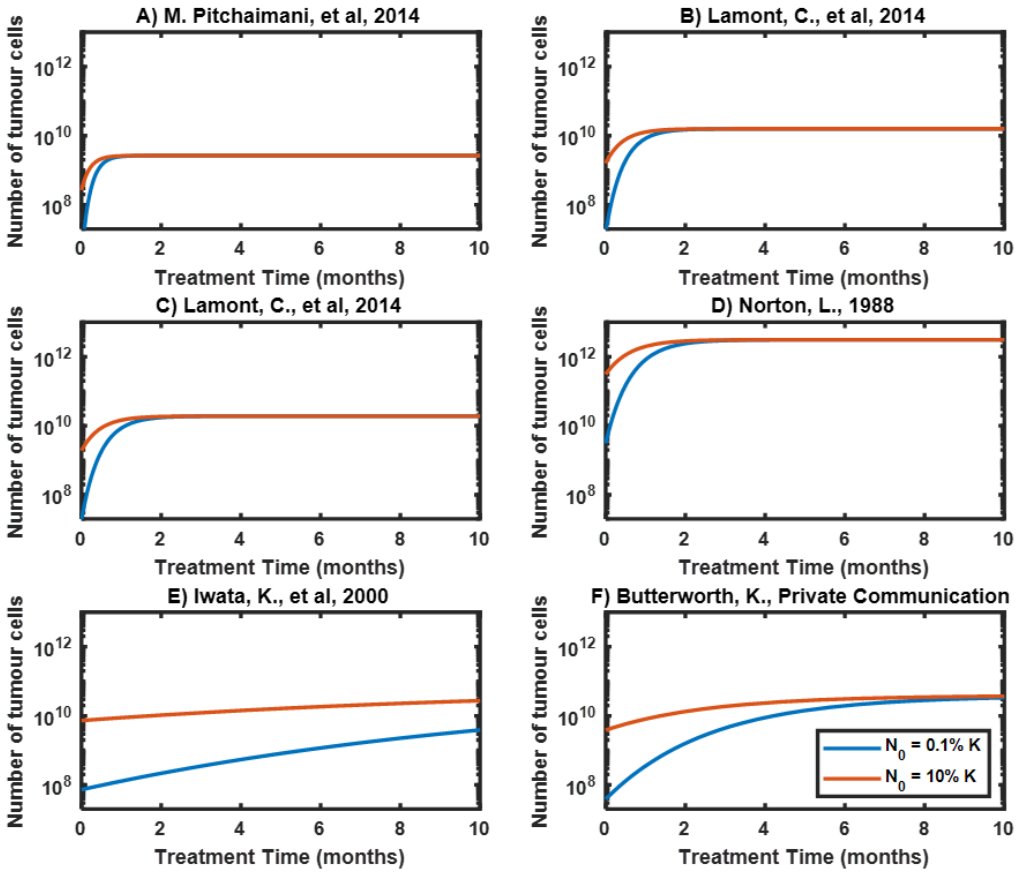

Figure 5.2 - Tumour growth curves for the Gompertz models A to F, with initial starting volumes of 0.1% and 10% of the maximum tumour volume (K).

5.2.2 Modelling the effect of ^{223}Ra on tumour growth

5.2.2.1 Dosimetric effect of ^{223}Ra treatment in bone tissue

When assessing radiation dose effects from radiopharmaceuticals in target tissues it is important to take into account the mean absorbed dose of radiation. This will be significantly important in modelling the radiation effect on tumour growth. Based on literature, we know that the dose per delivered activity, D_{act}, of this ^{223}Ra treatment in bone is 0.76 Gy/MBq. This is based on estimates of deposited dose from SPECT imaging of patients treated with ^{223}Ra [158,159]. We can then calculate the absorbed dose in the bone endosteum for a 70 kg patient, with a typical treatment schedule of 55 kBq/kg, as:

$$D_{act} \times A_0 = 0.76 \left(\frac{Gy}{MBq}\right) \times \left[0.055 \left(\frac{MBq}{kg}\right) \times 70\ (kg)\right] = 2.93\ Gy \qquad 5.3$$

where A_0 is the initial activity of a single ^{223}Ra treatment fraction injection.

Since the dose deposited in bone metastasis is unclear and may vary significantly for different patients and tissue locations, we assumed the bone metastatic mean absorbed dose to be the same as the absorbed dose for the bone endosteum tissue, as an approximation.

The instantaneous dose rate, $\dot{D}$, can then be calculated assuming an exponential decay of the primary ^{223}Ra atoms, as their half-life is significantly longer than that of the daughter isotopes. Thus, by assuming that the dose rate is directly proportional to the activity, the instantaneous dose-rate can be specified as:

$$\dot{D}(t) = \dot{D}_0 \times e^{-\lambda_e t} \qquad 5.4$$

where λ_e is the ^{223}Ra effective decay rate calculated from the ^{223}Ra effective half-life ($T_e = 8.2$ days [42]), and $\dot{D}_0$ is the initial dose rate. The total dose delivered by a single treatment can then be calculated as:

$$D = \int_0^\infty \dot{D}(t)\, dt = \int_0^\infty \dot{D}_0 \times e^{-\lambda_e t}\, dt = \frac{\dot{D}_0}{\lambda_e} \qquad 5.5$$

For a treatment delivering a dose $D = 2.93$ Gy with an effective decay rate of 3.52×10^{-3} h^{-1}, $\dot{D}_0$ can be calculated to be 1.03×10^{-2} Gy/h. As the ^{223}Ra treatment is typically delivered as a series of 6 fractions, the dose rate from each individual fraction is summed to give the total dose rate at any given time during the therapy.

5.2.2.2 Radiation effect on tumour growth

The radiation effect on tumour survival was evaluated for the ^{223}Ra treatment using the linear-quadratic model (section 1.4.2), based on literature data describing α-particle effects on *in vitro* experiments using bone metastatic cells derived from a prostate cancer patient (PC-3, ATCC, Manassas). Here, the radiosensitivity parameter of cells to α-particles (α_1) was found to be 1.82 Gy^{-1}. [103] As cell death results mainly from single α-particle interaction events, the relationship between the surviving fraction (SF) and the cell absorbed dose (D) is approximate to a log-linear model. [12] Thus, the survival fraction curve, which resulted from clonogenic assays using an external α-source, followed the linear equation parameters:

$$SF_{alpha}(D) = e^{-\alpha_1 D} \qquad 5.6$$

If there is no tumour growth, the radiation effect on the tumour volume is described by:

$$\Delta N(t) = -N(t) \times (1 - e^{-\alpha_1 \dot{D} \Delta t}) \qquad 5.7$$

where $N(t)$ is the number of cells at the time *t*. By applying the Taylor expansion method for small timesteps Δt, we can simplify the equation to:

$$\frac{dN(t)}{dt} = -N(t) \times \alpha_1 \times \dot{D}(t) \qquad 5.8$$

where $\dot{D}(t)$ is the absorbed dose rate in bone at a given time *t*. Taking into account the Gompertz growth behaviour of the tumour metastasis, together with the radiation effect, we can describe the ^{223}Ra treatment model on bone metastasis growth as:

$$\frac{dN(t)}{dt} = A_{growth} \times N(t) \times ln\left(\frac{K}{N(t)}\right) - N(t) \times \alpha_1 \times \dot{D}(t) \qquad 5.9$$

5.2.2.3 ^{223}Ra treatment exposure scenarios

The model described by equations 5.8 and 5.9 illustrate a uniform effect, which assumes that all cells are equally affected by the radiation dose. This assumption might not be accurate in practice, something that was raised as a possibility during the discussion in chapter 4 (section 4.4). In order to account for this possibly, we have also tested two other radiation distribution scenarios, both assuming that only a sub-population of cells, $N_p(t)$, are affected by the radiation dose.

The first scenario is an outer layer effect. In this scenario only the surface of the metastatic volume is exposed to radiation. This means that the number of treated cells, $N_p(t)$, is modelled by the number of cells present in a layer at the surface of the metastases, described by a thickness layer (T_{layer}). In this work, $N_p(t)$ was calculated assuming a cell radius of 5 μm in a tumour sphere with a cell volume occupation fraction of 60%. This approach is similar to the one used when calculating the maximum number of cells, K (section 5.2.1.2).

The second model scenario is a constant volume exposure. In this case $N_p(t)$ is constant, regardless of the tumour growth stage, except when $N(t) < N_{constant}$. This model scenario is described by the equation system:

$$N_p(t) = \begin{cases} N(t) & , N(t) < N_{constant} \\ N_{constant} & , N(t) \geq N_{constant} \end{cases} \qquad 5.10$$

For both of these scenarios, the differential equation that describes the tumour growth is then:

$$\frac{dN(t)}{dt} = A_{growth} \times N(t) \times ln\left(\frac{K}{N(t)}\right) - N_p(t) \times \alpha_1 \times \dot{D}(t) \qquad 5.11$$

Figure 5.3 shows a schematic representation of all the treatment exposure scenarios considered at different stages of tumour growth.

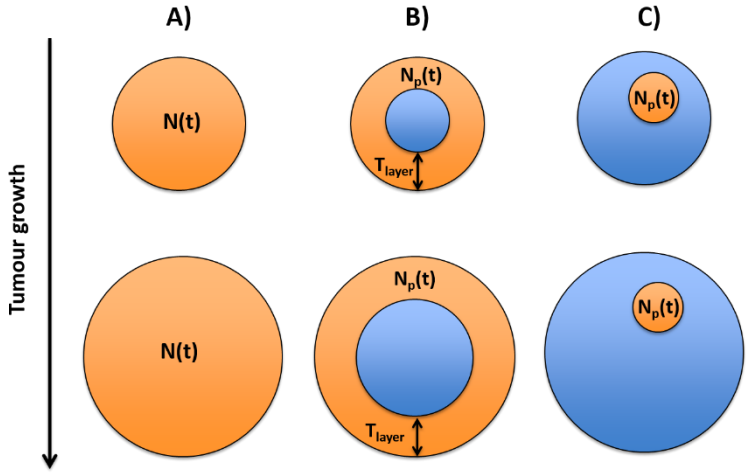

Figure 5.3 - Schematic representation of the radiation exposed (orange) and non-exposed (blue) tumour volumes for the uniform (A), outer layer (B) and constant volume (C) exposure scenarios.

These three model scenarios were then solved using Matlab 2016b (Mathworks, Inc., Natck, MA) for different assumptions of initial tumour volume and radiotherapy treatment delivery. For the uniform effect model we initially assumed a fixed initial dose rate $\dot{D}_0$ of 1.03×10^{-2} Gy/h, corresponding to the dose rate calculated for bone endosteum (section 5.2.2.1). In addition, we also optimized the differential equation parameters for the three model scenarios using a least-squares fit, given the placebo and treatment data from clinical observations described below. The variable parameters were $\dot{D}_0$ for the uniform effect, T_{layer} for the outer layer effect and $N_{constant}$ for the constant volume effect. The resulting best fit parameters, together with the corresponding uncertainties, were calculated from the least-squares fit function in Matlab.

The resulting analysis allowed us to predict the tumour growth delays for each of the assumed exposure scenarios, which can then be compared to clinical observations.

5.2.3 Clinical trial data

To provide a test for this model, published results for time until 1st SSE were obtained from the ALSYMPCA trial for placebo and ^{223}Ra treated groups. [43] Based on the assumption that skeletal events resulted from a particular level of metastatic burden, we assumed that skeletal events occurred when $N(t)$ reaches 80% of the maximum number of cells (K). The ratio between the number of cells that correspond to an SSE (N_{Met}) and the maximum number of cells (K) is here defined as S_{Met}:

$$S_{Met} = \frac{N_{Met}}{K} = 0.8 \qquad 5.12$$

This value was chosen empirically, based on biological and mathematical rationale. Biologically, it is plausible that S_{Met} should be close to 1, or in other words N_{Met} being close to K, as this represents the stage when the metastases are in significant competition for resources with normal tissue. This stage would be expected to be associated with significant symptomatic events. This is also mathematically reasonable, as if S_{Met} is very small, the metastatic growth rate will be too rapid, while if S_{Met} is very close to 1, no metastatic growth would be seen. We could then simulate the growth of metastases from different initial volumes to determine the time taken for a skeletal event to occur either with or without ^{223}Ra treatment.

Assuming that the control and treated populations were identical, a 'virtual patient population' was generated with a range of different initial tumour volumes which reproduced the observed time to failure in the control, untreated population, representing 123 first SSE in 307 patients. We then simulated the effects of ^{223}Ra treatment in this population using each of the radiation models, to predict responses in the treated population.

Specifically, for a placebo patient who failed at a given time $t_{placebo}$, at this timepoint their metastatic volume must be N_{Met}, corresponding to the first SSE occurrence. By substituting these values into equation 5.1, we can calculate a patient specific initial disease volume, N_0^p. We then model how this patient would have responded to treatment by simulating the growth of this tumour using the kinetics described in equation 5.11 for 6 cycles of ^{223}Ra treatment, beginning with an initial volume of N_0^p at t=0. This equation was solved using a differential equation solver method in Matlab (ODE45) and simulations were continued until the patient disease burden reached N_{Met}. By calculating this time for each patient in the population, a new simulated Kaplan-Meier curve for the treated population could be generated for each set of model assumptions. These were then compared to the actual clinical data of treated populations to evaluate how well they reproduced the treatment response. This comparison was based on the fitting quality parameter R^2 between their predicted time to SSE and the corresponding clinical observations.

5.2.4 Sensitivity analysis to the tumour growth model parameters

In order to understand the impact of tumour growth parameters on SSE delay, we analysed how varying A_{growth} and S_{Met} influenced time to SSE of untreated tumours, beginning from a single cell.

We also conducted an extensive sensitivity analysis of the influence of the growth parameters K, A_{growth}, and S_{Met} on the best fit variables for all the three tumour models analysed ($\dot{D}_0$ for the uniform effect, T_{layer} for the outer layer effect and $N_{constant}$ for the constant volume effect). In addition, we

report the effect of varying A_{growth}, S_{Met} and $\dot{D}_0$ on the quality of the fit (R^2) from each model's Kaplan-Meier curve to the ALSYMPCA treatment data.

For simplicity, during the analysis of the constant volume model, we used the normalization parameter $C_{Fraction}$, which corresponds to the ratio between the constant volume of radiation affected cells ($N_{Constant}$) and the tumour maximum number of cells (K). During the sensitivity analysis, we also explored the relation between $C_{Fraction}$ and $\dot{D}_0$ for different ranges of tumour growth parameters.

5.3 Results

5.3.1 Modelling the radiation effect on the tumour growth

Tumour evolution with time was calculated for the three radiation exposure models previously mentioned - uniform, outer layer and constant volume scenarios. For the three models, treatments were simulated on a 'virtual patient population' based on placebo-treated patients who would have a first skeletal event between 0 to 13 months from the treatment start date. Figure 5.4 shows the comparison between tumour growth with time, for the three models discussed in section 5.2.2.3 with and without the radiation treatment, starting at two illustrative times before the placebo patient would experience a skeletal event.

When these growth models were fit to the ALSYMPCA data (section 5.2.3), we found best-fit parameters of $\dot{D}_0 = 1.14 \times 10^{-4} \pm 0.19 \times 10^{-4}$ Gy/h for the uniform effect, $T_{layer} = 65.8 \pm 6.1$ µm for the outer layer effect and $N_{constant} = 2.02 \times 10^8 \pm 0.02 \times 10^8$ cells for the constant volume effect scenario, a constant volume that corresponds to near 0.5% K. For the outer layer and constant volume models, we fixed $\dot{D}_0$ as 0.0103 Gy/h, corresponding to the initial dose rate obtained from published estimates of deposited dose of patients treated with ^{223}Ra (section 5.2.2.1).

The corresponding Kaplan Meier curves for the simple uniform model based on bone endosteum and the best-fit version of each model are presented in Figure 5.5, together with the treatment and placebo data from the ALSYMPCA trial. Here, it's possible to see that the constant treatment model shows the closest Kaplan Meier curve fit in comparison to the ALSYMPCA treatment curve (R^2=0.971).

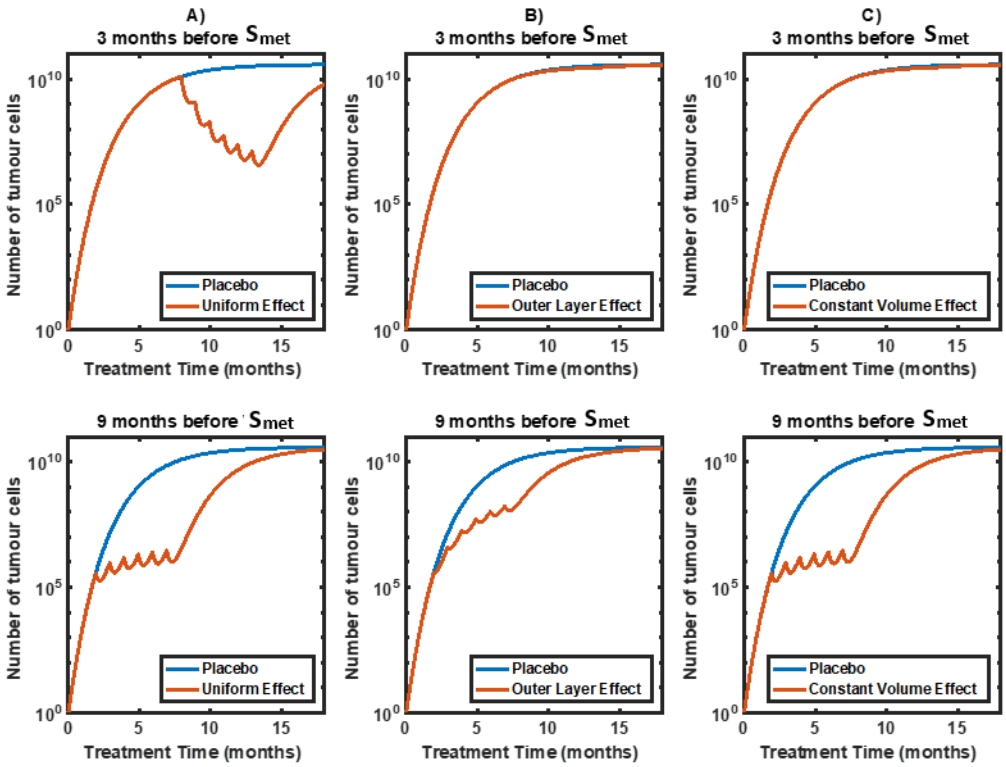

Figure 5.4 - Illustrative tumour growth curves for the uniform (A), outer-layer (B) and constant volume (C) exposure scenarios. The curves represent the progression of untreated/placebo (blue) metastases and progression when treated with ^{223}Ra at different growth stages (orange).

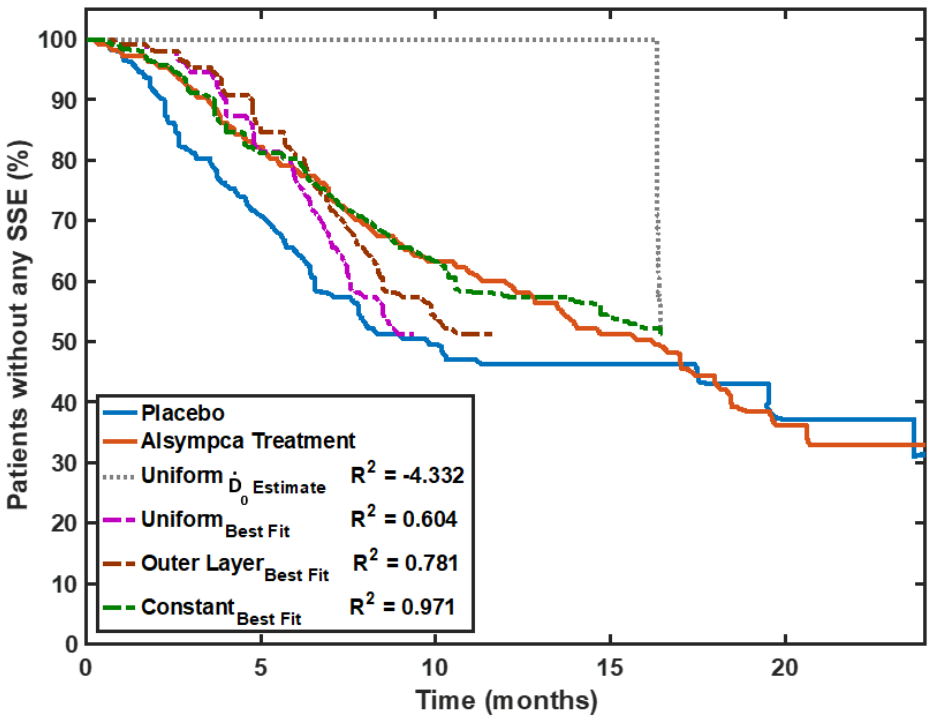

Figure 5.5 - Kaplan-Meier curves for the clinical data of placebo and treatment groups from the ALSYMPCA trial data [43], comparing to the uniform model fit with initial dose rate estimation ($\dot{D}_0$= 0.0103 Gy/h). The curves for the uniform, outer layer and constant volume effect model scenarios with best-fit parameters are also shown.

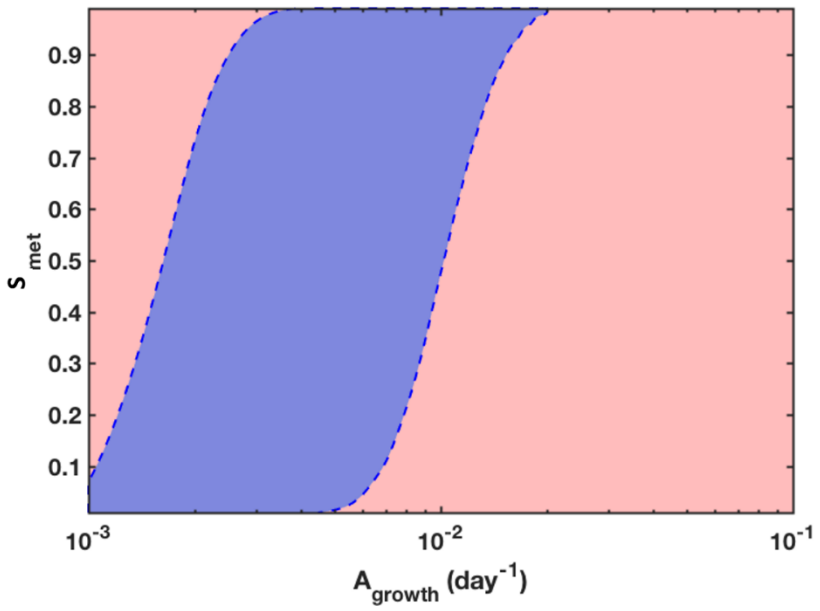

Figure 5.6 - Illustration of A_{growth} and S_{Met} model parameters which lead to plausible metastatic growth kinetics. For each parameter set, the time for a metastatic burden to develop from a minimal untreated tumour volume to a symptomatic skeletal event was calculated. Based on clinical responses, sets where this time was too short (<12 months) or too long (>6 years) were deemed to be unsuitable (pink areas) while those falling within these bounds were deemed to be plausible (blue area). The maximum number of cells (K) was set to 3.84 x 10^{10}.

5.3.2 Sensitivity analysis of tumour growth model parameters

As noted in the previous section, there are no robust data on bone metastatic growth kinetics or failure conditions. Thus, in order to fully understand the effect of A_{growth}, S_{Met}, K and $\dot{D}_0$ on tumour kinetics and treatment outcomes, we studied model predictions in a range of alternative parameter sets.

5.3.2.1 Influence of growth parameters on time to SSE of untreated tumours

We analysed how varying A_{growth} and S_{Met} influenced time to SSE of untreated tumours, beginning from a single cell (Figure 5.6). From these results we identified that models where A_{growth} is large (> 0.02) or small (<0.001), typically produce failure patterns not compatible with clinical observations (e.g. all patients failing in only a few months if A_{growth} is large, or taking many years if it is small). Reasonable S_{Met} values span a wider range, with larger S_{Met} typically being more compatible with faster growth rates and vice-versa for smaller S_{Met}.

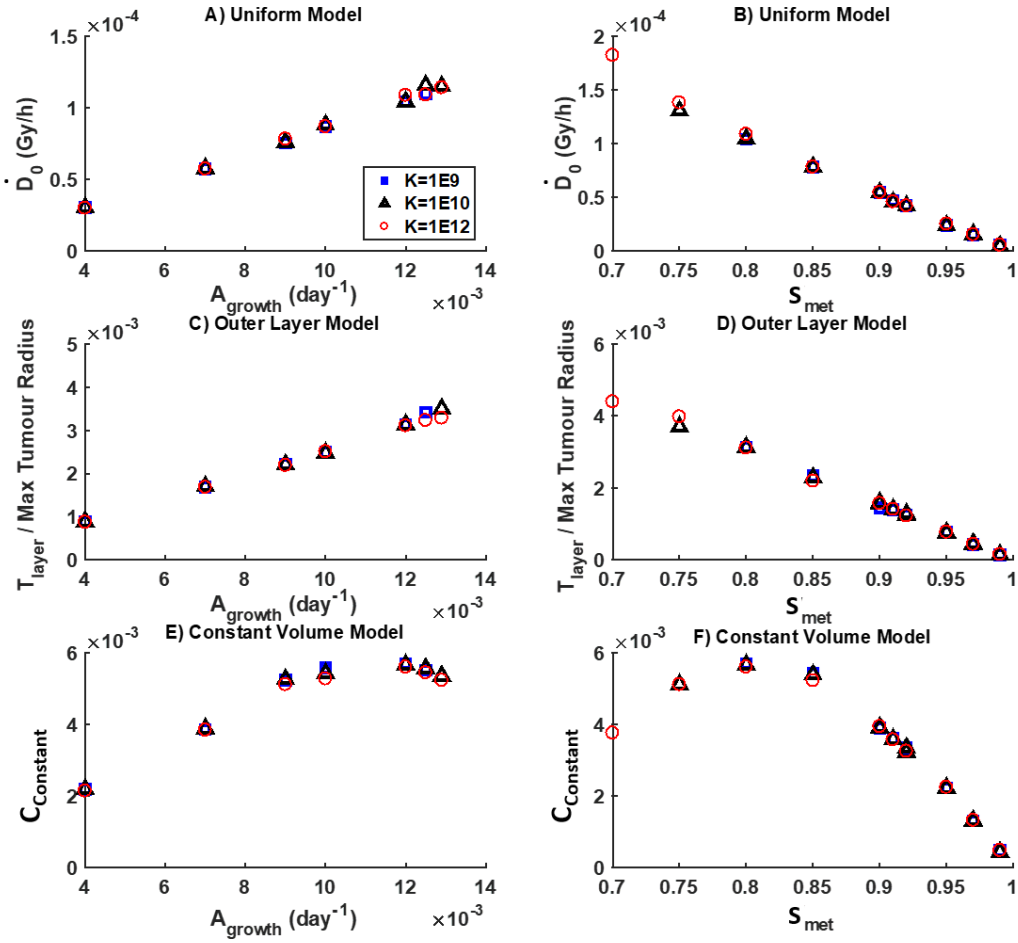

Figure 5.7 - Dependence of best fitting parameters for each radiation effect model on A_{growth} (A, C, E), S_{Met} (B, D, F) and maximum number of cells, K. The fitting parameters were initial dose rate ($\dot{D}_0$) in the uniform model, outer layer thickness (T_{layer}) for the outer layer model, and the constant volume fraction ($C_{Fraction}$) for the constant volume model. For A, C and E, S_{Met} was fixed at 0.8, and for B, D, and F, A_{growth} was fixed at 0.012 day^{-1}. An initial dose rate ($\dot{D}_0$) of 0.0103 Gy/h was used for the outer layer and constant volume models. All A_{growth} and S_{Met} values used are within the ranges of plausible metastatic growth kinetics.

5.3.2.2 Influence of growth parameters on model fit parameters

Figure 5.7 shows how model fit parameters depend on growth parameters. It can be seen that, in general, when the effective growth rate is increased (either by increasing A_{growth}, or decreasing S_{Met}), the best-fit dosimetric parameters also increase, to deliver higher doses and offset the increased growth rate. Interestingly, varying the parameter K has no significant effect on the model fits even when varied over several orders of magnitude. As this parameter acts to normalize the growth curve, this is not surprising, with the small differences between different normalized best fit parameters being connected to the effect of numerical uncertainties in the model fitting when using different K values.

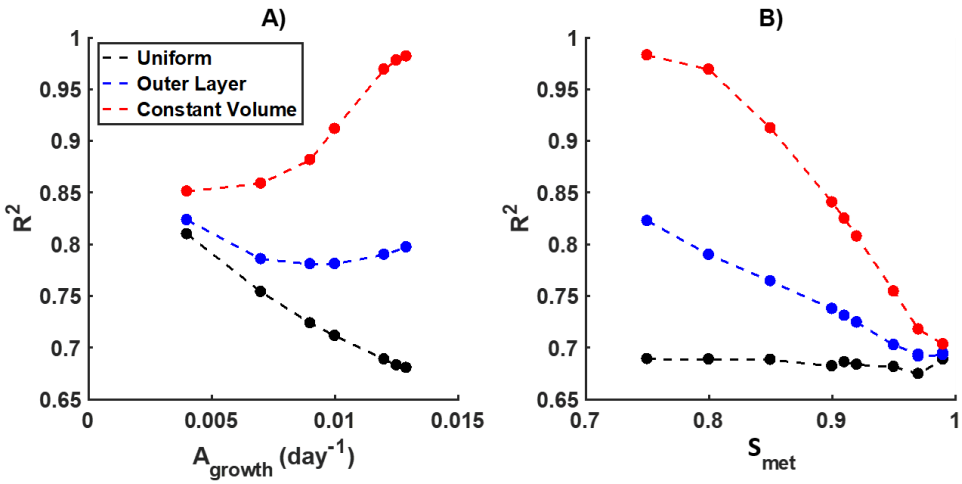

Figure 5.8 - Fit quality parameter (R^2) of different radiation model as a function of A_{growth} (A) and S_{Met} (B). S_{Met} was fixed at 0.8 for A, A_{growth} was fixed at 0.012 day^{-1} in B. An initial dose rate ($\dot{D}_0$) of 0.0103 Gy/h was used for the outer layer and constant volume models. All A_{growth} and S_{Met} values used are within the ranges of plausible metastatic growth kinetics.

Table 5.2 - Results of the highest fit quality (R^2) for the 3 tumour treatment models by varying the 3 main treatment model parameters. A_{growth} was varied between [0.001 : 0.04] day^{-1}, S_{Met} between [0.2 : 0.95] and $\dot{D}_0$ between [10^{-5} : 10^{-1}] (Gy/h), with the parameter K fixed at 10^{10} cells for all models. In the case of the uniform model, since its best fit parameter is $\dot{D}_0$, only the A_{growth} and S_{Met} parameters were varied.

	A_{growth} (day^{-1})	S_{Met}	$\dot{D}_0$ (Gy/h)	R^2
Uniform	0.0030	0.95	4.14 x 10-6	0.888
Outer Layer	0.0075	0.22	[0.008 : 0.012]	0.965
Constant	[0.009 : 0.0132]	[0.6 : 0.8]	[0.01 : 0.1]	0.984

However, although the quantitative values of the best-fit parameters change, the qualitative comparison of models and their fit quality remains similar. By comparing the quality of the three best fit models to the ALSYMPCA treatment data, varying both A_{growth} and S_{Met} parameters, it can be seen that the constant volume model has the best fit across the range of parameters considered (Figure 5.8).

As previously noted, both the outer layer and constant volume models depend not only on their model-specific parameter (T_{layer} or $C_{fraction}$), but also on the initial dose-rate $\dot{D}_0$. However, $C_{fraction}$ and $\dot{D}_0$ are strongly correlated and, as a result, it is not possible to fit these parameters independently. This is will be discussed in more detail below. Similar effects are seen for the outer layer model, with T_{layer} and $\dot{D}_0$ being highly covariant, meaning varying $\dot{D}_0$ does not significantly influence fit quality for this set of model parameters. An example of this is found from the best quality model fit analysis, whose parameters are reported in Table 5.2. Even though the best quality model fits happened for

different values of $\dot{D}_0$ and T_{layer}, the dose rate normalization factor $\dot{D}_0 \times T_{layer}$/Max Tumour Radius was almost constant (varying between [5.1 : 5.2] × 10^{-5} Gy/h).

Even when varying A_{growth}, S_{Met} and $\dot{D}_0$ together, the uniform and outer layer models still produce a poorer fit to the clinical data, with a maximum R^2 of 0.888 and 0.965 respectively (Table 5.2). For this analysis, the dose rate was sampled between 10^{-5} and 10^{-1} Gy/h. S_{Met} was sampled between 0.2 and 0.95, based on the same rationale from section 5.3.2.1, that SSE events would not happen in extremely early stages (S_{Met} < 0.2) or at late stages when tumour growth would be minimal (S_{Met} >0.95). A_{growth} ranges were selected for each S_{Met} value based on the criteria illustrated in Figure 5.6. Analyzing these results individually, we notice that the best uniform model fits correspond to extremely slow growth rates (A_{growth} = 0.003 day^{-1}) with SSE events happening in the very last stages of the tumour growth (S_{Met} = 0.95). In the case of the outer layer model, its best fit corresponds to an SSE occurring at very early stages of the tumour growth (S_{Met} = 0.22).

For both uniform and outer layer model cases, the tumour growth parameter combinations do not seem biologically reasonable. Most published tumour models show faster growth kinetics than those suggested by the uniform model (Table 5.1), while the low S_{Met} reported in the outer layer best fit scenario does not correspond to a stage where metastases are strongly competing for resources with normal tissue.

5.3.2.3 Influence of $C_{Fraction}$ and $\dot{D}_0$ on constant volume model

Focusing on the constant volume model, we have confirmed that the relationship between $\dot{D}_0$ and $C_{Fraction}$ was common across different growth parameters (Figure 5.9). It can be seen that, for all combinations of A_{growth} and S_{Met} considered, best fits converge to a single value of $\dot{D}_0 \times C_{Fraction}$ for all values of $\dot{D}_0$. This relationship breaks down slightly for very low dose rates when $C_{Fraction}$ becomes large, but it can be seen that this divergence is associated with a significant reduction in the quality of the fit, suggesting that these low dose-rate models less accurately reflect the underlying behavior. This is confirmed in Figure 5.10, which shows the dependence of the quality of the constant model fit to the ALYMPCA treatment data on the initial dose rate ($\dot{D}_0$).

Interestingly, from Figure 5.10, it can be seen that the best fitting models are typically those with higher assumed dose rates (>1×10^{-3} Gy/h) and growth model parameters similar to those found from the xenograft metastatic model (A_{growth} values ranging from 0.01 to 0.013, and for S_{Met} values between 0.75 and 0.8).

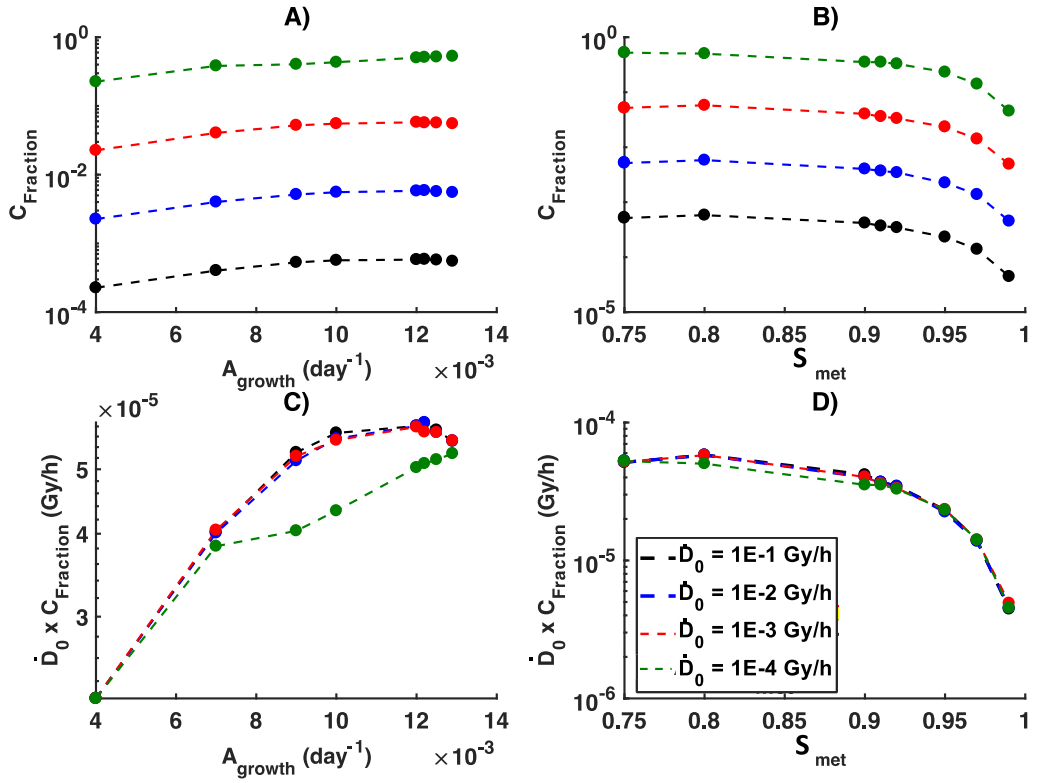

Figure 5.9 - Dependence of optimum $C_{Fraction}$ in constant volume model on initial dose rate ($\dot{D}_0$) when fit to the ALSYMPCA treatment data, for different values of A_{growth} (A) and S_{Met} (B). The dependence of the product $\dot{D}_0 \times C_{Fraction}$ is also shown, again for various A_{growth} (C) and V_{met} (D) values. S_{met} was fixed at 0.8 for A and C, A_{growth} was fixed at 0.012 day^{-1} in B and D. All A_{growth} and S_{Met} values used are within the ranges of plausible metastatic growth kinetics. $C_{Fraction}$ is the ratio between the constant volume of radiation affected cells ($N_{constant}$) and the tumour maximum number of cells (K).

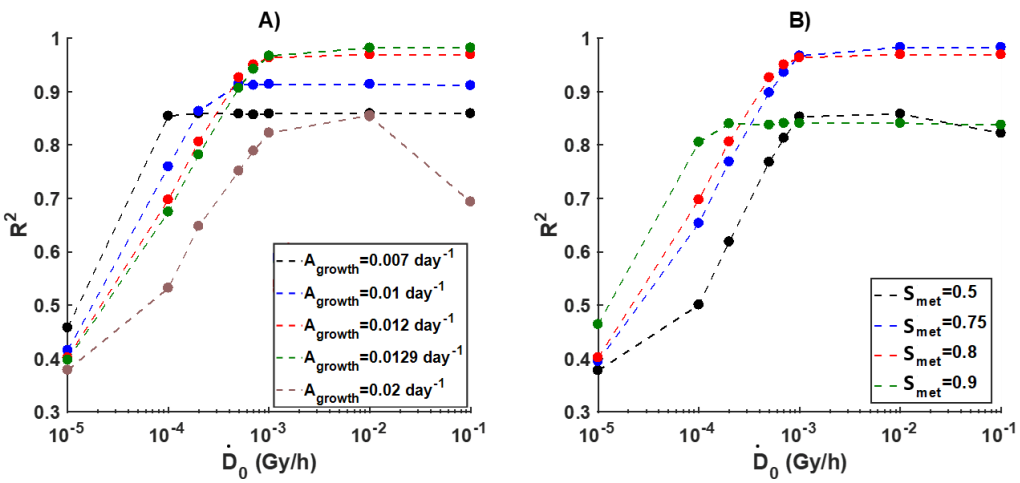

Figure 5.10 - Dependence of the fit quality (R^2) on the initial dose rate ($\dot{D}_0$) when the constant volume model is fit to the ALSYMPCA treatment data. R^2 values are presented for best fits for different A_{growth} (A) and S_{Met} (B) values. S_{Met} was fixed at 0.8 for A, A_{growth} was fixed at 0.012 day^{-1} in B. A_{growth} values higher than 0.013 and S_{Met} lower than 0.75 are outside the range of plausible metastatic growth parameter kinetics.

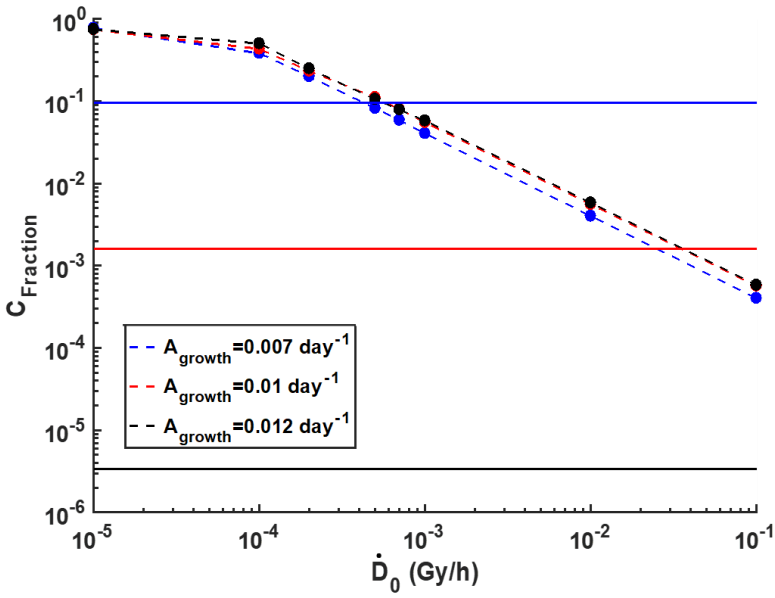

Figure 5.11 - Variation of $C_{Fraction}$ with $\dot{D}_0$ for different tumour growth rates. Horizontal lines represent the initial predicted tumour burden of the last patient in the untreated ALSYMPCA cohort to experience a SSE for a certain growth rate (A_{growth}). S_{Met} was fixed at 0.8. All A_{growth} and S_{Met} values used are within the ranges of plausible metastatic growth kinetics. $C_{Fraction}$ is the ratio between the constant volume of radiation affected cells ($N_{constant}$) and the tumour maximum number of cells (K).

These best-fitting dose rates correspond to relatively small fractions of cells being exposed to radiation – less than 10% of the maximum cell number, in most cases, as shown in Figure 5.11. Here, we show the variation of $C_{Fraction}$ with $\dot{D}_0$ for three different A_{growth} values, chosen based on some of the constant model best fit results (from Figure 5.10A). The horizontal lines display the extrapolated tumour volume for the last non-treated patient to reach a SSE, for each corresponding A_{growth} value. These non-treated patients would be the last to reach a skeletal event between 0 to 13 months, following the ALSYMPCA results.

For example, a non-treated patient from the ALSYMPCA trial, with an initial tumour burden of about 0.2% of the maximum tumour volume (K) would be the last to reach a SSE in these conditions if its metastatic growth rate parameter A_{growth} was 0.010 day^{-1} (red horizontal line from Figure 5.11). In comparison to this case, let us consider a treated patient with the same initial tumour burden and growth rate parameters but with an initial treatment dose rate $\dot{D}_0$ = 0.01 Gy/h. Based on the constant volume model, a $C_{Fraction}$ value near 0.6% would lead to the same treatment delay in time reported in the ALSYMPCA trial for this treated patient to reach a SSE.

This means that at the beginning of treatment, the whole tumour volume of this patient would be affected by the ^{223}Ra treatment up until the moment where $\mathrm{N(t)} \geq 0.006\mathrm{K}$, following equation 5.10. After that, the tumour volume affected by the treatment would be constant ($\mathrm{N_p(t)} = 0.006\mathrm{K}$). For

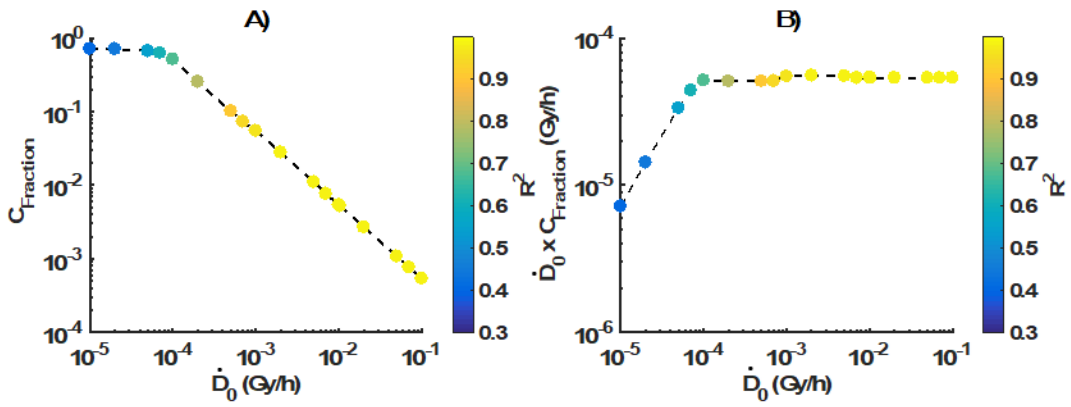

Figure 5.12 - Effect of initial dose rate ($\dot{D}_0$) on the best-fitting $C_{Fraction}$ (A) and the product of $\dot{D}_0$and $C_{Fraction}$ (B). These datasets were fitted with A_{growth} =0.0129 days^{-1}, S_{met}=0.8, and K=3.84x10^{10} cells. Points are coloured according to the fit quality (R^2) of the model to the ALSYMPCA treatment data. $C_{Fraction}$ is the ratio between the constant volume of radiation affected cells ($N_{constant}$) and the tumour maximum number of cells (K).

similar cases with the same $\dot{D}_0$ values but higher A_{growth} values, we expect lower proportions of the tumour to be affected by treatment (lower $C_{Fraction}$) in order for the constant model treatment SSE time delays to be similar to the ones reported in the ALSYMPCA data.

The small fractions of cells being exposed to radiation, in comparison to the maximum tumour volume (Figure 5.11), suggest that for many patients not all of their disease burden is exposed to radiation, although for lower dose-rates a portion of the population who are treated early in the disease progression may see complete coverage ($C_{Fraction} \sim 1$).

Using the tumour growth rate parameters from the xenograft data ($A_{growth} = 0.0129$ days^{-1}) and an S_{Met} = 0.8, chosen from the best fit results (Figure 5.10), we analysed the quality of the constant model fit to the ALSYMPCA treatment data based on the variation of $C_{Fraction}$ with $\dot{D}_0$ (Figure 5.12). Again, we see a strong correlation between $C_{Fraction}$ and $\dot{D}_0$, with the model primarily depending on their product, $\dot{D}_0 \times C_{fraction}$. We also observe a linear dependence between these terms at dose rates from 10^{-4} to 10^{-1} Gy/h. This is confirmed by Figure 5.12B, showing the best-fitting $\dot{D}_0 \times C_{Fraction}$ is constant for a wide range of initial dose rates. Thus, dosimetric uncertainties translate into significant uncertainties in the value of $C_{Fraction}$, but have no significant impact on fit quality.

However, some constraints can be placed on these values based on fit quality. Once the initial dose rate becomes significantly less than 1×10^{-3} Gy/h, the quality of the fit degrades significantly, suggesting that these models with high coverage ($C_{Fraction} > 10\%$) and low dose rate provide a less accurate representation of clinical data than higher dose rates with only small portions of the disease being exposed.

5.4 Discussion

In this chapter we report the results from mathematical modelling of the treatment outcomes of ^{223}Ra on bones metastases. During this process, we analysed tumour growth kinetics, following a Gompertz model, with the effects of α-particle radiation from ^{223}Ra. The time to the first SSE was then compared for each tested model with the clinical data available from the ALSYMPCA trial. An extensive sensitivity analysis was also conducted to further explore the effects of all the tumour growth model parameters involved.

The addition of the ^{223}Ra effect to the PC-3 based Gompertz tumour growth showed different results for the three exposure scenarios investigated in this work. The uniform effect, where the radiation affects the whole tumour volume, gave over-optimistic results, when using the initial dose rate estimate ($\dot{D}_0$ = 0.0103 Gy/h). This was noticeable in Figure 5.4 as 12 and 6 month growth delays in reaching N_{Met} were observed when compared to the placebo curves, for late and early tumour stages respectively. When comparing these results with the clinical data, it further proves to be an unrealistic model scenario (Figure 5.5). Even if taking a lower initial dose rate, the best-fit model still results in a different Kaplan-Meier curve compared to the clinical data, over-estimating the effects on patients with high disease burden and under-estimating the effects on patients with lower disease burden. The sensitivity analysis has also shown that this is the case regardless of the growth model parameters used (Figure 5.8). These results led us to conclude that the metastatic tumour cells cannot be experiencing a uniform dose exposure. This is particularly relevant since the assumption that there is a uniform radiopharmaceutical activity distribution in bone metastatic volume sites is frequently used for bone absorption radiation dose calculations and response modelling. [42,160–163]

Regarding the outer layer effect scenario, we observed growth delays of 3.0 and 5.0 months compared to the placebo curve, for early and late tumour stages respectively on Figure 5.4. However, these growth delays show that the model still predicts cell killing rates which are too high for early tumour growth stages and too low for later tumour growth stages. This is due to the changing fraction of cells affected by the penetration range of ^{223}Ra. This inadequacy of the model is further confirmed in Figure 5.5, where the best-fit model shows poor agreement with clinical data, which again is true for a range of growth parameters (Figure 5.8).

The third tested model scenario showed the best predictions of treatment effect. The treatment group results for the constant volume exposure scenario predicted very similar outcomes to the clinical data, as shown in Figure 5.5, especially until 10 months after treatment initiation (R^2 = 0.989 for the first ten months). The results from this model seem to indicate that the ^{223}Ra treatment saturates, affecting only a constant number of cells regardless of the tumour growth once its volume is above $N_{constant}$. The exact number of cells affected depends on the assumed dose rate in the metastatic

volumes, with $N_{constant}$ ranging from 5% to 0.05% of the maximum metastatic burden (K) for initial dose rates $\dot{D}_0$ varying from 0.001 to 0.1 Gy/h, respectively (Figure 5.9). For these cases, the fitting quality of the model is still high (R^2>0.96), as shown in Figure 5.10 and Figure 5.12. In addition, the overall best fit performance was found for model parameters similar to those derived from the xenograft mouse data (A_{growth} values ranging from 0.09 to 0.013 day^{-1}, and for S_{Met} values between 0.75 and 0.8, Figure 5.10), although a range of parameters produced similar fits.

These results further support the idea of a non-uniform ^{223}Ra biodistribution in the tumour microenvironment, with effects that saturate rapidly with tumour volume, which may possibly be related to poor blood vessel perfusion in metastatic sites.[164] This is in agreement with some evidence seen in the literature of inhomogeneous distributions of β and α-particle emitting radionuclides in pre-clinical models, where some of the target cells received no radiation. [165–168]

However, it should be noted that these models remain an idealized description of the metastatic tumour burden, and a number of refinements to this model will help building more accurate and predictive descriptions of bone metastases radionuclide therapy. Some of these limitations are related to the mathematical models of tumour growth kinetics. While the Gompertz model is well-established for primary tumours and a conceptually reasonable model of metastastic burden, it may be inadequate to simulate metastatic growth at earlier stages. Unfortunately, there is very limited growth data for human bone metastases in the literature. Analysis of a range of published clinical data in various tumour types produced unrealistic growth kinetics (Table 5.1, Figure 5.2). As a result, in this work we made use of parameters based on a human prostate cell line derived from a bone metastatic site, which showed the most realistic tumour growth predictions and was therefore chosen to be applied in our mathematical model. The lack of detailed, quantitative clinical data on the progression of metastatic burden in these patients leads to significant uncertainty in the A_{growth}, K and S_{Met} parameters which had to be estimated indirectly based on tumour studies in mice. While the model's general conclusions appear to be robust against variation in these parameters, more accurate growth data could significantly improve the confidence in specific fitted parameter values.

It is also important to understand that different tumour microenvironments will have different sub-populations of cells, such as quiescent cells. These sub-populations may have a significant impact in tumour eradication and should be considered in future model optimizations. [169–171] Important indirect radiation effects, such as bystander effects, should also be taken into account in future treatment model simulations. Despite the fact that it is difficult to fully characterize this effect in bone metastases, it clearly has a significant role in cell death, especially using high LET particles such as α-particles. [55,76,172,173] Further studies of radiation indirect effects and bone metastases development in humans, particularly tracking multiple independent metastases, are needed to develop more realistic models of metastatic growth.

Furthermore, the data from the clinical treatment observations used in this work would also benefit from increased statistical power. 10 months after treatment, the number of SSE is low (average below 7 SSE/month), which increases statistical uncertainties. In addition, this model involves an extrapolation from SSE to a single value of 'tumour burden', while in reality patients will likely have a number of metastatic sites that may have different sizes and growth rates. We have addressed part of this issue by analyzing the effect of different model parameters to the tumour growth, as shown in the parameter sensitivity analysis section. However, model refinements are still needed. Obtaining additional data at the level of individual metastases from imaging studies, would enable the development of more accurate treatment models.

Despite these limitations, the work presented in this chapter demonstrated that modelling the growth and radiation response of bone metastases in patients treated with ^{223}Ra is able to accurately reproduce clinical responses. Significantly, this analysis suggests that clinical responses can only be reproduced by assuming that a relatively low constant number of cells are exposed to α-particles. These observations support that conventional uniform dosimetric approaches are not valid to accurately predict the biological effects of α-particle radionuclide therapies. Further *in vivo* and *in vitro* studies regarding metastatic growth, tumour microenvironment and ^{223}Ra uptake mechanisms are necessary in order to plan more effective treatments in the future.

CHAPTER 6 : CONCLUSION

The work presented in this thesis has enabled laboratory α-particle radiation research studies by developing an in-house α-particle source irradiation system in an open-air environment. In addition, the *in vitro* studies and tumour growth model simulation results led to an improved understanding of the radiobiologic effects of novel radiotherapy modalities that involve α-particle radiation, in particular with the use of ^{223}Ra radioisotopes in the treatment of bone metastases.

First, we validated a novel α-particle irradiation system in chapter 2. Here, we designed an irradiation system and then tested the source irradiation uniformity, particle flux and energy deposition at targets placed at different distances from the source. By comparing the experimental and simulated flux results we proved that the Monte Carlo simulations used accurately reproduced the experimental results, especially for targets placed closer to the source. Similarly, the particle energy spectra obtained by using a charged particle detector was found to follow a similar probability density distribution as the simulated spectra, after applying a Gaussian filter.

The experimental flux and the simulated energy deposition results were important to calculate the α-source dose rate to the cell nucleus ($\dot{D}_{nucleus}$ = 1.57± 0.15 Gy/min). This calculated dose rate was fundamental for the *in vitro* experiments presented in chapter 4. The comparison between experimental results in chapter 4 and literature results of PC-3 clonogenic survival with external α-particle irradiations further validated the work shown in chapter 2.

In chapter 3 we tested for the first time the use of 3D printed polymer collimators for laboratory α-particle research. We also evaluated the collimated source irradiation uniformity, particle flux, and energy deposition, comparing to the experimental and simulation results shown in chapter 2. This allowed us to compare the distribution of α-particles emitted from a collimated and a non-collimated source. One of the main outcomes was a slight improvement of irradiation uniformity of the α-source, particularly on α-particle energy spectra. There was a smaller coefficient of variation of the normalized NOD when a collimated source was used.

During the Monte Carlo simulations in chapter 3, we based the simulated collimator geometry on a geometric analysis of the printed collimators. The simulation results also demonstrated that the energy spread of α-particles hitting a target is considerably reduced when a collimator is used, especially for targets placed closer to the α-source. Similarly, the LET spread from different α-particle interactions on

exposed cells also gets more uniform. As a result, the dose deposited from the α-source on a target is more precise. This is demonstrated by comparing the coefficients of variation of the calculated dose rates for a target placed 2.9 cm away from the source – 4.9% and 9.6% for a collimated and non-collimated source, respectively. The main conclusion from this chapter is that there are significant improvements that can be made to a laboratory α-source irradiation system by using polymer collimators built through accessible 3D printing techniques.

The *in vitro* studies presented in chapter 4 not only validated the work from chapter 2 and chapter 3, but also helped us quantify the different effects of X-ray and α-particle irradiation methods on cell survival and DNA damage. As expected, external α-particle irradiations led to lower cell survival for the same X-ray doses ($RBE_{SF=10\%} = 3.66 \pm 0.40$ for PC-3 cells) and more persistent DNA damage after 24h repair times, for all the radiation doses used.

Surprisingly, the clonogenic and DNA damage assays using external α-particle irradiations and internal irradiations with ^{223}Ra had significant differences. ^{223}Ra exposures led to lower cell survival for the same radiation doses. These differences were later shown to be partially related to a treatment volume effect of the Xofigo solution. For the same calculated dose, higher volumes of Xofigo were shown to cause greater cell death. This means that either the assumption of uniform ^{223}Ra exposure is not accurate or that there is also a non-radiation toxicity effect from the Xofigo solution. It is also possible that the two options are both true. Therefore, it is imperative that future studies are done in order to understand Xofigo's chemical composition and its effect on cells as well as understanding if the ^{223}Ra exposure is not uniform. For example, it would be important to understand the uptake mechanisms of ^{223}Ra for different cells and simulate how that possible uptake could impact the cell dosimetry.

It would also be important to continue the Xofigo *in vitro* experiments, for example with additional DSB DNA damage assays with internal ^{223}Ra exposures. This would complement the work presented in this chapter as the availability of Xofigo vials from the ADDRAD trial that could be used in our laboratory was a challenge that limited the number of possible experiments.

In chapter 5 we simulated the growth of bone metastasis from prostate cancer patients, adding the radiation effect of ^{223}Ra treatment. To do this we used a Gompertz model (sections 5.2.1 and 5.2.2) with 3 different radiation exposure scenarios (uniform, outer layer and constant volume scenarios). We then calculated the time it would take for simulated treated and control patients to reach the first symptomatic skeletal event (SSE) and compared the results with the data published from the ALSYMPCA trial. The obtained results proved that the uniform exposure model, which assumes that a ^{223}Ra treatment exposes all bone metastatic cells to the same dose, is not accurate, as suggested in chapter 4 discussion (section 4.4). This was shown to happen for a range of tumour growth parameters and initial dose rates.

Interestingly, the model with the best outcomes was the constant volume model, which assumes that ^{223}Ra radiation doses only affects up to a maximum volume of the metastatic tumour, no matter the tumour growth stage. In comparison to the ALSYMPCA SSE Kaplan-Meier curve results, the constant volume model's goodness of the fit metric, R^2, was higher than 0.98 for a variety of growth parameters and initial dose rates. Despite the limitations reported in these studies, these results suggest that we can accurately simulate clinical ^{223}Ra treatment results, having the best outcomes assuming that only a small portion of a metastatic tumour volume is affected by the treatment. This can have important implications in clinical applications of ^{223}Ra treatments using Xofigo or other radiopharmaceuticals. Based on these findings, the dosimetry assessment for Xofigo treatments can be significantly improved. On the other hand, ^{223}Ra treatment doses and fractions can be optimized for patients at different levels of bone metastatic disease progression in order to reach the best treatment response. This can be a significant step to allow a personalised medicine approach for best ^{223}Ra treatment outcomes.

It's still imperative that further *in vivo* and *in vitro* studies regarding metastatic growth, tumour microenvironment and ^{223}Ra uptake mechanisms are necessary in order to further validate the conclusions of this work and to plan more effective treatments in the future.

This thesis allowed us to better understand the radiobiological effects of α-particles in cells, especially in targeted radiotherapy treatments involving ^{223}Ra. This was possible to achieve through the development and simulation of an α-source irradiation system that was used for laboratory *in vitro* experiments. These experimental analyses, which compared the effects of different radiation treatments on cells, together with the tumour growth model simulations, were fundamental to better understand the impact of α-emitting radionuclides, such as ^{223}Ra, in the treatment of bone metastases.

REFERENCES

1. What is cancer? | Cancer Research UK. Accessed November 9, 2019. https://www.cancerresearchuk.org/about-cancer/what-is-cancer

2. Hanahan D, Weinberg RA. Hallmarks of cancer: The next generation. *Cell*. 2011;144(5):646-674. doi:10.1016/j.cell.2011.02.013

3. Ruddon RW. *Cancer Biology*. 4th ed. Oxford University Press; 2007.

4. The International Agency for Research on Cancer (IARC) report W. Latest global cancer data: Cancer burden rises to 18.1 million new cases and 9.6 million cancer deaths in 2018. *Int Agency Res Cancer*. 2018;(September):13-15. http://gco.iarc.fr/,

5. Siegel RL, Miller KD, Jemal A. Cancer statistics, 2018. *CA Cancer J Clin*. 2018;68(1):7-30. doi:10.3322/caac.21442

6. Lee J, Demissie K, Lu S-E, Rhoads GG. Cancer incidence among Korean-American immigrants in the United States and native Koreans in South Korea. *Cancer Control*. 2007;14(1):78-85.

7. Lichtenstein P, Holm N V, Verkasalo PK, et al. Environmental and heritable factors in the causation of cancer--analyses of cohorts of twins from Sweden, Denmark, and Finland. *N Engl J Med*. 2000;343(2):78-85. doi:10.1056/NEJM200007133430201

8. Schaid DJ. The complex genetic epidemiology of prostate cancer. *Hum Mol Genet*. 2004;13(90001):103R - 121. doi:10.1093/hmg/ddh072

9. Heidenreich a, Bolla M, Joniau S, et al. Guidelines on Prostate Cancer. *Update*. 2011;53(February):31-45. http://www.uroweb.org/fileadmin/tx_eauguidelines/2005/Pocket/Prostate_Cancer.pdf

10. Attard G, Parker C, Eeles RA, et al. Prostate cancer. *Lancet*. 2016;387(10013):70-82. doi:10.1016/S0140-6736(14)61947-4

11. Klotz L, Zhang L, Lam A, Nam R, Mamedov A, Loblaw A. Clinical results of long-term follow-up of a large, active surveillance cohort with localized prostate cancer. *J Clin Oncol*. 2010;28(1):126-131. doi:10.1200/JCO.2009.24.2180

12. Connolly RM, Carducci MA, Antonarakis ES. Use of androgen deprivation therapy in prostate

cancer: indications and prevalence. *Asian J Androl*. 2012;14(2):177-186. doi:10.1038/aja.2011.103

13. Maini CL, Sciuto R, Romano L, Bergomi S. Radionuclide therapy with bone seeking radionuclides in palliation of painful bone metastases. *J Exp Clin Cancer Res*. 2003;22(4 Suppl):71-74.

14. Stewart BW, Wild CP. *World Cancer Report 2014*. (Stewart, B. W., Wild CP, ed.). IARC Nonserial Publication; 2014.

15. Chappard D, Bouvard B, Baslé M, Legrand E, Audran M. Bone metastasis : Histological changes and pathophysiological mechanisms in osteolytic or osteosclerotic localizations . A review Les métastases osseuses : aspects histologiques et mécanismes The RANK-RANKL-OPG system. *Morphologie*. 2011;95(309):65-75. doi:10.1016/j.morpho.2011.02.004

16. Macedo F, Ladeira K, Pinho F, et al. Bone metastases: An overview. *Oncol Rev*. 2017;11(1). doi:10.4081/oncol.2017.321

17. Goyal J, Antonarakis ES. Bone-targeting radiopharmaceuticals for the treatment of prostate cancer with bone metastases. *Cancer Lett*. 2012;323(2):135-146. doi:10.1016/j.canlet.2012.04.001

18. Van Dodewaard-De Jong JM, Verheul HMW, Bloemendal HJ, De Klerk JMH, Carducci MA, Van Den Eertwegh AJM. New Treatment Options for Patients with Metastatic Prostate Cancer: What Is the Optimal Sequence? *Clin Genitourin Cancer*. 2015;13(4):271-279. doi:10.1016/j.clgc.2015.01.008

19. Slater JM. Ion Beam Therapy. 2012;320:3-17. doi:10.1007/978-3-642-21414-1

20. Terasawa T, Dvorak T, Ip S, Raman G, Lau J, Trikalinos TA. Review Annals of Internal Medicine Systematic Review : Charged-Particle Radiation Therapy for Cancer. 2009;(5).

21. Jacob Hayempour B. Clinical Medical Physics Methods in Radiotherapeutic Cancer Treatments. *J Neurol Disord*. 2013;01(01):10-12. doi:10.4172/2329-6895.1000103

22. Herskind C, Ma L, Liu Q, et al. Biology of high single doses of IORT: RBE, 5 R's, and other biological aspects. *Radiat Oncol*. 2017;12(1):1-14. doi:10.1186/s13014-016-0750-3

23. Brown JM, Carlson DJ, Brenner DJ. The tumor radiobiology of SRS and SBRT: Are more than the 5 Rs involved? *Int J Radiat Oncol Biol Phys*. 2014;88(2):254-262. doi:10.1016/j.ijrobp.2013.07.022

24. Couturier O, Supiot S, Degraef-Mougin M, et al. Cancer radioimmunotherapy with alpha-emitting nuclides. *Eur J Nucl Med Mol Imaging*. 2005;32(5):601-614. doi:10.1007/s00259-005-

1803-2

25. Kassis AI. Therapeutic Radionuclides: Biophysical and Radiobiologic Principles. *Semin Nucl Med*. 2008;38(5):358-. doi:10.1038/jid.2014.371

26. Tomblyn M. The role of bone-seeking radionuclides in the palliative treatment of patients with painful osteoblastic skeletal metastases. *Cancer Control*. 2012;19(2):137-144. doi:10.1177/107327481201900208

27. Zacho HD, Karthigaseu NN, Fonager RF, Petersen LJ. Treatment with bone-seeking radionuclides for painful bone metastases in patients with lung cancer: A systematic review. *BMJ Support Palliat Care*. 2017;7(3):230-237. doi:10.1136/bmjspcare-2015-000957

28. Silberstein EB, Elgazzar AH, Kapilivsky A. Phosphorus-32 radiopharmaceuticals for the treatment of painful osseous metastases. *Semin Nucl Med*. 1992;22(1):17-27. doi:10.1016/S0001-2998(05)80153-9

29. Zheng H, Luo R, Fan Y. Therapeutic effects of strontium-89 against osseous metastases of lung cancer: analysis of 126 cases. *Acad J first Med Coll PLA*. 2004;24(10):1194-1196. Accessed November 22, 2019. http://www.ncbi.nlm.nih.gov/pubmed/15485798

30. Ratsimanohatra H, Barlesi F, Doddoli C, et al. Use of 153Sm-EDTMP to relieve pain from bone metastasis in lung cancer. *Rev Mal Respir*. 2005;22(2):317-320. doi:10.1016/s0761-8425(05)85484-1

31. Minutoli F, Herberg A, Spadaro P, et al. [186Re]HEDP in the palliation of painful bone metastases from cancers other than prostate and breast. *Q J Nucl Med Mol Imaging*. 2006;50(4):355-362. Accessed November 22, 2019. http://www.ncbi.nlm.nih.gov/pubmed/17043634

32. Liepe K. 188 Re-HEDP therapy in the therapy of painful bone metastases . *World J Nucl Med*. 2018;17(3):133. doi:10.4103/wjnm.wjnm_85_17

33. Srivastava SC, Atkins HL, Krishnamurthy GT, et al. Treatment of metastatic bone pain with tin-117m Stannic diethylenetriaminepentaacetic acid: a phase I/II clinical study. *Clin Cancer Res*. 1998;4(1):61-68. Accessed November 22, 2019. http://www.ncbi.nlm.nih.gov/pubmed/9516953

34. Cabrera ME, Rey PM, Carrió I, Montes A, López DA. Response to 223Ra-dichloride in castration-resistant prostate cancer with bone metastasis: A case report. *Oncol Lett*. 2016;12(2):1323-1328. doi:10.3892/ol.2016.4762

35. Macklis RM, Kinsey BM, Kassis AI, et al. Radioimmunotherapy with alpha-particle-emitting immunoconjugates. *Science (80-)*. 1988;240(4855):1024-1026. doi:10.1126/science.2897133

36. Allen BJ, Raja C, Rizvi S, et al. Targeted alpha therapy for cancer. *Phys Med Biol*. 2004;49(16):3703-3712. doi:10.1088/0031-9155/49/16/016

37. Allen B. Clinical Trials of Targeted Alpha Therapy for Cancer. *Rev Recent Clin Trials*. 2008;3(3):185-191. doi:10.2174/157488708785700339

38. Philippa J. Cheetham, MD, Daniel P. Petrylak M. Alpha Particles as Radiopharmaceuticals in the Treatment of Bone Metastases: Mechanism of Action of Radium-223 Chloride (Alpharadin) and Radiation. *Oncol (willist Park*. Published online 2012.

39. Nilsson S, Larsen RH, Fosså SD, et al. First clinical experience with alpha-emitting radium-223 in the treatment of skeletal metastases. *Clin Cancer Res*. 2005;11:4451-4459. doi:10.1158/1078-0432.CCR-04-2244

40. Bayer. Xofigo 1100 kBq/mL solution for injection - Summary of Product Characteristics. Published online 2018:2-13.

41. Bé M, Chisté V, Dulieu C, et al. Table of Radionuclides. *Bur Int des Poids Mes*. 2008;1-6.

42. Pacilio M, Ventroni G, Vincentis G De, et al. Dosimetry of bone metastases in targeted radionuclide therapy. *Eur J Nucl Med Mol Imaging*. 2016;43:21-33. doi:10.1007/s00259-015-3150-2

43. Parker C, Nilsson S, Heinrich D, et al. Alpha emitter radium-223 and survival in metastatic prostate cancer. *N Engl J Med*. 2013;369:213-223. doi:10.1056/NEJMoa1213755

44. Joiner M, Van der Kogel A. Basic Clinical Radiobiology. Published online 2009.

45. Hill MA. Radiation damage to DNA: the importance of track structure. *Radiat Meas*. 1999;31(1-6):15-23. doi:10.1016/s1350-4487(99)00090-6

46. Zanto TP, Hennigan K, Östberg M, Clapp WC, Gazzaley A. Heavy Charged Particle Radiobiology: Using Enhanced Biological Effectiveness and Improved Beam Focusing to Advance Cancer Therapy. 2011;46(4):564-574. doi:10.1016/j.cortex.2009.08.003.Predictive

47. Xu XG, Bednarz B, Paganetti H. A review of dosimetry studies on external-beam radiation treatment with respect to second cancer induction. *Phys Med Biol*. 2008;53(13):R193-R241. doi:10.1088/0031-9155/53/13/R01

48. Levin WP, Kooy H, Loeffler JS, DeLaney TF. Proton beam therapy. *Br J Cancer*. 2005;93(8):849-854. doi:10.1038/sj.bjc.6602754

49. Schiller KC, Habl G, Combs SE. Protons, photons, and the prostate - Is there emerging evidence in the ongoing discussion on particle therapy for the treatment of prostate cancer? *Front Oncol*. 2016;6(JAN):1. doi:10.3389/fonc.2016.00008

50. Goitein M. Magical Protons? *Int J Radiat Oncol Biol Phys*. 2008;70(3):654-656. doi:10.1016/j.ijrobp.2007.10.057

51. Tisnek N, Kalanxhi E, Serkland CW, Iversen J, Belyakov O V., Dahle J. A238Pu irradiator for exposure of cultured cells with alpha-radiation: Construction, calibration and dosimetry. *Appl Radiat Isot*. 2009;67(11):1998-2002. doi:10.1016/j.apradiso.2009.08.003

52. Neti PVS V, De Toledo SM, Perumal V, Azzam EI, Howell RW. A Multi-port Low-Fluence Alpha-Particle Irradiator: Fabrication, Testing and Benchmark Radiobiological Studies. *Radiat Res*. 2004;161(6):732–738. doi:10.1021/nn300902w.Release

53. Fokas E, Kraft G, An H, Engenhart-Cabillic R. Ion beam radiobiology and cancer: Time to update ourselves. *Biochim Biophys Acta - Rev Cancer*. 2009;1796(2):216-229. doi:10.1016/j.bbcan.2009.07.005

54. Hill MA. Radiation damage to DNA: the importance of track structure. *Radiat Meas*. 1999;31(1-6):15-23. doi:10.1016/s1350-4487(99)00090-6

55. Sgouros G, Roeske JC, McDevitt MR, et al. MIRD Pamphlet No. 22 (abridged): radiobiology and dosimetry of alpha-particle emitters for targeted radionuclide therapy. *J Nucl Med*. 2010;51(2):311-328. doi:10.2967/jnumed.108.058651

56. Johnson D, Chen Y, Ahmad S. Dose and linear energy transfer distributions of primary and secondary particles in carbon ion radiation therapy: A Monte Carlo simulation study in water. *J Med Phys*. 2015;40(4):214-219. doi:10.4103/0971-6203.170785

57. Guan F, Peeler C, Bronk L, et al. Analysis of the track- and dose-averaged LET and LET spectra in proton therapy using the geant 4 Monte Carlo code. *Med Phys*. 2015;42(11):6234-6247. doi:10.1118/1.4932217

58. McMahon SJ, Paganetti H, Prise KM. LET-weighted doses effectively reduce biological variability in proton radiotherapy planning. *Phys Med Biol*. 2018;63(22):225009. doi:10.1088/1361-6560/aae8a5

59. Toohey RE, Stabin MG, Watson EE. The AAPM/RSNA physics tutorial for residents: Internal radiation dosimetry: principles and applications. *Radiographics*. 2000;20(2):533-546. doi:10.1148/radiographics.20.2.g00mc33533

60. Turner JE. *Atoms, Radiation, and Radiation Protection*. 3rd editio.; 2007.

61. Hobbs RF, Baechler S, Fu DX, et al. A model of cellular dosimetry for macroscopic tumors in radiopharmaceutical therapy. *Med Phys*. 2011;38(6):2892-2903. doi:10.1118/1.3576051

62. Sørensen BS, Overgaard J, Bassler N. In vitro RBE-LET dependence for multiple particle types.

Acta Oncol (Madr). 2011;50(6):757-762. doi:10.3109/0284186X.2011.582518

63. Franken NA, ten Cate R, Krawczyk PM, et al. Comparison of RBE values of high- LET α-particles for the induction of DNA-DSBs, chromosome aberrations and cell reproductive death. *Radiat Oncol*. 2011;6(1):64. doi:10.1186/1748-717X-6-64

64. Choi J, Kang JO. Basics of particle therapy II: relative biological effectiveness. *Radiat Oncol J*. 2012;30(1):1-13. doi:10.3857/roj.2012.30.1.1

65. Tracy BL, Stevens DL, Goodhead DT, Hill MA. Variation in RBE for Survival of V79-4 Cells as a Function of Alpha-Particle (Helium Ion) Energy. *Radiat Res*. 2015;184(1):33. doi:10.1667/rr13835.1

66. Rockwell S, Dobrucki I, Kim E, Marrison S, Vu V. Hypoxia and Radiation Therapy: Past History, Ongoing Research, and Future Promise. *Curr Mol Med*. 2009;9(4):442-458. doi:10.2174/156652409788167087

67. Lomax ME, Folkes LK, O'Neill P. Biological consequences of radiation-induced DNA damage: Relevance to radiotherapy. *Clin Oncol*. 2013;25(10):578-585. doi:10.1016/j.clon.2013.06.007

68. Wyman C, Kanaar R. DNA Double-Strand Break Repair: All's Well that Ends Well. *Annu Rev Genet*. 2006;40(1):363-383. doi:10.1146/annurev.genet.40.110405.090451

69. Nikjoo H. Radiation track and DNA damage. *Iran J Radiat Res*. 2003;1(1):3-16.

70. Dubrova YE, Plumb M, Brown J, et al. Stage specificity, dose response, and doubling dose for mouse minisatellite germ-line mutation induced by acute radiation. *Proc Natl Acad Sci*. 1998;95(11):6251-6255. doi:10.1073/pnas.95.11.6251

71. Dickinson BC, Chang CJ. Chemistry and biology of reactive oxygen species in signaling or stress responses. *Nat Chem Biol*. 2011;7(8):504-511. doi:10.1038/nchembio.607

72. Hada M, Sutherland BM. Spectrum of Complex DNA Damages Depends on the Incident Radiation. *Radiat Res*. 2006;165(2):223-230. doi:10.1667/rr3498.1

73. Sutherland BM, Bennett P V., Sidorkina O, Laval J. Clustered damages and total lesions induced in DNA by ionizing radiation: Oxidized bases and strand breaks. *Biochemistry*. 2000;39(27):8026-8031. doi:10.1021/bi9927989

74. Kakarougkas A, Jeggo PA. DNA DSB repair pathway choice: An orchestrated handover mechanism. *Br J Radiol*. 2014;87(1035). doi:10.1259/bjr.20130685

75. Maier P, Hartmann L, Wenz F, Herskind C. Cellular pathways in response to ionizing radiation and their targetability for tumor radiosensitization. *Int J Mol Sci*. 2016;17(1). doi:10.3390/ijms17010102

76. Prise KM, O'Sullivan JM. Radiation-induced bystander signalling in cancer therapy. *Nat Rev Cancer*. 2009;9(5):351-360. doi:10.1038/nrc2603

77. Nagasawa H, Little JB. Induction of Sister Chromatid Exchanges by Extremely Low Doses of a-Particles. *Cancer Res*. 1992;52(22):6394-6396.

78. Dabrowska A, Goś M, Janik P. "Bystander effect" induced by photodynamically or heat-injured ovarian carcinoma cells (OVP10) in vitro. *Med Sci Monit*. 2005;11(9):BR316-24. Accessed January 20, 2020. http://www.ncbi.nlm.nih.gov/pubmed/16127353

79. Di X, Bright AT, Bellott R, et al. A chemotherapy-associated senescence bystander effect in breast cancer cells. *Cancer Biol Ther*. 2008;7(6):682-690. doi:10.4161/cbt.7.6.5861

80. Widel M. Bystander effect induced by UV radiation; why should we be interested? *Postepy Hig Med Dosw (Online)*. 2012;66:828-837. doi:10.5604/17322693.1019532

81. Bazak J, Fahey JM, Wawak K, Korytowski W, Girotti AW. Enhanced aggressiveness of bystander cells in an anti-tumor photodynamic therapy model: Role of nitric oxide produced by targeted cells. *Free Radic Biol Med*. 2017;102:111-121. doi:10.1016/j.freeradbiomed.2016.11.034

82. Yang H, Asaad N, Held KD. Medium-mediated intercellular communication is involved in bystander responses of X-ray-irradiated normal human fibroblasts. *Oncogene*. 2005;24:2096-2103. doi:10.1038/sj.onc.1208439

83. Marín A, Martín M, Liñán O, et al. Bystander effects and radiotherapy. *Reports Pract Oncol Radiother*. 2015;20(1):12-21. doi:10.1016/j.rpor.2014.08.004

84. Schettino G, Folkard M, Prise KM, Vojnovic B, Held KD, Michael BD. *Low-Dose Studies of Bystander Cell Killing with Targeted Soft X Rays*. Vol 160.; 2003.

85. Wang R, Coderre JA. A Bystander Effect in Alpha-Particle Irradiations of Human Prostate Tumor Cells. *Radiat Res*. 2005;164(6):711-722. doi:10.1667/3475.1

86. Gaillard S, Pusset D, De Toledo SM, Fromm M, Azzam EI. Propagation Distance of the α-Particle-Induced Bystander Effect: The Role of Nuclear Traversal and Gap Junction Communication. Published online 2009. doi:10.1667/RR1658.1

87. Palmans H, Rabus H, Belchior AL, et al. Future development of biologically relevant dosimetry. *Br J Radiol*. 2015;88(1045). doi:10.1259/bjr.20140392

88. Santa Cruz GA. Microdosimetry: Principles and applications. *Reports Pract Oncol Radiother*. 2016;21(2):135-139. doi:10.1016/j.rpor.2014.10.006

89. Chang S-Y, Kim B-H. Understanding of the Microdosimetric Quantities Obtained by a TEPC. *J*

Nucl Sci Technol. 2008;45:213-216. doi:10.1080/00223131.2008.10875825

90. Coulot J. Therapeutic Applications of Monte Carlo Calculations in Nuclear Medicine. *Phys Med Biol*. 2003;48(15):2575-2575. doi:10.1088/0031-9155/48/15/701

91. Goodhead DT. Pannel discussion: Do non-targeted effects impact the relation between microdosimetry and risk? *Radiat Prot Dosimetry*. 2011;143(4):554-556. doi:10.1093/rpd/ncq393

92. Bolch WE, Eckerman KF, Sgouros G, Thomas SR. MIRD Pamphlet No. 21: A Generalized Schema for Radiopharmaceutical Dosimetry--Standardization of Nomenclature. *J Nucl Med*. 2009;50(3):477-484. doi:10.2967/jnumed.108.056036

93. Morio J, Pastel R, Gland F Le. An overview of importance splitting for rare event simulation. *Eur J Phys*. 2010;31(5):1295-1303. doi:10.1088/0143-0807/31/5/028

94. Andreo P. Monte Carlo simulations in radiotherapy dosimetry. *Radiat Oncol*. 2018;13:121. doi:10.1186/s13014-018-1065-3

95. Badger L. *Lazzarini's Lucky Approximation of Pi*. Vol 67.; 1994. Accessed November 27, 2019. http://www.jstor.org/about/terms.html.

96. Agostinelli S, Allison J, Amako K, et al. GEANT4 - A simulation toolkit. *Nucl Instruments Methods Phys Res Sect A Accel Spectrometers, Detect Assoc Equip*. 2003;506(3):250-303. doi:10.1016/S0168-9002(03)01368-8

97. Perl J, Shin J, Schümann J, Faddegon B, Paganetti H. TOPAS: An innovative proton Monte Carlo platform for research and clinical applications. *Med Phys*. 2012;39(November):6818. doi:10.1118/1.4758060

98. Goodhead DT, Bance DA, Stretch A, Wilkinson RE. A Versatile Plutonium-238 Irradiator for Radiobiological Studies with α-particles. *Int J Radiat Biol*. 1991;59(1):195-210. doi:10.1080/09553009114550181

99. Hill M a., Stevens DL, Kadhim M, Blake-James M, Mill a. J, Goodhead DT. Experimental techniques for studying bystander effects in vitro by high and low-LET ionising radiation. *Radiat Prot Dosimetry*. 2007;122(1-4):260-265. doi:10.1093/rpd/ncl429

100. Chauhan V, Howland M, Chen J, Kutzner B, Wilkins RC. Differential Effects of Alpha-Particle Radiation and X-Irradiation on Genes Associated with Apoptosis. *Radiol Res Pract*. 2011;2011:1-9. doi:10.1155/2011/679806

101. Staaf E, Brehwens K, Haghdoost S, et al. Characterisation of a setup for mixed beam exposures of cells to 241AM alpha particles and X-rays. *Radiat Prot Dosimetry*. 2012;151(3):570-579.

doi:10.1093/rpd/ncs024

102. M V JB, Shinde SG, S SK, et al. Dosimetry and Radiobiological Studies of Automated Alpha-Particle Irradiator. *J Environ Pathol Toxicol Oncol*. 2013;32(3):263-273. doi:10.1615/JEnvironPatholToxicolOncol.2013009650

103. Nilsson J, Bauden MP, Nilsson JM, Strand S-E, Elgqvist J. Cancer Cell Radiobiological Studies Using In-House-Developed α-Particle Irradiator. *Cancer Biother Radiopharm*. 2015;30(9):386-394. doi:10.1089/cbr.2015.1895

104. Lee KH, Shin JY, Kim EH. Measurement of activity distribution in an Am-241 disc source using peeled-off Gafchromic EBT3 films. *Appl Radiat Isot*. 2018;135(September 2017):192-200. doi:10.1016/j.apradiso.2018.01.037

105. *A Handbook of Radioactivity Measurements Procedures*. National Council on Radiation Protection and Measurements; 1985. Accessed August 16, 2018. http://www.ncrppublications.org/Reports/058

106. Sollazzo A, Brzozowska B, Cheng L, et al. Alpha Particles and X Rays Interact in Inducing DNA Damage in U2OS Cells. *Radiat Res*. 2017;000:RR14803.1. doi:10.1667/RR14803.1

107. Lee KM, Lee US, Kim EH. A practical alpha particle irradiator for studying internal alpha particle exposure. *Appl Radiat Isot*. 2016;115:304-311. doi:10.1016/j.apradiso.2016.06.023

108. Niroomand-Rad A, Blackwell CR, Coursey BM, et al. Radiochromic film dosimetry: Recommendations of AAPM Radiation Therapy Committee Task Group 55. *Med Phys*. 1998;25(11):2093-2115. doi:10.1118/1.598407

109. Butson MJ, Yu PK., Cheung T, Metcalfe P. Radiochromic film for medical radiation dosimetry. *Mater Sci Eng R Reports*. 2003;41(3-5):61-120. doi:10.1016/S0927-796X(03)00034-2

110. Mukherjee B, Gholami YH, Bhonsle U, Hentschel R, Khachan J. A unique alpha dosimetry technique using Gafchromic EBT3® film and feasibility study for an activity calibrator for alpha-emitting radiopharmaceuticals. *Br J Radiol*. 2015;88(1056). doi:10.1259/bjr.20150035

111. Ebert MA, Asad AH, Siddiqui SA. Suitability of radiochromic films for dosimetry of low energy X-rays. *J Appl Clin Med Phys*. 2009;10(4):232-240. doi:10.1120/jacmp.v10i4.2957

112. Gaillard S, Armbruster V, Hill M a, Gharbi T, Fromm M. Production and validation of CR-39-based dishes for alpha-particle radiobiological experiments. *Radiat Res*. 2005;163(3):343-350. doi:10.1667/RR3307

113. Lounis Z, Djeffal S, Morsli K, Allab M. Track etch parameters in CR-39 detectors for proton and alpha particles of different energies. *Nucl Instruments Methods Phys Res Sect B Beam*

Interact with Mater Atoms. 2001;179(4):543-550. doi:10.1016/S0168-583X(01)00601-2

114. Rana MA, Qureshi IE. Studies of CR-39 etch rates. 2002;198:129-134.

115. Ismail AH. Determination of a Critical Angle for Track Revelation for Different CR-39 Nuclear Track Detector Materials. *J Zankoy Sulaimani*. 2009;12(1):109-118.

116. Rizzi M, D`Aloia M, Castagnolo B. Semiconductor Detectors and Principles of Radiation-matter Interaction. *J Appl Sci*. 2010;10(23):3141-3155. doi:10.3923/jas.2010.3141.3155

117. Darwish RAL. Development of a transmission alpha particle dosimetry technique using A549 cells and a Ra-223 source for targeted alpha therapy. *Medi*. 2016;43(11).

118. Gholami Y, Zhu X, Fulton R, Meikle S, El-Fakhri G, Kuncic Z. Stochastic simulation of radium-223 dichloride therapy at the sub-cellular level. *Phys Med Biol*. 2015;60(15):6087-6096. doi:10.1088/0031-9155/60/15/6087

119. Roeske JC, Stinchcomb TG. The average number of alpha-particle hits to the cell nucleus required to eradicate a tumour cell population. *Phys Med Biol*. 2006;51(9). doi:10.1088/0031-9155/51/9/N02

120. Berger, M.J., Coursey, J.S., Zucker, M.A., and Chang J. *ESTAR, PSTAR, and ASTAR: Computer Programs for Calculating Stopping-Power and Range Tables for Electrons, Protons, and Helium Ions (Version 2.0.1)*. National Institute of Standards and Technology, Gaithersburg, MD; 2005. Accessed August 18, 2018. http://physics.nist.gov/Star

121. Li Z, Zhang Y, Sun S, Wang B, Wei L. A semi-empirical response function for Gamma-ray of Scintillation detector based on physical interaction mechanism. 2014;(1). http://arxiv.org/abs/1407.0799

122. Eftekhari Zadeh E, Feghhi SAH, Bayat E, Roshani GH. Gaussian Energy Broadening Function of an HPGe Detector in the Range of 40 keV to 1.46 MeV. *J Exp Phys*. 2014;2014:1-4. doi:10.1155/2014/623683

123. Taheri A, Lehdarboni MA, Gholipour R. Determination of Gaussian energy broadening parameters for organic scintillators. *J Instrum*. 2016;11(5). doi:10.1088/1748-0221/11/05/P05020

124. Beaton LA, Burn TA, Stocki TJ, Chauhan V, Wilkins RC. Development and characterization of an in vitro alpha radiation exposure system. *Phys Med Biol*. 2011;56(12):3645-3658. doi:10.1088/0031-9155/56/12/012

125. Park S, Kwak SW, Kang HB. High resolution alpha particle spectrometry through collimation. *Nucl Instruments Methods Phys Res Sect A Accel Spectrometers, Detect Assoc Equip*.

2015;784:470-473. doi:10.1016/j.nima.2014.11.045

126. Henley FJ, Oldham WG. Alpha particle collimator for micron-sized beam. *Rev Sci Instrum*. 1982;53(10):1581-1585. doi:10.1063/1.1136840

127. Sato A, Aoki M, Arimoto Y, et al. Novel method for beam dynamics study using an alpha particle source. *Instrumentation*. Published online 2006:1157-1159.

128. Liacouras P, George E, Grant GT, et al. Medical 3D Printing for the Radiologist. *RadioGraphics*. 2015;35(7):1965-1988. doi:10.1148/rg.2015140320

129. Murphy S V., Atala A. 3D bioprinting of tissues and organs. *Nat Biotechnol*. 2014;32(8):773-785. doi:10.1038/nbt.2958

130. Ehler ED, Barney BM, Higgins PD, Dusenbery KE. Patient specific 3D printed phantom for IMRT quality assurance. *Phys Med Biol*. 2014;59(19):5763-5773. doi:10.1088/0031-9155/59/19/5763

131. Kowarik S, Bogula L, Boitano S, et al. A novel 3D printed radial collimator for x-ray diffraction. *Rev Sci Instrum*. 2019;90(3). doi:10.1063/1.5063520

132. Thompson JM, Elliott A, D'Abrantes S, Sawakuchi GO, Hill MA. Tracking Down Alpha-Particles: the Design, Characterisation and Testing of a Shallow-Angled Alpha-Particle Irradiator. *Radiat Prot Dosimetry*. 2019;183(1-2):264-269. doi:10.1093/rpd/ncy300

133. Dahle J, Kalanxhi E, Tisnek N. Dosimetry of a238Pu-based α-particle irradiator and its biological application in a study of the bystander effect. *Anticancer Res*. 2011;31(6):2113-2120.

134. Stone MB, Siddel DH, Elliott AM, Anderson D, Abernathy DL. Characterization of plastic and boron carbide additive manufactured neutron collimators. *Rev Sci Instrum*. 2017;88(12):123102. doi:10.1063/1.4998930

135. Ridley CJ, Manuel P, Khalyavin D, Kirichek O, Kamenev K V. A novel compact three-dimensional laser-sintered collimator for neutron scattering. *Rev Sci Instrum*. 2015;86(9):095114. doi:10.1063/1.4931695

136. How do Coulter Counters Work? - Beckman Coulter. Accessed June 8, 2019. https://www.mybeckman.uk/support/faq/products/how-do-coulter-counters-work

137. FDA. Radium Ra 223 dichloride. *Label*. Published online 2013:352393. https://www.accessdata.fda.gov/drugsatfda_docs/label/2013/203971lbl.pdf

138. Kortei NK, Odamtten GT, Obodai M, Wiafe-Kwagyan M. Mycofloral profile and the radiation sensitivity (D10 values) of solar dried and gamma irradiated Pleurotus ostreatus (Jacq.Ex. Fr.) Kummer fruitbodies stored in two different packaging materials. *Food Sci Nutr*. 2018;6(1):180-

188. doi:10.1002/fsn3.545

139. Van Gerwen SJC, Rombouts FM, Riet KV t., Zwietering MH. A data analysis of the irradiation parameter for bacteria and spores under various conditions. *J Food Prot*. 1999;62(9):1024-1032. doi:10.4315/0362-028X-62.9.1024

140. Gava Mazzola P, Christina T, Penna V, Da AM, Martins S. Determination of decimal reduction time (D value) of chemical agents used in hospitals for disinfection purposes Disinfectantsdecimal reduction time (D-value)Escherichia coliStaphylococcus aureusBacillus subtilisBacillus stearothermophilus. 2003;10:1-10. http://www.biomedcentral.com/1471-2334/3/24

141. Moreira HMR, Guerra Liberal FDC, O'Sullivan JM, McMahon SJ, Prise KM. Mechanistic Modeling of Radium-223 Treatment of Bone Metastases. *Int J Radiat Oncol Biol Phys*. 2019;103(5). doi:10.1016/j.ijrobp.2018.12.015

142. Nilsson S, Strang P, Aksnes a. K, et al. A randomized, dose-response, multicenter phase II study of radium-223 chloride for the palliation of painful bone metastases in patients with castration-resistant prostate cancer. *Eur J Cancer*. 2012;48:678-686. doi:10.1016/j.ejca.2011.12.023

143. Sartor O, Coleman R, Nilsson S, et al. Effect of radium-223 dichloride on symptomatic skeletal events in patients with castration-resistant prostate cancer and bone metastases: Results from a phase 3, double-blind, randomised trial. *Lancet Oncol*. 2014;15(June):738-746. doi:10.1016/S1470-2045(14)70183-4

144. Chittenden SJ, Hindorf C, Parker CC, et al. A Phase 1, Open-Label Study of the Biodistribution, Pharmacokinetics, and Dosimetry of 223Ra-Dichloride in Patients with Hormone-Refractory Prostate Cancer and Skeletal Metastases. *J Nucl Med*. 2015;56(9):1304-1309. doi:10.2967/jnumed.115.157123

145. Kratochwil C, Bruchertseifer F, Rathke H, et al. Targeted Alpha Therapy of mCRPC with ^{225} Actinium-PSMA-617: Dosimetry estimate and empirical dose finding. *J Nucl Med*. 2017;58(10):jnumed.117.191395. doi:10.2967/jnumed.117.191395

146. Kratochwil C, Schmidt K, Afshar-Oromieh A, et al. Targeted alpha therapy of mCRPC: Dosimetry estimate of 213Bismuth-PSMA-617. *Eur J Nucl Med Mol Imaging*. 2018;45(1):31-37. doi:10.1007/s00259-017-3817-y

147. Sathekge M, Knoesen O, Meckel M, Modiselle M, Vorster M, Marx S. 213Bi-PSMA-617 targeted alpha-radionuclide therapy in metastatic castration-resistant prostate cancer. *Eur J Nucl Med Mol Imaging*. Published online March 2017. doi:10.1007/s00259-017-3657-9

148. El Naqa I, Pater P, Seuntjens J. Monte Carlo role in radiobiological modelling of radiotherapy

outcomes. *Phys Med Biol*. 2012;57(11):R75-97. doi:10.1088/0031-9155/57/11/R75

149. Iwata K, Kawasaki K, Shigesada N. A Dynamical Model for the Growth and Size Distribution of Multiple Metastatic Tumors. *J Theor Biol*. 2000;203(2):177-186. doi:10.1006/jtbi.2000.1075

150. Talkington A, Durrett R. Estimating tumor growth rates in vivo. 2016;V(10):1934-1954. doi:10.1007/s11538-015-0110-8.Estimating

151. Hartung N, MollardSeverine, Barbolosi D, et al. Mathematical Modeling of Tumor Growth and Metastatic Spreading : Validation in Tumor-Bearing Mice. Published online 2014:6397-6408. doi:10.1158/0008-5472.CAN-14-0721

152. Pitchaimani M, Ori GS, Eakin T. Unique Estimation of Solid Tumour Growth Gompertz Parameter and Its Sensitivity Behaviour 1 Introduction. 2014;4(18):2603-2617.

153. Lamont C, Beheshti A, Tracz A, Ebos JML, Hlatky L. Classical Mathematical Models for Description and Prediction of Experimental Tumor Growth. 2014;10(8). doi:10.1371/journal.pcbi.1003800

154. Norton L. A Gompertzian Model of Human Breast Cancer Growth. *Cancer Res*. 1988;48:7067-7071.

155. Iwata K, Kawasaki K, Shigesada N. A Dynamical Model for the Growth and Size Distribution of Multiple Metastatic Tumors. *J Theor Biol*. 2000;203(2):177-186. doi:10.1006/jtbi.2000.1075

156. Butterworth, K, Ghita M. Personal communication. Published online 2018.

157. Jati A, Tatli S, Morgan JA, et al. Imaging features of bone metastases in patient with gastrointestinal stromal tumors. *Diagnostic Interv Radiol*. 2011;(October 2011):391-396. doi:10.4261/1305-3825.DIR.5179-11.1

158. Lassmann M, Nosske D. Dosimetry of 223Ra-chloride: Dose to normal organs and tissues. *Eur J Nucl Med Mol Imaging*. 2013;40(2):207-212. doi:10.1007/s00259-012-2265-y

159. Yoshida K, Kaneta T, Takano S, Sugiura M. Pharmacokinetics of single dose radium-223 dichloride (BAY 88-8223) in Japanese patients with castration-resistant prostate cancer and bone metastases. *Ann Nucl Med*. 2016;30(7):453-460. doi:10.1007/s12149-016-1093-8

160. Denis-Bacelar AM, Chittenden SJ, McCready VR, et al. Bone lesion absorbed dose profiles in patients with metastatic prostate cancer treated with molecular radiotherapy. *Br J Radiol*. 2018;(October 2017):20170795. doi:10.1259/bjr.20170795

161. Liepe K, Hliscs R, Kropp J, Runge R, Franke W. Dosimetry of 188Re-Hydroxyethylidene Diphosphonate in Human Prostate Cancer. *J Nucl Med*. 2003;44:953-960.

162. Denis-Bacelar AM, Chittenden SJ, Murray I, et al. A radiobiological model of metastatic burden

reduction for molecular radiotherapy: Application to patients with bone metastases. *Phys Med Biol*. 2017;62(7):2859-2870. doi:10.1088/1361-6560/aa5e6f

163. O'Donoghue J a, Bardiès M, Wheldon TE. Relationships between Tumor Size and Curability for Uniformly Targeted Therapy with Beta-Emitting Radionuclides. *J Nucl Med*. 1995;36(10):1902-1909.

164. Huang CY, Guatelli S, Oborn BM, Allen BJ. Microdosimetry for targeted alpha therapy of cancer. *Comput Math Methods Med*. 2012;2012. doi:10.1155/2012/153212

165. Samaratunga RC, Thomas SR, Hinnefeld JD, et al. A Monte Carlo simulation model for radiation dose to metastatic skeletal tumor from rhenium-186(Sn)-HEDP. *J Nucl Med*. 1995;36(2):336-350. http://www.ncbi.nlm.nih.gov/pubmed/7830140

166. Kaplan WD, Zimmerman RE, Bloomer WD, Knapp RC, Adelstein SJ. Therapeutic intraperitoneal 32P: a clinical assessment of the dynamics of distribution. *Radiology*. 1981;138(3):683-688. doi:10.1148/radiology.138.3.7465847

167. Howell RW, Neti PVS V., Pinto M, Gerashchenko BI, Narra VR, Azzam EI. Challenges and Progress in Predicting Biological Responses to Incorporated Radioactivity. *Radiat Prot Dosimetry*. 2006;122(4):521-527. doi:10.1093/rpd/ncl448.CHALLENGES

168. Elgqvist J, Andersson H, Bäck T, et al. Therapeutic efficacy and tumor dose estimations in radioimmunotherapy of intraperitoneally growing OVCAR-3 cells in nude mice with (211)At-labeled monoclonal antibody MX35. *J Nucl Med*. 2005;46(11):1907-1915. doi:46/11/1907 [pii]

169. Onozato Y, Kaida A, Harada H, Miura M. Radiosensitivity of quiescent and proliferating cells grown as multicellular tumor spheroids. *Cancer Sci*. 2017;108(4):704-712. doi:10.1111/cas.13178

170. Luk CK, Keng PC, Sutherland RM. Radiation response of proliferating and quiescent subpopulations isolated from multicellular spheroids. *Br J Cancer*. 1986;54(1):25-32. doi:10.1038/bjc.1986.148

171. Luk CK, Keng PC, Sutherland RM. Regrowth and Radiation Sensitivity off Quiescent Cells Isolated from EMT6/Ro-fed Plateau Monolayers. *Cancer Res*. 1985;45(3):1020-1025.

172. Hatzi VI, Laskaratou D a., Mavragani I V., et al. Non-targeted radiation effects in vivo: A critical glance of the future in radiobiology. *Cancer Lett*. 2015;356(1):34-42. doi:10.1016/j.canlet.2013.11.018

173. Anzenberg V, Chandiramani S, Coderre J a. LET-Dependent Bystander Effects Caused by Irradiation of Human Prostate Carcinoma Cells with X Rays or Alpha Particles man Prostate Carcinoma Cells with X Rays or Alpha Parti-. 2008;476:467-476.

174. Goss C. *Simplify3D Settings Manual*.; 2019.